



NUREG/CR-7167

# Assessing the Potential for Bioremediation of Uranium In Situ Recovery Sites

United States Nuclear Regulatory Commission Official Hearing Exhibit	
In the Matter of:	STRATA ENERGY, INC. (Ross In Situ Recovery Uranium Project)
	ASLBP #: 12-915-01-MLA-BD01
	Docket #: 04009091
	Exhibit #: JT1060-00-BD01
	Admitted: 10/1/2014
	Rejected:
Other:	Identified: 10/1/2014 Withdrawn: Stricken:

## AVAILABILITY OF REFERENCE MATERIALS IN NRC PUBLICATIONS

### NRC Reference Material

As of November 1999, you may electronically access NUREG-series publications and other NRC records at NRC's Public Electronic Reading Room at <http://www.nrc.gov/reading-rm.html>. Publicly released records include, to name a few, NUREG-series publications; *Federal Register* notices; applicant, licensee, and vendor documents and correspondence; NRC correspondence and internal memoranda; bulletins and information notices; inspection and investigative reports; licensee event reports; and Commission papers and their attachments.

NRC publications in the NUREG series, NRC regulations, and Title 10, "Energy," in the *Code of Federal Regulations* may also be purchased from one of these two sources.

1. The Superintendent of Documents  
U.S. Government Printing Office  
Mail Stop SSOP  
Washington, DC 20402-0001  
Internet: [bookstore.gpo.gov](http://bookstore.gpo.gov)  
Telephone: 202-512-1800  
Fax: 202-512-2250
2. The National Technical Information Service  
Springfield, VA 22161-0002  
[www.ntis.gov](http://www.ntis.gov)  
1-800-553-6847 or, locally, 703-605-6000

A single copy of each NRC draft report for comment is available free, to the extent of supply, upon written request as follows:

Address: U.S. Nuclear Regulatory Commission  
Office of Administration  
Publications Branch  
Washington, DC 20555-0001

E-mail: [DISTRIBUTION.RESOURCE@NRC.GOV](mailto:DISTRIBUTION.RESOURCE@NRC.GOV)  
Facsimile: 301-415-2289

Some publications in the NUREG series that are posted at NRC's Web site address <http://www.nrc.gov/reading-rm/doc-collections/nuregs> are updated periodically and may differ from the last printed version. Although references to material found on a Web site bear the date the material was accessed, the material available on the date cited may subsequently be removed from the site.

### Non-NRC Reference Material

Documents available from public and special technical libraries include all open literature items, such as books, journal articles, transactions, *Federal Register* notices, Federal and State legislation, and congressional reports. Such documents as theses, dissertations, foreign reports and translations, and non-NRC conference proceedings may be purchased from their sponsoring organization.

Copies of industry codes and standards used in a substantive manner in the NRC regulatory process are maintained at—

The NRC Technical Library  
Two White Flint North  
11545 Rockville Pike  
Rockville, MD 20852-2738

These standards are available in the library for reference use by the public. Codes and standards are usually copyrighted and may be purchased from the originating organization or, if they are American National Standards, from—

American National Standards Institute  
11 West 42<sup>nd</sup> Street  
New York, NY 10036-8002  
[www.ansi.org](http://www.ansi.org)  
212-642-4900

Legally binding regulatory requirements are stated only in laws; NRC regulations; licenses, including technical specifications; or orders, not in NUREG-series publications. The views expressed in contractor-prepared publications in this series are not necessarily those of the NRC.

The NUREG series comprises (1) technical and administrative reports and books prepared by the staff (NUREG-XXXX) or agency contractors (NUREG/CR-XXXX), (2) proceedings of conferences (NUREG/CP-XXXX), (3) reports resulting from international agreements (NUREG/IA-XXXX), (4) brochures (NUREG/BR-XXXX), and (5) compilations of legal decisions and orders of the Commission and Atomic and Safety Licensing Boards and of Directors' decisions under Section 2.206 of NRC's regulations (NUREG-0750).

**DISCLAIMER:** This report was prepared as an account of work sponsored by an agency of the U.S. Government. Neither the U.S. Government nor any agency thereof, nor any employee, makes any warranty, expressed or implied, or assumes any legal liability or responsibility for any third party's use, or the results of such use, of any information, apparatus, product, or process disclosed in this publication, or represents that its use by such third party would not infringe privately owned rights.

# Assessing the Potential for Bioremediation of Uranium In Situ Recovery Sites

Manuscript Completed: September 2013  
Date Published: June 2014

Prepared by:  
S. B. Yabusaki<sup>1</sup>, Y. Fang<sup>1</sup>, S. R. Waichler<sup>1</sup>, C. C. Fuller<sup>2</sup>,  
K. Akstin<sup>2</sup>, P. E. Long<sup>3</sup>, and M. Fuhrmann<sup>4</sup>

<sup>1</sup>Pacific Northwest National Laboratory

<sup>2</sup>U.S. Geological Survey

<sup>3</sup>Lawrence Berkeley National Laboratory

<sup>4</sup>U.S. Nuclear Regulatory Commission

Mark Fuhrmann, NRC Project Manager

Office of Nuclear Regulatory Research



## Abstract

In situ bioremediation (ISB) may be a more effective alternative for the restoration of uranium in situ recovery (ISR) sites than current methods. ISB involves the stimulation of indigenous microorganisms that catalyze the immobilization of targeted contaminants. Many of the post-operational contaminants found at ISR sites (e.g., uranium, vanadium, selenium, molybdenum) are in oxidized, soluble forms. This is a result of the ISR process in which oxidizing solutions are injected into the subsurface to liberate uranium from its solid matrix. In this case, ISB would be directed at the chemical reduction of these contaminants to their immobile forms. While the technique has the potential for more effective restoration, shorter restoration periods, and lower cost, it is an unproven technology that relies on the stability of uranium and other metals that are left in place. Consequently, there is a need to better understand the behavior of the uranium in the bioremediated system during and after the restoration. Licensees have been conducting studies into the effectiveness of ISB, therefore an independent examination, such as that documented in this report, is important for anticipated regulatory decisionmaking regarding its acceptability.

This report is the third in a series of technical NUREG/CRs that are intended to provide background and evaluation of uranium ISB technology. The purpose of this report is to assess the potential effectiveness of ISB for uranium ISR sites, identify performance issues, and guide future implementation and monitoring. To address the limitations of the current knowledge base of field-scale ISB uranium behavior, the approach in this document is to augment the available geological, hydrological, and chemical data from existing ISR sites with 1) laboratory studies of biologically mediated removal of uranium from solution using sediment taken from a leached out uranium ore body, 2) previous studies of uranium ISB in shallow, alluvial aquifers, and 3) coupled process modeling of hypothetical field-scale ISR restoration including: coupled flow, transport, and biogeochemical processes. The models are intended to help integrate and scale up the predicted effects from the laboratory to the field. The experimental and modeling studies presented here suggest that biostimulation of indigenous bacterial populations can be effective in lowering aqueous concentrations of uranium at ISR sites to acceptable levels.



# Contents

<b>Abstract</b> .....	<b>iii</b>
<b>Contents</b> .....	<b>v</b>
<b>Figures</b> .....	<b>ix</b>
<b>Tables</b> .....	<b>xvii</b>
<b>Executive Summary</b> .....	<b>xix</b>
<b>Acknowledgments</b> .....	<b>xxi</b>
<b>Acronyms and Abbreviations</b> .....	<b>xxiii</b>
<b>1 Introduction</b> .....	<b>1-1</b>
1-1 Demand for Uranium .....	1-1
1.1 Uranium Mining in the U.S.....	1-2
1.1.1 Uranium Ore Deposits .....	1-2
1.2 In Situ Recovery of Uranium.....	1-3
1.2.1 Requirements for ISR .....	1-5
1.2.2 Lixiviants for ISR.....	1-5
1.2.3 ISR Life Cycle.....	1-6
1.2.4 ISR Impacts and Containment Issues.....	1-7
1.3 Restoration of Uranium ISR Sites .....	1-7
1.3.1 General Description.....	1-7
1.3.2 Restoration Processes and Phases .....	1-9
1.3.3 Regulatory Standards for Restoration .....	1-11
1.4 Bioremediation .....	1-12
1.5 Document Description .....	1-14
1.5.1 Document Purpose, Approach, and Objectives .....	1-14
1.5.2 Document Contents.....	1-15
<b>2 Geochemistry and Restoration Issues</b> .....	<b>2-1</b>
2.1 Geochemistry of Roll Front Deposits .....	2-1
2.2 Geochemistry of Uranium ISR.....	2-2
2.3 ISR Restoration Issues.....	2-2
2.4 Uranium Bioremediation .....	2-4
2.5 Findings from Uranium Bioremediation Field Research in Shallow Aquifers....	2-6
2.6 Insights from Field Studies .....	2-9
2.7 ISR Biorestoration Potential .....	2-10
<b>3 Laboratory Studies of Biostimulated Uranium Reduction in ISR Aquifer Sediments and Suboxic Remobilization of Sequestered Uranium (C.C. Fuller and K. Akstin)</b> .....	<b>3-1</b>
3.1 Introduction .....	3-1

3.1.1	Objectives.....	3-1
3.1.2	Kingsville ISR Site Description.....	3-1
3.2	Methods .....	3-6
3.2.1	Sediment and Groundwater Collection and Analyses .....	3-6
3.2.2	AGW Design and Composition .....	3-9
3.2.3	Batch Experiments to Determine Electron Donors .....	3-10
3.2.4	Column Set Up and Operation.....	3-12
3.2.5	Column Effluent.....	3-15
3.2.6	Solid Phase Sampling .....	3-18
3.2.7	Microbial Assay .....	3-21
3.2.8	Spectroscopic Measurements.....	3-23
3.3	Results.....	3-26
3.3.1	Batch Experiments .....	3-26
3.3.2	Column Effluent.....	3-31
3.3.3	Solid Phase Characterization of Column Sediments.....	3-43
3.3.4	X-ray Spectroscopy and $\mu$ XRF Mapping of Column Sediment.....	3-54
3.3.5	Microbial Assay .....	3-78
3.4	Discussion of Experimental Findings.....	3-84
3.4.1	Biogeochemical Processes During Biostimulation .....	3-84
3.4.2	Stability of Immobilized Uranium.....	3-90
3.4.3	Comparison to Model Simulation of Biostimulated Reduction .....	3-93
3.5	Summary of Experimental Findings.....	3-94
<b>4</b>	<b>Simulation of Uranium Bioremediation in ISR Sediment Columns.....</b>	<b>4-1</b>
4.1	Uranium Bioremediation Modeling Studies.....	4-1
4.2	Findings from Column Experiments using Kingsville Dome ISR Sediments ....	4-2
4.3	Conceptual Bioremediation Model.....	4-7
4.4	Simulator Description .....	4-9
4.5	Simulation Description.....	4-9
4.6	Biologically-Mediated Processes: Shallow Groundwater Plume versus Deep ISR .....	4-12
4.7	Model Implementation .....	4-13
4.7.1	Uranium Speciation .....	4-15
4.7.2	Major Ion Reactions.....	4-16
4.7.4	Kinetic Reactions.....	4-17
4.8	Biostimulation Modeling Approach for the Column Experiments.....	4-18
4.9	Column Simulation Results .....	4-18
4.10	Biostimulation Studies: Deep ISR vs Shallow Aquifer.....	4-27
<b>5</b>	<b>Field-Scale Flow and Transport Modeling .....</b>	<b>5-1</b>
5.1	Overview .....	5-1

5.2	Field-Scale Coupled Process Simulator .....	5-2
5.2.1	Physical System .....	5-4
5.2.2	Model Flow System .....	5-5
5.2.3	Flow and Transport Results .....	5-10
5.3	Findings .....	5-23
<b>6</b>	<b>Field-Scale Post-ISR Biore Restoration Modeling .....</b>	<b>6-1</b>
6.1	Biore Restoration Concepts .....	6-1
6.2	Modeling Approach .....	6-2
6.3	Field-Scale Biore Restoration Modeling Results .....	6-3
6.3.1	10 Days .....	6-8
6.3.2	30 Days .....	6-16
6.3.3	Modeling Results: Injectate without Terminal Electron Acceptors .....	6-26
6.4	Background Injectate.....	6-27
6.4.1	Lactate .....	6-27
6.4.2	Acetate .....	6-28
6.4.3	U(VI).....	6-28
6.4.4	Adsorbed U(VI).....	6-29
6.4.5	U(IV).....	6-30
6.4.6	Fe(II).....	6-30
6.4.7	Phyllosilicate Fe(III) .....	6-31
6.4.8	Goethite.....	6-31
6.4.9	FeS.....	6-32
6.4.10	Sulfate .....	6-32
6.4.11	Sulfide .....	6-33
6.5	Summary of Field-Scale Model Findings .....	6-34
<b>7</b>	<b>Conclusions.....</b>	<b>7-1</b>
7.1	Considerations .....	7-4
7.2	Potential Approach.....	7-4
7.2.1	Field Characterization and Monitoring .....	7-5
7.2.3	Long-Term Monitoring .....	7-11
<b>8</b>	<b>Reference List.....</b>	<b>8-1</b>



## Figures

Figure 1-1	Weighted-average price of uranium purchased by owners and operators of U.S. civilian nuclear power reactors, 1994-2011 deliveries. ....	1-1
Figure 1-2	Uranium roll front development in confined sandstone interval showing transport of oxidized U and its' precipitation in the reduced zone (NRC, 1997).....	1-3
Figure 1-3	Schematic diagram of typical 5-spot and 7-spot injection/production well patterns (NRC, 1997). ....	1-4
Figure 1-4	Conceptual representation of the ISR process, operations, and facilities (illustration reproduced with permission from the World Nuclear Association). ....	1-6
Figure 2-1	Downgradient metal concentrations responding to acetate injection at the Rifle IFRC site. Concentrations were measured in well CD-01 from June 2010 to May 2012. (Courtesy of Ken Williams, LBNL) .....	2-7
Figure 3-1	Location of Kingsville Dome ISR site in south Texas.....	3-3
Figure 3-2	Samples were obtained by drilling into an ore zone after uranium recovery operations were finished.....	3-4
Figure 3-3	The sediment sample used for the bioremediation experiments was obtained from a depth of 580-590 feet.....	3-5
Figure 3-4	Column experimental apparatus illustrating (A) column and effluent collection, (B) effluent tubing with gas purged jacketing to minimize oxygen invasion and effluent collection bottle, (C) influent reservoir with gas mixture purge and outlet lines, (D) influent lines with gas jacketing, (E) peristaltic pump in purged housing. F) Column L2 after 46 days of biostimulation showing dark banding forming in sediment (arrow) and Sterivex filter on outlet for microbial assay test in gas jacketed housing upstream of effluent collection bottle.....	3-13
Figure 3-5	ISR sediment uranium batch uptake experiment 1. Dissolved uranium ( $\mu\text{M}$ ) versus time for different electron donor amendments. Data points are for each batch bottle duplicate. Control has no added electron donor or dissolved U(VI). The "No electron donor" bottle has 20 $\mu\text{M}$ dissolved uranium, but no added electron donor.....	3-27
Figure 3-6	ISR sediment uranium batch uptake experiment 2. (A). Dissolved uranium as ratio of initial total dissolved (20 $\mu\text{M}$ ) and (B) dissolved iron versus time for different headspace $\text{H}_2$ partial pressure amendments as electron donor, and headspace $\text{pCO}_2$ to control pH. Data points are for each batch bottle duplicate. Control has no added electron donor or dissolved U(VI). No electron donor bottle has 20 $\mu\text{M}$ dissolved uranium added, but no hydrogen added to headspace. IR is gamma irradiated. ....	3-30
Figure 3-7	Columns L1 and L2 Effluent Concentrations. Part A. Column L1 and L2 effluent dissolved uranium and iron concentrations versus days since start of lactate addition for the duration of suboxic elution of column L2 (top), and expanded time scale for biostimulated reduction (bottom).....	3-34

Figure 3-8	Cumulative loading of uranium on column L1 and L2 sediment versus time of the experiment. U loading during biostimulation (U <sub>red</sub> ) is calculated by the difference between the influent and effluent uranium times sample volume and divided by total dry mass of sediment. Loading is summed up to a given sampling time .....	3-38
Figure 3-9	Column L2 effluent dissolved uranium (red triangles) and iron (blue diamonds) during suboxic elution versus days since start of lactate addition. This is an expanded scale for Fe and time from Figure 3.7A. Effluent samples were collected with a fraction collection throughout the suboxic elution except for the period between 97 and 132 days, when samples were collected into serum bottles with outlet lines fully jacketed with equilibration gas. Oxygen (0.5%) was added to equilibration gas at day 133. Outlet line to fraction collector was jacketed with equilibration gas starting at day 138. Low Fe in effluent between days 133 and 138 was likely because of oxidation and precipitation in outlet line. The pump housing with equilibration gas flush was installed at day 153. ....	3-41
Figure 3-10	Column L5 suboxic AGW elution of the ISR 3712 B-C 580-590 sediment. Effluent dissolved uranium (blue diamonds) and iron (red triangles) versus days. Column L1 dissolved U (green diamonds) during biostimulated reduction with 20 μM U(VI) influent is shown for comparison.....	3-43
Figure 3-11	Solid phase uranium concentrations of sediments recovered after biostimulated reduction period (column L1) and after suboxic elution (column L2 and L5). (A) Uranium concentrations in columns L1, L2, and L5 by interval with pre-column sediment shown for comparison. (B) Mass distribution of uranium uptake by column interval in μmoles for columns L1 and L2 as the increase above initial total U of pre-column sediment. (C) Fraction of total uranium uptake in column by interval for columns L1 and L2. ...	3-49
Figure 3-12	Extractable iron concentration in column sediments by interval for (A) column L1 after biostimulated reduction and (B) column L2 after suboxic elution, with pre-column sediment shown for comparison. HCl represents ferrous iron as defined by 1 hour 0.5 N HCl extraction in absence of oxygen, and HH represents both ferrous and ferric as defined by 1 hour room temperature hydroxylamine hydrochloride extraction. ....	3-51
Figure 3-13	(A). Total sulfur concentration in column sediments by interval for column L1 after biostimulated reduction and column L2 after suboxic elution, with pre-column sediment shown for comparison. (B). S isotopic composition of total sulfur expressed as parts per thousand δ <sup>34</sup> S (‰).....	3-54
Figure 3-14	U LII XANES spectra of column sediments after biostimulated reduction with lactate (L1) and suboxic elution (L2). ISR pre-column background sediment, and after suboxic elution of the pre-column sediment (L5) are shown for comparison. Numbers (e.g R1) refer to column subsection interval with lower numbers closer to inlet. Sample spectra are shown in solid lines and fits in open symbols. Models for crystalline U(IV) (uraninite, UO <sub>2</sub> ) and U(VI) (andersonite), are shown for comparison.....	3-56
Figure 3-15	(A) U L <sub>II</sub> k <sup>3</sup> -weighted EXAFS spectra and (B) Fourier transformed radial distribution of EXAFS spectra (not corrected for phase shift) for ISR column	

	sediments after biostimulated reduction with lactate (L1) and suboxic elution following biostimulated reduction (L2). Pre-column experiment sediment and the crystalline urananite model are shown for comparison. Letters and numbers (e.g. R1) refer to column subsection interval with lower numbers closer to inlet. Uranium concentrations listed are total concentrations measured by hot nitric acid dissolution and include pre-column background U. ....	3-59
Figure 3-16	ISR pre-column sediment thin section: (A) Optical scan; (B) meso-scale XRF tri-color map of whole thin section panel at 30 x 30 $\mu\text{m}$ resolution with U shown in red, Fe in green, and Ca in blue. U is shown as difference between fluorescence above and below the U $L_{III}$ edge to remove contribution from Rb fluorescence. (C) Area of interest for BL2-3 XRF mapping bounded by yellow. Scale bars are in units of microns.....	3-61
Figure 3-17	X-ray microprobe XRF maps of region 1 and 2 for ISR pre-column sediment thin section shown in Figure 3.16. (A) $\mu\text{XRF}$ map of region 1 at 5 x 5 $\mu\text{m}$ resolution with iron shown in green, uranium in red and calcium in blue. Color brightness increases with concentration. (B) Region 2 scanned at 10 x 10 $\mu\text{m}$ resolution at a single energy with the image shown for iron in green, total U in red and calcium in blue. Images are mirror of Figure 3.16C and rotated 90° counter clockwise. Yellow circles mark grains where U $L_{III}$ $\mu\text{XANES}$ spectra were attempted. The spectrum for the circled area in panel B is shown in Figure 3.18 (ISR Pre-column pt 1). Scale bars are in units of microns. ....	3-62
Figure 3-18	U $L_{III}$ $\mu\text{XANES}$ spectra of points on thin sections of column sediments after biostimulated reduction with lactate (L1), suboxic elution (L2) and ISR pre-column background sediment. Letter and numbers (e.g R1) refer to column, subsection, interval with lower numbers closer to inlet (e.g. O <sub>x</sub> 1), thin section panel (B =bottom; T = top), grain, and point on grain within each thin section. Sample spectra are shown in solid lines and fits in open symbols. Models for U(IV) (crystalline urananite, UO <sub>2</sub> ) and U(VI) (andersonite, uranyl carbonate) are shown for comparison. Sample IDs and linear combination fits of percentage U(IV) and U(VI) are shown in Table 3.10. Locations of point XANES data collection are shown in Figures 3.17, 3.20B, 3.20E, 3.23A, 3.24A, 3.24B, 3.26, 3.28C, and 3.30.....	3-63
Figure 3-19	Column L1-R1 bottom panel of thin section: (A) Optical scan; (B) meso-scale XRF tri-color map of whole thin section panel with U shown in red, Fe in green, and Ca in blue, with areas of interest bounded by yellow. Scale bars are in units of microns. (C) is zoom of area 2 of meso-scale XRF map in B, with grains of interest denoted (e.g. 2A). (D) is a higher zoom of large iron grain (2A) in panel C bounded by yellow.....	3-65
Figure 3-20	X-ray microprobe U oxidation state maps of grains 2A, 2B, and 2C in lactate column sample L1-R1 thin section shown in Figure 3.19. Panel A is a U oxidation state map of grain 2A where iron is shown in blue, U(VI) in green, and U(IV) in red. Panel (B) shows only U(IV) and U(VI). Total counts for small grain in upper left of 2A are 391 for U(IV) and 634 for U(VI). The total counts from the large grain are 5347 for U(IV) and 5962 for U(VI). Panel (C) is an iron	

- $\mu$ XANES map illustrating distribution of iron sulfide (red), iron oxide (green) and S (blue). These are mirror images of Figure 3.19 and rotated 90° counter clockwise. Points in panel B depict locations of U  $\mu$ -XANES spectra shown in Figure 3.18 (L1-R1 B G2 pt 1, 2, and 3), and in panel C locations of Fe  $\mu$ -XANES spectra shown in Figure 21 (L1-R1 g2 pt 1 and 2). Panels (D) and (E) are U oxidation state maps of smaller grains (2B and 2C) shown in enlarged area of Figure 3.19C, with U(IV) in red, U(VI) in green, and Fe in blue. Total counts are 2151 for U(IV) and 3252 for U(VI) for the area imaged in D, and 5850 for U(IV) and 6918 for U(VI) in E. The U  $\mu$ -XANES spectrum collected at the center of grain 2C is shown in Figure 3.18 (L1-R1 B G2c). Scale bars are in units of microns. .... 3-66
- Figure 3-21 Fe XANES spectra of points on ISR column L1 sediment thin sections, and iron model reference mineral spectra. Points are shown in Figures 20C and 23B..... 3-67
- Figure 3-22 Column L1-R2 top panel of thin section: (A) Optical scan and (B) meso-scale XRF tri-color map with U shown in red, Fe in green, and Ca in blue. Area of interest is bounded by yellow and is enlarged in C. Bottom panel of thin section L1-R2: (D) optical scan, and (E) meso-scale XRF tri-color map of whole thin section panel with U shown in red, Fe in green, and Ca in blue. Area of interest (grain 3) is bounded by yellow. Scale bars are in units of microns..... 3-69
- Figure 3-23 X-ray microprobe maps of thin section L1-R2 top panel, grain 1 of crescent shaped iron grain shown in Figure 3.22C, but rotated 90 counter clockwise, and mirror image. (A) is tri-color U oxidation state map U(IV) shown in red, U(VI) in green, and Fe in blue. Total counts in image area 12209 for U(IV) and 16374 for U(VI). (B) is iron phase map with iron sulfide shown in red, ferrihydrite (iron oxide) in green, and sulfur in blue. Sulfur and iron sulfide map together as purple. Points in A depict locations of U  $\mu$ -XANES spectra shown in Figure 3.18 (L1-R2 T G1 pt 1, 2, and 3), and in B locations of Fe  $\mu$ -XANES spectra shown in Figure 3.21 (L1-R2 T g1 pt 1, 2, 3, and 4). Scale bars are in units of microns..... 3-70
- Figure 3-24 (A) X-ray microprobe U oxidation state map of L1-R2 bottom panel grain 3 in Figure 3.22E with U(IV) shown in red, U(VI) in green, and Fe in blue. Circle denotes the location of U  $\mu$ XANES spectrum L1-R2 B G3 shown in Figure 3.18. Total counts in imaged area are 21746 for U(IV) and 28354 for U(VI). (B) U oxidation state map of L1-R2 top grain 1B on Figure 3.22C with U(IV) in red, U(VI) in green, and Fe in blue. Circle denotes the location of the U  $\mu$ XANES spectrum L1-R2 T G1b. Total counts in imaged area are 694 for U(IV) and 3748 for U(VI). Scale bars are in units of microns. .... 3-71
- Figure 3-25 Column L2-Ox1 bottom panel of thin section: (A) Optical scan, and (B) meso-scale XRF tri-color map of whole thin section panel with U shown in red, Fe in green, and Ca in blue. (C) shows area of interest for BL 2-3 microprobe mapping bounded by yellow in B. Scale bars are in units of microns..... 3-72
- Figure 3.26 (A) X-ray microprobe XRF map of region thin section L2-Ox1 shown in yellow rectangle in Figure 3.25C. Fe is in green, U red and Ca blue. Color brightness increases with concentration. Images are mirror of Figure 3.25 and rotated 90° counter clockwise. Grains 1 and 2 are bounded by yellow ovals. (B) Detailed XRF map of grain 2 at 5 x 5 um resolution. U  $\mu$ XANES locations are

	bounded by yellow circles. U $\mu$ XANES spectra for these points are shown in Figure 3.18 and denoted L2-Ox1 B G1 pt 1 for grain 1 in A, and L2-Ox1 B pt 2 and 2b in B. Scale bars are in units of microns.....	3-73
Figure 3-27	Column L2-Ox3 top panel of thin section: (A) Optical scan; (B) meso-scale XRF tri-color map of whole thin section panel with U shown in red, Fe in green, and Ca in blue. (C) is an enlargement of the area of interest for X-ray microprobe mapping bounded by yellow in B. Scale bars are in units of microns. ....	3-74
Figure 3-28	A) X-ray microprobe XRF map at 5 x 5 $\mu$ m resolution map of the area within yellow oval in Figure 3.27C thin section L2-Ox3 top, where U is shown in red, Fe in green, and Ca in blue. The map is a mirror image and rotated 90° counter clockwise of the area in Figure 3.27. (B) 2 x 2 $\mu$ m resolution map of the high U grain circled in A showing U(IV) distribution in high area concentration increasing with color warmness (blue to red). (C) is U oxidation state of the same area in B, where U(IV) is in red, U(VI) in green, and Ca in blue. Fe was not shown because of very low concentration relative to U(IV). U $\mu$ -XANES spectrum was collected at center of highest U area of the grain and shown in Figure 3.18 (L2-Ox3 T G1 pt1). Total counts in imaged area are 2570 for U(IV) and 1049 for U(VI). Scale bars are in units of microns. ....	3-75
Figure 3-29	Column L2-Ox3 bottom panel of thin section: (A) Optical scan; (B) BL10-2 meso-scale XRF tri-color map of whole thin section panel with U shown in red, Fe in green, and Ca in blue. Area of interest for higher resolution $\mu$ XANES imaging bounded by yellow is enlarged in C. Scale bars are in units of microns. ....	3-76
Figure 3-30	X-ray microprobe U oxidation state maps of L2-Ox3 bottom panel grain 1, the circled grain in Figure 3.29C. (A) U oxidation state at 2 x 2 $\mu$ m resolution where U(IV) in red, iron is shown in green and Ca in blue. U(VI) is not shown because of very low concentration relative to U(IV). (B) U(IV) distribution of the same grain where concentration increases with color warmness blue to red. U $\mu$ -XANES spectrum was collected at center of highest U area in top part of the grain and is shown in Figure 3.18 (L2-Ox3 B G1 pt1). Total counts in XANES mapped area are 50078 for U(IV) and 2339 for U(VI). ....	3-77
Figure 3-31	(A) Column L2 backpressure at influent end of column versus time. Pressure is in pounds per square inch above atmospheric pressure. (B) Bromide tracer versus volumes of tracer influent for column L2 at the end of biostimulated reduction, and for column L5 with no biostimulation to represent initial condition of columns, plotted as the ratio of effluent to influent bromide concentration. Bromide elution for column L2 is plotted as one minus the ratio of measured bromide to the initial influent concentration.....	3-89
Figure 4-1	Effluent lactate (blue symbols) and acetate (red symbols) concentrations from column 1 (solid symbols) and column 2 (open symbols). ....	4-4
Figure 4-2	Effluent Fe(II) concentrations from column 1 (blue diamonds) and column 2 (red squares).....	4-5
Figure 4-3	Effluent U(VI) concentrations from column 1 (blue diamonds) and column 2 (red squares).....	4-6

Figure 4-4	Effluent sulfate concentrations from column 1(blue diamonds) and column 2 (red squares).....	4-7
Figure 4-5	Lactate concentrations in column effluent: comparison of model and observations from columns 1 and 2. ....	4-19
Figure 4-6	Acetate concentrations in column effluent: comparison of model and observations from columns 1 and 2. ....	4-20
Figure 4-7	Fe(II) concentrations in column effluent: comparison of model and observations from columns 1 and 2. ....	4-21
Figure 4-8	Sulfate concentrations in column effluent: comparison of model and observations from columns 1 and 2. ....	4-22
Figure 4-9	U(VI) concentrations in column effluent: comparison of model and observations from columns 1 and 2. ....	4-23
Figure 4-10	FeS(s) abundance as a function of distance from column entrance at the end of the 83-day biostimulation. (1 dm = 10 cm) .....	4-24
Figure 4-11	Sorbed U(VI) abundance as a function of distance from column entrance at the end of the 83-day biostimulation.....	4-25
Figure 4-12	U(IV) concentration as a function of distance from column entrance at the end of the 83-day biostimulation. ....	4-26
Figure 4-13	Fe(II) silicate abundance as a function of distance from column entrance at the end of the 83-day biostimulation.....	4-27
Figure 5-1	Model grid 1. The square domain is 196 m on a side, has the same spacing in the x- and y-directions, and contains 25,921 nodes. Blue dots are injection wells, red dot is extraction well.....	5-6
Figure 5-2	Model grid 1 center area, showing small cells used in the vicinity of the wells. ....	5-7
Figure 5-3	Model grid 2. The square domain is 396 m on a side, has the same spacing in the x- and y-directions, and contains 76,729 nodes. Blue dots are injection wells, red dot is extraction well.....	5-8
Figure 5-4	Model grid 2 center area, showing small cells used in the vicinity of the wells. ....	5-9
Figure 5-5	Top: change in hydraulic head in meters caused by pumping wells, in comparison to the background flow state, grid 1. Bottom: change in hydraulic head caused by pumping wells, in comparison to the background flow state, grid 2.....	5-11
Figure 5-6	Top: paths of particles initially placed around injection wells, and color contours of head change, grid 1. Bottom: paths of particles initially placed around injection wells, and color contours of head change, grid 2. ....	5-12
Figure 5-7	Travel time histograms for particles released from the perimeter of the injection wells. The travel time intervals are in days: < 10, 10 to 30, 30 to 100, 100 to 300, 300 to 1000, and > 1000. Results are presented for the four combinations of flow(east to west, and southwest to northeast) and regional groundwater gradient (0.0005, 0.005).....	5-14
Figure 5-8	Grid 1, Gradient 5e-04 E-W, D=0, tracer concentrations over time. Green dots are well locations.....	5-15

Figure 5-9	Grid 2, Gradient 5e-04 E-W, D=0, tracer concentrations over time. ....	5-16
Figure 5-10	Grid 2, Gradient 5e-04 E-W, D=10, tracer concentrations over time. ....	5-17
Figure 5-11	Grid 1, Gradient 0.005 SW-NE, D=0, tracer concentrations over time. ....	5-18
Figure 5-12	Grid 2, Gradient 0.005 SW-NE, D=0, tracer concentrations over time. ....	5-19
Figure 5-13	Grid 2, Gradient 0.005 SW-NE, D=10, tracer concentrations over time. ....	5-20
Figure 5-14	Tracer concentrations at 1000 days for 4 base cases (D=0) and 4 dispersion cases (D=10), grid 2. Black lines delineate capture zones, wherein particles within contour line are captured by the extraction well in advective transport.....	5-22
Figure 6-1	Lactate concentration (M) distribution after 2 days of injection from perimeter wells.....	6-4
Figure 6-2	Acetate concentration (M) distribution after 2 days of injection from perimeter wells.....	6-5
Figure 6-3	Aqueous Fe(II) concentration (M) distribution after 2 days of injection from perimeter wells.....	6-6
Figure 6-4	Sulfate concentration (M) distribution after 2 days of injection from perimeter wells.....	6-7
Figure 6-5	Aqueous U(VI) concentration (M) distribution after 2 days of injection from perimeter wells.....	6-8
Figure 6-6	Adsorbed U(VI) concentration (M) distribution after 10 days of biostimulation from injection wells.....	6-9
Figure 6-7	U(IV) concentration (M) distribution after 10 days of biostimulation from injection wells.....	6-10
Figure 6-8	FeOOH (goethite) concentration (M) distribution after 10 days of biostimulation from injection wells.....	6-11
Figure 6-9	FeS concentration (M) distribution after 10 days of biostimulation from injection wells.....	6-12
Figure 6-10	Adsorbed Fe(II) concentration (M) distribution after 10 days of biostimulation from injection wells.....	6-13
Figure 6-11	Lactate-driven phyllosilicate Fe(III) concentration (M) distribution after 10 days of biostimulation from injection wells. ....	6-14
Figure 6-12	Acetate-driven phyllosilicate Fe(III) concentration (M) distribution after 10 days of biostimulation from injection wells. ....	6-15
Figure 6-13	Aqueous sulfide concentration (M) distribution after 10 days of biostimulation from injection wells.....	6-16
Figure 6-14	Lactate concentration (M) distribution after 30 days of injection from perimeter wells.....	6-17
Figure 6-15	Acetate concentration (M) distribution after 30 days of injection from perimeter wells.....	6-18
Figure 6-16	Aqueous Fe(II) concentration (M) distribution after 30 days of injection from perimeter wells.....	6-19

Figure 6-17	FeOOH (goethite) concentration (M) distribution after 30 days of injection from perimeter wells.....	6-20
Figure 6-18	Sulfate concentration (M) distribution after 30 days of injection from perimeter wells.....	6-21
Figure 6-19	FeS concentration (M) distribution after 30 days of lactate biostimulation. ....	6-22
Figure 6-20	Aqueous sulfide concentration (M) distribution after 30 days of lactate biostimulation. ....	6-23
Figure 6-21	Aqueous U(VI) concentration (M) distribution after 30 days of lactate biostimulation. ....	6-24
Figure 6-22	Adsorbed U(VI) concentration (M) distribution after 30 days of lactate biostimulation. ....	6-25
Figure 6-23	U(IV) concentration (M) distribution after 30 days of lactate biostimulation.....	6-26
Figure 6-24	Lactate concentration distribution using continuous background concentrations of electron acceptors at 2, 10, 20, and 30 days. ....	6-28
Figure 6-25	Acetate concentration distribution using continuous background concentrations of electron acceptors at 2, 10, 20, and 30 days. ....	6-28
Figure 6-26	U(VI) concentration (M) distribution at 2, 10, 20, and 30 days using injectate with continuous background concentrations of electron acceptors. ....	6-29
Figure 6-27	Adsorbed U(VI) concentration distribution at 2, 10, 20, and 30 days using injectate with continuous background concentrations of electron acceptors. ....	6-29
Figure 6-28	U(IV) mineral concentration (M) distribution at 2, 10, 20, and 30 days using injectate with continuous background concentrations of electron acceptors. ....	6-30
Figure 6-29	Aqueous Fe(II) concentration distribution at 2, 10, 20, and 30 days using injectate with continuous background concentrations of electron acceptors. ....	6-30
Figure 6-30	Lactate-based phyllosilicate Fe(III) concentration distribution at 2, 10, 20, and 30 days using injectate with continuous background concentrations of electron acceptors.....	6-31
Figure 6-31	Acetate-based phyllosilicate Fe(III) concentration distribution at 2, 10, 20, and 30 days using injectate with continuous background concentrations of electron acceptors.....	6-31
Figure 6-32	FeOOH (goethite) concentration distribution at 2, 10, 20, and 30 days using injectate with continuous background concentrations of electron acceptors. ....	6-32
Figure 6-33	FeS mineral concentration distribution at 2, 10, 20, and 30 days using injectate with continuous background concentrations of electron acceptors. ....	6-32
Figure 6-34	Aqueous sulfate concentration distribution at 2, 10, 20, and 30 days using injectate with continuous background concentrations of electron acceptors. ....	6-33
Figure 6-35	Aqueous sulfide concentration distribution at 2, 10, 20, and 30 days using injectate with continuous background concentrations of electron acceptors. ....	6-33
Figure 7-1	Summary of activities leading to full-scale bioremediation deployment in the field. Hexagons represent characterization steps. Rectangles represent analysis and design steps (Long et al., 2008). ....	7-10

## Tables

Table 3-1	Kingsville Dome groundwater chemistry from wells sampled August 5-6, 2009. Major and minor cations determined by ICP-OES of filtered (0.45 $\mu\text{m}$ ), acidified samples. Anions determined by ion chromatography of filtered samples. The following elements are not reported since below method detection limits: Co, Cu, P, F (< 2E-8, 8E-8, 1E-6 M, 5E-7M). "n/m" indicates not measured. ....	3-8
Table 3-2	Artificial groundwater composition for column and batch experiments. Lactate, nutrients, trace elements and vitamins added only to AGW during biostimulation. ....	3-10
Table 3-3	Column parameters: dimensions and weights. ....	3-15
Table 3-4	Total dissolved iron in batch experiment 1 samples filtrates (<0.2 $\mu\text{m}$ ) for duplicate bottles for each electron donor. ....	3-27
Table 3-5	Integrated loss and gain from column effluent concentrations during lactate biostimulation. U, sulfate, and lactate losses are the difference between influent and effluent concentration multiplied by sample volume summed over the biostimulation period. Acetate produced (net) is millimoles transported out of the column. Acetate consumed is the difference between lactate consumed and effluent acetate. Total amount of U, reduced Fe, and total S in sediments recovered from columns are the measured concentrations minus pre-column sediment concentration in each subsectioned intervals times mass of dry sediment recovered. L2 sediments were analyzed following suboxic elution. Units are all millimoles except for uranium, which is in micromoles.....	3-37
Table 3-6	Kingsville Dome ISR 3712 B-C 580-590 sediment grain size distribution as determined by Coulter grain size analyzer.....	3-44
Table 3-7	Mineral weight percent of Kingsville Dome ISL sediment 3712 B-C 580-590 (pre-column) as determined by quantitative x-ray diffraction. ....	3-44
Table 3-8A	Column sediment solid phase uranium concentrations and whole column mass for column L1 after biostimulated reduction, column L2 after suboxic elution following reduction, and column L5 after suboxic elution. ....	3-46
Table 3-9	Summary of uranium oxidation state from best fits of bulk U XANES spectra of column sediment samples. U(IV) and U(VI) are expressed as fractions of total uranium from linear combination fitting. UO <sub>2</sub> only represents fits to sample spectra using only crystalline uraninite model. UO <sub>2</sub> + Andersonite represents fit results using crystalline uraninite as U(IV) component and andersonite for U(VI) component. * indicates measurement of second split of sample in July 2012, with first measurement in March 2010 for pre-column sediment, and December 2011 for L1-R2. All XANES were collected on U L <sub>II</sub> edge with the exception of the pre-column sample collected on the U L <sub>III</sub> edge in March 2010. $\chi^2$ represents the sum of the square of difference between sample spectrum and the fit of the spectrum using the fraction of the components listed, and is specific to individual samples. Sample spectra and fits are shown in Figure 3.14. ....	3-57

Table 3-10	Summary of uranium oxidation state from best fits of individual point $\mu$ XANES spectra on column sediment thin sections. U(IV) and U(VI) are expressed as fraction of total uranium from linear combination fitting of crystalline uraninite (UO <sub>2</sub> ) for the U(IV) component and either andersonite (AND) or U(VI) sorbed to ferrihydrite (FHY) for U(VI) components. U L <sub>III</sub> edge $\mu$ XANES were collected using a 1- $\mu$ m beam size at SSRL BL 2-3. $\chi^2$ represents the sum of the square of difference between sample spectrum and the fit of the spectrum using the fraction of the components listed, and is specific to individual samples. Sample spectra and fits are shown in Figure 20. Sample IDs represent column, interval section, thin section panel, grain and point on grain. Locations are shown on XRF maps of thin sections in Figures 3.17, 3.20, 3.23, 3.24, 3.26, 3.28 and 3.30. * denotes U $\mu$ XANES points on large iron sulfide grains.....	3-64
Table 3-11	Microbial assay of Kingsville Dome ISR pre-column sediment sample 3712 BC 580-59 showing microbial phylotypes, relative abundance, and closest BLAST hits. ....	3-81
Table 3-12	Geobacter clones from sediments recovered at the end of the lactate amendment batch uranium uptake experiment using the 3712 BC580-590 sediment.....	3-83
Table 3-13A	Sequences obtained from effluent filter collected during later stages of Fe(III) reduction. ....	3-83
Table 3-14	Summary of electron transfer during biostimulated reduction in column L1. Lactate and acetate consumed are from integrated column effluent concentrations (see Table 3.5). Reduction of U is from integrated increase in sediment recovered from column L1. Sulfate reduction is the sum integrated dissolved sulfide in effluent and the increase in total sulfur in column sediments. Iron reduction is the sum integrated dissolved iron in the effluent and the extracted iron from column sediments (see footnotes). Manganese reduction is the sum of the integrated effluent dissolved Mn and the total sediment Mn, assuming that it is all reduced. ....	3-87
Table 4-1	Hydrologic parameters for Column 1: Darcy flux, pore velocity, residence time, porosity, and dispersivity. The flow rate to the column changed at day 14; thus, the multiple values represent those before and after that time point. ....	4-10
Table 5-1	Hypothetical sand-sandstone aquifer attributes.....	5-1
Table 5-2	Well attributes for 5-spot pattern. ....	5-2
Table 5-3	Model domain and sensitivity parameters.....	5-5
Table 5-4	Grid testing attributes for Grid 1 and 2. ....	5-5
Table 5-5	Particle travel time statistics.....	5-13
Table 7-1	Prioritized Information and Monitoring Parameters for Assessment of Bioremediation of U(VI). Adapted from Long et al. (2008). ....	7-7

## Executive Summary

In situ recovery (ISR) of uranium, also known as solution mining or in situ leaching (ISL), involves the delivery of an extraction solution (typically composed of groundwater with added oxygen and bicarbonate) to uranium deposits resulting in the solubilization of uranium minerals. The uranium-bearing solution can then be pumped to the surface where uranium (and other minerals) can be separated, processed, and packaged. A common result of ISR is the persistence in groundwater of elevated concentrations of uranium and other metals, in spite of remediation techniques such as groundwater extraction (above ground treatment e.g., ion exchange, reverse osmosis) and recirculation. Complete restoration to pre-operational groundwater values is rare and it may take several years to satisfy regulatory criteria. In shallow uranium-contaminated aquifers, it has been demonstrated that indigenous microorganisms can be stimulated to chemically reduce mobile (i.e. soluble) uranium, U(VI), to immobile U(IV), even at sites where abiotic reducing agents were ineffective. The principal conclusion from this study is that in situ bioremediation (ISB) of uranium ISR sites is a potentially viable alternative to standard restoration approaches.

A key attribute of uranium ISR sites is that pre-ISR baseline conditions are naturally reducing. Thus, the bioremediation principle for uranium ISR sites is based on a return to pre-ISR hydrologic and geochemical conditions. The potential for engineered ISB was evaluated with laboratory experiments using microbiologically preserved sediments from a post-ISR site at the Kingsville Dome operation of Uranium Resources, Inc. in Texas. Lactate was used to stimulate indigenous microorganisms that catalyzed the reduction of U(VI), resulting in the precipitation of uranium from simulated groundwater flowing through column experiments. Analysis of sediment from the columns after the experiments showed that all uranium was precipitated as U(IV). In light of the potential disruption to the native microbial community by ISR operations (e.g., prolonged exposure of anaerobes to oxygen), the success of this experiment was considered to be an encouraging outcome. However, the effectiveness of biostimulated reduction as a viable long-term restoration strategy requires control of dissolved oxygen to maintain the stability of the bioreduced uranium as well as the (re)established anaerobic microbial community. Even the introduction of groundwater with low levels of dissolved oxygen to a sediment column following biostimulated reductive precipitation of uranium resulted in the slow reversal of the process and oxidative release of uranium.

A reactive transport model was developed that reproduced observations from the column experiments. The model incorporated equilibrium and kinetic reactions including biologically mediated terminal electron accepting processes (TEAPs) for solid phase Fe(III), aqueous U(VI), and aqueous sulfate; aqueous and nonelectrostatic surface complexation for Fe(II) and U(VI); calcite, siderite, FeS, S secondary minerals; sulfide promoted dissolution of Fe(III) minerals, and major ion chemistry. This enabled the model to simulate the concentrations and timing of the monitored components in the column experiments.

A hypothetical field-scale 5-spot ISR well pattern comprised of a central extraction well surrounded by 4 injection wells was simulated by a model using confined aquifer geometries

and material properties associated with sandstone uranium ore deposits. Even with the simplified hydrology and assumed homogeneous distribution of properties, the operation of the 5-spot well pattern leads to nonuniform flow fields; i.e. flow rates are location-dependent. Thus, some parts of the aquifer in the most direct flow paths between the injection wells and the production well are exposed to considerably more injectate than paths with longer travel times. This is important when considering how injected fluids will be distributed and therefore where, when and how much bioremediation will take place. Furthermore, the convention of using an extraction pumping rate 1% more than the total injection rates of the four perimeter wells was found to not necessarily be adequate to prevent excursions of injectate and/or mobilized metals. While most of the material injected in the perimeter wells of the five-spot pattern will be captured by the central pumping well, higher regional gradients increase the opportunity for excursions of injectate beyond the capture zone. Flow patterns will be substantially more complex for large well-fields in naturally heterogeneous subsurface systems.

Biostimulation was modeled using injected groundwater amended with lactate in each of the four perimeter wells of the 5-spot pattern. Scenarios for ISB were investigated using the biogeochemical reaction network observed in the column study. The quality of injected water significantly affected bioremediation reaction rates. One implication is that removal of terminal electron acceptors, such as sulfate, from groundwater that is amended with lactate and reinjected into the treatment zone, should decrease the amount of lactate needed over time. While the introduction of less carbon might reduce the potential for biofouling (which can plug wells and sediment making injection of more water difficult), it will also decrease the amount of FeS mineral produced. These minerals help maintain the low redox potential that controls the quality of restored water. Some U(VI) is sorbed on the sediment but the removal of uranium from the water column geochemically causes the sorbed uranium to enter solution making it available for bioreduction to very low solubility U(IV). This cycle of liberating U(VI) into solution followed by bioreduction progressively depletes U(VI) from the solid phase of the treatment zone and establishes a lower redox potential for the system, with nearly complete conversion of uranium to the reduced low solubility form.

The interplay between variable flow rates in the subsurface and biological reaction rates results in spatially variable distributions of uranium and other components of interest. Under the modeling assumptions, bioremediated areas should become stabilized within months. While stabilization of a site with naturally occurring regions of lower permeability may take longer, bioremediation of post-ISR aquifers has the potential to more effectively restore groundwater quality in less time than the current state of practice. This conclusion is based on previous studies of ISB of uranium in shallow aquifers, laboratory studies using preserved sediments from an unrestored ISR aquifer, and numerical simulations of a hypothetical field implementation with lactate biostimulation of indigenous metal reducing bacteria. Absent from the weight of evidence favoring bioremediation of uranium ISR sites is a well-conceived field study. The unique attributes of each ISR site are likely to prevent a "one size fits all" approach to ISB. It is therefore important to develop a sufficiently mechanistic understanding of the site-specific processes, properties, and conditions controlling ISB. This will help determine if biostimulation can be successful at a given site and, if it can, what approach will be the most effective.

## Acknowledgments

Mark Pelizza and Bobby Jemison, URI, were instrumental in providing access to the Kingsville Dome ISR site for sampling, drilling for ISR-mined sediments, providing water quality data sets used in this analysis, and helpful comments on the draft report. Bill Deutsch, PNNL (retired), led the drilling campaign and coordinated field activities with URI.

We thank the following NRC staff members for their contributions to this document: Steve Cohen and Doug Mandeville for their guidance and useful discussions, and Elise Striz who provided valuable insights and comments in her review of this document. We especially thank Earl Greene (USGS) and Tom Nicholson (NRC) for their help and encouragement.

We thank the following USGS scientists for their efforts on this study: Alex Blum for XRD analysis, Shelley Hoefft for assistance in HPLC measurements and guidance in microbial protocols, Steve Silva for total and isotopic composition of sulfur in sediments, Julie Kirshtein for microbial assay work, and Larry Miller for many discussions on microbial and biogeochemical processes. Sam Webb and Ben Kocar of SSRL are acknowledged for assistance in micro-focused X-ray imaging. John Bargar of SSRL provided uranium reference spectra and guidance in XAS data collection and interpretation. Portions of this research were conducted at the Stanford Synchrotron Radiation Lightsource, a national user facility operated by Stanford University on behalf of the US Department of Energy, Office of Basic Energy Sciences. The SSRL Structural Molecular Biology Program is supported by the Department of Energy, Office of Biological and Environmental Research, and by the National Institutes of Health, National Center for Research Resources, Biomedical Technology Program.

Massively parallel processing simulations were performed on the Chinook supercomputer at the Environmental Molecular Sciences Laboratory (EMSL), a national scientific user facility sponsored by the Department of Energy's Office of Biological and Environmental Research and located at Pacific Northwest National Laboratory.



# Acronyms and Abbreviations

## Organizational Acronyms

BER	Office of Biological and Environmental Research in DOE/SC
CESD	Climate and Environmental Sciences Division of DOE/SC/BER
DOE	U.S. Department of Energy
EPA	U.S. Environmental Protection Agency
IFRC	Integrated Field Research Challenge; SBR program
NRC	U.S. Nuclear Regulatory Commission
SBR	Subsurface Biogeochemical Research; CESD research program
SC	(DOE) Office of Science
UMTRA	(DOE) Uranium Mill Tailings Remedial Action program

## Terminology

% (v/v)	volume percent
% (wt/v)	weight to volume percent for solid in solution
$\mu\text{mol/g}$	micromoles per gram of solid
[U]	dissolved uranium
$\mu\text{M}$	micromoles per liter
$\mu\text{mol}$	micromoles
‰	parts per thousand used to express $\delta^{34}\text{S}$
16S rRNA clone library	technique to identify microorganism phylogeny by comparison to known gene sequences
AGW	artificial groundwater
As	arsenic
AVS	acid volatile sulfide
Ca	calcium
cc/min	gas flow rate in cubic centimeters per minute
$\text{CO}_2$	carbon dioxide
DGGE	denaturing gradient gel electrophoresis; gene sequence comparison technique
DNA	deoxyribonucleic acid
DO	dissolved oxygen
DWS	drinking water standard
Eh	redox potential
Fe	iron
Fe(II)	iron in the +2 oxidation state, ferrous iron
Fe(III)	iron in the +3 oxidation state, ferric iron
$\text{FeCO}_3$	siderite
FeS	iron sulfide mineral
$\text{FeS}_2$	pyrite
g/L	mass of solid in grams per liter of solution
GPR	ground penetrating radar
GW	groundwater
ISB	in situ bioremediation
ISI	in situ sediment incubator

ISL	in situ leach
ISR	in situ recovery
IX	ion exchange; also targeted cation removal by sorption to resin beds
K <sub>d</sub>	adsorption partition coefficient
KeV	kiloelectron volts
meq/L	milliequivalents per liter
Mg	magnesium
mL	milliliters
MLS	multilevel sampler
mM	millimoles per liter
mmol	millimoles
mmol/g	millimoles per gram of solid
Mn	manganese
Mn(II)	manganese in the +2 oxidation state
Mn(IV)	manganese in the +4 oxidation state
Mo	molybdenum
mRNA	messenger ribonucleic acid
N <sub>2</sub>	nitrogen gas
N <sub>2</sub> O	nitrous oxide gas
NA	not applicable
O <sub>2</sub>	oxygen gas
ORP	oxidation-reduction potential
Pb	lead
pe	negative log <sub>10</sub> of the electron activity
pH	negative log <sub>10</sub> of the hydrogen ion activity
PLFA	phospholipid fatty acid; analysis for microbial community structure using fatty acid biomarkers
Ra	radium
rDNA	ribosomal deoxyribonucleic acid
RNA	ribonucleic acid
RO	reverse osmosis
rRNA	ribosomal ribonucleic acid
S	sulfur
Se	selenium
<i>Sp.</i>	biological species
TDS	total dissolved solids
TEA	terminal electron acceptor
TEAP	terminal electron accepting process
U	uranium
U(IV)	uranium in the +4 oxidation state
U(VI)	uranium in the +6 oxidation state
V	vanadium
XRF	X-ray fluorescence
δ <sup>34</sup> S	sulfur-32 isotopic composition as difference from standard reference material
μM	micromoles per liter
UO <sub>2</sub>	uraninite

# 1 Introduction

## 1.1 Demand for Uranium

In 2010, nuclear energy from 104 reactors accounted for 19.2% of the electricity generated in the U.S. (Nuclear Energy Institute). The U.S. currently has the highest uranium requirements of any country, more than double that of the next country, France (World Nuclear Association). This is in spite of the fact that the last nuclear power plant built in the U.S. was Tennessee's Watts Bar 1 in 1996.

Uranium is acquired as uranium oxide ( $U_3O_8$ ) concentrate, which is the end product from the mining industry. Over the last 5 years, the annual U.S. mine production of uranium has remained relatively stable at ~2000 tonnes of  $U_3O_8$ . This is a small fraction of the U.S. requirement, compelling the U.S. to import the bulk of its uranium. In 2011, U.S. civilian nuclear power reactors purchased ~25,000 tonnes  $U_3O_8$  (equivalent) at a weighted-average price of \$55.64 per pound, an increase over 2010 when ~21,300 tonnes  $U_3O_8$  were purchased at a weighted average price of \$49.29 (**Figure 1.1**). This is significant in the aftermath of the March 11, 2011 disaster at the Fukushima Daiichi Nuclear Power Plant when the Japanese and German governments announced plans to phase out nuclear power generation. To some degree, new and planned reactor construction in China, Russia, and India are offsetting the potential loss in demand.

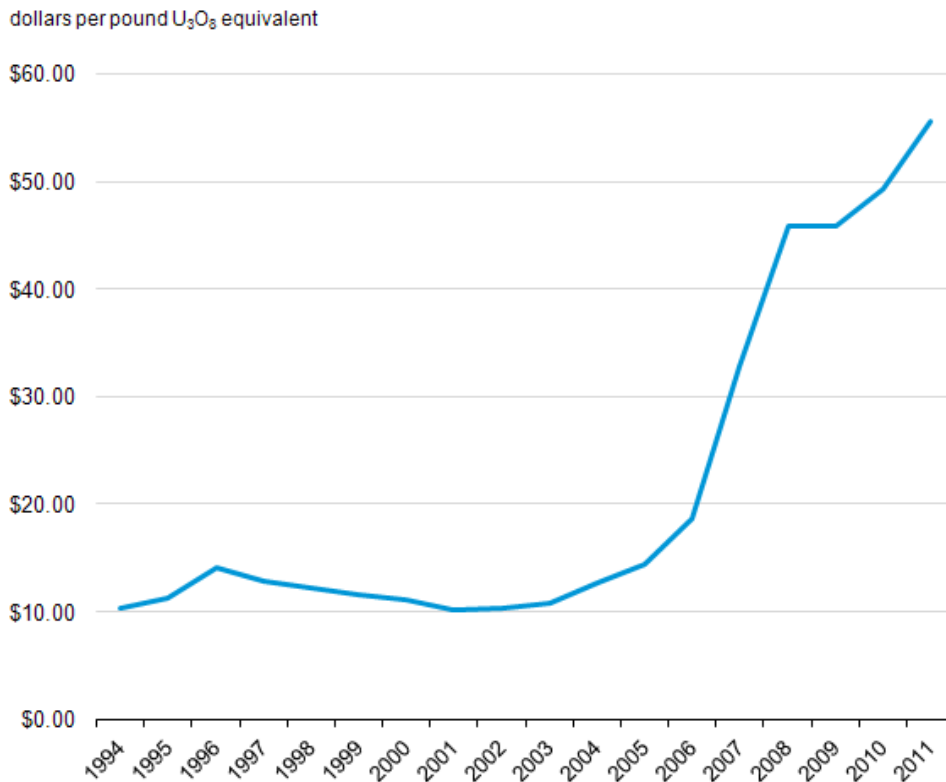


Figure 1.1  
Weighted-average price of uranium purchased by owners and operators of U.S. civilian nuclear power reactors, 1994-2011 deliveries.

Sources: U.S. Energy Information Administration: 1994-2002-Uranium Industry Annual reports. 2003-2011-Form EIA-858, "Uranium Marketing Annual Survey".

## 1.2 Uranium Mining in the U.S.

Uranium is ubiquitous in the subsurface with a general crustal abundance of about 3 ppm. Uranium ore deposits at in situ recovery (ISR) sites typically exceed 500 ppm. The general requirement for uranium recovery is to find an ore body that is sufficiently concentrated and recoverable to economically justify exploitation. Some of the advantages of ISR over conventional open cut and underground mining are: (1) little surface disturbance, (2) no tailings or waste rock, (3) economical exploitation of lower uranium content ores, (4) minimal exposure of workers to dust, heavy machinery, radiation and confined space hazards, (5) no large open cut or underground mine to rehabilitate and (6) lower capital, infrastructure and manpower requirements.

Of the 6 uranium production facilities operating in the U.S. in 2011, 5 were ISR plants (Alta Mesa, Crow Butte, Hobson/La Pangana, Smith Ranch-Highland, Willow Creek), while the other (White Mesa Mill) employed conventional milling of uranium-bearing ore. ISR plants account for the bulk of the U.S. uranium production. Worldwide, ISR extraction has been steadily increasing and in 2011 accounted for nearly half of all production, led by Kazakhstan.

### 1.2.1 Uranium Ore Deposits

**Types of Orebodies.** Uranium deposits can be found in three principal rock types: (1) igneous rock of hydrothermal origin, (2) Precambrian pyrite-containing conglomerates, and (3) more recently formed sedimentary rock. In the latter category are sandstone formations associated with chemically reducing conditions. The focus of this report is on uranium roll front deposits in saturated sandstone formations with sufficient access and permeability for ISR to be effective.

Uranium roll front ore deposits develop through a sequence of steps beginning with recharge moving downward through uranium-bearing sandstone (**Figure 1.2**). Dissolved oxygen in the water percolating through the sandstone oxidizes and mobilizes the solid-associated uranium. When the aqueous oxidized form of uranium, U(VI) (e.g.,  $\text{UO}_2^{++}$ ,  $\text{UO}_2\text{-CO}_3$  complexes, etc.), is transported in the groundwater to a zone of lowered redox potential (i.e., chemically reducing conditions), oxygen is the initial terminal electron acceptor depleted via reduction to water. Subsequently, mobile uranium in the +6 oxidation state is transformed through redox reactions to the +4 oxidation state. Under most environmental conditions, this results in the formation of an immobile, essentially insoluble, solid uranium mineral (e.g., uraninite, pitchblende, etc.). The reduction of the U(VI) is generally thought to be mediated by microbial processes, requiring organic matter for carbon and electron donor to enrich the biological respiration of terminal electron acceptors that include U(VI).

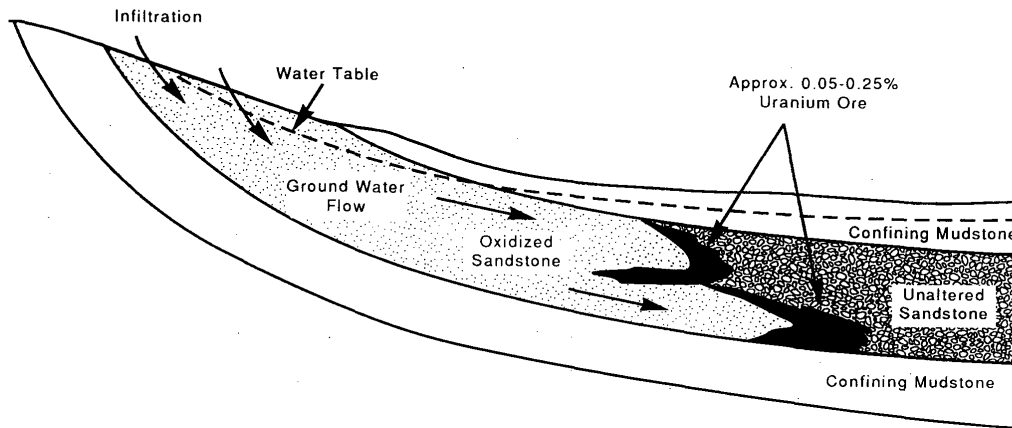


Figure 1.2 Uranium roll front development in confined sandstone interval showing transport of oxidized U and its' precipitation in the reduced zone (NRC, 1997).

The lenticular, crescent-shaped deposits are formed at the redox interface with reducing conditions downgradient and oxidizing conditions upgradient. Over time, the continuous supply of oxidizing uranium-bearing groundwater can deplete the reduced mineral phases (e.g., pyrite) and organic carbon resulting in the migration of the reduction front in the direction of groundwater flow. The crescent tips are often strung-out, resulting in tabular blanket deposits. This continual advancement results in long (~100s of meters), concentrated uranium deposits. Depending on the number and integrity of the low permeability confining interbeds (e.g., shale, mudstone), a system of tabular, sometimes interconnected roll fronts can develop. Individual ore bodies in the sandstone lenses vary in size, but they are commonly a few tens of meters wide and several meters thick. For a given roll front of interest, the continuity of the bottom and top confining impermeable layers is key to controlling the hydraulics required by ISR.

### 1.3 In Situ Recovery of Uranium

In situ recovery (ISR), also known as solution mining or in situ leach (ISL), involves the delivery of a solution to uranium deposits at depth that will result in the solubilization of solid-associated uranium. In this case, the technique targets uranium-bearing roll front deposits in typically confined aquifers where the uranium minerals exist primarily in the reduced oxidation state U(IV), maintained by chemically reducing conditions (i.e., low redox potential, or Eh). While in the past, and currently in some other countries, harsh chemicals were used, this is no longer the case in the United States. Currently, lixiviant, which is the solution pumped into the

ore zone to extract the uranium, consists of groundwater pumped from the ore zone and then returned to the subsurface after adding oxygen (either as O<sub>2</sub> gas bubbled into the water or as hydrogen peroxide). The oxygen added to the water converts the low solubility U(IV) of the ore minerals to U(VI) which has much higher solubility. At some locations, depending on the mineralogy, a source of carbon dioxide is also added (either as CO<sub>2</sub> gas or as sodium bicarbonate). This provides carbonate ions to complex uranium, enhancing its solubility. At other sites there is sufficient carbonate in the ore zone that none needs to be added. The pregnant solution containing the extracted uranium is then pumped to the surface where uranium (and other minerals) can be separated, processed, and packaged. In a typical ISR mine unit, hundreds of wells are drilled approximately 30-40 m apart in a “grid pattern” over ore bodies found in sandstone groundwater aquifers (**Figure 1.3**).

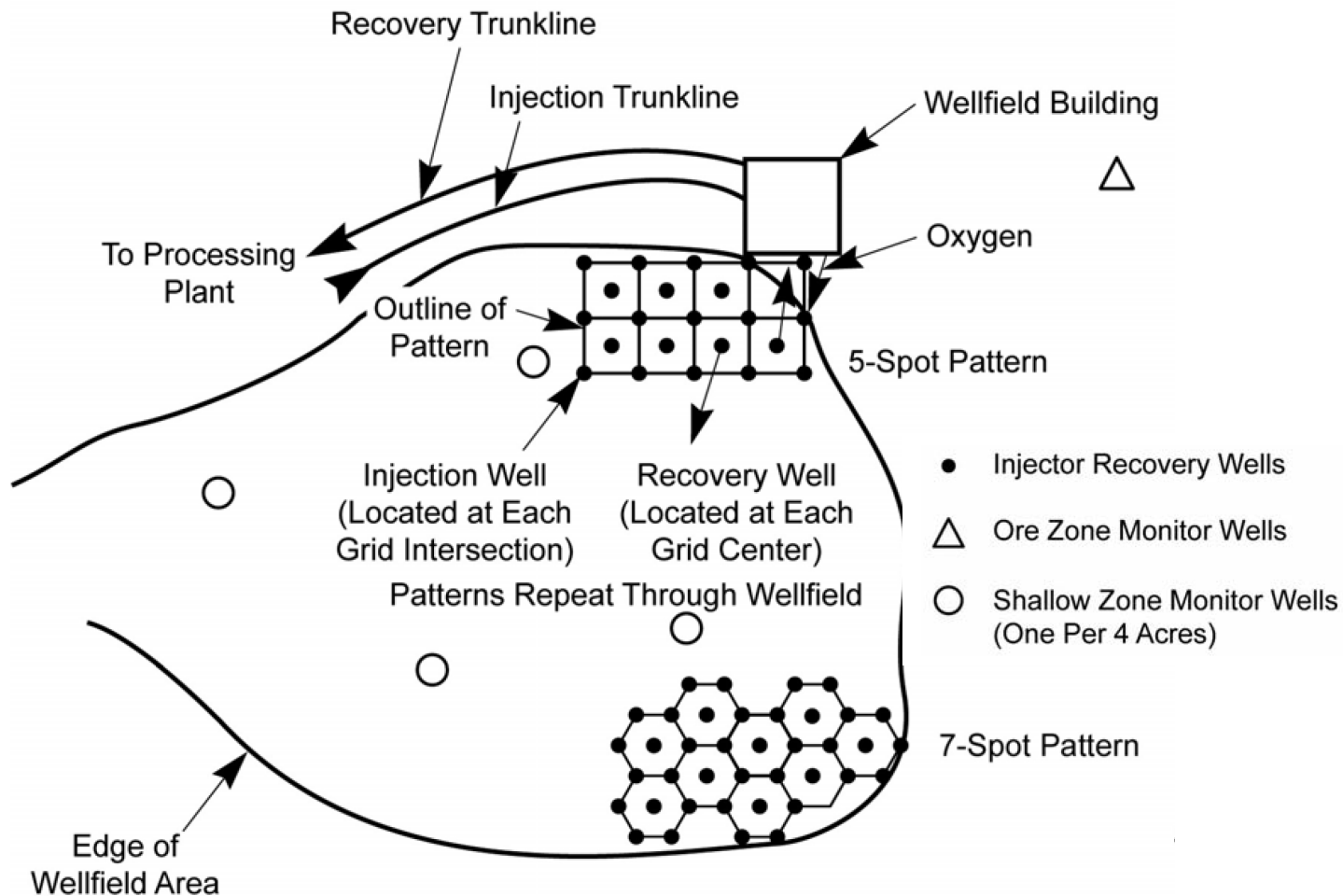


Figure 1.3 Schematic diagram of typical 5-spot and 7-spot injection/production well patterns (NRC, 1997).

### 1.3.1 Requirements for ISR

Uranium ISR extraction is most feasible when the following conditions are met.

- 1) The formation hosting the uranium mineralization is water-saturated in an aquifer confined above and below by relatively impermeable strata (e.g., shale or mudstone). The confining layers allow more hydraulic control and containment. ISR has been successfully employed in partially saturated aquifers (e.g., Hobson Project, Texas) but this is not a common scenario for a roll front deposit because of potential issues with oxygenation, drawdown, and sensitive water resources.
- 2) The permeability of the host sandstone unit is sufficiently permeable,  $> 4\text{E-}13 \text{ m}^2$  (0.4 Darcy, 0.3 m/d hydraulic conductivity equivalent), to permit lixivants to be introduced and circulated using a system of injection and pumping wells. This is the upper end of the sandstone permeability range.
- 3) The uranium ore is accessible to the circulated lixiviant and in a chemical form that is leachable by the lixiviant.

### 1.3.2 Lixivants for ISR

Uranium can be liberated into solution through dissolution of the uranium-bearing solid matrix using: (1) acid (e.g., sulfuric acid), (2) oxidation of the U(IV) minerals (e.g., uraninite) using an oxidant (e.g., oxygen, hydrogen peroxide, sodium chlorate, sodium hypochlorite, or potassium permanganate), and/or (3) alteration of the geochemistry that favors the formation of stable aqueous U(VI) complexes using salt solutions (e.g., sulfate, bicarbonate, carbonate, and ammonium). The ideal lixiviant is one that will oxidize the uranium in the ore and contains a complexing agent that will dissolve and form strong aqueous complexes that remain dissolved and interact little with the host rock (Davis and Curtis, 2007).

In the U.S., the lixivants used for uranium ISR are typically comprised simply of an oxidant and alkaline complexant. Currently, the typical lixiviant is a low strength solution of bicarbonate and oxygen maintained at circumneutral pH. At some sites, it is only necessary to add oxygen to groundwater to form the lixiviant since reactions in the subsurface then generate sufficient carbonate to complex uranium. The oxygen is incorporated into the lixiviant by dissolving oxygen gas into the groundwater using above ground saturators or by sparging at depth in the injection well. The pH is primarily used to control calcium solubility, which affects secondary mineral formation. In the past, the difficulty of restoring groundwater quality to an acceptable condition when ammonia-based lixivants were used led to a shift to oxygen and sodium bicarbonate- or carbon dioxide-based leaching chemistry by the early 1980s (Tweeton and Peterson, 1981). In addition to environmental issues, another concern with the use of strong acid or base solutions is pore clogging from secondary mineral formation (Montgomery, 1987; Nigor et al., 1982; Mudd, 1998).

It should be noted that acid can be an effective, albeit non-selective, lixiviant; especially where carbonate minerals are in relatively low abundance. For example, ISR in Kazakhstan generally employs high acid concentrations without oxidants in their lixiviants. In the U.S., however, the use of oxygen/bicarbonate lixiviants is preferable to the regulatory agencies and the public, primarily for environmental considerations.

### 1.3.3 ISR Life Cycle

After the initiation of lixiviant introduction and the first arrival of elevated uranium concentrations at the production wells, it does not take very long (~days) for the concentrations to peak (typically 300 – 600 mg/l). This is followed by a rapid decline that slows as concentrations reach 25 - 70 mg/l, which is the general production range (Schmidt, 1987). The lower end of the range is tolerable at higher sustained pumping rates. When uranium concentrations decrease to 10 - 20 mg/l, the economics of an ISR operation typically dictates an end to the extraction phase. This may take 8 months to 3 years, with most uranium ISR operations ending after less than 2 years. Schmidt (1987) stated that 86% of the uranium in the Ruth (Wyoming) ore zone was recovered during an 11-month extraction of the subsurface with sodium bicarbonate solution using oxygen as the oxidant. Dissolved uranium concentrations peaked at 130 mg/l (as  $U_3O_8$ ) after 3 months of leaching and steadily declined thereafter to 56.3 mg/l after 11 months. Figure 1.4 shows a conceptual representation of the ISR process and associated facilities.

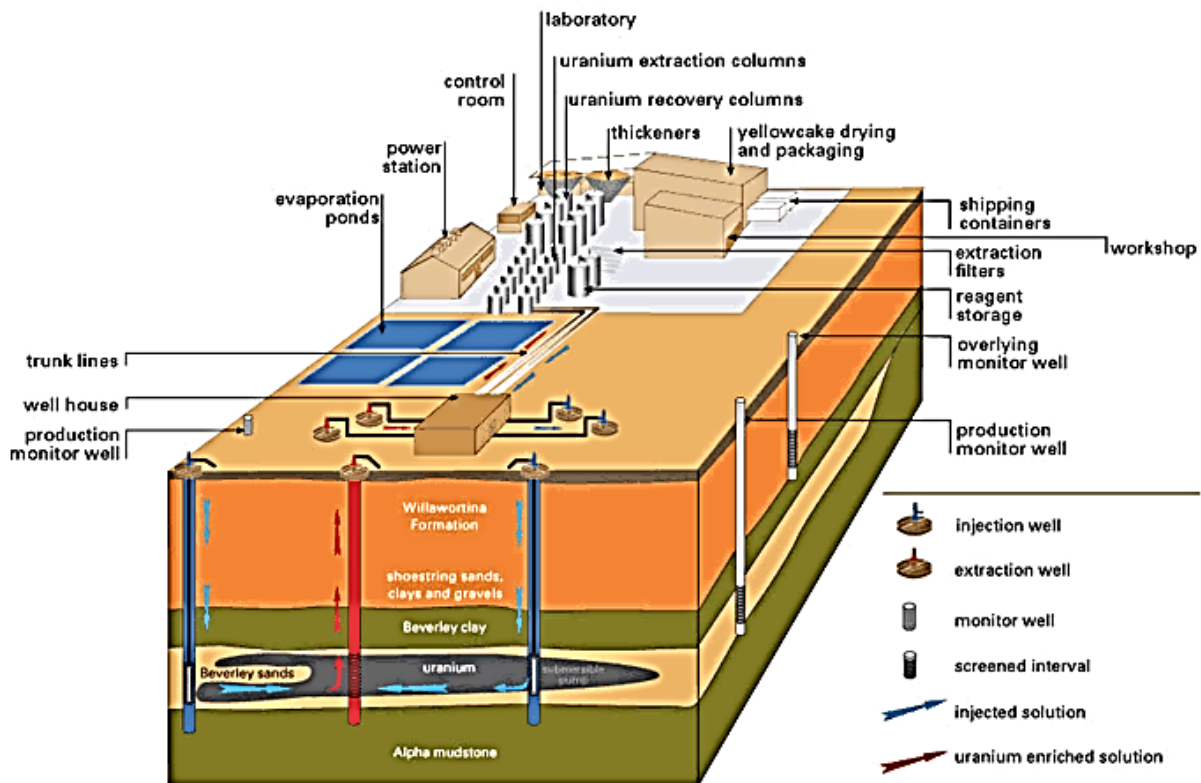


Figure 1.4 Conceptual representation of the ISR process, operations, and facilities (illustration reproduced with permission from the World Nuclear Association).

### **1.3.4 ISR Impacts and Containment Issues**

ISR targets ore bodies in aquifers which lie beneath the water table. This raises some potential environmental issues. Leaching solution that escapes from the leach area can contaminate the extraction zone periphery with leached-out contaminants. The principal issues associated with ISR uranium extraction performance include (1) controlling the lixiviant transport and reactions in naturally complex physically, geochemically, and biologically heterogeneous subsurface materials; (2) restoring groundwater to pre-operational water quality, and (3) disposing of large volumes of wastewater and solutions. Post-ISR groundwater is often characterized by significantly elevated concentrations of a number of regulated parameters. Redox sensitive elements are especially likely to be present at elevated concentrations; these include uranium, arsenic, selenium, molybdenum, and vanadium. Other parameters that have been observed to not return to their baseline levels include: chloride, conductivity, calcium, sodium, total dissolved solids, and radium-226. Thus, the primary concerns are for the excursion of the regulated contaminants into adjacent groundwater resources (Lands and Council, 1999) and the incomplete or ineffective restoration of the ISR-impacted aquifer. The design of an ISR operation for a targeted uranium ore body is mandated by regulation to include the containment of the introduced lixiviants and mobilized contaminants (e.g., Mo, As, Se, V, Ra-226) as well as the mobilized uranium. The objective is to prevent contamination of groundwater away from the ISR-impacted zone by siting and designing the operation of injection and pumping well networks to control solution migration and prevent unintended excursions. Furthermore, monitoring wells outside the treatment zone are used to detect potential excursions of injectate or mobilized contaminants. This includes vertical excursions into overlying and underlying formations that may result from casing failures and improperly sealed exploration bores (Marlowe, 1984; Staub, 1986). The likelihood for this occurring increases with the number and age of wells (Marlowe, 1984).

Water-quality effects within the well field during ISR are caused primarily by chemical reactions between the oxygen in the lixiviant and the geologic medium containing the uranium ore (Davis and Curtis, 2007). Numerous chemical interactions are possible between the lixiviant and the uranium ore, associated secondary minerals, and host rock formation. Common radioactive constituents that may be mobilized by uranium ISR activities include uranium, radium, radon, and their respective daughter products. Trace elements of concern with respect to water quality include arsenic, vanadium, zinc, selenium, molybdenum, iron, and manganese (Kasper et al., 1979).

## **1.4 Restoration of Uranium ISR Sites**

### **1.4.1 General Description**

Once the economically extractable uranium has been removed in 1-3 years and ISR operations cease, the residual concentrations of uranium and other groundwater contaminants are known to persist at concentrations in excess of regulatory limits. The process introduces a considerable amount of oxidant to the area. The general issue is the recalcitrance of the oxidized contaminants to return to their less mobile lower oxidation states. Ideally, the restoration of the groundwater quality at an ISR site would simply be the reversal of the

oxidation and complexation processes engineered by the delivery of lixiviants to the ore body. However, the use of chemical reductants to lower the redox potential of the groundwater has not generally been effective (Schmidt, 1987).

To achieve restoration, constituents added to the groundwater for extraction and those mobilized during the extraction process must be removed or rendered immobile. In some cases, it may also be necessary to chemically treat the geologic formation in order to reverse or inhibit reactions initiated during the extraction phase. The optimum restoration technique for a given site will largely be dictated by the inherent geologic, geochemical, and hydrologic conditions of that site, supported by operational observations.

Early proponents (Buma, 1979) argued that natural geochemical processes within aquifers could restore ISR-contaminated groundwater. The assumption was that reductants present in the post-ISR sediments would lead to precipitation of reduced compounds; scavenging of metals by pyrite, organic matter, calcite and ferric oxyhydroxides; and adsorption by quartz, feldspars, and clays. While this may be a plausible scenario, it is difficult to predict the time required and the rates at which natural geochemical processes could attenuate the mobilized contaminants (Rojas, 1987), let alone answer the question whether reducing conditions would ever return via natural processes.

In fact, natural attenuation, alone, has not been demonstrated to be effective in regulatory time frames; consequently, intervention is required to restore the groundwater quality to acceptable levels. During the restoration phase the concentrations of regulated elements mobilized during leaching must be decreased below restoration targets. The primary regulatory restoration goal is to return the geochemistry to (or very near) pre-operational water quality. Failing this, it is possible to apply for alternate concentration limits, which are above baseline concentrations but judged by the regulator to be protective of human health. Thus, numerical values of measured, pre-operational groundwater parameters (typically ~35) determine the primary restoration levels.

The restoration of an ISR site typically requires long-term operation of pumps and may require much longer duration than the uranium extraction period. In this regard, the decommissioning experience at ISR uranium production facilities indicates that, in general, groundwater restoration represents a significant portion (approximately 40%) of the total costs of decommissioning (Davis and Curtis, 2007). The major cost of groundwater restoration activities is directly related to the volume of water pumped from or recirculated through the ore zone aquifer.

Recent surety bond estimates for ISR facilities indicate that the groundwater restoration portion of the total costs of decommissioning are higher than the approximately 40% shown in the 1994 data. The surety estimate for the Highland uranium project was \$10.5 million out of the \$15 million subtotal without overhead or contingency (70%) (PRI, 2006a), while the surety estimate for Smith Ranch was \$11 million out of \$14.3 million (77%) (PRI, 2006b).

Consequently, post-ISR restoration is an important part of the ISR license application process administered by the NRC. Specifically, the applicant must provide technical and financial assurances that the site can and will be restored to levels that are acceptable to the

regulating agencies. If the potential restoration of groundwater quality after leaching cannot be demonstrated, the commercial license will not be granted.

#### **1.4.2 Restoration Processes and Phases**

Restoration is based on techniques that attempt to remove residual lixiviant and lower aqueous concentrations of uranium and other contaminants that became elevated during ISR operations. Three basic methods can be applied to achieve restoration:

**Groundwater Sweep.** In the initial phase of restoration, contaminated groundwater is continuously pumped from selected wells in the ISR well field without recirculation. The intent is to remove mobile contaminants from areas that have been affected by the lixiviant during ISR and draw in uncontaminated native groundwater from outside the leach zone to replace the pumped groundwater. This method is called groundwater sweep. Typically, with respect to the contaminants associated with the ISR operations (uranium, chloride, radium, etc.), groundwater quality improves significantly during the groundwater sweep process (Schmidt, 1989; Rio Algom, 2001). One issue, however, is that large amounts of solution have to be disposed of in water storage facilities, evaporation ponds, sprayed on land surface or injected into deep disposal wells after treatment.

Groundwater sweep alone is typically insufficient and uneconomical for complete groundwater restoration of commercial-scale ISR operations. Because of heterogeneities in the aquifers, the fresh groundwater that is brought into the ore zone does not completely displace the residual lixiviant (Deutsch et al., 1985). Many pore volumes<sup>1</sup> of groundwater would need to be pumped in order to reach the original baseline conditions, perhaps millions of gallons for a 10-acre leach field. Finally, as described below, groundwater sweep may cause oxic groundwater from upgradient of the deposit to enter into the extracted area, making it more difficult to reestablish chemically reducing conditions.

**Surface Treatment and Recirculation.** To minimize the storage and disposal of pumped groundwater and more effectively restore the groundwater to regulatory standards, it is usually necessary to use an above-ground treatment method to remove contamination from the extraction zone. In this second phase of ISR site restoration, the recovered solution from the well field is treated to reduce contaminant levels. The treated groundwater is then recirculated into the contaminated aquifer zone using the same ISR pattern of coordinated injection and pumping wells to displace the residual contaminants and control and isolate the zone of groundwater restoration. In this way, contaminated groundwater in the aquifer is continuously diluted and displaced by less contaminated injected solutions. Ideally, the reinjected solution contains only concentrations at baseline values or below because reinjected contaminants will prolong the procedure. Contaminants in the pumped groundwater can be removed via (1) ion exchange resin beds that remove the metal and metalloid cations from solution via sorption, (2) reverse osmosis (RO) to separate the contaminants using high pressure across a semi-permeable membrane, and/or less frequently (3) electro dialysis. Reverse osmosis is the most

---

<sup>1</sup> Pore volume, in this context, is the groundwater volume in the ore zone. It is a reference unit for describing the amount of liquid circulated.

common method used to treat the contaminated groundwater, but is usually employed after a groundwater sweep of one pore volume to remove the highest levels of contaminants from solution. Alternatively, the recovery stream can be run through the ion exchange beds prior to being fed to the reverse osmosis treatment. This is because the well field at the beginning of the restoration is still producing considerable amounts of uranium and other constituents (e.g., large uranyl-bicarbonate complex molecule, calcium carbonate), which can clog the RO membranes. The relatively clean water stream (RO permeate) is injected back into the formation and the high TDS waste water stream (RO reject) is typically sent to deep disposal wells.

The primary advantages of utilizing continuous water treatment systems in aquifer restoration, or a combination of groundwater sweep followed by treatment and reinjection is 1) reduction in the total dissolved solids in the contaminated groundwater, 2) reduction in the quantity of groundwater removed from the aquifer to meet restoration criteria, 3) reduction in the volume of wastewater requiring disposal, 4) desorption of contaminants responding to the lower aqueous concentrations, and 5) the means to introduce reagents to the formation to reverse or inhibit deleterious chemical reactions.

**Reagent Amendment.** A third restoration phase can be used to introduce a reagent into the aquifer to control the solubility of contaminants. The general intent is to return the uranium roll front deposit to the chemically reducing conditions that maintained the pre-operational baseline water quality. This is because the solubilities of many of the metal and metalloid contaminants of concern (e.g. uranium, selenium, molybdenum, and arsenic) were lower under pre-ISR mining conditions. Examples include adding reducing agents such as hydrogen sulfide gas, sodium hydrosulfide, or oxygen scavengers to the recirculating water to re-establish reducing conditions in the ore-bearing unit of the aquifer (Cameco-Resources, 2012)(Deutsch et al., 1985; Schmidt, 1989; Rio Algom, 2001) to precipitate trace metals, including uranium. The pH may also be raised (e.g., using potassium carbonate) to facilitate further removal of calcium, metals, and radionuclides.

**Stabilization.** At the end of the groundwater treatment/recirculation phase, aquifer water is monitored for six months to a year according to a schedule accepted by the regulatory authority to ensure that regulatory standards have been met, no significant impact on the water quality in adjacent aquifers has occurred, and there are no trends in the water quality indicative of future deterioration. After the regulatory agencies confirm satisfactory achievement of all restoration parameter goals, the restoration phase is officially complete and the stabilization phase commences. Post-restoration stability monitoring is critical in understanding the effectiveness of restoration efforts and the potential for long-term water quality impacts.

The stabilization phase was introduced by the Wyoming Department of Environmental Quality after experience with ISR operations had shown a pattern of increasing concentrations of monitored parameters that persisted after operations and restoration (Schmidt, 1987). In some cases, restoration had to be restarted. There are a number of possible explanations for the post-restoration increase in monitored parameters. Uncontaminated groundwater from the oxic upgradient side of the uranium roll front may be drawn into an ore zone resulting in the reoxidation and re-solubilization of contaminants reduced and immobilized during restoration. This would also make it more difficult to re-establish chemically reducing conditions. Contaminants adsorbed to various mineral phases may slowly be desorbing. Restoration may

have been achieved only in the vicinity of the sampling wells; consequently, large volumes of contaminated groundwater may remain between the wells or in pores with limited access to the bulk flow. Advection would eventually transport the contaminants residing between the wells and/or diffusing from the less mobile pore space into the bulk flow field, to the sampling wells. Subsurface heterogeneities in aquifer properties would exacerbate the persistence of monitored contaminants as uncontaminated groundwater may be preferentially swept through the ore zone in a few of the most transmissive flow paths, effectively bypassing lower permeability zones with residual lixiviant and elevated contaminants.

The persistence of elevated concentrations of uranium and other contaminants during the restoration and stabilization phases of the ISR life cycle reflects the significant disturbance imparted by the lixiviant. If the return to baseline geochemistry is based on the restoration of the pre-mining chemically reducing conditions, then there needs to be a solid-phase reservoir of low redox potential to sustain those conditions. One concern is that the residual post-ISR solid phase reservoir of Fe(II) and sulfide has been heavily depleted by the introduced oxidants to the degree that restoration in regulatory time frames is infeasible.

In general, it is not easy to determine the extent the reduced minerals are oxidized in a typical ISR mining operation. One possible indicator is the monitoring of dissolved sulfate during ISR operations. Schmidt (1989) reported that sulfate concentration at the Ruth ISR pilot-scale test site peaked at 280 mg/liter after 2 months of leaching and declined toward the ambient background concentration of 100 mg/liter after 5 months of leaching. This suggests that the sulfide minerals in good hydrologic contact with the groundwater were significantly oxidized during the extraction phase of operation. The expectation is that uraninite and other reduced minerals present in low permeability regions (i.e., poor hydrologic contact with the bulk groundwater flow) would be oxidized more slowly and less completely during the extraction phase. The open question is whether these reduced phases will have sufficient influence to support a return to baseline reducing conditions.

### **1.4.3 Regulatory Standards for Restoration**

After ISR operations are completed, NRC requires the licensee to restore water quality to either: pre-operational (baseline) levels, drinking water standards, or alternate concentration limits, which are above baseline concentrations but judged by the regulator to be protective of human health. As of 2009, no NRC regulated ISR site (11 well fields at three sites and 34 early licensed R&D facilities) had been documented to have restored all groundwater constituents of concern within the extraction area to pre-operational background conditions (NRC, 2009b, NRC, 2009c), which is the primary regulatory standard for restoration as defined in 10 CFR Part 40 Appendix A Criterion 5B(5). In a survey of 77 ISR well fields in Texas, Hall (2009) concluded that all had received amended restoration goals for at least one regulated constituent after operators expended a reasonable degree of effort to restore groundwater following established guidelines, as determined by the Texas Commission on Environmental Quality.

In RIS 2009-05 (NRC, 2009d), the NRC recently affirmed that all restored aquifers at NRC licensed ISR sites must meet the groundwater quality standards in 10 CFR Part 40 Appendix A

Criterion 5B(5). Criterion 5B(5) states: “At the point of compliance, the concentration of a hazardous constituent must not exceed—

- (a) The Commission approved background concentration of that constituent in the ground water;
- (b) The respective value given in the table in paragraph 5C if the constituent is listed in the table and if the background level of the constituent is below the value listed; or
- (c) An alternate concentration limit established by the Commission.”

## 1.5 Bioremediation

In situ bioremediation (ISB) has been proposed and, in some cases, tested for the restoration of uranium ISR sites. ISB involves the stimulation of indigenous microorganisms that catalyze the destruction (of organic contaminants) or immobilization of targeted inorganic contaminants. Many of the post-operational contaminants found at ISR sites (e.g., U, V, Se, Mo) are in oxidized form as a result of the circulated lixiviants. In this case, ISB is directed at the conversion of mobile redox sensitive components in oxidized states to their chemically reduced immobile form.

The elevated concentrations of uranium and other mobilized metals during ISR are primarily the result of the manipulation of the subsurface chemistry to conditions that thermodynamically favor their solubility. The persistence of these contaminants in spite of restoration approaches based on extraction (e.g., pumping) and above ground treatment (e.g., ion exchange, reverse osmosis) underscore the importance of (re)establishing a chemical regime similar to the pre-ISR baseline, which does not favor the mobilization of these metals. Unless ISR operations have irreversibly altered the subsurface geochemistry, the concept of returning the system to a previous redox state where metal concentrations are below actionable levels may be more tractable.

Yet, attempts to lower the redox potential using inorganic chemical reductants have not been observed to significantly accelerate the lowering of aqueous uranium concentrations (Schmidt, 1987). The suggestion here is that the lowering of redox potential, while necessary to prevent oxidation and mobilization of sparingly soluble reduced metal phases, may not be sufficient to achieve the reduction of uranium and possibly other redox-sensitive metals, even when the reduction is thermodynamically favored. Recent field studies (Williams et al., 2011) have demonstrated that microbial mediation is often necessary to enzymatically catalyze uranium reduction in natural environmental systems even in the presence of Fe(II) and sulfide (i.e., abiotic uranium reduction is negligible). Also, complexed uranium in solution seems to require lower redox potential than the free ion in order to be reduced. From this perspective, bioremediation may be more efficient and effective at reducing metal contaminants, as well as lowering the redox potential, than chemical reductants.

ISB has been tested in shallow aquifer systems (e.g., Rifle and Oak Ridge IFRCs) with some success (Anderson et al., 2003; Vrionis et al., 2005; Williams et al., 2011; Wu et al., 2006b). Insights from this body of work can be useful to uranium ISR. Conceptually, one

potential advantage of applying ISB to ISR sites is that the goal is to return the system to a pre-ISR redox condition characterized by very low dissolved oxygen that thermodynamically favored low contaminant concentrations.

It should be recognized that biostimulation can be non-specific with respect to the microorganisms and terminal electron accepting processes that are catalyzed. For example, the iron reducing bacteria (FeRB) that are responsible for the rapid and effective reduction of Fe(III) and U(VI) during field biostimulation experiments at the Rifle site, are eventually outcompeted by sulfate reducing bacteria (SRB) for the acetate electron donor (Fang et al., 2009; Yabusaki et al., 2007; Yabusaki et al., 2011). Impacts of the SRB activity include 1) the bulk of the acetate electron donor is eventually supporting SRB, not the FeRB that are responsible for uranium reduction, 2) the oxidation of the electron donor by SRB leads to the production of significant amounts of bicarbonate, which enhances U(VI) desorption, 3) significant amounts of biomass are produced when SRB become dominant, and 4) the bulk of the sulfate reduced by the SRB ends up in mineral form (e.g., iron sulfides and elemental sulfur). Ostensibly, the enrichment of organisms that do not reduce uranium, consume most of the electron donor, promote U(VI) desorption, and generate materials that may clog pores is disconcerting. However, pore clogging in the Rifle aquifer has not been observed to be significant, desorbed U(VI) is more bioavailable for biologically mediated reduction, and the reduced sulfide and sulfur minerals provide a buffer against oxidation. While the SRB activity in the shallow uranium contaminated Rifle aquifer is a complication but not necessarily an obstacle to bioremediation effectiveness, there are no guarantees that the physical, geochemical, and biological conditions in the deeper sandstone ISR setting will be as conducive. Furthermore, the disturbance of the microbial community from prolonged exposure to ISR lixiviants and the effect on the response to biostimulation is not well understood.

Another insight from the study of in situ uranium bioremediation in shallow alluvial aquifers is that bioreduced U(IV) in the field is more recalcitrant to oxidation than in lab experiments (Campbell et al., 2011; Sharp et al., 2011). It has been observed that biomass on the U(IV) mineral, uraninite, significantly inhibits dissolution/oxidation. Impurities in the groundwater may be incorporated into the uraninite crystal structure resulting in lower solubility. Finally, transport limited by the tortuous paths within and between sediment grains can create microenvironments that locally maintain reducing conditions.

The attraction to ISB is the potential for more effective restoration, shorter restoration periods, and lower cost. The cost driver is significant because financial surety for restoration costs must be provided as a prerequisite to ISR operations and maintained until restoration is approved. The principal drawback of using ISB to restore uranium ISR sites is that it is an unproven technology that relies on indigenous microorganisms to 1) catalyze the reduction of uranium and other ISR mobilized contaminants, and 2) permanently return the ISR-impacted aquifer to pre-operational conditions to stabilize the immobilized contaminants left in place. The dearth of well-monitored field experiments to test the approach under a realistic range of conditions is currently a considerable limitation. Consequently, there is a need to better understand the engineering of the required biogeochemical reactions and the long-term behavior of the restored aquifer.

## 1.6 Document Description

The issue of predicting and demonstrating the long-term effectiveness of uranium bioremediation is common to all applications of the ISB technology. This document is the third in a series of NUREG/CR reports that are intended to provide background and guidance on uranium bioremediation technology. In these reports, the complexity of uranium biogeochemistry during ISB is addressed by mathematical models of coupled flow, transport, and biogeochemical processes that incorporate knowledge from the few intensively monitored field biostimulation experiments that have been performed, albeit in shallow aquifer systems. The objective is to develop a systematic framework to better understand the impact of site-specific material properties and conditions on uranium bioremediation. The first report, “Technical Basis for Assessing Uranium Bioremediation Performance (Long et al. 2007),” provided an overview of uranium bioremediation, including biogeochemistry principles, design considerations, field performance indicators and a general approach for assessing the performance of uranium bioremediation in the field. The second report, “Processes, Properties, and Conditions Controlling In situ Bioremediation of Uranium in Shallow, Alluvial Aquifers (Yabusaki et al. 2010),” focused on field experiments and modeling of uranium bioremediation in a shallow, alluvial aquifer, as well as sensitivity analyses of aqueous uranium concentrations to process model parameters. The study analyzed multiple electron donors (i.e., acetate, lactate, ethanol); multiple electron acceptors (i.e., oxygen, nitrate, iron, sulfate) in addition to U(VI); density effects of groundwater amendments; and enhancement of dissolved oxygen via water table fluctuation and surface flooding.

### 1.6.1 Document Purpose, Approach, and Objectives

The purpose of this document is to provide guidance on the potential effectiveness of ISB for ISR uranium sites and strategies for monitoring the performance of these applications.

While a few ISR sites (e.g., Smith Ranch) have attempted ISB restoration, these cases have generally been without comprehensive monitoring of key biological and geochemical parameters (e.g., 16S ribosomal RNA, DO, ORP). One exception is the dissolved hydrogen biostimulation field experiment (Cabezas et al., 2011) at the Kingsville Dome site, which is described in Chapter 2 of this report. However, this work notwithstanding, there is currently very little information on ISB at actual ISR field sites.

To address the limitations of the current knowledge base of ISR behavior and the absence of bioremediation field studies at post-ISR uranium sites, the interim scoping approach taken here is to 1) build on the available geological, hydrological, and chemical data from existing ISR sites, 2) factor in new knowledge and insights from bioremediation field research in shallow, uranium-contaminated groundwater, 3) perform uranium biogeochemical reactive transport laboratory studies using post-ISR sediments, 4) develop a model of biogeochemical reactions for the column experiments, and 5) extrapolate the model reaction network to a hypothetical field uranium ISR setting with a standard arrangement of pumping and injection wells. Coupled process modeling is used to provide the platform for integrating and upscaling the behaviors brought about by the biostimulation. The focus is on uranium behavior and the goal is to identify potential issues for ISR bioremediation that should be considered in the design of field studies.

Issues that will be addressed include the impact of the lixiviants on the biogeochemistry, biostimulation injectate composition, interplay between the nonuniform groundwater flow and biologically-mediated reaction rates, and the effectiveness and efficiency of uranium bioremediation using a standard pattern of pumping and injection wells.

## **1.6.2 Document Contents**

After this introductory chapter, the document continues with Chapter 2, Geochemistry and Restoration Issues, describing the 1) geochemistry of the uranium roll front deposits, 2) geochemistry of uranium ISR, 3) ISR restoration issues, 4) uranium bioremediation research, and 5) ISR biorestoration potential.

Chapter 3, Laboratory Studies, describes batch and column experiments performed by the USGS using Kingsville Dome post-ISR sediments to investigate 1) the ability of the indigenous microbial population for biostimulated reduction of uranium and resulting sequestration of uranium from the influent artificial ground water flowed through packed columns, 2) the extent of release of uranium in response to suboxic conditions following electron donor amendment, 3) the form of the sequestered uranium, and 4) changes in sediment chemistry at the end of the biostimulation and re-oxidation stages of the experiments.

Chapter 4, Simulation of Uranium Bioremediation in ISR Sediment Columns, describes the 1) uranium bioremediation modeling studies, 2) findings from the biostimulated reduction stage of the column experiments using Kingsville Dome ISR sediments, 3) conceptual biorestoration model, 4) simulator and simulation description, 5) comparison of shallow groundwater and deep ISR biologically-mediated processes, 6) modeling approach, 7) simulation results, and 8) key findings.

Chapter 5, Field-Scale Flow and Transport Modeling, describes the 1) hypothetical ISR model specifications, 2) field-scale coupled process simulator, 3) flow and transport modeling results, and 4) findings and implications.

Chapter 6, Field-Scale Post-ISR Biorestoration Modeling, describes the 1) biorestoration concepts guiding the modeling, 2) modeling approach for the hypothetical biorestoration simulations, 3) baseline modeling results, 4) background injectate modeling results, and 5) summary of findings.

The final chapter, Chapter 7, Conclusions, Findings, and Recommendations provides 1) a summary of the major conclusions and findings, 2) recommendations including a recommended path forward for ISB restoration at post-ISR sites, and 3) guidance on field characterization and monitoring.



## 2 Geochemistry and Restoration Issues

The financial impact of the typical ISR groundwater restoration phase can be seen in the increased surety bond estimates for recent licensing applications. (A surety bond is required by the NRC to ensure that sufficient funding will be available for post-ISR decommissioning costs.) These costs generally reflect the long duration of active restoration and stabilization required at ISR uranium extraction sites, sometimes more than 10 years, which is much longer than the 1- to 3-year period of uranium extraction. Furthermore, no ISR site has restored all regulated components to pre-operational background conditions (NRC, 2009c), which is the regulatory standard for restoration.

Given the cost and duration of the typical uranium ISR groundwater restoration, two motivating questions for this report are:

- 1) Why are uranium ISR sites difficult to restore?

and

- 2) Can bioremediation improve the efficiency and effectiveness of restoring ISR sites to pre-operational conditions?

### 2.1 Geochemistry of Roll Front Deposits

In the oxidized sandstone and groundwater upgradient of the uranium roll front, the iron minerals include goethite, hematite and magnetite; whereas sulfate minerals include gypsum. Uranium under these oxidizing conditions occurs as U(VI), the hexavalent oxidation state, in dissolved, adsorbed, or mineral form. As oxic groundwater approaches the upgradient edge of the roll front, the remaining dissolved oxygen in the groundwater is consumed in redox reactions via abiotic oxidation of the reduced minerals and/or microbially-mediated oxidation of organic carbon. In both cases, the transfer of electrons to the oxygen terminal electron acceptor yields water as the product of the reduction reaction.

Microorganisms gain energy by mediating the electron transfer process, using bioavailable carbon as a source of electrons and substrate for growth. The oxygen-depleted zone of the roll front can support anaerobic bacteria that mediate other terminal electron accepting processes (TEAPs) if sufficient carbon and nutrients are bioavailable. In addition to U(VI), these TEAPs include nitrate, manganese, Fe(III), and sulfate. Consequently, the reduced uranium minerals [e.g., U(IV) as pitchblende and coffinite] in the roll front are associated with the reduced forms of these terminal electron acceptors. Fe(II), sulfide, and elemental sulfur minerals dominate the solid phase products. The low redox potential supported by these reduced chemical components provides a buffer against oxidants entering the roll front and can be sufficiently low to thermodynamically favor the abiotic reduction of U(VI).

The low redox potential baseline or pre-operational conditions at ISR sites are thus characterized by negligible dissolved oxygen concentrations, micromolar concentrations of nitrate, iron, and sub-micromolar uranium concentrations. These conditions are maintained

primarily by the solid phase reservoir of low redox potential and the presence of bioavailable organic matter that provides the substrate for microbially-mediated reduction of terminal electron acceptors (e.g., dissolved oxygen, nitrate, Fe(III), sulfate, U(VI)). Other redox-sensitive trace metals of interest are vanadium, selenium, arsenic, and molybdenum. Similar to uranium, vanadium and selenium under oxic conditions are mobile, and form sparingly soluble minerals when reduced. Conversely, arsenic and molybdenum are generally immobile under oxic conditions and are mobilized via bioreductive dissolution of and/or desorption from Fe(III) minerals. The redox potential in oxidized zones is typically about +150 mV, in the ore zone it varies from -150 to +100 mV and can be as low as -330 mV in more highly reduced sands.

## **2.2 Geochemistry of Uranium ISR**

The introduction and circulation of lixiviants during uranium ISR is designed to manipulate 1) the redox potential to a more oxidizing state that favors the conversion of U(IV) minerals to the +6 oxidation state (U(VI)), and 2) the groundwater chemistry to thermodynamically favor aqueous U(VI) over solid-associated forms. While ISR is targeting uranium, uranium is a trace component of the mineral assemblage. In this sense, the lixiviant-induced reactions are non-specific and the bulk of the consumed lixiviant is facilitating the oxidation of the reduced iron and sulfur minerals, leading to the formation of Fe(III) oxides and oxyhydroxides and sulfate (Deutsch et al., 1983). Complexants are used to increase the solubility and mobility of the U(VI).

The introduction and circulation of lixiviants during uranium ISR significantly disrupts the processes responsible for creating and maintaining the lower pre-operational concentrations of uranium, vanadium, selenium, molybdenum, and arsenic. In particular, the oxygen commonly used in U.S. ISR operations to oxidize the U(IV) minerals in the ore (e.g. uraninite and coffinite), is consumed primarily in the oxidation of other reduced minerals that comprise the reservoir of low redox potential. In this case, the oxidation of Fe(II) minerals leads to secondary mineral formation of Fe(III) oxides and oxyhydroxides. Oxidation of elemental sulfur and sulfides results in elevated sulfate concentrations. The extent of the oxidation depends on the lixiviant, lixiviant concentration and residence time, and the abundance and availability of the reduced mineral phases. This “non-specific” impact of the lixiviant is also responsible for the mobilization of vanadium and selenium, as well as major ion complexes. Aqueous concentrations of uranium and the other components elevated by ISR are subject to re- and co-precipitation when the oxidizing potential is diminished (Rojas, 1987). This may occur when the transporting solution comes in contact with unleached, reduced sandstone. This reversal of the ISR process does not naturally occur under regulatory time frames for the bulk of the leached ore zone. In fact, the persistence of uranium and other contaminants elevated during ISR operations, in spite of years of restoration effort, is a strong motivation for investigating more efficient and effective restoration approaches.

## **2.3 ISR Restoration Issues**

In Chapter 1, three basic restoration methods were described for removing residual lixiviant and lowering aqueous concentrations of uranium and other contaminants that became elevated during ISR operations: groundwater sweep, above ground treatment, and reagent injection.

Here we describe scenarios that might explain the persistence of contaminant concentrations in spite of these restoration methods.

Post-ISR groundwater sweep involves pumping the ISR-contaminated groundwater out of the aquifer and allowing uncontaminated groundwater to be drawn in to replace it. If there are no other sources of contaminated groundwater, this approach alone would restore the aquifer. The general ineffectiveness of this approach to restore an ISR-impacted aquifer to baseline conditions implies that the lixivants and/or contaminated groundwater are not completely removed. Residual lixiviant can react with the solid phases, continuing uranium leaching and contaminant production. Residual contamination from ISR extraction could be maintained in low permeability zones that are not accessed by the bulk flow paths. Analogously at the pore scale, intergranular and intragranular pore spaces with limited transport access may also sequester residual contaminants. These residual contaminants can become long-term diffusion-limited sources.

If the residual lixiviant and aqueous contaminants from ISR processes are removed by the groundwater sweep, then persistent contaminant concentrations are due to sources in the leached aquifer. Any uranium in solution can be considered to be U(VI) because of the extremely low solubility of U(IV). Thus, the persistence of U(VI) and oxidized forms of other redox sensitive metals (e.g., vanadate, selenate) implies continuing oxidation of key components of the reduced mineral assemblage or continuing release of oxidized forms of the contaminants. Continuing oxidation in spite of the groundwater flush can occur if groundwater is becoming oxidized through solid phase reactions or the groundwater entering the ISR-impacted aquifer contains oxidants.

Chemically reducing groundwater drawn in during groundwater sweep can be oxidized through reactions with minerals that act as oxidants. Fe(III) minerals, especially oxides and oxyhydroxides formed during ISR mining, can potentially provide a reservoir of oxidizing potential. The capacitance of this reservoir will depend on the type and concentration of oxidant used in the lixiviant, and the extent and duration of contact with the solid phases.

Oxidizing groundwater can potentially enter the ISR zone of the aquifer. One scenario for this to occur is when groundwater is being drawn from the upgradient side of the redox interface of the roll front, where oxidizing conditions exist. Another scenario is oxidation of produced groundwater prior to reinjection. This could occur during handling such as surface treatment or reagent addition. In either case, the oxidizing groundwater could potentially continue the oxidation and release of uranium and other redox sensitive contaminants.

Continuing release of oxidized forms of uranium and other contaminants is possible in spite of lowered redox potential groundwater that thermodynamically favors reduction. In this case, the reaction kinetics significantly limit the rate of reduction. Nonequilibrated redox couples are not indicative of the system redox potential (e.g., Eh, ORP). For example, U(VI) may be present and possibly increasing in concentration under sulfate reducing conditions even though the U(VI)/U(IV) redox couple is higher on the redox ladder and energetically more favorable. Reinjected groundwater is sometimes augmented with chemical reducing agents (e.g., hydrogen sulfide) to create conditions designed to remove the redox-sensitive contaminants (e.g., U, Se, V) from solution. This restoration technique has been used with varying degrees of

success (Cameco-Resources, 2009; Crow Butte Resources, 2000). At the Ruth pilot scale test site in Johnson County, Wyoming, six weeks of hydrogen sulfide injection lowered concentrations of dissolved uranium, selenium, arsenic, and vanadium by at least one order of magnitude (Schmidt, 1987). However, the reducing conditions were temporary as uranium, arsenic, and radium concentrations began to increase 1 year later. More recent studies have determined that natural mineral assemblages can be much more resistant to abiotic Fe(II)-driven uranium reduction than model minerals (Jeon et al., 2005) and that abiotic sulfide promoted reduction of uranium can be strongly inhibited by bicarbonate (Sani et al., 2005). This could explain the cases where sulfide-promoted reduction of U(VI) is ineffective (Yabusaki et al., 2011).

## 2.4 Uranium Bioremediation

Bioremediation of uranium ISR sites is not a novel concept. Results from the few sites (e.g., Smith Ranch) that have attempted to use a bioremediation approach to restore uranium ISR sites have not been sufficiently successful to warrant widespread adoption. Most of these efforts have been relatively ad hoc approaches where the limited descriptions that are available do not provide sufficient detail to ascertain the bioremediation design or monitoring results. One notable exception that has been presented (Cabezas et al., 2011) but not yet published is a field biostimulation experiment at a post-ISR site in Kingsville Dome, Texas, led by Dr. Lee Clapp at the Texas A&M University-Kingsville. In this bioremediation design, dissolved hydrogen serves as the electron donor and reductant, and bicarbonate is the carbon source. Biostimulation of the indigenous microbial community with a 2-month pulse of dissolved hydrogen lowered U(VI) concentrations to the pre-operational baseline condition and have maintained those conditions for 2 years. Monitoring included data on 15 water quality measures.

The U.S. DOE has sponsored field research studies to investigate in situ bioremediation of shallow uranium-contaminated groundwater plumes (Anderson et al., 2003; Vrionis et al., 2005; Williams et al., 2011; Wu et al., 2006a; Wu et al., 2006b) in much smaller field systems, on the order of 10 m. Intensive characterization and monitoring have provided comprehensive data sets and new knowledge on the biogeochemistry of uranium under engineered biostimulation of indigenous microorganisms. Drilling techniques that minimize sediment sample disturbance without introducing additional fluids are used to recover sediments suitable for physical, geochemical and biological characterization and experimentation. Coupled process modeling is an important component of these research studies with the goal of achieving a quantitative and predictive understanding of the subsurface processes controlling uranium bioremediation. Spatially variable hydraulic conductivity, porosity, and dispersivity needed for the modeling are characterized using particle size distribution, density, surface area, and porosity in conjunction with field geophysics (e.g., neutron, gamma, resistivity logging) and aquifer flow and transport studies.

In these research studies, minerals and adsorbed components, especially those involved in active redox couples (Fe, Mn, S, U, Se, V, As), are characterized through a variety of techniques including point counts, extraction, x-ray diffraction, and x-ray fluorescence (XRF), as well as spectroscopic techniques that provide elemental associations and oxidation states. A

key concept is the labile fraction of the solid phase components, which addresses availability for chemical and biologically-mediated reactions. For example, total uranium (e.g., measured by XRF) in sediments at the crustal abundance level (~3 mg/L), is generally much higher than the carbonate extractable uranium associated with surface complexes. Similarly, the bioavailability of phyllosilicate Fe(III) terminal electron acceptors is greater than crystalline forms. These determinations required more refined analytical characterizations than bulk approaches alone.

Groundwater from the monitoring wells is analyzed for water quality (e.g., pH, temperature, specific conductivity), major ions, and metals similar to the typical ISR operations. However, unlike most ISR operations, there is more attention to the oxidation states and speciation of the aqueous components. In particular, dissolved oxygen and oxidation-reduction potential (ORP) or Eh are monitored as well as sulfide and methane.

A key modeling need is to be able to predict the evolving concentrations of the oxidation states for key redox couples under the interplay of flow, transport, and biogeochemical processes. To this end, the shallow uranium bioremediation field research studies employ laboratory-scale experiments using native sediment, groundwater, and microorganisms. These experiments allow detailed observation of the uranium biogeochemical dynamics under controlled conditions using microcosm, chemostat, batch, and column configurations. Most importantly, the experiments provide important insights on the dominant reactions and associated kinetics for various electron donor-microorganism combinations using native populations and aquifer materials.

Finally, the largest departure from the typical ISR operation is the focus on the microbial ecology before, during, and after biostimulation. In the shallow uranium bioremediation field studies, molecular biological techniques are used to identify 1) microorganisms that comprise the native microbial community (e.g., Campbell et al., 2012), 2) microorganisms that become active in response to particular electron donors (e.g., Wrighton et al., 2012), and 3) specific metabolic responses by the active microorganisms to electron donor amendments, geochemical conditions, and interactions with the microbial community (e.g., Fang et al., 2012). The principal interest is in microorganisms that can be stimulated to catalyze useful reactions such as the conversion of aqueous contaminants to immobile, solid-associated form. There are other behaviors of interest that will also control the efficiency and effectiveness of the bioremediation such as microorganisms that 1) consume significant amounts of the provided electron donor, 2) inhibit or reverse the desired reactions (e.g., oxidizers involved in redox cycling), 3) maintain desirable redox conditions, 4) produce significant biomass, and 5) facilitate the continuing effectiveness of bioremediation.

The efficiency and effectiveness of the biologically mediated reactions can be affected by ISR operations and can, in turn, affect ISR operations. Of most concern is the impact of the injected lixiviant on key members of the microbial community. Oxygen and other oxidants used to enhance leaching inhibit the growth of anaerobic microorganisms and can have toxic effects on strict anaerobes. The degree of disruption to the microbial community, especially to microorganisms that catalyze the reduction of uranium and other metal contaminants, is an important and open issue. Conversely, amending groundwater with carbon electron donors

can stimulate growth in microorganisms that leads to the accumulation of biomass in the pore spaces. If the biomass accumulations are sufficiently large, flow rates and flow paths can be altered.

## **2.5 Findings from Uranium Bioremediation Field Research in Shallow Aquifers**

The U.S. Department of Energy (DOE) has been sponsoring Integrated Field Research Challenge (IFRC) projects at a former Uranium Mill Tailings Remedial Action (UMTRA) site in Rifle, Colorado; Area 3 at the Y-12 facility in Oak Ridge, Tennessee; and the 300 Area of the Hanford Site in Washington. These comprehensive interdisciplinary studies are investigating the behavior of uranium in the subsurface environment, including the potential for field-scale bioremediation (Anderson et al., 2003; Gu et al., 2005; Yabusaki et al., 2008). While these were shallow sites addressing uranium groundwater plumes, there are several findings from these studies that could be useful to the investigation of bio restoration of ISR sites.

### **Ineffectiveness of abiotic uranium reduction under experimental time scales.**

Field experiments in the shallow alluvial aquifer at the Old Rifle former uranium mill and tailings site in Colorado have found no evidence of significant abiotic uranium reduction in the presence of elevated Fe(II) or sulfide. In these experiments, U(VI) was thermodynamically favored to be reduced to U(IV). The literature is somewhat equivocal, for example, uranium reduction has been shown by abiotic reaction on the surfaces of solid phases that form during biostimulation, such as iron sulfides (Hyun et al, 2012; Hua, 2008). In contrast, there is a body of research in shallow uranium-contaminated groundwater plumes that has observed uranium to be largely recalcitrant to abiotic reduction via pre-existing reduced natural mineral assemblages in aquifer sediments. The Fe(II) behavior at the Rifle site is consistent with the Jeon et al. (2005) finding that abiotic U(VI) reduction on natural mineral assemblages with Fe(II) was negligible with the exception of Fe contents above 18%. Similarly, thermodynamically favored sulfide promoted U(VI) reduction has not been observed at the Rifle Site even when ~10 mM sulfate has largely been converted to sulfide by sulfate reducing bacteria (Yabusaki et al., 2011). The literature is variable but the Rifle field experiments are consistent with the Sani et al. (2005) observation that elevated bicarbonate concentrations, not uncommon to many environmental situations, can limit the rate of abiotic U(VI) reduction by sulfide. This may explain why the restoration of some ISR sites, such as the Ruth pilot test site in Johnson, Wyoming benefited, at least temporarily, from injected sulfide (Schmidt, 1987) and others, such as the Smith Ranch-Highland site in Converse County, Wyoming (Borch et al., 2012) did not.

### **Metal reducing bacteria can be stimulated to catalyze the reduction of uranium and other metal contaminants under experimental time scales.**

In light of the general difficulty of abiotically reducing U(VI) in shallow groundwater systems, it is notable that there has been considerable success using engineered biostimulation of indigenous microorganisms to catalyze the reduction of mobile U(VI) to immobile U(IV) as sparingly soluble minerals or solid associated forms. In saturated sediments, this ability has been demonstrated with a variety of electron donors (Barlett et al., 2012) and microorganisms

including ethanol-oxidizing sulfate reducing bacteria at the Oak Ridge Site (Cardenas et al., 2010) and acetate-oxidizing iron reducing bacteria at the Rifle Site (Anderson et al., 2003). This removal of uranium from solution can lower concentrations below actionable levels provided there is sufficient transport, active U(VI)-reducing microorganisms, and bioavailable electron donor to treat the zone of interest.

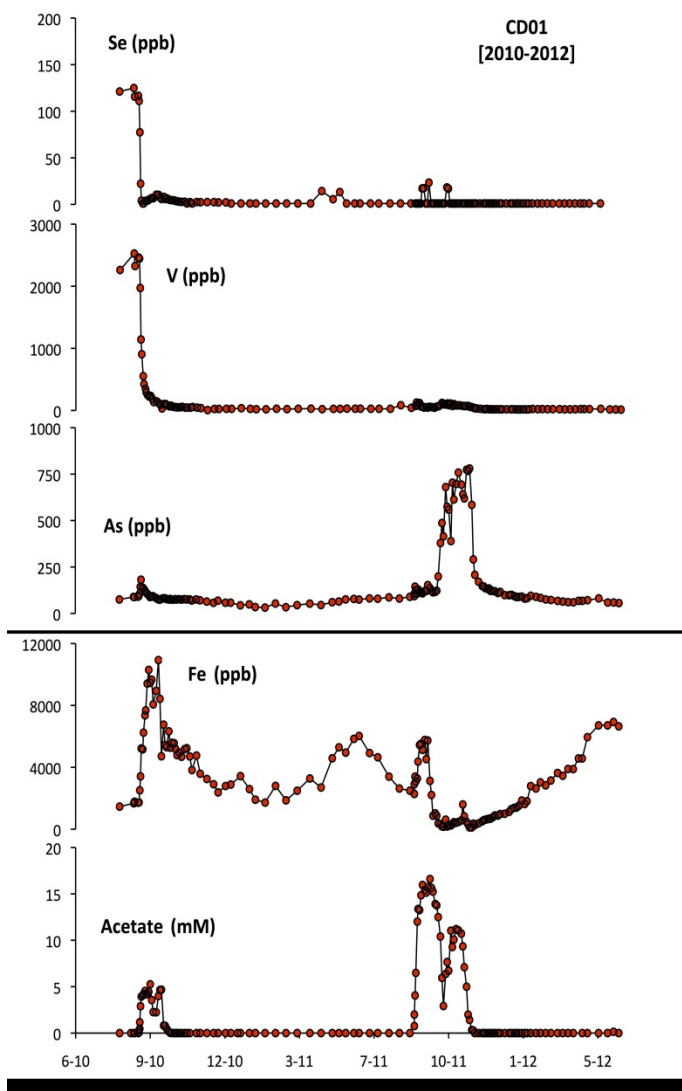


Figure 2.1 Downgradient metal concentrations responding to acetate injection at the Rifle IFRC site. Concentrations were measured in well CD-01 from June 2010 to May 2012. (Courtesy of Ken Williams, LBNL)

Although U(VI) was the target of the bioremediation studies at the Rifle Site, other metals and metalloids including V (vanadium), Se (selenium), Mo (molybdenum), and As (arsenic) were affected by the biostimulation events (Figure 2.1). Vanadium was the original ore of interest when the Old Rifle Mill opened in 1924. In a recent field experiment in 2010, ambient V concentrations were reduced from 2300 ppb to less than 20 ppb after 23 days of acetate amendment (Yelton et al., 2012). Se concentrations were reduced from 120 ppb to less than 5 ppb after 7 days (Williams et al., 2012). ~15 ppb Mo in the form of molybdate was removed from groundwater down to 1 ppb at the same time its structural analogue, sulfate, was depleted via respiration by sulfate-reducing bacteria. Dissolved arsenic concentrations increased from ~90 to ~150 ppb during iron reduction, followed by larger increases up to 600 ppb once sulfate reduction became the dominant metabolic pathway and aqueous sulfide concentrations increased (Stucker et al., 2012). Once acetate amendment ceased, the arsenic concentrations dropped below influent concentrations.

**Biogenic U(IV) can be in non-mineral form.**

Recent laboratory studies (Bernier-Latmani et al., 2010) have shown that, depending on the geochemical conditions, the biogenic U(IV) product may either be crystalline nanoparticulate

uraninite or monomeric U(IV) complexes that are associated with biomass and mineral surfaces. Monomeric U(IV) has been shown to be preferentially produced as a result of the interaction of U(VI) with phosphate (Boyanov et al., 2011; Veeramani et al., 2011). The emerging conceptual model for U(IV) associated with biomass appears to involve the binding of U(IV) to phosphato moieties on the cell biomass. Conversely, in the absence of phosphate, magnetite was shown to reduce U(VI) to uraninite. Thus, phosphate appears to preclude the precipitation of uraninite and to play a critical role in the formation of monomeric U(IV) (Bargar et al., 2013).

Monomeric U(IV) is more labile than uraninite and this property has been used to develop extraction techniques that can distinguish between uraninite and monomeric U(IV) (Alessi et al., 2012). The higher susceptibility of monomeric U(IV) to oxidation is a concern for uranium in situ bioremediation. The characterization of the stability of monomeric U(IV) complexes in aquifers will be the subject of future applications of the recently developed extraction technique. Of particular interest is the sorption affinity and morphology of molecular-scale U(IV) structures adsorbed to various minerals of interest (e.g., alumina, silica, and montmorillonite).

### **Electron donor is consumed primarily in sulfate, Fe(III), and C(IV) TEAP reactions.**

Only a small fraction of the electron donor is supporting the U(VI) and other desirable trace metal TEAP reactions (e.g., Se, V). Thus, the bulk of electron donor is consumed in biologically-mediated TEAP reactions involving the reduction of Fe(III), sulfate, and C(IV) terminal electron acceptors. At the Rifle Site, the metal-reducing bacteria can be outcompeted by sulfate-reducing bacteria for the available acetate. In this case, acetate must generally be provided in excess of the SRB demand to maintain U(VI) bioreduction (Williams et al., 2011).

### **Products of the biostimulation (e.g., bicarbonate, biomass, Fe(II), sulfide, elemental sulfur, methane) can alter the hydrologic and geochemical conditions controlling uranium mobility.**

The products of the biologically-mediated oxidation of electron donor impart several changes to the hydrologic and geochemical conditions in the aquifer. Elevated bicarbonate resulting from the oxidation of acetate, lactate, or ethanol is thermodynamically favored to complex with U(VI) and other metals leading to the desorption of adsorbed forms of these metals. When biostimulation ceases, the vacated surface complexation sites can be repopulated by the adsorption of aqueous metal species.

The reduction products (e.g., Fe(II), sulfide, elemental sulfur, methane) from the biologically-mediated TEAP reactions can participate in subsidiary reactions that lead to the formation of secondary minerals (e.g., FeS, calcite). While the precipitation of these minerals in situ can potentially incorporate uranium, the consistent observation has been for these reduced secondary minerals to provide a reservoir of low redox potential that can protect the aquifer against rapid oxidation (Abdelouas et al., 2000). Subsequent oxidation of solid-associated and mineral forms of Fe(II) can lead to the secondary formation of “fresh” Fe(III) mineral surfaces that are more reactive. The formation of secondary minerals as well as the production of biomass can lead to pore-clogging, which can limit the distribution of electron donor and the effectiveness of the bioremediation (Li et al., 2009).

## **Microorganisms controlling important TEAP reactions are subject to evolving geochemistry and community interactions.**

Engineered biostimulation will be a significant perturbation to the native microbial community. Consequently, the metabolic status of key microorganisms will evolve with concentration changes in electron donors and acceptors, nutrients, biomass, geochemistry, and interactions within the microbial community (e.g., competition, shared metabolites, population stress). At the Rifle Site, observed changes include community composition (e.g., Anderson et al., 2003), cell numbers (e.g., Chandler et al., 2010), activity (e.g., Wilkins et al., 2009), reaction rates (e.g., Williams et al., 2011) and attachment/detachment (e.g., Kerkhof et al., 2011).

## **2.6 Insights from Field Studies**

There were also some important insights from the shallow aquifer uranium bioremediation research studies, which can potentially be generalized to the bioremediation of uranium ISR sites.

**One size does not fit all.** The shallow uranium bioremediation research sites have different site attributes that cannot be effectively addressed with the same deployment strategies. For example, ethanol and glucose were found to be effective electron donors at the Oak Ridge Y-12 site, which is characterized by low pH and high nitrate, aluminum, and calcium. Under the sub-oxic, high alkalinity, circumneutral pH conditions at the Rifle Site, acetate was the selected electron donor. There were also differences in the hydrogeology that affected the electron donor delivery strategy.

Natural uranium deposits are not immune to hydrologic, geochemical, and microbiological variability. The expectation is that effective and efficient restoration of ISR sites will be founded on an understanding of site-specific processes, properties and conditions. Key attributes include the hydrogeologic setting, dissolved oxygen, bicarbonate, major ion chemistry, terminal electron acceptor concentrations, and reactive mineral distribution. An important complication is the extent to which the lixiviant and ISR extraction has altered the hydrology, geochemistry, and status of the microbial community.

**Laboratory ≠ Field.** In many cases, the use of model minerals, limited chemical components, artificial groundwater, pure cultures, and/or batch/microcosm/chemostat experiments results in behaviors that are not consistent with the field observations. Examples of these laboratory-scale effects include abiotic uranium reduction, uranium re-oxidation and remobilization, and generally higher reaction rates versus the field. Some of these behaviors observed in batch and column experiments can be attributed to the use of sediments from a smaller size fraction (e.g., < 2 mm) than the complete in situ particle size distribution. Consequently, the proportion of the more reactive fines is over-weighted.

Laboratory-scale studies are still an indispensable characterization activity that provides a framework for understanding field-scale behaviors; however, care needs to be practiced when extrapolating lab-scale behavior to the field. Laboratory studies should therefore include experiments using sediments, groundwater, and the microbial community from the targeted

aquifer to better characterize and understand the site-specific system response to electron donors.

**Work within the natural biogeochemical tendencies of the system.** Approaches that work within the processes, properties, and conditions that a given aquifer will naturally support, are more likely to succeed than approaches that try to impose artificial conditions. The farther the targeted conditions are away from the natural unmitigated state of the subsurface system, the more difficult it will be to achieve long-term success. For example, a uranium bioremediation design that relied on maintaining locally reducing conditions in an otherwise oxic aquifer would require considerably more effort than at the Rifle site, which is naturally suboxic. In this respect, returning an ISR-impacted aquifer to a state similar to the naturally reducing conditions of the pristine uranium roll front deposit should increase the prospects for successfully engineering bioremediation.

**Recalcitrance of bioreduced U(IV) to re-oxidation.** In spite of laboratory studies that have identified reoxidation and remobilization of bioreduced uranium (Komlos et al., 2008a; Komlos et al., 2008b; Moon et al., 2007; Moon et al., 2009), recent studies (Campbell et al., 2011; Sharp et al., 2011) have identified recalcitrance of uraninite to reoxidation, especially under in situ conditions that include the presence of biofilms and the full complement of geochemical components. One implication is that uranium reduced to U(IV) during ISR bioremediation may potentially withstand periods of residual oxygen exposure as the redox potential is lowered to near-native conditions.

## 2.7 ISR Bioremediation Potential

There have been relatively few field-based studies that have been published on the cause(s) of the recalcitrance of uranium ISR sites to restoration. While *in situ* bioremediation has been attempted at uranium ISR sites, there are no publications of bioremediation field studies that have been designed and monitored to better understand the site processes, properties, and conditions that control its effectiveness. The need for such studies is tempered by the cost and complexity of comprehensively interrogating a deep aquifer with a large range of biogeochemical states. However, there is no substitute for well-conceived field studies of the uranium ore sites, alteration of those sites by ISR operations, and the engineering of biologically mediated reactions intended to more effectively and efficiently restore pre-operational conditions.

# 3 Laboratory Studies of Biostimulated Uranium Reduction in ISR Aquifer Sediments and Suboxic Remobilization of Sequestered Uranium (C.C. Fuller and K. Akstin)

## 3.1 Introduction

### 3.1.1 Objectives

The laboratory experimental studies with aquifer sediment recovered from an unconsolidated sand U-ore body previously extracted by in situ recovery (ISR) are described in this chapter. Flow-through column and batch experiments were designed to investigate the ability of the indigenous microbial population for biostimulated reduction of uranium and resulting sequestration of uranium from the influent artificial ground water flowed through packed columns. The extent of release of uranium in response to return to suboxic conditions also was tested on a column following uptake of uranium during biostimulated reduction. Analyses of sediments recovered from columns at the end of the biostimulation and re-oxidation stages were conducted to characterize the form of the sequestered uranium and to quantify changes in sediment chemistry during the course of the experiments. Biostimulation column experiments were conducted using an artificial ground water to represent the major ion chemistry of the aquifer and were continued well into sulfate reduction to simulate long-term in situ bioremediation effort.

Bioremediation strategies for uranium contaminated aquifers are based on the ability of the microbial community to reduce the highly soluble hexavalent uranium (U(VI)) to sparingly soluble +4 oxidation state (U(IV)) which then precipitates to form phases such as uraninite thereby immobilizing uranium and lowering dissolved concentrations (Lovley et al, 1991). Bioremediation is achieved through stimulation of the ambient microbial population through amendment of the aquifer with suitable electron donor to consume oxygen and promote anaerobic conditions. Dissimilatory metal reducing bacteria have been shown to concomitantly reduce U(VI) with the bioreduction of Fe(III) phases, both in the laboratory (Lovley et al, 1992), and field tests in shallow aquifers (Anderson et al, 2003). Sulfate reducing bacteria have also been shown to reduce uranium directly through enzymatic mechanisms (Lovley et al, 1993). In addition to direct enzymatic reduction by microbes, U(VI) reduction may also occur by abiotic reaction with products of biogeochemical reduction processes, such as iron sulfides (Veeramani et al, 2013; Hyun et al, 2012; Hua, 2008). However, the importance of abiotic, non-enzymatic uranium reduction has not been demonstrated at the field scale.

### 3.1.2 Kingsville ISR Site Description

Aquifer sediments were recovered from the Kingsville Dome ISR facility in a roll front deposit previously extracted using ISR. The Kingsville ISR facility is located about 40 miles southwest of Corpus Christi, Texas, and about 8 miles southeast of Kingsville, in Kleberg County (**Figure 3.1**). The uranium ore bodies of the Kingsville Dome area are found in the Goliad Formation, Miocene to Pliocene deposits of unconsolidated sand and sandstone. The Goliad is mostly

fluvial deposits and is part of the South Texas Gulf Coastal Plain Physiographic Province. The Evangeline aquifer is associated with the Goliad formation.

Uranium in the South Texas uranium belt is thought to have leached from volcanic ash generated by volcanic activity further west which was deposited as portions of the Catahoula formation (Nicot et al. 2010, Galloway, 1977). Uranium ore at Kingsville Dome is in roll front deposits, formed as oxidized groundwater carrying dissolved U(VI) came into contact with reducing conditions which are thought to have been generated by H<sub>2</sub>S bearing water migrating upward, around the Kingsville salt dome, from sour hydrocarbon deposits. The ore deposits are 30 to 70 feet wide and are found at depths of 500 to 750 feet. According to the 2011 URI Annual report, the Kingsville dome ISR area contains proven reserves of 0.050 million tons of U<sub>3</sub>O<sub>8</sub> at percent grade of 0.088%. Since July, 2009 no extraction activities have taken place on the 2135 acre site.

At Kingsville Dome, as described by Arrendondo (1991) from thin sections, the Goliad material is “fine to medium grained, calcareous quartz sand and silt with minor amounts of chert, K-feldspar, volcanic rock fragments, pyrite, marcasite, leucoxene, pyrite and marcasite intergrowths, Ca-montmorillonite, gypsum, and traces of plagioclase, kaolinite, metamorphic rock fragments, mica, chlorite, and barite.” While quartz comprises up to 30% of the framework grains, coatings of clay (primarily Ca-montmorillonite) and calcite are common.

XRD of Kingsville uranium bearing material, showed only quartz, calcite, kaolinite, and Ca-montmorillonite. One of the ten XRD samples showed uraninite, otherwise no U minerals were observed. Uranium appears to be in several forms, besides uraninite. SEM/EDAX showed U in the clay fraction with some being non-crystalline and adsorbed on the surfaces of thin authigenic Ca-montmorillonite clay coatings in quartz sand grains. It is also associated with detrital iron-titanium oxide minerals that have been replaced by iron disulfide minerals, pyrite and marcasite. Electron density microphotos of heavy minerals show Fe, Ti, U, S, and Ca with U commonly occurring with Ti (Arrendondo, 1991).

At the ISR site, wellfield 13, there are three stacked roll-front deposits, each about 10 feet thick with several feet between them. Coring was done at the north end of the site (**Figure 3.2**). Samples were taken close to borehole AA 24 in the A & B sands. **Figure 3.3** shows the material taken from a depth of 580-590 feet that was used in the bioremediation experiments.

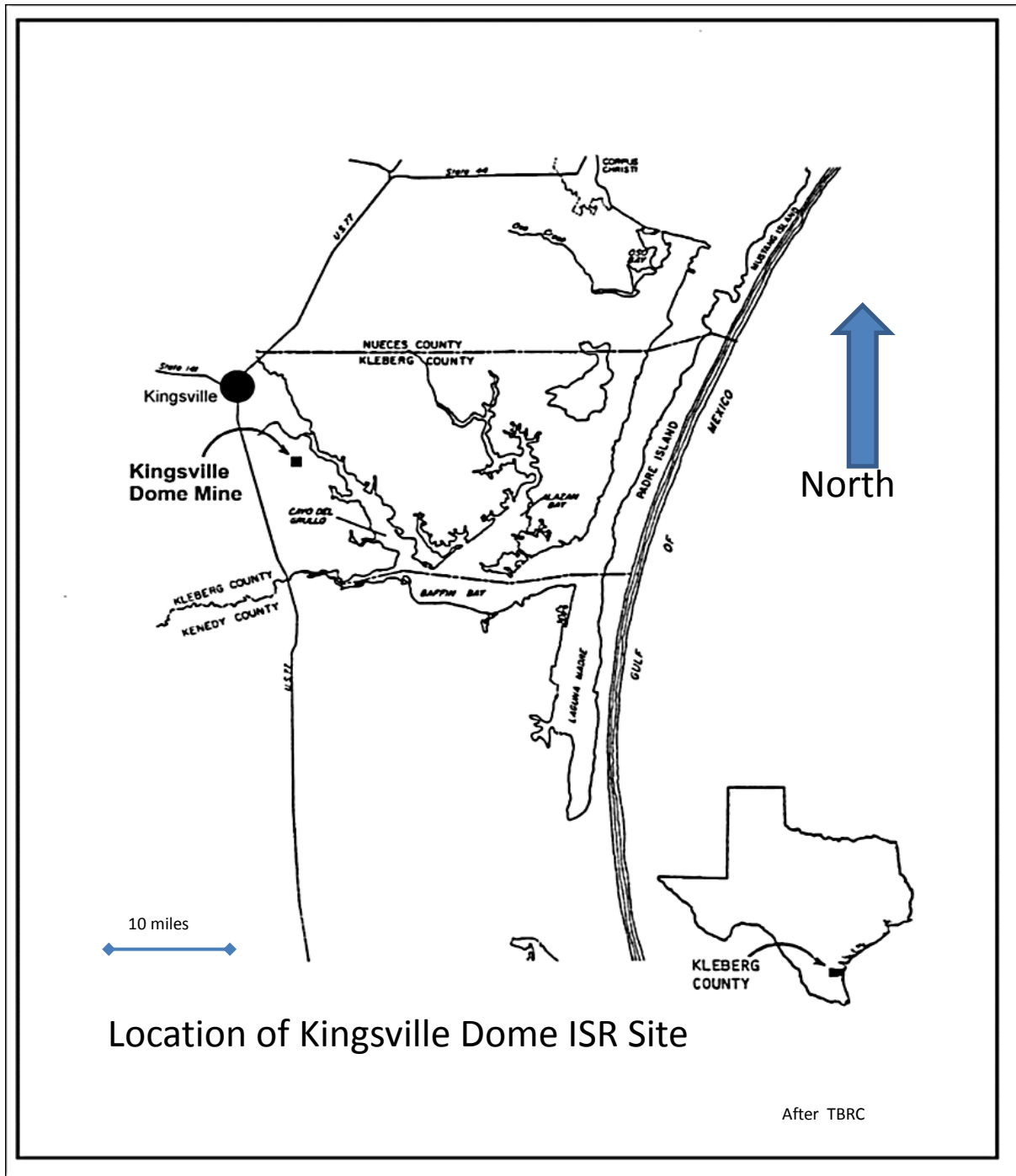


Figure 3.1 Location of Kingsville Dome ISR site in south Texas.



Figure 3.2 Samples were obtained by drilling into an ore zone after uranium recovery operations were finished.



3.3 The sediment sample used for the bioremediation experiments was obtained from a depth of 580-590 feet.

## **3.2 Methods**

### **3.2.1 Sediment and Groundwater Collection and Analyses**

#### **3.2.1.1 Aquifer sediment sampling**

Aquifer sediments were collected August 5 to 7, 2009, from two drill holes across three vertically stacked roll front deposits, which all have had U extracted by in situ leaching. The upper and lower ore deposits (A, C) are thought to be from the reduced portions of the roll fronts while the middle zone (B) is from the oxidized region of the roll front. Because of near complete loss of sediments from core barrel during recovery, only one sediment sample, 3712 BC 580-590, was recovered from the corer. The sediment sample was transferred directly into a Mylar bag with minimal handling to avoid contamination, and immediately sealed with scrubbers to remove oxygen. The remaining samples were recovered by washing sediment out of the bore hole with a high-pressure water stream. Samples were immediately sealed in Mylar/foil pouches containing scrubbers to remove oxygen.

Upon return to Menlo Park, the sediment samples were transferred from the Mylar pouches to 2-quart Mason jars in an anaerobic chamber. The jar lids were fitted with a port and valve to allow lowering internal pressure to facilitate sealing the jars. A split of each sample was dried in the anaerobic chamber at room temperature. The sediments are comprised of medium sand to clay size material that ranged from gray to greenish gray color, and were non-cohesive. The sand fraction appeared to include dark mineral grains. The samples recovered by washing out of bore holes included varying amounts of blue-green blebs of clay which could not be removed from the samples. This material was suspected to be from bentonite clay (drilling mud) added to facilitate drilling and not from the natural deposit. The sample recovered from the corer (3712 BC 580-590) did not contain the clay blebs. The un-dried aquifer materials were stored at 4°C in the absence of oxygen in the Mason jar. An oxygen indicator was placed in each jar and in an empty jar to verify that oxygen was not leaking into the sample. In addition, internal pressure measurements prior to opening jars for subsampling indicated that jars remained sealed during storage.

The experimental studies were intended to investigate the ability of the indigenous microbial population for biostimulation reduction and were conducted with the 3712 BC 580-590 ISR aquifer sediment. Sediments were handled aseptically within the anaerobic chamber. In addition all materials were sterilized prior to use, if possible. In particular, storage jars and column apparatus were sterilized by autoclaving. Subsampling implements such as spatulas were sterilized by wiping with alcohol swabs to minimize contamination of microbial community. Subsampling from the jars was conducted in the anaerobic chamber using sterilized apparatus.

#### **3.2.1.2 Groundwater sampling and analysis**

Groundwater was sampled from six wells near the drilling site at the Kingsville Dome ISR operation, August 5-7, 2009. The wells are screened within reduced (13402, 13406, 13307,

13209) and oxidized (13408, 13310) zones of the roll front deposits. In situ leaching of uranium deposit has occurred in this part of the aquifer. Wells were pumped at 75 L/min for a minimum of 3 casing volumes. Groundwater samples were collected off of a tee-fitting in the pump effluent tubing and filtered through 0.45 micron cartridge filters using a peristaltic pump. Groundwater dissolved oxygen concentration was measured using Chemetrics dissolved oxygen vacu-vial filled with Rhodazine D™ which has a minimum detection limit of  $3.2 \times 10^{-6}$  M (0.1 mg/L). The well sampling pump outflow, split from the TEE fitting, was routed through an inverted funnel (~30 mL) that was provided with the vacu-vial ampoules. The ampoule tip was submerged in the funnel and broken underwater after 3 minutes of flow through the funnel at about 100 mL/min. After the 1 minute color development period, absorbance of the dissolved oxygen complex was measured on a Chemetrics V2000 spectrophotometer.

The groundwater samples all had similar major ion chemistry and pH (**Table 3.1**). Low to non-detectable dissolved sulfide and very low dissolved oxygen (<0.3 mg/L; <9 μM) were measured in these wells. These low dissolved oxygen concentrations are consistent with the relatively high observed Fe(II) concentrations. Total alkalinity ranged from 12 to 15 milliequivalents per liter. Groundwater was near saturation with respect to calcite and gypsum, with very high calculated pCO<sub>2</sub> (35 to 51%) for the measured pH and alkalinity.

Dissolved iron ranged from 165 to 380 μM (7.9 to 21 mg/L). Field measurements of ferrous iron all exceeded the analytical limit of 6 mg/L. Siderite was slightly oversaturated in all samples (log SI 0.2 to 0.5). Dissolved uranium, [U], ranged from 20 to 53 μM (4700 to 12,500 μg/L). Assuming the dissolved U is U(VI), its speciation is dominated (>97%) by calcium uranyl carbonate complexes based on equilibrium speciation modeling of groundwater chemistry using PHREEQC and stability constants in Davis and Curtis (2007). Dissolved Mo, likely molybdate, ranged from 12 to 48 μM (1200 to 4,600 μg/L). Vanadium was below the ICP-OES method detection limit (0.5 μM or 25 μg/L). There is no apparent trend among U, V and Fe concentration for these wells.

Groundwater data provided by URI for this well field has similar concentration ranges for Ca, Cl, sulfate, alkalinity and U for the most recent samples collected (June 2008) to those shown in **Table 3.1**. The pH values previously reported are 0.7 to 1.1 units higher likely because of CO<sub>2</sub> outgassing prior to pH measurement. Groundwater pH data presented here was collected in a flow cell that had continuous flow from a diversion of the well pump outlet (at a rate of 100 to 200 mL/min through the flow cell).

Table 3.1 Kingsville Dome groundwater chemistry from wells sampled August 5-6, 2009. Major and minor cations determined by ICP-OES of filtered (0.45 µm), acidified samples. Anions determined by ion chromatography of filtered samples. The following elements are not reported since below method detection limits: Co, Cu, P, F (< 2E-8, 8E-8, 1E-6 M, 5E-7M). "n/m" indicates not measured.

Well	13402	13406	13307	13208	13209	13310	units
Field parameters							
pH	6.12	6.22	6.13	6.19	6.09	6.10	
dissolved O <sub>2</sub>	<0.1	<0.1	<0.1	<0.1	0.19	0.24	mg/L
H <sub>2</sub> S	n/m	n/m	n/m	n/m	0.17		mg/L
ferrous iron	>6	>6	>6	>6	>6	>6	mg/L
Alkalinity <sup>a</sup>	1.39E-02	1.16E-02	1.20E-02	1.16E-02	1.12E-02	1.24E-02	eq/L
Alkalinity <sup>b</sup>	1.45E-02	1.19E-02	1.26E-02	1.19E-02	1.20E-02	1.30E-02	eq/L
Ca	1.87E-02	1.78E-02	1.79E-02	1.83E-02	1.88E-02	2.01E-02	mol/L
K	6.36E-04	7.31E-04	5.87E-04	7.77E-04	7.60E-04	7.18E-04	mol/L
Mg	4.53E-03	4.33E-03	3.87E-03	4.87E-03	4.58E-03	4.76E-03	mol/L
Na	2.58E-02	2.75E-02	2.43E-02	2.64E-02	2.77E-02	2.59E-02	mol/L
Si	3.89E-04	4.01E-04	3.57E-04	5.01E-04	4.80E-04	5.48E-04	mol/L
Cl	1.89E-02	2.02E-02	1.82E-02	2.00E-02	2.01E-02	1.88E-02	mol/L
SO <sub>4</sub>	2.12E-02	2.21E-02	2.10E-02	2.42E-02	2.33E-02	2.26E-02	mol/L
U	5.25E-05	2.93E-05	1.97E-05	2.66E-05	2.86E-05	3.06E-05	mol/L
Fe	2.92E-04	1.65E-04	3.16E-04	1.41E-04	3.83E-04	3.25E-04	mol/L
Mo	1.22E-05	3.45E-05	1.33E-05	4.35E-05	4.84E-05	2.42E-05	mol/L
Ni	2.21E-06	1.70E-06	1.36E-06	1.19E-06	8.52E-07	6.81E-07	mol/L
Sr	2.19E-04	2.02E-04	2.01E-04	1.85E-04	2.08E-04	2.24E-04	mol/L
V	<5E-07	<5E-07	<5E-07	<5E-07	<5E-07	<5E-07	mol/L
Zn	2.57E-05	1.93E-05	1.54E-05	1.33E-05	7.95E-06	6.88E-06	mol/L
Ionic Balance <sup>c</sup>	-1.3	-2.2	-2.6	-4.1	-1.6	0.2	%
PHREEQC calculations:							
pCO <sub>2</sub>	0.51	0.35	0.45	0.36	0.46	0.49	atm
log SI calcite	-0.01	-0.01	-0.06	-0.05	-0.13	-0.05	
log SI siderite	0.49	0.28	0.5	0.17	0.51	0.47	
log SI gypsum	0.01	0.01	0.01	0.05	0.04	0.06	

- Measured total alkalinity in samples after return to Menlo Park. Iron oxidation and precipitation occurred during this time interval.
- Measured total alkalinity corrected for proton release resulting from iron oxidation and precipitation by assuming 2 equivalents H<sup>+</sup> released per mole Fe.
- Ionic balance uses corrected alkalinity values.

### 3.2.2 AGW Design and Composition

Artificial groundwater (AGW) used for both batch and column experiments was developed to simulate the average major ion chemistry of groundwater sampled at the Kingsville Dome ISR site (**Table 3.1**). AGW composition is shown in **Table 3.2**. The  $p\text{CO}_2$  was fixed based on Kingsville groundwater with dissolved calcium concentration iteratively adjusted in PHREEQC simulations to yield the desired pH of 6.3 for the column influent. The resulting calculated alkalinity of  $5.6\text{E-}3$  M was about a factor of 2 lower than groundwater from the field site ( $1.1$  to  $1.3\text{E-}2$  M) which had a calculated  $p\text{CO}_2$  range of 35 to 51%. The 15%  $p\text{CO}_2$  was chosen to avoid the need to pressurize the experimental apparatus to work at the higher  $p\text{CO}_2$ . Both calcite and gypsum, phases present in the aquifer material, are slightly undersaturated in the AGW with log Saturation Index (SI) of -0.23 for both, but were calculated to be at saturation in the Kingsville aquifer. For the biostimulation stage of the column experiments and for batch experiments, the AGW was amended with dissolved phosphate, ammonia, trace elements, and vitamins, as shown in Table 2. Dissolved uranium as U(VI) was added from a 1 mM stock solution prepared from dissolution of reagent grade  $\text{UO}_3$  with sulfuric acid.

The initial batch experiment was conducted at pH 6.9 because of availability of 3.5%  $p\text{CO}_2$  gas mixture. The AGW used for this initial batch experiment had the total carbonate and calcium lowered to  $4.62\text{E-}3$  and  $8.32\text{E-}3\text{M}$ , respectively, in order to maintain condition of saturation with respect to calcite for this  $\text{CO}_2$  partial pressure.

AGW for columns was prepared in 3.5 L batches in tared 5-L glass reservoirs (Kontes model KC14395 5000) fitted with 3-hole screw caps (Kontes 953930) that were threaded for gas inlet and outlet, and liquid outlet tubing fittings. Calcium sulfate was dissolved in 3 L deionized water, with appropriate volumes of concentrated salt solutions then added to yield desired final concentrations of all major ion components except for  $\text{NaHCO}_3$  and U(VI). The reservoir was then sterilized by autoclave, along with inlet and gas purging tubing assemblies. After autoclaving, the reservoir was sealed until cooled. The remaining AGW components and amendments were then added through  $0.22\ \mu\text{m}$  filters to sterilize them. Reservoir weight was recorded after each addition, and after autoclaving. For the lactate column influent reservoirs, sodium lactate solution was added from a 1 M stock solution prepared from lactic acid and sodium hydroxide. This stock solution was filter sterilized and stored at  $4^\circ\text{C}$  in an autoclaved serum bottle flushed with nitrogen. After addition of all components, the AGW reservoirs were flushed with 15%  $p\text{CO}_2$  balance  $\text{N}_2$  gas mixture for one hour at  $\sim 1$  L/min through a gas dispersion stone. The inlet tubing apparatus was installed, and the reservoir flushed for another 30 minutes before attaching to a column. A continuous flow of the gas mixture was bubbled through the reservoir at  $\sim 50$  ml/min and vented through an airlock for the duration of the experiment.

The hydrogen amended columns used the same AGW composition and preparation method but without addition of sodium lactate. Suboxic AGW used to test remobilization of sequestered uranium was prepared by the same method but without the additions of dissolved U(VI), electron donor, nutrients, vitamins and trace elements. The suboxic AGW reservoir was purged with the desired gas mixture (see below).

Table 3.2 Artificial groundwater composition for column and batch experiments. Lactate, nutrients, trace elements and vitamins added only to AGW during biostimulation.

Constituent	moles/L	without lactate
Ca	2.05E-02	
Na	2.96E-02	1.96E-02
Mg	4.87E-03	
K	7.77E-04	
U	2.00E-05	
NH <sub>4</sub>	1.40E-04	0
Cl	4.52E-02	
SO <sub>4</sub>	1.00E-02	
Total CO <sub>3</sub>	1.13E-02	
lactate	1.00E-02	0
PO <sub>4</sub>	8.00E-07	0
pH	6.23	
alkalinity	5.59E-03	
Trace elements, vitamins		
CoCl <sub>2</sub> •6H <sub>2</sub> O	8.0E-07	
MnCl <sub>2</sub> •4H <sub>2</sub> O	5.1E-07	
ZnCl <sub>2</sub>	5.1E-07	
H <sub>3</sub> BO <sub>3</sub>	9.7E-08	
Na <sub>2</sub> MoO <sub>4</sub> •2H <sub>2</sub> O	1.6E-07	
NiCl <sub>2</sub> •6H <sub>2</sub> O	1.0E-07	
CuCl <sub>2</sub> •2H <sub>2</sub> O	1.2E-08	
CoCl <sub>2</sub> •6H <sub>2</sub> O	8.0E-07	
p-amino-benzoic acid	1.2E-08	
biotin	2.7E-09	
folic acid	1.5E-09	
pyridoxine•HCl	1.6E-08	
thiamine•HCl	5.0E-09	
riboflavin	4.4E-09	
nicotinic acid	1.4E-08	
pantothenic acid	3.5E-09	
thioctic acid	8.1E-09	
vitamin b12	2.0E-11	

### 3.2.3 Batch Experiments to Determine Electron Donors

Uranium uptake experiments were conducted with the ISR sediment to determine if indigenous microbial populations in the sediment enhanced U uptake when amended with

different electron donors. An increase in U uptake in the presence of an electron donor compared to U uptake in the absence of electron donor was inferred to result from microbial reduction. These experiments were conducted in batch mode under anaerobic conditions. The results were used to guide the choice of electron donor to use in column experiments. Splits of the ISR sediment were transferred into sterilized serum bottles followed by addition of 60 mL of AGW to yield a solid to liquid ratio of 50 g/L.

The initial experiment (Batch 1), started in May 2010, used the pH 6.9 AGW and had an imposed  $p\text{CO}_2$  of 3.5%. Twelve serum bottles with 3 g of sediment and 60 mL AGW were sealed in the anaerobic chamber, removed from the chamber, then purged with 3.5%  $\text{CO}_2/\text{N}_2$  balance gas stream for 30 minutes to remove hydrogen gas from the bottles and to achieve the desired  $p\text{CO}_2$  and pH. The bottles were then put on an orbital shaker. After 24 hours an initial sample was collected through the septum cap with a  $\text{N}_2$  flushed syringe, and filtered through a 0.2  $\mu\text{m}$  filter. The filtrate was acidified and processed for dissolved U and ICP analysis. Aliquots of 1 mM uranyl sulfate were added to each bottle to attain an initial dissolved U(VI) concentration of 20  $\mu\text{M}$  in all bottles except two pairs. One pair of bottles had no added U to test for U desorption from the ISR sediment. The other pair had U added to 40  $\mu\text{M}$ . Electron donors were added to three pairs of bottles. Hydrogen gas was added to one pair of bottles to attain a  $\text{H}_2$  partial pressure of 0.35 for an equilibrium dissolved  $\text{H}_2$  of 270  $\mu\text{M}$ . Sodium acetate was added to two bottles to yield 10 mM initial concentration. Sodium lactate was added to two bottles for initial concentrations of 10 and 20 mM to each of two bottles. No electron donor amendments were made to the other six bottles: 2 without added [U], 2 with 20  $\mu\text{M}$  [U], and 2 with 40  $\mu\text{M}$  [U]. The latter two pairs were used as controls to monitor U uptake in the absence of electron donor amendment. All bottles with added [U] were then sampled to establish initial actual [U]. Bottles were mixed on an orbital shaker at room temperature and subsampled periodically over the next twelve weeks initially at 2 or 3 day intervals with longer intervals based on changes in [U]. Bottle weights were recorded before and after each addition and sampling. At the end of the experiment, sediments were recovered in the anaerobic chamber, frozen at -80°C for microbial assay.

A subsequent set of batch experiments was conducted to test the viability of sediments in response to hydrogen amendment and test the effect of different dissolved  $\text{H}_2$  concentrations on U uptake and reduction. This experiment was initiated in June after no appreciable decrease in [U] was observed in the  $\text{H}_2$  amended column experiment (see Section on  $\text{H}_2$  columns below). The same sediment as in both the column experiments and in the first batch experiment, and at the same solid to AGW ratio (50 g/L) was used. Both the 3.5% and 15%  $\text{CO}_2$  AGW were used to test for any difference resulting from pH 6.9 and 6.3. An initial [U] of 20  $\mu\text{M}$  was used in all bottles and was added with the AGW. A range of dissolved  $\text{H}_2$  also was tested that spanned the dissolved  $\text{H}_2$  imposed on the column reservoir (5%), to the level added to the first batch experiment (~40%), and an intermediate level (20%). These  $\text{H}_2$  partial pressures in the headspace resulted in equilibrium dissolved  $\text{H}_2$  of 40, 312, and 156  $\mu\text{M}$ , respectively. Batch bottles were processed and subsampled as described for the first experiment. Sediments were not recovered for microbial assay.

### 3.2.4 Column Set Up and Operation

Five columns of identical dimensions were packed for this study. Two columns (L1 and L2) had lactate added as an electron donor to stimulate indigenous microbes for reduction of uranium. One (L1) was subsectioned at the end of the biostimulation stage and sediments recovered for geochemical and microbial analyses. The second column (L2) was used to test remobilization of sequestered uranium (re-oxidation of U(IV) and desorption or dissolution of U(VI)) in response to suboxic conditions to simulate conditions in an aquifer following cessation of electron donor addition. This is termed the oxidation stage. A second pair of columns was set up to investigate biostimulated uranium reduction by dissolved hydrogen as the electron donor and subsequent remobilization under suboxic conditions (H1 and H2). The fifth column (L5) was used for a conservative anion breakthrough test (bromide) to determine column hydrodynamic parameters prior to biostimulation, and to determine the extent of mobilization of the remaining uranium associated with the aquifer sediment following in situ leaching by imposing suboxic conditions following the bromide tracer breakthrough and elution.

#### 3.2.4.1 Columns

Glass 2.2 cm inner diameter columns with adjustable length bed supports were used (Millipore VL22X250). Inlet and outlet bed supports were 20 micron pore size.

#### 3.2.4.2 Plumbing and pumps

Column inlet and outlet tubing was 1/16" OD PTFE with 1/4"-20 flangeless fittings to connect to 4-way valves at about 12" from column inlet and outlet fittings. A pressure gauge was installed at a TEE fitting upstream of the inlet 4-way valve and downstream of the pump. All tubing from the reservoir cap to effluent collection outlet was encased within 1/4" ID 1/8" wall Tygon R3607 tubing to jacket the influent and effluent tubing. The gas mixture was continuously flowed throughout the jacketing to minimize gas exchange through influent and effluent tubing and oxygen contamination. Tygon tubing was attached to nylon TEE connectors at each fitting and at the column inlet and outlet with a length of Tygon connecting adjacent TEE connectors to provide a continuous purge of the entire length of influent and effluent tubing. The jacketing purge gas was flowed at 50 cc/min in the same direction as the AGW flow starting at the feed line of the reservoir to the column effluent outlet, bypassing the peristaltic pump, the pressure gauge, valves and the columns (see **Figure 3.4**).

The influent AGW was pumped from the reservoir through the columns using an ISMATEC 8-roller multi-channel pump fitted with 1.1 mm ID and later 0.76 mm ID Tygon R3606 double stop tubing that was attached to jacketed reservoir and inlet tubing with nylon hose barbs. All tubing and fittings were autoclaved before use.



Figure 3.4 Column experimental apparatus illustrating (A) column and effluent collection, (B) effluent tubing with gas purged jacketing to minimize oxygen invasion and effluent collection bottle, (C) influent reservoir with gas mixture purge and outlet lines, (D) influent lines with gas jacketing, (E) peristaltic pump in purged housing. F) Column L2 after 46 days of biostimulation showing dark banding forming in sediment (arrow) and Sterivex filter on outlet for microbial assay test in gas jacketed housing upstream of effluent collection bottle.

### 3.2.4.3 Gas phase and oxygen control

Commercially-prepared, high-purity gas mixtures of 15% CO<sub>2</sub>, 85% N<sub>2</sub> were used for the biostimulated reduction stage of the lactate columns and 15% CO<sub>2</sub>, 5% H<sub>2</sub>, 85% N<sub>2</sub> was used for the hydrogen amended column experiments. An oxygen scrubber was fitted in line to remove residual oxygen in the commercial mixture. Reservoirs were continuously purged with the gas mixture at about 25 cc/min, after the initial flush, and vented through airlocks. Jacketed tubing (described above) also was continuously purged with this gas mixture. For the suboxic elution of the lactate columns, the gas stream was delivered using a 3-channel gas flow controller to dilute a 20% O<sub>2</sub>, 15% CO<sub>2</sub>, 65% N<sub>2</sub> premixed cylinder with N<sub>2</sub> and CO<sub>2</sub> to attain the desired oxygen content while maintaining 15% CO<sub>2</sub>. The pO<sub>2</sub> of the mixture was set to attain the desired dissolved oxygen concentration. The mass flow controller was calibrated using a TCD detector gas chromatograph. Because of gas exchange across pump tubing walls resulting from pressure from pump rollers, the peristaltic pump was housed within an acrylic box that was continuously purged with the gas mixture for the specific experiment. This housing was constructed for the hydrogen amended columns and later used for the suboxic elution of lactate column experiment. Significant loss of hydrogen and influx of oxygen was discovered during the course of the hydrogen biostimulation and the suboxic elution of lactate experiments, respectively, as discussed below. The purged pump housing eliminated the problem with gas exchange across pump tubing.

### 3.2.4.4 Column packing

The sediments from core KVD 3712 BC 580-5590 were used for column biostimulation experiments. Columns were slurry packed with wet aquifer sediment in an anaerobic glove chamber. Sediments were mixed with AGW to a consistency similar to pancake batter by adding about 20 mL of AGW to 100 grams of damp aquifer sediment and mixing thoroughly. Starting and ending weights of the sediment slurry container were recorded during column packing. The sediment slurry was subsampled to tared glass vials to determine water content upon drying. Each column with its inlet and outlet fittings and tubing including 4-way valves at each end was weighed empty. Dead volumes of tubing, frit and fittings were determined by weighing the column assembly full of deionized water with the inlet and outlet bed supports adjusted inwards until they met and subtracting the empty weight.

An empty column with the inlet bed support and fittings attached was mounted vertically with the inlet end down. AGW was added through the inlet valve with a syringe until a few millimeters above the inlet bed support frit. The sediment/AGW mixture was added with a spatula to the column in increments of about 0.5 cm. A rubber policeman was used to move any sediment that adhered to column walls to the sediment bed. The column was tapped and sediment was allowed to settle for about 5 minutes before adding the next increment. AGW was added as needed to maintain a lens of water (1-2 mm) above the sediment. This process was repeated until the sediment was at a height of about 10.5 cm above the inlet frit. The sediment in the packed column was allowed to settle overnight. On the following day, any overlying water (~5 mL) was removed from the top of the sediment bed with an automatic pipette and retained in a tared vial to determine the mass of water and sediment removed. Small amounts of fines were inadvertently removed by this process. The walls of the column

were cleaned with damp tissue. The outlet bed support and fittings were installed with frit adjusted to the level of the top of the sediment. Additional AGW was pushed through the column by syringe. The packed column was allowed to stand for an additional 24 hours. The outlet frit was then adjusted downward to the sediment surface as needed to expel excess overlying water through the outlet tubing. Inlet and outlet valves were then closed and the column was removed from the anaerobic chamber and weighed. Columns are mounted vertically with the outlet end up, and the influent and effluent plumbing attached to the appropriate 4-way valves. Flow of the gas mixture through the inlet and outlet tubing jackets was initiated, and flow of influent AGW containing dissolved U(VI), electron donor and other amendments through column commenced.

### 3.2.4.5 Column parameters; pore volume, solid density

Measured dimensions and weights of columns used for lactate experiments are shown in **Table 3.3**. Column pore volume and porosity were determined from total sediment weight used in packing the columns, total weight of column minus empty weight, and the dimensional volume minus volume of bed support fittings, inlet and outlet tubing. Pore volume and total dry sediment mass were similar in the two columns, which were intended to be identical.

Table 3.3 Column parameters: dimensions and weights.

L1	L2	L5	Parameter
2.22	2.22	2.22	Column diameter, cm
10.5	10.1	10.1	Column length of sediment, cm
78.50	78.13	79.04	Total sediment weight, wet, in column
0.28	0.28	0.27	Water weight of sediment, from split during packing
56.86	56.59	58.01	Calculated dry sediment in column, g
17.8	16.2	17.9	Calculated water component of wet sediment in column, g
1.58	1.58	1.58	Dead volume of inlet and outlet tubing, measured; cm <sup>3</sup>
17.8	16.2	17.9	Pore volume of packed column, cm <sup>3</sup>
40.6	39.1	39.1	Total column bed volume (from measured dimensions), cm <sup>3</sup>
0.44	0.41	0.46	Column porosity, calculated
2.49	2.47	2.74	Sediment density, calculated, g/cm <sup>3</sup>

### 3.2.5 Column Effluent

#### 3.2.5.1 Sampling

Samples of column effluent were collected on a continuous basis throughout the duration of the reduction of the column experiments into tared autoclaved serum bottles that were flushed with the 15% CO<sub>2</sub> balance N<sub>2</sub> gas mixture. The outlet tubing was fitted with a sterile 0.22-µm

pore size 25-mm diameter sterile cartridge filter with an attached hypodermic needle that was inserted into 1-cm thick butyl rubber serum bottle stopper. A second needle connected to an airlock was inserted that allowed the headspace of the bottle to vent during sample collection (**Figure 3.4A**). This collection method was intended to maintain anaerobic conditions in the effluent sample bottle during collection and subsequent storage. Sample bottles were changed every 24 to 60 hours. Filters were replaced as needed with about three dead volumes allowed to flow through filter and needle before attaching to the collection bottle. Sample volume was determined by the weight of effluent collected, and the flow rate from volume divided by the duration of sample collection. Every other sample was acidified to 1% (v/v) with nitric acid for dissolved U and dissolved cation analyses. Samples were acidified at least 24 hours prior to subsampling analysis, and may have been stored at room temperature for up to two weeks before subsampling. The other samples were stored under refrigeration and were not acidified. These unacidified samples were used for analysis of dissolved sulfate, headspace and total dissolved carbonate, and, lactate and acetate (columns L1 and L2). Separate samples for dissolved sulfide analysis were collected periodically into 5-mL glass vacuivials previously flushed with the gas mixture and containing 1 mL 10% (wt/v) zinc acetate to preserve sulfide by precipitating as zinc sulfide.

Following the biostimulation reduction stage, a bromide tracer in AGW without lactate or U was passed through column L2 and then eluted with AGW with no U or lactate (see below). Samples were collected during the tracer input and elution using a fraction collector. Subsequently, AGW with no U, lactate, or added dissolved oxygen was passed through column L2 for 32 days with effluent collected in serum bottles, as described above. Effluent samples during the addition of dissolved oxygen to the influent (oxidation stage) of column L2, and during all of the column L5 sub-oxic elution were collected in plastic scintillation vials using a fraction collector programmed at the desired sampling interval. Sample vials were tared before use, capped and weighed after sample collection. Correction was made for evaporative loss during and after sample collection prior to capping based on evaporative loss from control vials containing similar volume of AGW. Samples for U and dissolved cations were acidified to 1% (v/v) with nitric acid.

Influent reservoirs were sampled through the 4-way valve between the pump and the column when each new reservoir was installed.

Dissolved oxygen was measured in both the column influent (pump outflow) and column effluent. Samples were collected in 7-cc serum bottles through syringe needles extending to near the bottom of the bottle and the exit needle inserted just below the stopper. These oxygen bottles were overfilled two to three bottle volumes and had negligible gas headspace volume.

### **3.2.5.2 Bromide tracer**

Measurement of the breakthrough and rise to plateau of a conservative anion (bromide) and subsequent elution was conducted to determine column hydrodynamic parameters prior to biostimulation (column L5). A bromide tracer was also passed through column L2 after biostimulation, but prior to suboxic elution, to determine if changes in pore volume and dispersion occurred during biostimulation. A reservoir containing bromide (360 mg/L) in AGW (no U, lactate, vitamins or nutrients) equilibrated with 15% CO<sub>2</sub>/N<sub>2</sub> gas mixture was flowed for 6

pore volumes through column L5 and for 10 pore volumes through the column L2. Continuous samples of effluent were collected using a fraction collector at 4 hour intervals for 3 days, followed by 6 hour intervals for the duration of the bromide pulse. Following the bromide pulse, a reservoir with AGW with no bromide, U, or lactate was installed and equilibrated with 15% CO<sub>2</sub>/N<sub>2</sub> mixture. Bromide elution samples were collected at the same frequency as bromide pulse sampling. After 8 4-hour samples, the effluent collection time was increased to 6 hours with effluent samples collected over the next 4 days to capture the tail of eluted bromide. Splits of every fourth or fifth sample were acidified for [U] analysis. Oxygen was added to the gas mixture of column L2 after 32 days of elution with AGW with the no oxygen gas mixture (see below). Bromide sampling of column L5 ended at 11 pore volumes (PV) (day 13). Elution of column L5 with suboxic AGW commenced by including oxygen in the reservoir purge gas mixture (0.5% O<sub>2</sub>/15%CO<sub>2</sub>/N<sub>2</sub>) for a 0.4 mg/L (12 μM) dissolved oxygen.

### 3.2.5.3 Analyses

Dissolved U in effluent and batch samples was measured using a kinetic phosphorescence analyzer (Chemchek Instruments Model KPA1), following pretreatment of an aliquot of acidified sample. The pretreatment consisted of drying on a hotplate in a glass scintillation vial, reconstituting in 1 mL of concentrated nitric acid, adding 7-10 drops of 30% H<sub>2</sub>O<sub>2</sub>, and heating to dryness. The dried sample was reconstituted in 0.1N HNO<sub>3</sub> and sonicated prior to KPA analysis. The pretreatment removes constituents (e.g. chloride, lactate) that quench uranium phosphorescence. KPA measures only U(VI), but in the unlikely event that any dissolved or colloidal U(IV) was present in the effluent samples it was likely oxidized to U(VI) during the pretreatment process and also measured as [U].

Dissolved cation concentrations (Fe, Ca, K, Mg, Mn, Na, etc) in effluent samples were measured by ICP-OES. The ICP-OES also measures total dissolved sulfur which includes both sulfate and sulfide species. Dissolved sulfide concentrations were measured in preserved samples by the colorimetric method described by Cline (1969). Dissolved sulfate in the un-acidified samples was measured by ion chromatography, while pH and alkalinity were calculated from the pCO<sub>2</sub> and total dissolved carbonate measured in the un-acidified samples. This method was used because lactate, acetate, and sulfide contribute to acid neutralization during Gran titration. Headspace CO<sub>2</sub> of un-acidified samples was measured on TCD detector gas chromatograph prior to other subsampling from these bottles. Subsequently a 5-mL aliquot of the effluent sample was transferred by syringe to a N<sub>2</sub> flushed serum bottle and acidified. The CO<sub>2</sub> evolved from dissolved carbonate was measured by GC. The alkalinity and pH measured in influent AGW (without lactate) collected by the same method but directly from the pump outlet gave comparable values to pH measured by electrode and to alkalinity determined by Gran titration on separate aliquots of this AGW. Lactate and acetate in the un-acidified samples were measured by HPLC with a UV detector.

Dissolved oxygen concentrations were measured in the 7 cc serum bottles in the anaerobic glove chamber colorimetrically using Chemette dissolved oxygen ampoules and a Chemetrics V2000 spectrophotometer. The ampoule tip was inserted into silicone tubing that was connected to a Luerlok fitting and a needle inserted to near the bottom of the bottle. A vent needle was inserted just through the stopper. On breaking the ampoule tip, sample was drawn

into the ampoule in about 5 seconds with an equal volume replaced by the anaerobic chamber atmosphere through the vent needle. After the 1 minute color development period, absorbance of the dissolved oxygen complex was measured on the spectrophotometer.

### **3.2.6 Solid Phase Sampling**

#### **3.2.6.1 Column Sectioning and Sample Preservation**

Sediments were recovered from column L1 at the end of the reduction stage and from column L2 and L5 at the end of the oxidation stage for chemical analyses and microbial assay (column L1 only). Columns were dismantled and the sediment subsampled in the anaerobic glove chamber. While maintaining the column vertically with the outlet end up, the outlet fittings up to the bed support were removed and a section of PVC pipe inserted. The column was then inverted and inlet fittings removed. The sediment was extruded out of the column into ~2-cm vertical sections with push up distance and length of sediment bed measured before and after each subsection was extruded. Each subsection was weighed and homogenized by mixing with a sterilized Teflon spatula. A split of sediment was taken to determine water content upon drying. Each column subsection was about 11 to 12 grams of dry sediment. For column L1, a second split of about 1 g was transferred to a whirlpak bag for microbial assay. The remaining sediment was split between a 2-mL micro-centrifuge tube for gamma spectrometry, and a glass scintillation vial. These containers were double bagged in Mylar pouches containing oxygen scrubbers. The bags were heat sealed and stored at -80° C until analyzed.

#### **3.2.6.2 Total U screening by gamma spectrometry**

Total uranium content of the column subsections and the KVD 3712 BC 580-590 sediment prior to biostimulation (termed pre-column sediment, here after) was determined by gamma spectrometry following the method outlined in Fuller et al (1999). The 63 KeV gamma emission of the <sup>238</sup>U daughter <sup>234</sup>Th was measured on a high resolution germanium detector gamma spectrometer. This method assumes that the <sup>234</sup>Th daughter is in secular equilibrium. Because the L1 samples measured immediately at the end of the biostimulation reduction likely were not in secular equilibrium, the total uranium of these samples measured by gamma spectrometry is considered a lower limit. These total uranium values were used primarily to determine which samples to use for X-ray adsorption spectroscopic measurements and as a guide for dilutions for chemical extraction analyses. Total uranium concentrations determined by hot nitric acid extraction (see below) were used for mass balance calculations and for comparison to loading calculated by integrating the difference between influent and effluent dissolved U.

#### **3.2.6.3 Chemical analyses**

Five gram splits of recovered sediment from columns were dried at room temperature in the anaerobic chamber for chemical analyses. The dried sediment was homogenized and a 1-gram split was ground with an agate mortar and pestle for nitric acid extraction and total S measurement. The unground remainder was used for partial chemical extraction of ferric and ferrous iron, acid volatile sulfide, nitric acid and HF total dissolution, and total carbonate

analysis. A split of the pre-column sediment was also analyzed by the techniques outlined below to compare with this sediment following biostimulation reduction and suboxic elution.

### 3.2.6.3.1 Extractions

Hot nitric acid and peroxide extraction was used to determine total uranium and other constituents such as calcium and iron. This method is based on EPA method 3050 and dissolves most sedimentary phases except for silicates. Briefly, 0.1 gram of the ground sediment was placed in a tared glass vial and treated with ~2 mL 0.5 N HNO<sub>3</sub> added drop wise to minimize samples loss as aerosol during effervescence of carbonates. The aquifer sediment contained about 20% (w/w) carbonate as CaCO<sub>3</sub>. The pre-treated sample was dried at 90°C on a hot plate and cooled. 3 ml of concentrated HNO<sub>3</sub> was added and a glass bulb placed on top of the vial. The sample was refluxed for 24 hours at 90°C. After cooling, 0.5 mL of 30% H<sub>2</sub>O<sub>2</sub> was added and allowed to stand for 30 minutes. The reflux bulb was removed and the sample evaporated to dryness at 90°C. The dry weight was recorded and 10 mL of 0.1N HNO<sub>3</sub> added to reconstitute the sample. The sample was sonicated for 30 minutes and allowed to settle overnight. An aliquot of supernatant was removed with a syringe, passed through a 0.22 µm filter, and diluted appropriately for analysis by KPA for U and ICP. The U concentration determined using this hot nitric acid extraction and the gamma spectrometry total U measurement generally agreed within 10%.

Total dissolution via hydrofluoric acid digest was also performed to provide a measure of iron content of silicate phases not leached by the hot HNO<sub>3</sub> digest. Briefly 0.1 g of ground sediment was placed in a 10 mL Teflon reaction vial. Samples were pre-treated to remove carbonates as described above, then dried. Samples were then digested in a mixture of 2.5 mL concentrated HF and 0.5 mL concentrated HNO<sub>3</sub> at 90°C for 4 days. After drying, samples were reconstituted in 5 mL of 0.5M HCl, and then processed for ICP and KPA analyses as described above. HCl is required to redissolve the large amount of calcium fluoride formed during the reaction of Ca from carbonates with HF.

Extractable ferrous (Fe(II)) and reducible iron were determined by 0.5 N HCl and 0.5 N HCl/0.25M hydroxylamine hydrochloride (HH) extractions of un-dried, unground sediments, respectively. The difference between these two extractions has been defined operationally as the poorly crystalline ferric iron available for microbial reduction (Lovley and Phillips, 1987). The extractions were conducted in the anaerobic chamber on anaerobically preserved sediments. A separate split of each sample was taken for drying to determine water content to allow reporting concentrations as per gram of dry sediment. Briefly, 0.5 g of sediment was transferred to a tared polycarbonate Oak Ridge centrifuge tube and 30 mL of either 0.5 N HCl and 0.5N HCl/0.25 M hydroxylamine hydrochloride was added. Each sample was extracted in duplicate using each solution. Tubes were mixed on an end over end shaker (12 RPM), and 3 mL of extraction solution recovered by filtering through 0.22 µm syringe filter. Extractions with 0.5 N HCl were sampled at 1 and 24 hours. HH extractions were sampled after 1 hour and 24 hours. Tubes were weighed after each subsample to account for the volume removed. Fe(II) concentrations in the HCl extraction solutions were determined by the ferrozine colorimetric method (Stookey, 1970). The total iron concentration in the 0.5 N HCl extraction solutions was determined by adding hydroxylamine hydrochloride to a separate aliquot of the filtered extraction solution to

reduced dissolved Fe(III), and analyzed by the ferrozine method. Total Fe extracted by HH was determined directly by ferrozine since extraction reduces Fe(III).

### 3.2.6.3.2 Carbonate, total sulfur, acid volatile sulfur

Total carbonate content of the pre- and post-column sediments was determined by measuring the CO<sub>2</sub> evolved upon acidification. Briefly, 0.5 to 1.0 g splits of dried sediment were placed into 120 cc serum bottles which were sealed and flushed with N<sub>2</sub>. Five mL of 2N HNO<sub>3</sub> were injected into the bottle after removing an equal volume of headspace. After mixing on an orbital shaker, a 60-cc syringe fitted with a 3-way valve and a needle was inserted into the stopper. The excess gas pressure was allowed to displace the plunger upwards and volume of displacement recorded. After closing the valve and removing the syringe from the bottle, the syringe was connected to the injection loop of a TCD detector GC to measure CO<sub>2</sub> content of the gas phase. The percent carbonate in the solid was calculated by multiplying the gas phase CO<sub>2</sub> concentration by the sum of the bottle volume and syringe displacement and dividing by the initial sample weight.

Total sulfur content and S isotope ratio of the dried, ground column sediment and pre-column material were measured using a Carlo Erba elemental analyzer (EA) coupled to a Micromass Isoprime mass spectrometer. This method provides a measure of all forms of S present in the sample. An increase in the % total S would reflect reduction of sulfate in the AGW during biostimulation and precipitation of reduced sulfur species, such as FeS. The S isotopic ratio, expressed as  $\delta^{34}\text{S}$ , can be used as an indicator of fractionation of S isotopes during microbial reduction of S (Habicht and Canfield, 1997), resulting in a lighter isotopic ratio (lower  $\delta^{34}\text{S}$ ) of the reduced S. This fractionation results from the kinetic isotope effect in which the reaction rates for heavier isotopes (e.g. <sup>34</sup>S) are slower resulting in a depletion of the heavier isotope in the product relative to the reactants. Briefly, 3 mg of the homogenized ground sediment sample was weighed on a microbalance into tin capsules with approximately 2 mg of V<sub>2</sub>O<sub>5</sub> added. The samples are combusted at 1000°C. The EA traps water and separates the resulting CO<sub>2</sub> and N<sub>2</sub> from the SO<sub>2</sub> which is measured using an IR detector and then sent to the mass spectrometer. The N<sub>2</sub> and CO<sub>2</sub> are vented. The samples are run in batches of 30 at 10 sample intervals. Each interval is surrounded by four reference standards (NBS SRM bovine liver) run in a range of sizes to capture the range of S in the samples. A blank is included in the run. The standards are calibrated against Canyon Diablo Troilite (CDT) for  $\delta^{34}\text{S}$ . The <sup>34</sup>S isotope composition is expressed as a difference in the ratio relative to the CDT in parts per thousand or per mil (‰). The  $\delta^{34}\text{S}$  and %S values are corrected for instrumental drift and size linearity.  $\delta^{34}\text{S}$  values are also corrected for oxygen contribution. One standard deviation of the standards throughout a run is  $\pm 0.5$  ‰ or better for  $\delta^{34}\text{S}$ , and 0.01 %S. Duplicates measured every fifth sample agreed within 0.05% S and within 0.5 per mil  $\delta^{34}\text{S}$ .

Acid volatile sulfur (AVS) content was measured on sediments recovered from the lactate columns (L1 and L2), and the pre-column sediment using a modified version of the diffusion method of Hsieh and Yang (1989). AVS is a measure of sulfide (S<sup>-2</sup>) species in the sample such as FeS that are liberated upon acidification forming H<sub>2</sub>S gas. The method used does not reduce more oxidized forms of S such as elemental sulfur or S<sup>-1</sup> in FeS<sub>2</sub>. In the anaerobic chamber, dried column sediment samples (0.3 g) are placed in 100 mL serum bottles along with

1 mL of 1 M ascorbic acid to eliminate oxidation of AVS by ferric minerals (Hsieh et al, 2002). A 10 x 75 mm test tube containing 3 mL of alkaline zinc acetate (3% w/v zinc acetate in 2N NaOH) is placed in the serum bottle, with opening upwards and resting on the shoulder of the bottle. The alkaline zinc acetate solution traps the H<sub>2</sub>S gas evolved on acidification forming a zinc sulfide precipitate. A 1-cm magnetic spin bar is placed in the bottom of the bottle. The serum bottles are then sealed and 10 mL of 6N HCl is injected through the serum bottle stopper with a syringe directly onto the sediment sample carefully avoiding the contact with the zinc acetate solution. The bottles are removed from the anaerobic chamber and placed on a stir plate with gentle stirring. After 30 hours, the zinc acetate tubes are recovered. After weighing each tube, an additional 0.5 mL of 2N NaOH is added, and the tubes are stoppered, then sonicated for 30 minutes to disperse the ZnS precipitate. Weights are recorded at each step to determine exact volumes. The resulting suspension of zinc sulfide is subsampled and sulfide is determined colorimetrically by the Cline method (see above). The method was tested using a reference synthetic solid (70% FeS; 30%FeS<sub>2</sub>). The measured AVS within 24 hours was equivalent to the S in the FeS component. No additional S was recovered after longer equilibration times consistent with previous studies that acid without added reductants only volatilizes the S<sup>-2</sup>, and not higher oxidation states such as S<sup>-</sup> in FeS<sub>2</sub>, or elemental S. Replicates of this reference sample agreed to within ± 5%, and duplicates of column samples agreed within ±10%. The effect of CO<sub>2</sub> evolved from the carbonates present in the ISR samples during acidification on AVS recovery by alkaline zinc acetate was found to be negligible. Other treatments such as acidic Cr(II) to reduce higher oxidation states of S were not attempted. Instead, the difference between total sulfur increase (column minus pre-column total S) and the AVS is used as a measure of higher oxidation states of S precipitated during the biostimulated reduction stage of the column experiments.

### 3.2.7 Microbial Assay

Microbial characterization of sediments and effluent filters were conducted by the USGS microbiology laboratory in Reston, VA. The general approach taken was to extract DNA, and perform bacterial Terminal Restriction Fragment Length Polymorphism (TRFLP) fingerprinting and quantitative Polymerase Chain Reaction (qPCR) analyses of *Geobacter* and sulfate reducing bacteria (SRB) on all samples. In addition selected samples were further characterized by cloning *Geobacter* 16S rRNA gene, and/or *dsrB* gene coding for the dissimilatory sulfite reductase involved in sulfate reduction. The intent was to 1) gain an understanding of microbial dynamics in these experiments as biostimulation of U(VI) reduction occurred, as well as during potential remobilization of uranium, 2) assess where in the column the microbial abundances were highest and relate that to chemistry and solid phase analyses, and 3) determine potentially important *Geobacter sp.* and sulfate reducing organisms involved in these processes.

The sample sets included sediments recovered from the Kingsville Dome ISR site collected in August, 2009, after in situ leaching had been stopped for about two years. Sediment samples recovered at the end of the first batch experiments with the 3712B-C 580-590 ISR core material which were amended with acetate, lactate, or H<sub>2</sub>. Sediments recovered from column L1 at the end of the biostimulation stage also were assayed, as well as filters of effluent collected from column L2 during lactate addition. The first filter was started at the end of the period of high

effluent ferrous iron concentration and continuing for 20 days (19.5 PV). The second filter was collected over the next 14 days during which time effluent sulfide began to increase.

### **3.2.7.1 Batch and column sediments**

Sediment was subsampled from batch experiment 1 bottles at the end of the 60 day experiment. After settling, the overlying water was removed in the anaerobic chamber. About one gram of wet sediment was transferred to a whirl pak bag using a sterilized spatula. Samples were sealed in Mylar bags and frozen at -80°C. One gram splits of column L1 sediments were sampled immediately upon sectioning of the column in the anaerobic chamber. The subsamples were processed and preserved as described for batch samples.

### **3.2.7.2 Effluent filters**

Millipore Sterivex 0.2 µm filter capsules were installed in the column L2 effluent line within a gas purged holder to limit exposure to oxygen. The effluent was collected as described above, downstream of the Sterivex filter. Following the collection period, the filter capsules ports were sealed and the cartridge was stored at -80°C. Filter capsules and sediment samples were shipped on dry ice to the microbiology lab.

### **3.2.7.3 Measurement methods**

**DNA Extraction.** The 10-20g each of frozen aquifer sediments samples and the 0.5-1g frozen sediment samples from the batch and column experiments were thawed and then extracted using the MoBio ultraclean soil DNA megaprep kit according to manufacturer's instructions (MoBio, Inc., Carlsbad, CA). Sterivex capsule filters of column L2 effluent were thawed and extracted as previously described using the Qiagen (Gentra) puregene kit with slight modifications. (Qiagen, Inc., Valenica, CA) (Ward et al. 2007). Briefly, 0.9mL of lysis buffer with 4.5µL proteinase K was added to the filters and incubated with gentle rotation for 10 minutes at 80°C. Volumes of solutions used in subsequent protein precipitation and DNA precipitation steps were scaled up accordingly (3X) to reflect the 3X volume increase in lysis step compared to manufacturer's instructions (0.9mL instead of 0.3mL).

**Bacterial 16S rRNA Gene PCR and TRFLP Fingerprinting.** The polymerase chain reaction (PCR) technique was used to amplify bacterial DNA from samples, targeting the evolutionally conserved ribosomal RNA gene, 16S rRNA. This technique allows for the amplification of a specific segment of DNA of interest from the bulk DNA. Enough of the amplification product from PCR (amplicon) is produced such that it can then be detected and characterized further (cloning and sequencing or fingerprinting depending on the question being asked). PCR was performed as previously described using the 16S rRNA gene primers 46f-FAM and 519r (Jones et al 2006, Lane 1991, Brunk et al 1996). A DNA fingerprinting method, the terminal restriction fragment length polymorphism (TRFLP) technique was also used to look at bacterial community differences between samples. This technique involves the enzymatic digestion of the PCR product, which has a fluorescent tag. The enzyme has a specific DNA recognition sequence and only cuts the DNA where that sequence exists. Therefore, depending on the PCR product's DNA sequences, enzyme digested products of varying size will be

produced. The fragments from the end which contains the fluorescent tag can then be electrophoresed (size separated) and the fluorescence detected, generating a fragment size profile which is unique to that population of organisms with those sequences. This fingerprint can be compared to other samples to evaluate similarities and differences between the sample communities or within a community over time. TRFLP was performed as previously described (Jones et al 2006). Briefly, PCR amplicons were digested with Mn(II), precipitated, and electrophoresed on an ABI 310 genetic analyzer to generate fingerprint profiles. Fingerprint data were binned using the software R, and imported into the SAS based JMP8 statistical package (SAS, Cary, NC) for clustering analysis.

**Real time quantitative PCR (qPCR) for *Geobacter* and SRB.** qPCR was performed on all samples for *Geobacter* using the 16S rRNA gene primers Geo494f and Geo825r (Anderson et al. 1998, Holmes et al 2002), and for SRB using the functional gene *dsrB* primers drp-2060f and dsr4r (Wagner et al 1998, Geets et al. 2006). The procedure including cycling temperatures and times are as previously published (Wilson et al. 2010).

**Clone Library Construction and Sequencing.** *Geobacter* and SRB clone libraries were constructed for selected samples. PCR was performed using the *Geobacter* specific and SRB specific primer sets above. PCR conditions; *Geobacter* 30 cycles of 94°C (30 s), 53° C (30 s), and 72° C (30s) followed by a 7 minute 72°C extension incubation. SRB PCR was also 30 cycle and conditions were identical except for the annealing temperature was 56°C rather than 53°C. Amplicons were purified by wizard prep (Promega, Madison, WI.), and cloned into TA vector according to manufacturer's instructions (Invitrogen, Carlsbad, CA). Single clones were picked and analyzed for insertion by PCR with M13f and M13r primers. PCR products were sequenced by single pass PCR sequencing (Beckman Coulter Genomics, Danvers, MA.).

**Sequencing Analysis.** Plasmid vectors were trimmed using the awk program vbgone (Varnum Engineering, Seattle, WA.) Sequences were oriented and aligned in Macvector 12 using ClustalW (MacVector, Cary, NC). Phylogenetic trees were built in MacVector12 using the Neighbor Joining method and TamuraNei distance with bootstrapping (1000 replicates) or BESTTREE. Representative sequences from each phylotype were checked for highest similarity to sequences in Genbank database using the Basic local alignment tool (Blast).

### 3.2.8 Spectroscopic Measurements

Sediments recovered from sub-sectioning columns L1, L2 and L5 were used for X-ray absorption spectroscopic (XAS) measurement to determine oxidation state and the local molecular structure of sequestered uranium. The pre-column material was included for comparison.

#### 3.2.8.1 Bulk XAS

X-ray absorption near edge spectroscopy (XANES) and Extended X-ray Absorption Fine Structure (EXAFS) measurements were made on anaerobically stored ISR sediments from columns and pre-column material at Stanford Synchrotron Light Source (SSRL) beam lines (BL) 4-1 and 11-2. Analysis of XANES spectra is used to provide a quantitative measure of the

different oxidation states of an element in a sample. EXAFS spectra are used to derive the local atomic structure surrounding the element of interest in the sample. Qualitatively, EXAFS spectra can be compared to reference or model compound spectra to identify the presence of specific forms in this case, of uranium. Bulk XAS measurements provide information on the entire mass of the element of interest in the portion of sample illuminated by the X-ray beam. Beam size was typically 1 mm high by 8 mm wide with the sample placed at a 45° angle to the incoming X-ray beam, which resulted in an illumination area of 1 x 11.3 mm for the 1.2 mm thick sample.

In the anaerobic chamber, un-dried samples were ground with agate mortar and pestle, and packed into 1/32" thick polycarbonate holders with 10 mil Kapton tape windows. Uranium L-II and L-III edge fluorescence spectra were collected in an anaerobic stage to eliminate exposure to oxygen during sample collection.

For XANES, a minimum of three replicate scans of fluorescence spectra of each sample was collected across either the U-LII or U-LIII edge using either a 30-element (BL 11-2) or 13-element (BL 4-1) germanium array detector. Internal calibration of the monochromator was made using either a Y or Mo foil placed on a second ion chamber "down-stream" of the sample stage, with foil edges collected at the start of each scan. The sample spectra were deadtime corrected and adjusted for drift of the monochromator prior to averaging. The averaged spectra were background subtracted and normalized using SIXPACK software (Webb, 2005). The resulting corrected spectra were fit to one or more reference U(IV) and U(VI) model spectra using the least squares fitting module in SIXPACK. Spectra of crystalline uraninite, andersonite, phosphuranylite and U(VI) sorbed to ferrihydrite provided by John Bargar, Stanford Synchrotron Radiation Lightsource, were used for model compounds. The model spectra were collected at other beam time sessions but also calibrated with internal reference foil for either the U-LII or U-LIII edge. The least squares linear combination fitting (LC) procedure yields fractional components of U(IV) and U(VI) in the sample. The best fit was based on the lowest residual chi squared value. That is, the components those yielded the minimum difference between the sample spectra and the fit of the components.

Bulk EXAFS spectra were collected on a limited number of samples because of availability of beam time. Up to 12 replicate scans were collected. Spectra were deadtime corrected and averaged as described above. The background corrected and extracted EXAFS signal was converted to frequency (k) space, weighted by  $k^3$ , and Fourier transformed. The low uranium concentration of the column samples limited the usable data collection range to about k of 9 at best. The  $k^3$  weighted spectra and its Fourier transform were used to qualitatively compare to model compounds. Linear combination fitting and shell by shell fitting of column samples was not attempted because of the significant contribution of initial (or background) uranium present in the pre-column sediment and the limitations of spectral data quality for lower concentration samples.

### **3.2.8.2 Microfocused synchrotron XRF and XAS**

Thin sections of column sediment were prepared for imaging by microfocused X-ray fluorescence (XRF) and for discrete point XANES at the SSRL BL 2-3 and BL 10-2 X-ray microprobes, which provide spatial resolution of up to 1 and 20  $\mu\text{m}$ , respectively. The

microfocused beam XRF ( $\mu$ XRF) provides elemental distributions or maps of elements in a thin section. The mapping can be conducted at several energies across the critical X-ray absorption edge of the element (e.g. U) in question to provide maps of oxidation state for the area of interest (Mayhew et al, 2011).

Petrographic thin sections of sediment recovered from columns L1 and L2, and the pre-column sediment were prepared by embedding the sediment in epoxy resin, then cut and polished to 30- $\mu$ m thickness, and mounted on a quartz slide. Briefly, about 3 grams of the anaerobically stored sediment was dried by spreading into a thin layer on a 6"-diameter paper filter in the anaerobic chamber. After drying, the sediment was transferred to a 10 mL polypropylene beaker with clumps gently broken up, as needed, if formed during drying. This made about a 0.5 cm thick layer in the beaker. Epotek 301 2-FL resin (Epoxy Technologies, Inc) that had been outgassed in the anaerobic chamber was mixed and poured onto the dried sediment covering the sediment with at least another 0.5 cm layer. The beakers were then placed in the anaerobic chamber airlock which was then evacuated to  $-10^3$  Hg to remove any gas phase entrained within the dried sediment. The resin cured at room temperature over the next three days with additionally vacuum applied to maintain desired pressure. After hardening, the resin pucks are removed from the beakers, labeled, and sealed in Mylar bags with oxygen scrubbers for shipment for thin section fabrication by Spectrum Petrographics (Vancouver, WA). Fabrication of thin sections entailed vertical slicing of the pucks and recast the slices into larger blocks using the same room temperature curing resin. Slices were cut from the block and mounted and polished using low oxygen and heat methods. The completed thin sections were transported in Mylar bags and stored in the anaerobic chamber until measured on the SSRL X-ray microprobes.

Thin sections were imaged using a flatbed scanner with the scanned image enlarged to provide a location map. The entire area of each thin section was mapped at SSRL BL10-2 using a 20- $\mu$ m nominal beam size focused through a capillary tube using 30  $\mu$ m steps and 50 msec dwell time. Fluorescence data were collected at each pixel as the sample was stepped under the beam at energies of 17,100 and 17,200 eV. A difference map was then constructed using SMAK, the Microprobe Analysis Tool Kit ([http://home.comcast.net/~sam\\_webb/smak.html](http://home.comcast.net/~sam_webb/smak.html)) to remove the contribution of Rb fluorescence to the U fluorescence window. Single and multi-element XRF maps depicting relative concentration were then constructed for each thin section to depict the distribution of U, Fe, Ca and other elements of interest. These maps also are used to locate areas for more detailed mapping at BL 2-3.

Selected areas of thin sections with higher U concentration were imaged using the SSRL BL2-3 X-ray microprobe using a 1  $\mu$ m focused monochromatic X-ray beam with fluorescence data collected at 50 to 200 msec dwell time as the sample was translated across the beam. The effective pixel size was of 2 x 2  $\mu$ m in most cases, and 5 x 5  $\mu$ m for larger grains. The U enriched areas of the thin sections mapped with the X-ray microprobe were either individual grains or coatings on grain exteriors. Maps were collected at multiple energies across the U-LIII absorption edge at 17,170, 17,175, 17,178, and 17,190 eV. The resulting maps were processed using a least squares fitting routine in the SMAK software to calculate the fraction of U(IV) and U(VI) at each pixel based on the contribution of each component to the normalized fluorescence yield at these energies in XANES spectra of model U(IV) and U(VI) compounds.

This XANES mapping routine is further described in Sharp et al (2011) and (Mayhew et al, 2011). U-LIII XANES spectra were then collected at specific points using a 1  $\mu\text{m}$  beam spot size on thin sections that had sufficient U to provide usable data. These points were chosen based on apparent distribution of U(IV) and U(VI) from the XANES maps, and locations optimized for maximum signal.

### 3.3 Results

#### 3.3.1 Batch Experiments

The initial batch experiment with the Kingsville Dome in situ leached sediment (KVD 3712 BC 580-590) was conducted starting in May 2010, to test the uptake of dissolved uranium under anaerobic conditions to determine if amendment with electron donors would result in enhanced uptake putatively from the reduction of U(VI) to insoluble U(IV) by the indigenous microbial population in the aquifer material. The results were used to determine the electron donors to use in biostimulation column experiments. In the absence of electron donor, no significant change in dissolved U(VI) concentration (20  $\mu\text{M}$ ) was observed over the 60 day duration of the experiment (**Figure 3.5**). In all experiments dissolved U increased to about 0.5  $\mu\text{M}$  over the 24 hour pre-equilibration period before addition of U(VI) and electron donors. In the control bottles (no added U or electron donor), dissolved U(VI) increased to 0.7  $\mu\text{M}$  over the next 4 weeks. The observed release of dissolved U(VI) likely was the result of desorption from surface complexation sites of the aquifer sediments. In the bottles with no electron donor amendment, no measurable change in 20  $\mu\text{M}$  dissolved U(VI) ([U]) was observed over the duration of the experiment indicating no significant adsorption of U(VI) under the experimental conditions.

Dissolved uranium decreased starting at about 3 days after addition in the  $\text{H}_2$  amended bottles and continued through 28 days, after which time a near constant [U] of 0.7  $\mu\text{M}$  was measured that is similar to the [U] control bottle. The sediment in the hydrogen amended bottles turned black in color after 28 days likely because of FeS precipitation suggesting bioreduction of both sulfate in the AGW and iron in the aquifer sediment. Dissolved iron in bottle H1 was 7.6  $\mu\text{M}$  at 16 days compared to 2.8  $\mu\text{M}$  in the control bottle (**Table 3.4**). Dissolved Fe had decreased to 1.9  $\mu\text{M}$  by the next sample at 28 days, the time when the dark color was first observed. Dissolved iron in the H2 experiment bottle was 71  $\mu\text{M}$  at 16 days and had decreased to 2.4  $\mu\text{M}$  by the next sampling. These results are consistent with bioreductive dissolution of ferric iron in sediments with the subsequent decrease attributed to FeS precipitation.

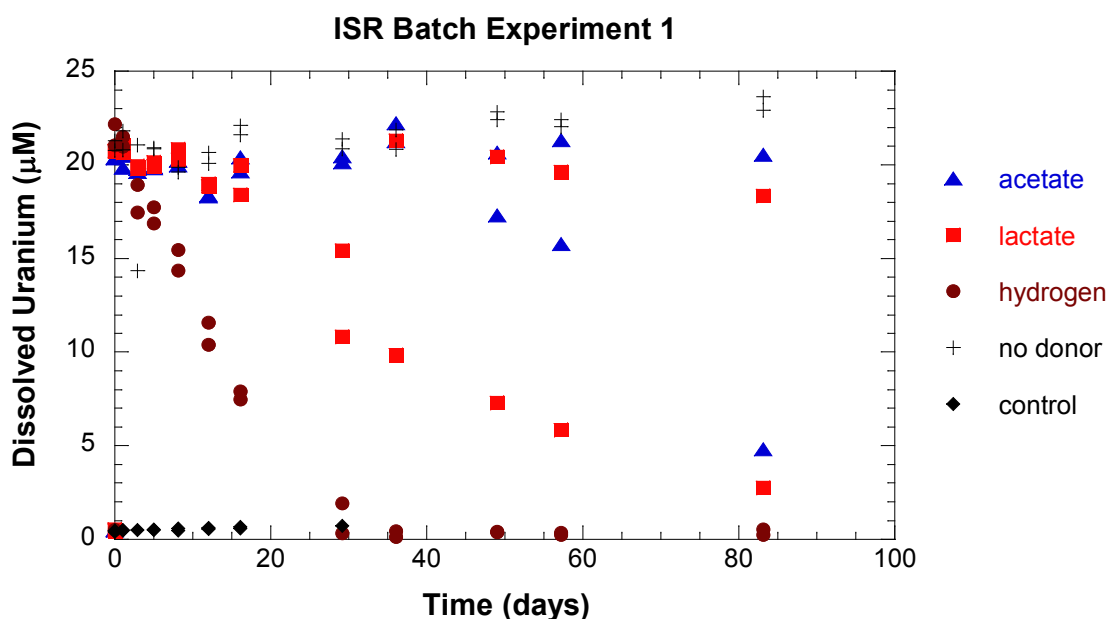


Figure 3.5 ISR sediment uranium batch uptake experiment 1. Dissolved uranium ( $\mu\text{M}$ ) versus time for different electron donor amendments. Data points are for each batch bottle duplicate. Control has no added electron donor or dissolved U(VI). The “No electron donor” bottle has 20  $\mu\text{M}$  dissolved uranium, but no added electron donor.

Table 3.4 Total dissolved iron in batch experiment 1 samples filtrates ( $<0.2 \mu\text{m}$ ) for duplicate bottles for each electron donor.

Time (hours)	Dissolved iron ( $\mu\text{M}$ )							
	No electron donor		Acetate		Lactate		Hydrogen	
	C1	C2	A1	A2	L1	L2	H1	H2
387	2.8	2.3	5.2	5.7	78	9.0	7.6	71
700	4.7	4.3	10	7.4	2.1	36	1.9	2.4
1176	11	11	13	13	5.2	108	5.6	6.9

The [U] in the 20 mM lactate amended bottle (L1) decreased starting at 12 days and continued throughout the course of the experiment with 3  $\mu\text{M}$  [U] measured at the last time point (**Figure 3.5**). The sediment in this bottle also began to darken in color starting at 28 days. 78  $\mu\text{M}$  [Fe] was measured in this bottle at 16 days and decreased to 2.1  $\mu\text{M}$  by the next time point at 29 days (**Table 3.4**). Curiously, the [U] in the 10 mM lactate amended bottle (L2) was only slightly lower than in the control bottle throughout the experiment, but the [Fe] increased from 36 to 108  $\mu\text{M}$  between 29 and 49 days. This lag in [Fe] and no appreciable decrease in [U] in bottle L2 suggest a lower biomass of iron and uranium reducing bacteria in the sediment L2 at the start of the experiment with iron reduction occurring at a later time compared to L1. The difference between the two lactate bottles also may be the result of a higher (20 mM) lactate amendment to bottle L1 than to bottle L2 (10 mM), which may also have resulted in the observed lag in reduction of L2 compared to L1.

The [U] in the acetate amended bottles did not change significantly from the initial 20  $\mu\text{M}$  concentration through 35 days. After this time [U] in one bottle (A1) began to decrease over time and was at 5  $\mu\text{M}$  at the last sampling point. No measurable decrease in [U] was observed in the other acetate bottle. Sediment in bottle A1 began to darken in color by 35 days while no color change was observed in the other bottle, A2. A small increase in [Fe] was measured in both acetate amended bottles compared to the unamended bottles. The observed differences in the replicate bottles may reflect heterogeneity in microbial biomass in the 3-g splits of ISR sediments used in the batch experiment. Heterogeneity is expected to be less of an issue in column experiments because of larger sediment mass used (~50 g).

The near complete uptake of [U] in both  $\text{H}_2$  amended bottles and in one of the lactate bottles in contrast to the unamended bottles with 20  $\mu\text{M}$  U(VI) suggest that the uranium uptake was likely the result of biostimulated reduction. Abiotic reduction of uranium by  $\text{H}_2$  has been shown to be insignificant (Junier et al, 2009). This result combined with the observed release of significant [Fe] followed by decrease in [Fe] in the  $\text{H}_2$  and lactate amended bottles along with observed darkening of sediment over time suggests the presence of viable microbes capable of reducing iron, U, and sulfate that are present in the ISR influenced aquifer sediments. Dissolved sulfide was not measured in this experiment. The variability in the results among duplicate bottles for both lactate and acetate amended bottles suggests heterogeneity in microbial biomass in the 3 gram splits of sediments used in these batch experiments. Based on the apparent reduction of U, iron and sulfate with both hydrogen and lactate it was decided to use both hydrogen and lactate as electron donors in two sets of column experiments to investigate biostimulated reduction of U(VI) by the indigenous microbial biomass in the ISR sediment. Assuming sufficient biostimulated reduction and sequestration of U(IV) occurred, these columns also would be used to test the remobilization of uranium in response to suboxic conditions following cessation of electron donor.

A subsequent set of batch experiments was conducted to test the viability of sediments in response to hydrogen amendment and test the effect of different dissolved  $\text{H}_2$  concentrations on U uptake and reduction. This experiment was initiated in June 2011 after no appreciable decrease in [U] was observed in the  $\text{H}_2$  amended column experiment after 3 months of flow (see  $\text{H}_2$  amended columns in Section 3.3.2.1). This batch experiment used the same sediment used in both the column experiments and the first batch experiment, and at the same solid to AGW ratio (50 g/L). Both the 3.5% and 15%  $\text{CO}_2$  AGW were used to test for differences resulting from the different pH (pH 6.9 and 6.3, respectively). A range of dissolved  $\text{H}_2$  also was tested that spanned the  $\text{H}_2$  partial pressure imposed on the column reservoir (5%), to the level added to the first batch experiment (~40%), and an intermediate level (20%). These  $\text{H}_2$  partial pressures in the headspace resulted in equilibrium dissolved  $\text{H}_2$  of 40, 312, and 156  $\mu\text{M}$ , respectively. The control bottles (20  $\mu\text{M}$  [U] initial, no  $\text{H}_2$ ) had no measurable change in [U] over the 60 day experiment (**Figure 3.6**). Near complete uptake of [U] was observed for all levels of  $\text{H}_2$  amendment and for the different AGW. In bottles with 40%  $\text{H}_2$  in the headspace, a slightly faster decrease in [U] was observed with 3.5%  $\text{CO}_2$  AGW than with the 20%  $\text{CO}_2$  AGW. Longer lag times in [U] uptake were observed for a lower  $\text{H}_2$ , with near complete uptake observed by 62 days for the 20%  $\text{H}_2$  and 70% uptake for the 5%  $\text{H}_2$  amendment by 62 days. Similar to the first batch experiments, dissolved Fe was low in the control bottles throughout the experiment. [Fe] increased to 18  $\mu\text{M}$  in 3.5%  $\text{CO}_2$ , 40% $\text{H}_2$  bottles through 20 days, and then decreased to near

detection by 62 days. In contrast, [Fe] in the 15% CO<sub>2</sub> AGW increased to between 130 and 145 μM over the first 35 days for all three H<sub>2</sub> amendments (**Figure 3.6**). [Fe] in the 20 and 40% H<sub>2</sub> amended bottles then decreased to <1 μM by day 62, with the 5% H<sub>2</sub> bottle [Fe] decreasing to about 10 μM with little subsequent change by the end of the experiment.

Total dissolved sulfur, measured by ICP in acidified samples, was equal to the AGW sulfate through day 36 for all bottles. The ICP sulfur is likely dominated by sulfate since samples were acidified several weeks prior to ICP analysis resulting in a loss of at least some of the dissolved sulfide as H<sub>2</sub>S gas. Dissolved S in the H<sub>2</sub> amended bottles decreased after this time with the greatest decrease observed for the 3.5% CO<sub>2</sub> AGW 40% H<sub>2</sub> condition. Dissolved sulfide at the end of the experiment increased with increasing H<sub>2</sub> in the 15% CO<sub>2</sub> AGW with concentrations of 0.04, 0.7, and 2.2 mM for the 5%, 20 and 40% H<sub>2</sub> headspace amendments, respectively. The dissolved sulfide in the 3.5% CO<sub>2</sub>, 40% H<sub>2</sub> bottles was 3.9 mM at end of the experiment. Batch bottles using sediment sterilized by gamma irradiation (25 kGy <sup>137</sup>Cs) 10 months prior to the batch experiment had similar results for U, Fe and total dissolved S (data not shown) indicating that either the sterilization was incomplete or bacterial spores were still viable (Tuominen et al, 1994) since abiotic sulfate reduction is not known to occur except at very slow rates.

The results of this batch experiment indicate that the microbial biomass in the archived ISR sediment is still viable and able to reduce U, Fe, and sulfate. Greater reduction is evident with the 40% H<sub>2</sub> amendment in both AGW recipes. The sulfate reduction rate may be greater for the higher pH 6.9 (3.5% CO<sub>2</sub> AGW) condition as indicated by greater decrease in total dissolved sulfur. The conditions of the column AGW influent (5% H<sub>2</sub>, 15% CO<sub>2</sub>) showed significant reduction of U and Fe but had a lag of about 30 days prior to onset of significant U reduction. This result is in contrast to the hydrogen columns where no measurable decrease in [U] or release of iron occurred over 70 days. Possible causes of this difference are discussed below.

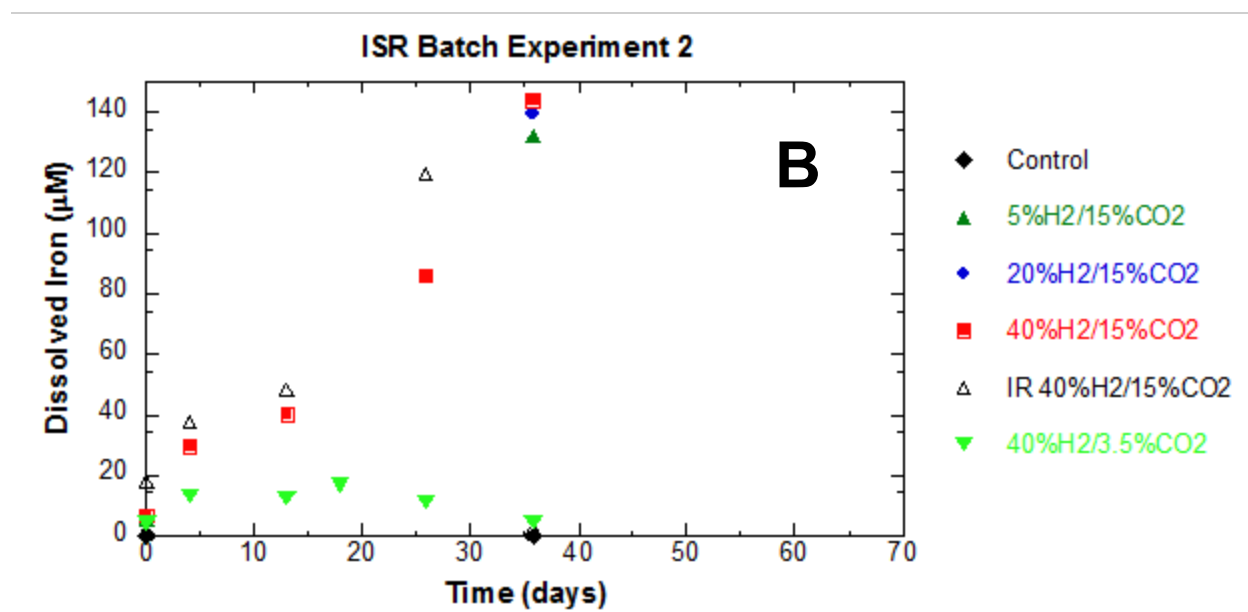
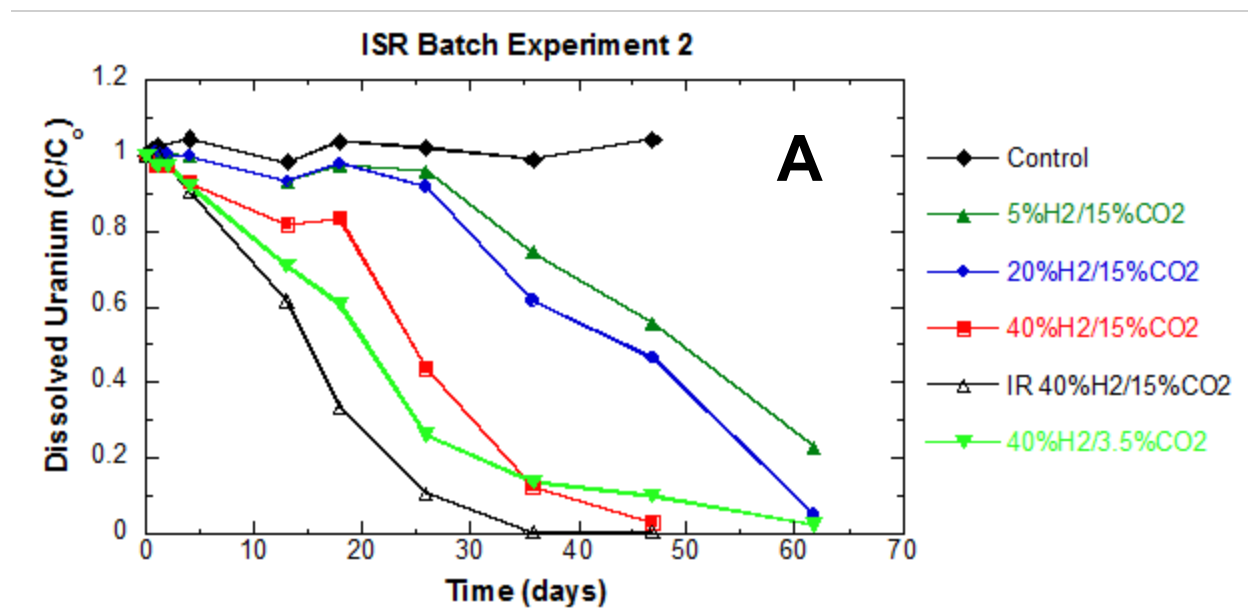


Figure 3.6 ISR sediment uranium batch uptake experiment 2. (A). Dissolved uranium as ratio of initial total dissolved (20  $\mu\text{M}$ ) and (B) dissolved iron versus time for different headspace  $\text{H}_2$  partial pressure amendments as electron donor, and headspace  $\text{pCO}_2$  to control pH. Data points are for each batch bottle duplicate. Control has no added electron donor or dissolved U(VI). No electron donor bottle has 20  $\mu\text{M}$  dissolved uranium added, but no hydrogen added to headspace. IR is gamma irradiated.

### 3.3.2 Column Effluent

The following section describes the column effluent chemistry over the course of the biostimulation and sub-oxic elution experiments.

#### 3.3.2.1 Reduction stage

**H<sub>2</sub> Amended Columns.** Two columns were packed with ISR sediment on February 24, 2011. Flow of H<sub>2</sub> amended AGW was started on March 10, 2011. The influent reservoir was equilibrated with a 5% H<sub>2</sub> partial pressure which yields an equilibrium dissolved H<sub>2</sub> concentration of 40 μM. The AGW influent was also amended with ammonium, phosphate, trace elements and vitamins (see Methods) to promote microbial activity and growth. An initial flow rate of 0.05 ml/minute was used for the first 1.2 days, a volume equivalent to 6 column pore volumes and residence time of 0.2 days. The flow rate was subsequently decreased to 0.012 ml/min to increase residence time and decrease back pressure in the column.

Effluent [U] increased to 15 μM in the second sample (0.4 to 3.7 PV) and equaled the influent [U] of 20 μM after 8 PV (data not shown). The lower [U] in the initial samples likely represents dilution with AGW without [U] used for packing the column, and adsorption of U(VI) to surface complexation sites on the aquifer sediment surfaces. Subsequently, no significant change in effluent [U] relative to influent was observed. Effluent dissolved Fe ([Fe]) and Mn ([Mn]) increased over the first 5 days then decreased through 50 days. The release of [Fe] and [Mn] from columns H1 and H2 was similar in timing and extent to the effluent [Fe] and [Mn] observed in the lactate columns before the onset of iron reduction (data not shown). The decrease of [Fe] in both the hydrogen columns between 10 and 65 days suggest that no significant reductive dissolution of iron oxides, such as by dissimilatory Fe reduction, was occurring in the columns, contrasting the large increase in [Fe] observed in the lactate columns. Results of the H<sub>2</sub> amended batch experiments suggested U reduction had at most a lag of 20 days before measurable decrease in [U] was observed, despite a significantly lower solid to liquid ratio in the batch bottles (50 g/L) than in columns (3500 g/L), and, therefore, lower biomass.

Because of the lack of significant [U] uptake over the first 20 days and decrease in [Fe], measurement of dissolved H<sub>2</sub> in both column effluent and in the influent at the pump outlet was attempted using a thermal ionization detector. Samples were collected in N<sub>2</sub> purged 2-cc vial containers with syringe needles as inlets. Displaced gas volume was vented through a syringe needle connected to an air-lock. The volume of the water collected was determined by weight and the fractional loss of dissolved H<sub>2</sub> from headspace displacement accounted for. No H<sub>2</sub> was detected in either type of sample despite a continuous 5% H<sub>2</sub> in gas stream through both the reservoir and tubing jacketing, which exited near the effluent sample outlet. It was suspected that gas exchange across pump tubing walls resulting from pressure from pump rollers caused loss of dissolved H<sub>2</sub> from the influent stream. To eliminate the loss of H<sub>2</sub>, an acrylic box was fabricated to house the peristaltic pump and tubing (**Figure 3.4E**). This box was continuously purged with the experimental gas mixture. This purged pump housing eliminated the problem with gas exchange across pump tubing and the measured H<sub>2</sub> in both the influent and effluent streams became consistent with an equilibrium dissolved H<sub>2</sub> of 40 μM.

The H<sub>2</sub> amended columns were then operated for an additional 60 days, with no measurable decrease in dissolved U or sulfate, and no significant increase in dissolved Fe observed, all indicating that no significant microbial reduction was occurring in the aquifer sediments. This time period exceeded the lag time before the onset of measurable change in dissolved U in batch systems with the same hydrogen partial pressure (30 days, **Figure 3.6**). Additional effluent samples for dissolved H<sub>2</sub> indicated that H<sub>2</sub> was entering columns but no measurable loss of H<sub>2</sub> occurred within the columns. No measurable decrease in [U], increase in dissolved iron, or decrease in sulfate, were observed; all indicators of biostimulated microbial reduction expected for amendment with hydrogen electron donor. This suggests that reduction by the ambient microbial biomass was occurring at too low a rate to lower solution concentrations of these constituents in effluent at the experimental flow rates. Stopping influent flow for 24 hours and restarting also did not produce measurable changes in these constituents. Because of the apparent lack of significant microbial reduction, the H<sub>2</sub> amended columns were stopped. These column experiments contradicted the observed U reduction in batch experiments. The sediments in batch systems were in contact with the same volume of solution for the entire duration allowing progressive changes in dissolved concentration to be observed whereas the pore volume of the column had a residence time of about 1 day so that only changes in concentration of the influent that occur over 1 day would result. Because no organic carbon source was added in the influent stream to the column there was likely no increase in microbial biomass during the column experiments. It is concluded that under the conditions of the column experiment H<sub>2</sub> amendment alone is not suitable for sustaining biostimulated reduction to significantly lower dissolved uranium in the Kingsville aquifer following ISR operations.

**Lactate Amended Columns.** The flow of lactate amended AGW through columns L1 and L2 commenced on February 24, 2011. Significant reduction of Fe and U was evident in effluent profiles (Figure 3.7A). Because back pressure at the column inlet increased over the first 15 days, the influent flow rate was decreased from 0.05 to 0.011 ml/min. Back pressure continued to increase in both columns over the 83 day biostimulation experiment. Effluent dissolved U increased over the first 2 pore volumes to the influent 20 µM concentration (Figure 3.7A). The slow increase likely was due in part to dilution by initial pore water from column packing that had no [U] and to adsorption of U(VI) by aquifer sediment. The latter may be minimal since no measurable uptake of U(VI) was observed in batch experiments. Effluent [U] was constant and about equal to the influent [U] over the first 8 pore volumes (8 days). Subsequently, effluent [U] started decreasing and was <0.05 µM by day 50 (62 PV) indicating significant uptake, likely by reduction. The [U] effluent curves for columns L1 and L2 were very similar. Effluent dissolved iron (operationally defined as ferrous iron, [Fe]) initially was 10-15 µM and then began to increase starting at about 10 days and reached its' maximum of about 300 µM in both columns (Figure 3.7A). [Fe] in column L1 reached its' maximum concentration after 32 days and then decreased to <5 µM by day 48. [Fe] in column L2 reached maximum effluent concentration by day 22 then decrease to <5 µM by day 48.

Effluent lactate decreased by 30% after 6 days and continued to decrease to near the detection limit by day 18, with little or no measurable lactate in the effluent through the remaining duration of the biostimulation stage (**Figure 3.7B**). This high rate of lactate consumption is consistent with significant microbial activity with a likely concomitant increase in biomass. Acetate, an oxidation product of lactate, increased from 0 (the influent concentration)

to about 3 mM in both columns by day 12. Acetate was then relatively constant through day 55 after which it increased and approached the influent lactate concentration (10 mM) during the last 20 days of the biostimulation stage. These results suggest that the acetate produced by lactate oxidation is in turn utilized by other microbial processes within the column. The consumption of acetate diminished (effluent acetate increased) at about the time effluent [Fe] decreased to low levels suggesting that acetate consumption may be linked to ferric iron reduction. Dissolved sulfate decreases at a linear rate over the entire biostimulation period (**Figure 3.7B**). Measurable dissolved sulfide in the effluent was first detected at day 6 but was low (<0.5mM) through day 37 and day 45 in columns L1 and L2, respectively, after which dissolved sulfide increased irregularly through to the end of the biostimulation experiment. The timing of the increase in sulfide to >1 mM was similar to [Fe] decreasing to <5  $\mu$ M. This is consistent with iron reduction proceeding until easily reducible ferric iron is depleted followed by onset of significant sulfate reduction (Fang et al, 2009).

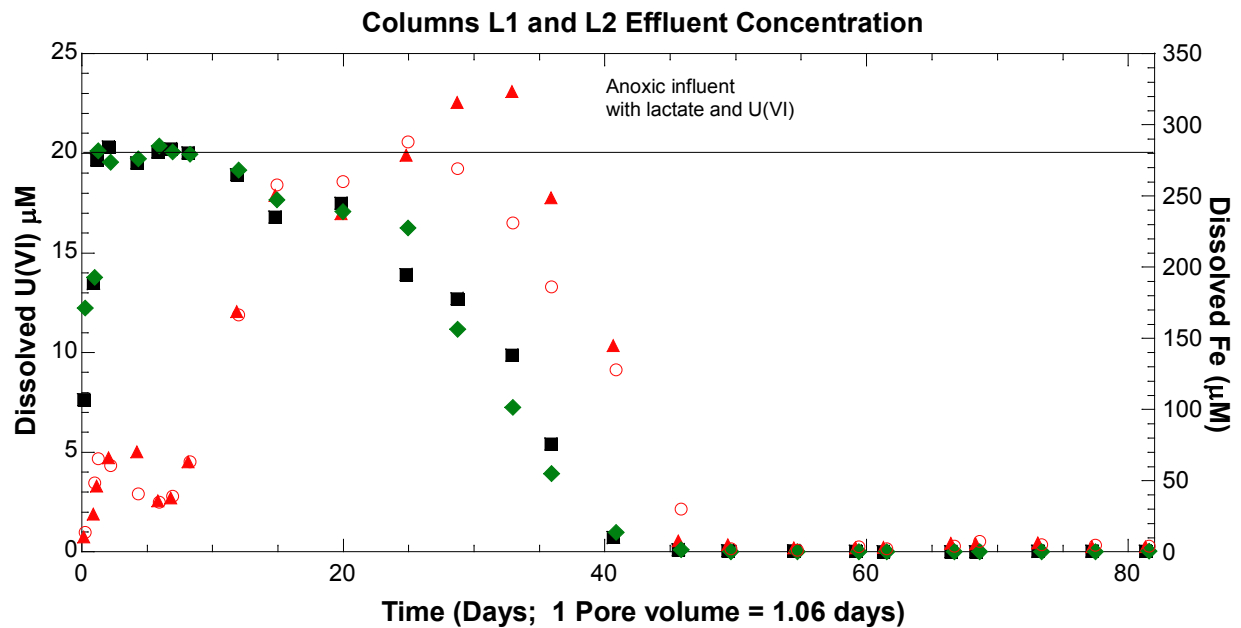
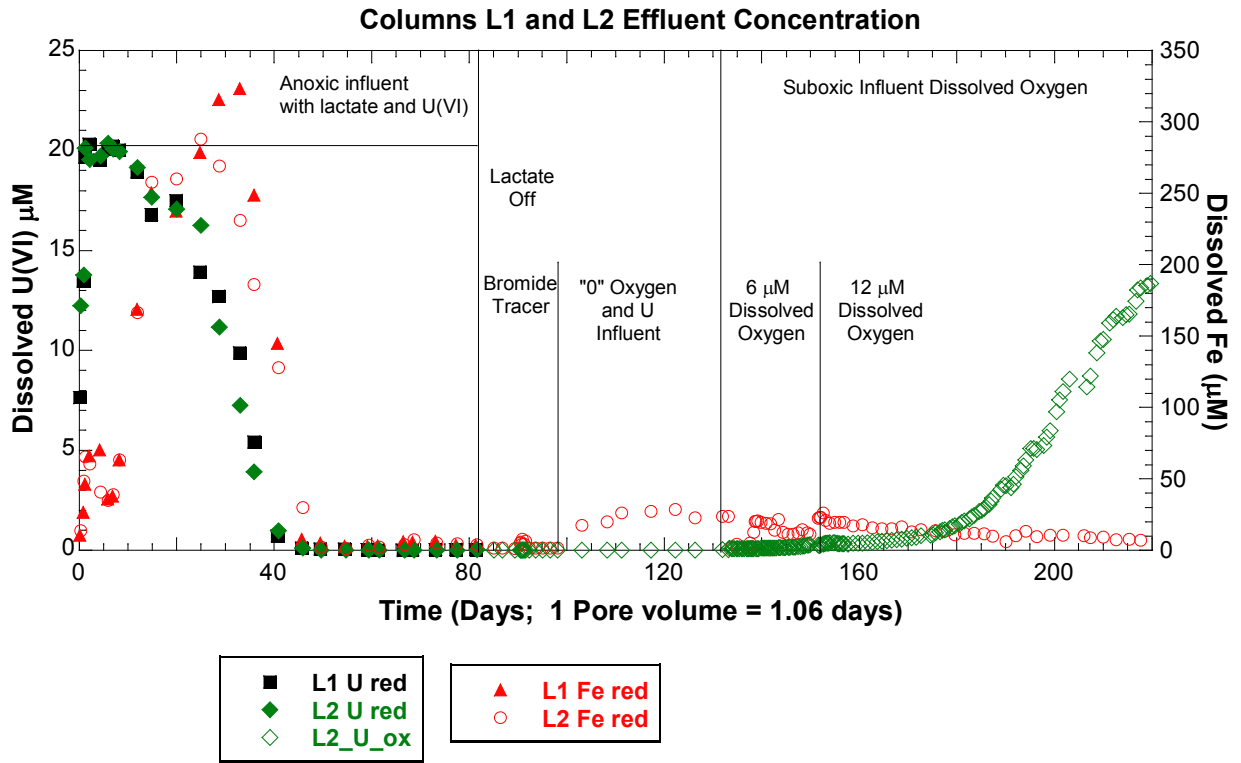


Figure 3.7 Columns L1 and L2 Effluent Concentrations. Part A. Column L1 and L2 effluent dissolved uranium and iron concentrations versus days since start of lactate addition for the duration of suboxic elution of column L2 (top), and expanded time scale for biostimulated reduction (bottom).

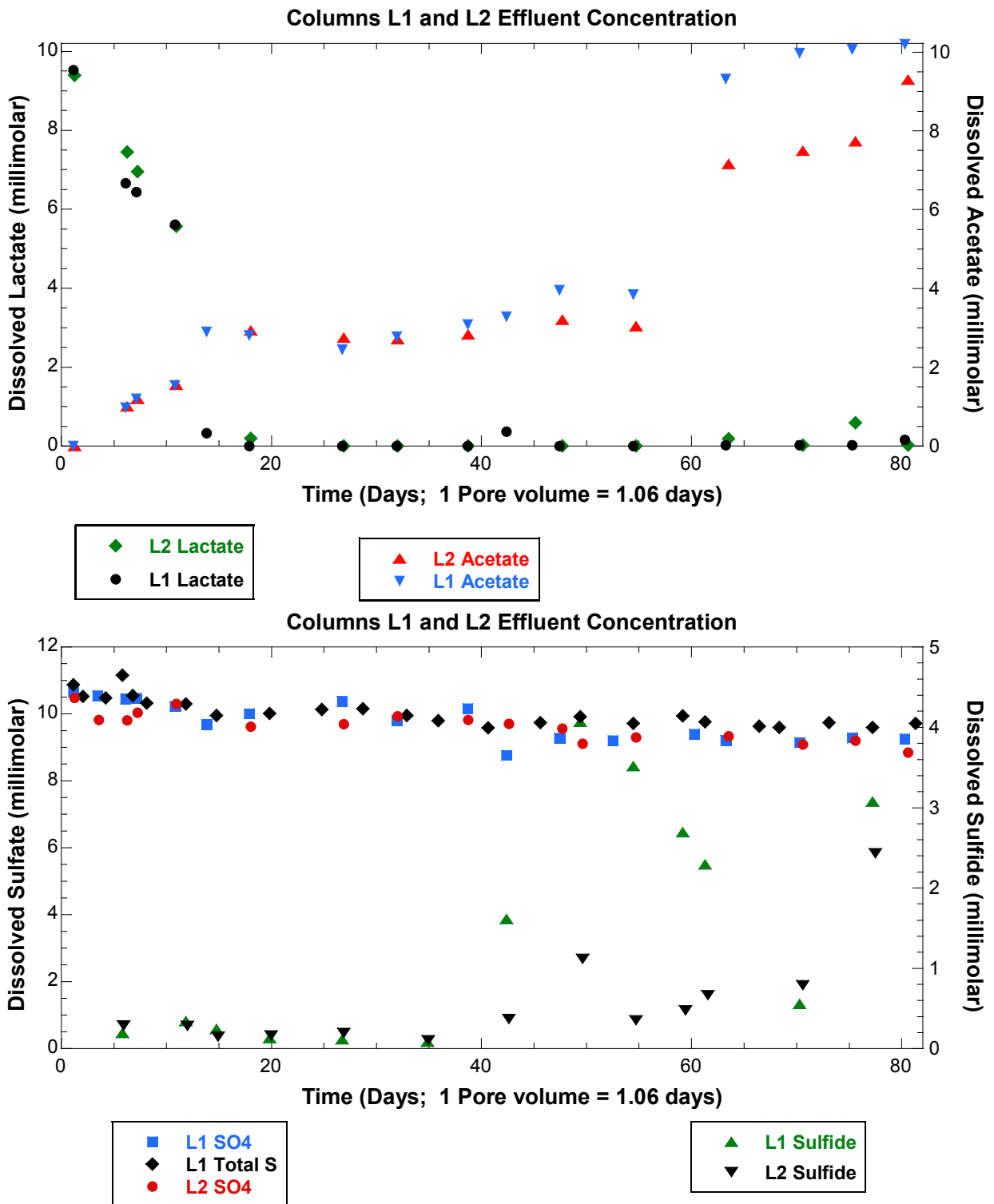
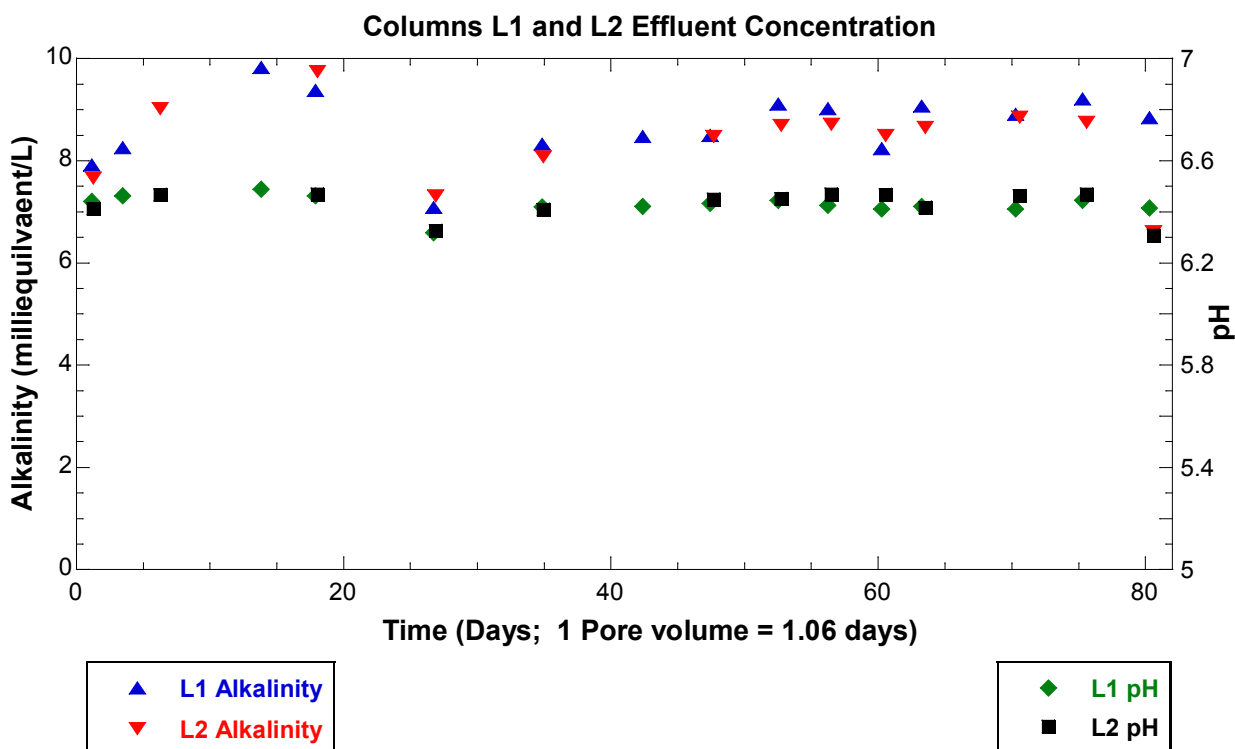


Figure 3.7 Columns L1 and L2 effluent Concentrations Part B. lactate and acetate concentrations (top) and dissolved sulfate, total dissolved sulfur (ICP) and sulfide (bottom) for the biostimulated period of the column experiments.

Column L1 effluent alkalinity increased over the first 15 days of biostimulation from 6.3 meq/L in the influent to almost 10 meq/L. Subsequently, effluent alkalinity decreased over the next 15 days to about 8 meq/L, after which it slowly increased to 9 meq/L by day 50 with little change for the remainder of the biostimulation period (**Figure 3.7C**). Effluent pH increased about 0.2 pH units and varied little during the biostimulation period. Effluent alkalinity and pH for column L2 were similar to column L1 except for the last two sampling points. The increase in alkalinity is consistent with microbial oxidation of lactate and acetate. No significant change in effluent dissolved Ca was observed suggesting that precipitation of  $\text{CaCO}_3$  in response to increased dissolved carbonate and increased pH was not sufficient to lower dissolved Ca by a measurable amount. Analysis of column sediments for inorganic carbonate by  $\text{CO}_2$  evolution on acidification showed no measurable change in total carbonate content indicating that  $\text{CO}_2$  produced during lactate and acetate oxidation was transported out of the column and not precipitated as  $\text{CaCO}_3$ .



**Figure 3.7 Columns L1 and L2 effluent concentrations. Part C. alkalinity and pH versus time for the biostimulation period of the column experiment.**

The effluent water chemistry data were integrated to estimate total loading of uranium, reduction and dissolution of iron, loss of sulfate, production of sulfide, and production of total dissolved carbonate. For U, sulfate, and lactate loss (or consumption) was calculated for each sample by subtracting the measured effluent concentration from the average measured concentrations in the influent reservoir. The change in concentration was then multiplied by the volume in liters of effluent sample collected. For total dissolved carbonate ( $\text{TCO}_2$ ), the production during each sample collection period is the difference between the measured concentration and the average influent concentration measured in reservoirs multiplied by the volume of AGW collected for each sample. The change in concentration of samples not

analyzed was set to the average of adjacent measured samples and then multiplied by its respective sample volume. The resulting change in each constituent in units of millimoles (micromoles for U) in each sample was then summed over the duration of the biostimulation. Net acetate produced was determined by integrating the mass measured in effluent samples. Acetate consumed during the experiment was assumed to equal the difference between lactate consumed and net acetate produced. The results of the total mass of production or loss of these constituents from the effluent integrations are summarized in **Table 3.5**.

Table 3.5 Integrated loss and gain from column effluent concentrations during lactate biostimulation. U, sulfate, and lactate losses are the difference between influent and effluent concentration multiplied by sample volume summed over the biostimulation period. Acetate produced (net) is millimoles transported out of the column. Acetate consumed is the difference between lactate consumed and effluent acetate. Total amount of U, reduced Fe, and total S in sediments recovered from columns are the measured concentrations minus pre-column sediment concentration in each subsectioned intervals times mass of dry sediment recovered. L2 sediments were analyzed following suboxic elution. Units are all millimoles except for uranium, which is in micromoles.

Constituent	L1 effluent	L1 sediment	L2 effluent	L2 sediment
U uptake	17.0	16.0	16.9	13.9
U released (suboxic)			4.6	2.1
Fe reduced	0.164	0.303	0.15	0.197
Fe released (suboxic)			0.03	
Lactate consumed	12.4		11.96	
Acetate produced (net)	6.47		5.42	
Acetate consumed	5.94		6.72	
Total CO <sub>2</sub> produced	5.1		4.6	
Sulfate reduced	1.4		1.6	
Sulfide produced	1.9		0.9	
S retained		4.65		3.16

The calculated loading of U was divided by the total dry mass in the column and plotted as micrograms U per gram solid versus time (**Figure 3.8**). Normalizing U uptake by total dry weight assumes uniform distribution of U uptake by the entire sediment mass. The normalized U loading versus time was nearly identical in columns L1 and L2. The normalized total U uptake at the end of the biostimulation stage was about 70 µg U/g in each column.

Comparison of the integrated sulfate decrease with sulfide increase indicates a greater amount of sulfide produced than the integrated decrease in effluent sulfate. This comparison is based on effluent sulfide only and does not include solid phase sulfide, such as FeS precipitation. Inclusion of solid phase sulfide summed over the entire column sediment mass results in a factor of 4 or more S reduced than can be accounted for in the decrease in dissolved sulfate (see below). One possibility to explain this difference is that oxidation of sulfide occurred in the effluent sample bottles between collection of the effluent samples used for sulfate analysis by ion chromatography analysis. These samples were collected in sterile

serum bottles that had been flushed with the zero oxygen gas mixture into which effluent flowed through a 0.22  $\mu\text{m}$  filter with headspace vented through an airlock. Little difference is observed between total S measured by ICP in acidified effluent samples and sulfate in unacidified effluent samples measured by ion chromatography when both are plotted versus time or volume passed. This comparison suggests that the sulfide in the unacidified samples had oxidized either during storage or in preparation for sulfate analysis. The decrease in total S and sulfate over time in the effluent is an indicator only of S removed from the influent by precipitation of sulfide in the column and thus not a measure of total sulfate reduction.

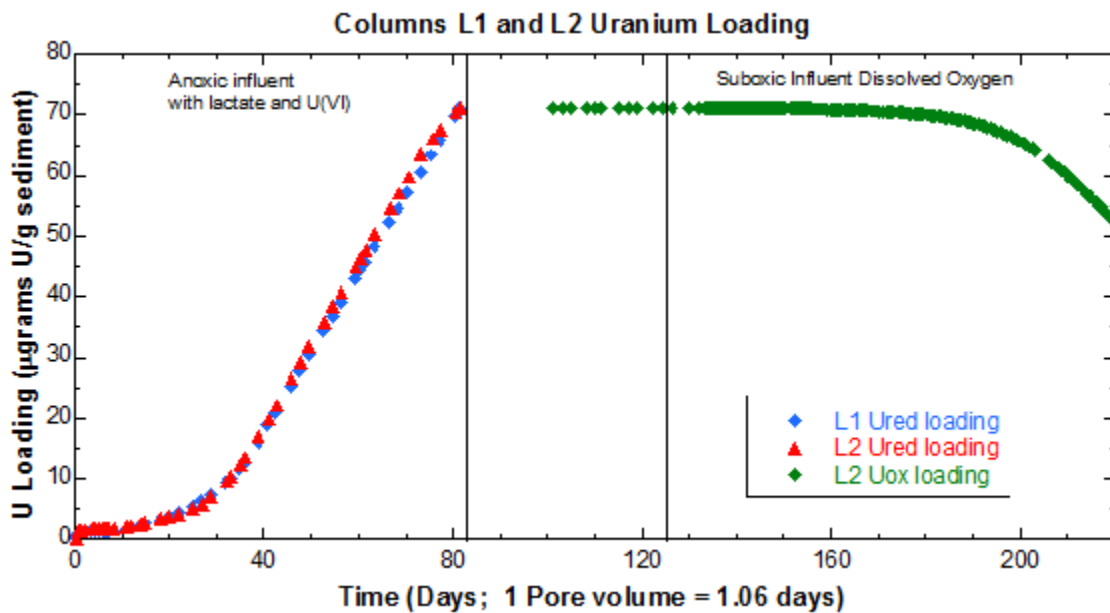


Figure 3.8 Cumulative loading of uranium on column L1 and L2 sediment versus time of the experiment. U loading during biostimulation (Ured) is calculated by the difference between the influent and effluent uranium times sample volume and divided by total dry mass of sediment. Loading is summed up to a given sampling time

Unmeasured sampling intervals are set equal to average of adjacent intervals. Uranium loading during the suboxic elution (Uox loading) for column L2, is the total loading at end of biostimulation minus the sum of the product of effluent uranium times the sample volume divided by the total dry mass of sediment.

### 3.3.2.2 Suboxic elution - extent of uranium remobilization

The near complete removal of [U] from the influent over the course of the biostimulation stage in the lactate columns suggests that the stimulation of ambient microbial population in the Kingsville Dome aquifer after in situ recovery of U may be an effective means of remediating dissolved uranium in groundwater following the extraction process. The removal of dissolved uranium, which is in the +6 oxidation state, likely occurred predominantly by reduction to U(IV) and precipitation, since the +4 oxidation state has much lower solubility than U(VI) for the groundwater chemistry of the Kingsville Dome site. Measurement of the U oxidation state and characterization of the form of the U removed during biostimulation is presented in section 3.3.4. Determining the stability of the bio-reduced uranium in response to changes in groundwater chemistry, such as presence of dissolved oxygen at suboxic levels, is needed to evaluate if the biostimulation process would be an effective tool for long term remediation of ISR influenced aquifers. Pre-operational dissolved oxygen concentrations are not well known with most reported values below the working range of dissolved oxygen meters (0.5 mg/L). A lower value of 0.2 mg/L (6  $\mu$ M) was chosen to test suboxic conditions typically found in deep aquifers.

The stability of bio-reduced U was tested by elution of column L2 after biostimulation by flowing AGW with no [U] or lactate through the column (see above). Prior to suboxic elution but after biostimulation, a bromide pulse was passed through column L2. A reservoir containing bromide (360 mg/L) in AGW (no U, lactate, vitamins or nutrients) equilibrated with 15% CO<sub>2</sub>/N<sub>2</sub> gas mixture was flowed through the column for 5 pore volumes (days 85 to 90) to determine the pore volume at the end of biostimulation. Following the bromide pulse, a reservoir with AGW with no bromide, U, or lactate was equilibrated with 15% CO<sub>2</sub>/N<sub>2</sub> mixture (no O<sub>2</sub>) and flowed through the column to elute bromide. After seven 4-hour samples, the effluent collection time was increased to 6 hours with effluent samples collected over the next 4 days to capture the tail of eluted bromide. Elution of bromide was sampled for a total of 7 days. Splits of every fourth or fifth sample during the bromide pulse and tail sampling were acidified for [U] analysis. Elution of the column with this U-free AGW equilibrated with 15% CO<sub>2</sub>/N<sub>2</sub> gas mixture (with no added oxygen) continued for the next 32 days (June 3 –July 8, 2011, day 101 to 133), with samples collected in serum bottles at 2 to 3 day intervals. Subsequently (starting July 8, day 133), oxygen at 0.5% was included in the gas mixture entering the reservoir and jacketing to attain an equilibrium dissolved oxygen concentration (DO) of 0.21 mg/L (6  $\mu$ M). A high flow rate of the gas mixture was used for one hour to equilibrate the reservoir with this new gas mixture. On day 151, three weeks after the start of suboxic elution, measurement of dissolved oxygen in the column effluent (see method above) yielded 1.4 mg/L (44  $\mu$ M). The outflow sampled directly from the reservoir upstream of the peristaltic pump yielded a DO of 0.2 mg/L. These measurements indicated that atmospheric oxygen was entering the influent in the pump tubing as a result of the pumping process. Dissolved oxygen entering the influent during biostimulation likely was consumed rapidly by aerophilic bacteria near the column inlet and did not affect influent lactate concentration. On day 153, the pump was installed within the acrylic housing that was purged with the same 0.5% O<sub>2</sub>/15%CO<sub>2</sub>/N<sub>2</sub> mixture. The resulting DO in both pump outlet and in the column effluent was 0.4 mg/L (12  $\mu$ M), which remained constant throughout the remainder of the suboxic elution that continued for 67 more days to day 220.

During the bromide pulse and elution, and prior to addition of oxygen to the influent reservoir, effluent U was less than  $0.01 \mu\text{M}$  ( $<3 \mu\text{g/L}$ ) (**Figure 3.9**). Dissolved Fe fluctuated irregularly between  $1.4$  and  $7.8 \mu\text{M}$  during the bromide pulse and tail. Starting at day 101, effluent Fe increased rapidly to  $18 \mu\text{M}$ , and subsequently varied between  $18$  and  $24 \mu\text{M}$  over the remaining 30 days prior to introduction of  $\text{O}_2$  in the gas stream. Following introduction of  $\text{O}_2$  to the reservoir and jacketing gas at  $0.5\%$  at day 133, the effluent U increased rapidly to  $0.1 \mu\text{M}$  ( $20 \mu\text{g/L}$ ), within a couple pore volumes, and then remained near this level over the next 5 days. From this point onwards (day 133), effluent samples were collected using the fraction collector to facilitate shorter collection periods. After day 140, the effluent U concentration started increasing, with the rate increasing with time, reaching  $0.13 \mu\text{M}$  ( $30 \mu\text{g/L}$ ) by day 144 and  $0.25 \mu\text{M}$  ( $60 \mu\text{g/L}$ ) by day 150. Effluent dissolved Fe decreased somewhat linearly from day 120 onwards, but decreased to a minimum between day 133 and day 138. This decrease in Fe that coincided with use of the fraction collector was likely due to oxidation and precipitation in the tubing connecting the column effluent to the fraction collector. The effluent line to the fraction collector was jacketed and purged with the gas mixture starting at day 138, which resulted in effluent Fe increasing to about the concentration measured prior to use of the fraction collector, about  $20 \mu\text{M}$ . Subsequently, effluent  $[\text{Fe}]$  decreased throughout the remainder of the experiment and was about  $6$  to  $7 \mu\text{M}$  by the end of the experiment at day 220. The cumulative Fe transported out of the column in the effluent during suboxic elution is attributed to oxidative dissolution of reduced iron phases, like iron sulfides, with some of the ferrous iron transported out the column prior to significant oxidation to ferric iron because of the well-known effect of carbonate and sulfate complexation of ferrous iron slowing the rate of ferrous oxidation in AGW.

Release of U, likely from oxidation and dissolution, increased throughout the suboxic elution with the overall rate of release increasing greatly after about day 180. This is evident from the increase in effluent U from  $0.5 \mu\text{M}$  at day 180 to over  $12 \mu\text{M}$  by day 220, when the experiment was terminated. Effluent Fe decreased from about day 150 through the end of the experiment. The decrease in effluent Fe was approximately coincident with the increase in the rate of effluent  $[\text{U}]$  suggesting that the apparent increase in the rate of U oxidation may be the result of depletion of iron sulfides which are competing for dissolved oxygen. Very little change in effluent sulfate was measured during the suboxic elution indicating that sulfides did not oxidize completely to sulfate and/or that sulfate from sulfide oxidation was not readily released to solution.

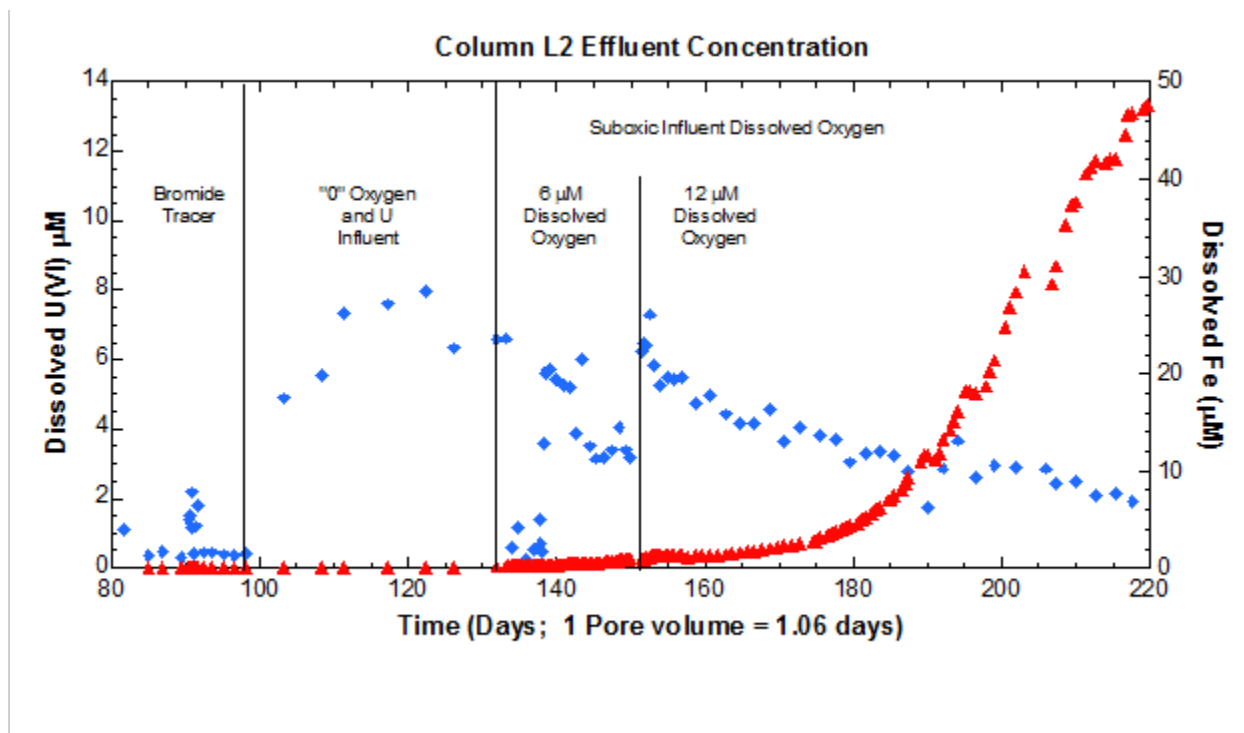


Figure 3.9 Column L2 effluent dissolved uranium (red triangles) and iron (blue diamonds) during suboxic elution versus days since start of lactate addition. This is an expanded scale for Fe and time from Figure 3.7A. Effluent samples were collected with a fraction collection throughout the suboxic elution except for the period between 97 and 132 days, when samples were collected into serum bottles with outlet lines fully jacketed with equilibration gas. Oxygen (0.5%) was added to equilibration gas at day 133. Outlet line to fraction collector was jacketed with equilibration gas starting at day 138. Low Fe in effluent between days 133 and 138 was likely because of oxidation and precipitation in outlet line. The pump housing with equilibration gas flush was installed at day 153.

The integrated mass of U remobilized was determined on a per gram basis over the duration of the oxidation stage for column L2 from the effluent [U]. The mass of U in each effluent sample (concentration times sample volume) was divided by the total dry sediment weight in the column and then subtracted from the calculated total U loading during the biostimulated reduction period (**Table 5** and **Figure 3.8**). By day 180 about 2% of the total cumulative U uptake during biostimulated reduction had been remobilized, with more than 26% remobilized by the end of the experiment. The U loading in excess of the initial sediment U content over the course of the reduction and sub-oxic elution stages is shown in **Figure 3.8**. Although the experiment was ended after 220 days, the trajectory of both the effluent dissolved U and U loading after day 180 suggests that most if not all of U uptake during reduction would be remobilized from the sediment into solution, even at dissolved oxygen concentrations of 0.4 mg/L. The entire mass of U uptake is estimated to be eluted by 160 days (150 pore volumes) after the start of suboxic elution (experiment day 133) by extrapolation of U mass versus time in **Figure 3.8**.

A fifth column of Kingsville sediment, L5, was not subject to bioreduction. This column was used to determine the potential for re-mobilization of the remaining uranium associated with the aquifer sediment ( $57 \pm 7 \mu\text{g/g}$  or  $0.24 \pm 0.03 \mu\text{mol/g}$ ) following in situ leaching. The results of this

column are used to estimate the contribution of this source of U to the observed mass of U remobilized during suboxic elution of column L2. The effluent profile for the elution of column L5 is shown for dissolved U and Fe (**Figure 3.10**). The profile of U eluted from column L1 during the biostimulation stage is shown for comparison. The column pump was contained within the acrylic housing with continuous gas purging throughout the duration of the experiment, initially with no oxygen (15% CO<sub>2</sub>/balance N<sub>2</sub>), and subsequently with oxygen included (0.5% O<sub>2</sub>/15%CO<sub>2</sub>/balance N<sub>2</sub>) for a 0.4 mg/L (12 μM) dissolved oxygen starting at 11 PV (day 13). After an initial 1.6 PV of flow with AGW with no dissolved U or added oxygen, AGW with dissolved bromide was flowed from PV 1.6 to 6.5 (7.8 days). Subsequently, Br tracer was eluted with Br-free AGW, also with no added dissolved oxygen. Effluent Br was monitored for an additional 6 PV to day 15.

Effluent [U] was 5μM over the first 3 days, then decreased to <2 μM over the next 2 days. It continued to decrease through the duration of the elution, although a small increase to 1.1 μM occurred between 7 and 12 PV, which coincided with change to bromide-free AGW, but preceded introduction of dissolved oxygen at 12 PV. Dissolved uranium decreased through 43 PV at which point [U] was ~0.2 μM and the experiment was ended. The total integrated U released from the ISR sediments to solution during the column L5 experiment was 3.0 μg/g (0.013 μmol/g), which is about 4.6% of the total U in the ISR sediment, as recovered from the field site. About 1.7 μg/g or 60% of the total U released from column L5 occurred prior to introduction of dissolved oxygen at 13 PV. By comparison, a much lower mass of U (0.03 μg/g) was released from column L2 over 44 PV during the Br tracer prior to introduction of dissolved oxygen. The total U released during the column L5 experiment is about 3.5% of the total U remobilized from column L2 during suboxic elution. These results suggest that either this fraction of residual U in the Kingsville sediments after ISR was either mobilized during the biostimulation stage of column L1 and L2, or that the biostimulation limited the release of the residual U during suboxic elution.

Dissolved Fe in column L5 increased over the first 2 days to about 35 μM and was relatively constant until day 12. After this point and from the start of 12 μM dissolved oxygen, effluent Fe began to decrease exponentially to less than 2 μM by the end of the experiment, except for a small increase between 18 and 20 days. Since dissolved Fe in effluent (<0.2 μM filtrate) is likely ferrous iron, desorption of Fe<sup>2+</sup> or dissolution of a ferrous iron phase is the likely source of effluent iron. A similar initial increase in effluent iron in columns L1 and L2 was observed during the first few days prior to large increase in effluent Fe from day 10 through 40 (**Figure 3.7A**). Column L5 was subsectioned for solid phase analyses as described for columns L1 and L2.

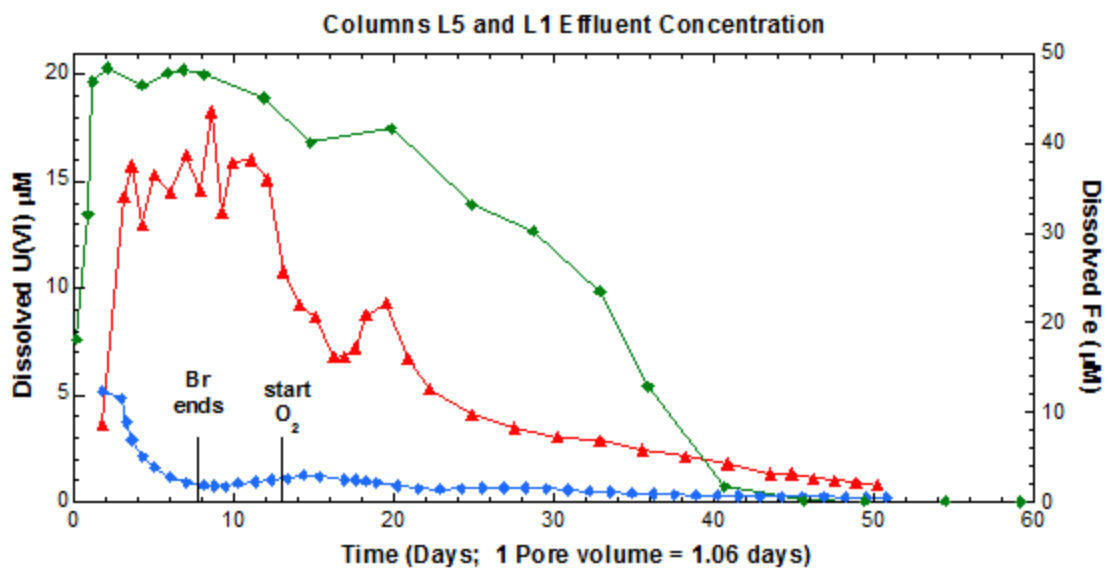


Figure 3.10 Column L5 suboxic AGW elution of the ISR 3712 B-C 580-590 sediment. Effluent dissolved uranium (blue diamonds) and iron (red triangles) versus days. Column L1 dissolved U (green diamonds) during biostimulated reduction with 20  $\mu\text{M}$  U(VI) influent is shown for comparison.

### 3.3.3 Solid Phase Characterization of Column Sediments

The following section describes results of geochemical and microbial characterization of sediments recovered at the end of biostimulation (column L1), suboxic elution (column L2 and L5), and the sediment recovered from coring of Kingsville Dome that was used for the column experiments (3712 BC 580-590).

The Kingsville Dome ISR sediment used for this study is primarily fine sand and silt (**Table 3.6**) and has a  $\text{N}_2$ -BET surface area of  $11.4 \text{ m}^2/\text{g}$ . Quantitative X-ray diffraction analysis shows that the sediment is comprised primarily of quartz, 42%, calcite, 22%, and feldspars, 21% (**Table 3.7**), indicative of the calcareous sandstone. Clays, primarily muscovite and halloysite, comprise 10% of the mass. Iron, as oxides, account for 3%, and as sulfides 1.6%, as marcasite and pyrite. Gypsum is about 0.4% by weight. Total carbonate, as determined by acid volatilization, is 12.4% weight, is equivalent to  $20.8 \pm 0.2$  weight % as  $\text{CaCO}_3$ , and comparable to the 22% calcite from XRD. The total S content of 0.75% measured by EA is equivalent to 2.7%  $\text{FeS}_2$  after accounting for S in gypsum.

Table 3.6 Kingsville Dome ISR 3712 B-C 580-590 sediment grain size distribution as determined by Coulter grain size analyzer.

Grain Size microns	Weight %
<20.7	15.1
20.7 - 63	17.8
63 - 122	29.1
122 - 257	31.7
256 - 494	4.7
494 - 1041	1.6

Table 3.7 Mineral weight percent of Kingsville Dome ISL sediment 3712 B-C 580-590 (pre-column) as determined by quantitative x-ray diffraction.

Mineral	Weight %
Non-Clays	
Quartz	41.7
Kspar (ordered Microcline)	1.5
Kspar (orthoclase)	10.2
Plagioclase (albite, var. cleavelandite)	3.0
Plagioclase (oligoclase; NC)	0.8
Plagioclase (andesine)	3.7
Plagioclase (anorthite)	1.8
Calcite	22.3
Pyrite	0.4
Marcasite	1.2
Gypsum	0.4
Ferrihydrite (Humbug Creek)	3.0
Total non-clays	90.1
Clays	
Halloysite	4.9
Muscovite	5.1
Total clays	9.9
Total	100.0

### 3.3.3.1 Uranium

A total uranium concentration of the Kingsville ISR sediment of  $57 \pm 7$   $\mu\text{g/g}$  ( $0.24 \pm 0.03$   $\mu\text{mol/g}$ ) was measured in the pre-column sediment (as recovered from the field site) by hot nitric acid extraction. This concentration indicates that >95% of the uranium had been removed by the in situ recovery process assuming that the sampled sediment originally contained ore of 0.088% grade. The remaining U likely was inaccessible to ISR lixiviant and/ or not readily

oxidized. The total U distribution in the pre-column sediment is slightly higher in finer grain size fractions with 74% in the <125  $\mu\text{m}$ , 22% in the 125-250  $\mu\text{m}$  fraction, and 5% in the >250  $\mu\text{m}$  fraction. The fractions comprise 62, 32 and 6% of the total sediment mass, respectively.

At the end of the bioreduction stage, the total U concentration in column L1 sediments ranged from 230  $\mu\text{g/g}$  (1  $\mu\text{mol/g}$ ) at the inlet to near background in the interval at the outlet end (70  $\mu\text{g/g}$  or 0.3  $\mu\text{mol/g}$ , Table 3.8A) indicating preferential U attenuation in the upstream end of the column. The net uptake of U for each interval (total minus the initial or pre-column U) shows that greater U uptake occurred near the inlet (**Figure 3.11**). The net increase in total U mass (concentration for each interval times its total dry weight of sediment recovered) for each interval shows a similar distribution of uptake. The fractional uptake by each interval shows that 95% of U removal occurred over the first 6 cm of the column. The total U uptake for column L1 (sum of the interval concentrations times mass), 16.0  $\mu\text{moles}$ , is similar to the total uptake, 17.0  $\mu\text{moles}$ , estimated by integrating the change in effluent [U] over the biostimulation reduction period (Table 3.5).

Total U concentrations in sediment from column L2 ranged from 76 to 169  $\mu\text{g/g}$  (0.32 to 0.71  $\mu\text{mol/g}$ ), and after correcting the background U concentration, 19 to 112  $\mu\text{g/g}$  (0.08 to 0.47  $\mu\text{mol/g}$ ) (**Table 8A**). Comparison of the U distribution after suboxic elution (column L2) to before elution (column L1) shows that U remobilization occurred from the upstream half of the column, in particular, from the 2-4 cm interval, and that some U was higher near the outlet end. These comparisons assume that U distribution in column L2 sediment at the end of the biostimulation period was the same as measured in column L1. It is unknown if the higher U near the outlet is the result of greater uptake during biostimulation or if U was retained near the outlet end during suboxic elution. The measured total U in column L2 (sum of the interval concentrations times mass) is 13.9  $\mu\text{moles}$ . Assuming that the total U uptake during biostimulation was the same in both columns, the difference between solid U represents a remobilization of 2.1  $\mu\text{mol}$  U, or about 15% of the total uptake. The U uptake in both columns calculated from the integrated change in effluent [U] during biostimulation was the same (**Table 3.5**). By comparison, 4.6  $\mu\text{mol}$  of U remobilized during the suboxic elution was calculated from the integrated effluent [U], which is about 27% of the 17.0  $\mu\text{moles}$  U uptake during biostimulation remobilized during suboxic elution.

The sediment U content in column L5 decreased from the initial background of 13.2  $\mu\text{moles}$  to 12.7  $\mu\text{moles}$  during the elution with no dissolved oxygen AGW followed by suboxic AGW. Sediment U concentration varied little among the subsampled intervals (**Table 3.8**). A total U release of 0.56  $\mu\text{mol}$  was estimated from the sum of the measured U in each sediment interval multiplied by its dry mass. The integrated effluent [U] over the duration of the elution was 0.74  $\mu\text{mol}$ . These estimates of U release represent 4 to 5 % of the total initial U in column L5. The effluent history indicates most of the release occurred during the first 8 pore volumes prior to introduction of dissolved oxygen. It is unknown if an equivalent amount of background U was remobilized during the first 8 pore volumes of the biostimulation experiment. Regardless, the amount of U released from the pre-column ISR sediment does not account for the differences in uptake and release calculated from the integrated changes in effluent [U] and the U extracted from the recovered sediment.

Table 3.8A Column sediment solid phase uranium concentrations and whole column mass for column L1 after biostimulated reduction, column L2 after suboxic elution following reduction, and column L5 after suboxic elution.

Column interval	Distance from inlet (cm)	Interval total dry weight (g)	Interval weight fraction of whole column	Total U (HNO <sub>3</sub> ) (µg/g)	stdev <sup>a</sup>	Total U (µmol/g)	Change from pre-col U (µmol/g)	Total U interval (µmol)	Change in U interval (µmol)	Fraction of uptake by interval
L1-R1	0-1	6.22	0.112	230		0.97	0.73	6.02	4.52	0.28
L1-R2	1-3	10.92	0.197	192	1.0	0.81	0.57	8.80	6.17	0.39
L1-R3	3-5	10.87	0.196	134		0.56	0.32	6.10	3.49	0.22
L1-R4	5-7.5	11.24	0.203	78		0.33	0.09	3.66	0.96	0.06
L1-R5	7.5-10	16.24	0.293	70		0.29	0.05	4.76	0.86	0.05
L1 total		55.49						29.3	16.0	
Effluent total									17.0	
L2-Ox1	0-2	12.66	0.232	170		0.71	0.47	9.03	5.99	0.43
L2-Ox2	2-4	9.09	0.167	77		0.32	0.08	2.94	0.75	0.05
L2-Ox3	4-6.5	13.75	0.252	93	1.7	0.39	0.15	5.39	2.09	0.15
L2-Ox4	6.5-8	8.27	0.152	121		0.51	0.27	4.20	2.21	0.16
L2-Ox5	8-10	10.75	0.197	121		0.51	0.27	5.45	2.87	0.21
L2 total		54.52						27.0	13.9	
L5-1	0-2	11.07	0.201	55.3	0.2	0.23	0.01	2.57	0.09	
L5-2	2-4	9.11	0.165	53.6		0.23	0.01	2.05	0.14	
L5-3	4-6	11.51	0.209	53.6		0.22	0.02	2.59	0.17	
L5-4	6-8	11.07	0.201	55.9		0.23	0.01	2.60	0.06	
L5-5	8-10	12.32	0.224	55.1		0.23	0.01	2.85	0.11	
L5 average						0.23	0.01			
L5 total		55.09						12.7	0.57	
Effluent total									0.74	
ISR pre-column sediment				57.2	7.0	0.24				

a. Standard deviation of replicate analyses propagated through calculation.

**Table 3.8B. Column sediment solid phase extractable and total iron concentrations for column L1 after biostimulated reduction, column L2 after suboxic elution following reduction, and column L5 after suboxic elution.**

Column interval	distance from inlet (cm)	1 hr HCl <sup>a</sup> Fe(II) (μmol/g)	stdev <sup>d</sup>	increase Fe(II) from pre-col	1 hr HCl Total Fe (μmol/g)	stdev <sup>d</sup>	1 HR HH Fe <sup>b</sup> (μmol/g)	stdev <sup>d</sup>	Reducible <sup>c</sup> HH Fe-Fe(II) (μmol)	Fe(II) increase interval (μmol)	Total iron HF dissolution (μmol/g)	Hot HNO <sub>3</sub> iron (μmol/g)
L1-R1	0-1	10.3		7.0	10.2		11.8	1.0	1.4	43.8	255	198
L1-R2	1-3	8.9	0.1	5.7	8.7	0.1	9.6	0.9	0.7	61.7	267	214
L1-R3	3-5	8.7		5.4	8.6		9.8	0.8	1.1	58.5	249	184
L1-R4	5-7.5	8.1		4.8	8.1		9.4	0.4	1.3	53.9	239	192
L1-R5	7.5-10	8.5	0.1	5.2	8.6	0.1	9.7	1.6	1.1	85.2	252	192
L1 average		8.9		5.6	8.8		10.0		1.1			
L1 total										303	14000	10700
Effluent total										164		
L2-Ox1	0-2	6.8	0.9	3.5	6.9	1.1	7.0	0.2	0.2	44.5	239	194
L2-Ox2	2-4	7.4		4.1	7.3		8.0	0.0	0.6	37.4	244	197
L2-Ox3	4-6.5	6.5	0.2	3.2	6.4	0.2	6.6	0.5	0.2	43.9	249	191
L2-Ox4	6.5-8	7.0		3.7	7.0		8.2	0.2	1.1	31.0	255	196
<b>L2-Ox5</b>	<b>8-10</b>	<b>7.0</b>		<b>3.7</b>	<b>6.9</b>		<b>8.5</b>	<b>0.1</b>	<b>1.5</b>	<b>39.8</b>	<b>242</b>	<b>192</b>
L2 average		6.9		3.7	6.9		7.7		0.7			
L2 total										196	13400	10600
Difference L1-L2										107		
pre-column		3.3	0.0				4.4	0.1	1.1		235	165

- a. 1 hr HCl: sediment extracted with 0.5N HCl for 1 hour at room temperature  
b. HH: sediment extracted with 0.25 N hydroxylamine hydrochloride in 0.5 N HCl at room temperature for 1 hour.  
c. Reducible Fe is difference between HH extractable Fe and Fe(II) measured by 0.5N HCl.  
d. Standard deviation of replicate analyses propagated through calculation.

**Table 3.8C. Column sediment solid phase total and acid volatile sulfur concentrations for column L1 after biostimulated reduction, column L2 after suboxic elution following reduction, and column L5 after suboxic elution.**

Column interval	total S (mmoles/g)	stdev <sup>a</sup>	S increase from pre-column (mmol/g)	stdev <sup>a</sup>	total S retained (mmoles) <sup>b</sup>	stdev <sup>a</sup>	$\delta^{34}\text{S}$ total ‰	stdev <sup>a</sup>	calculated $\delta^{34}\text{S}$ increase <sup>c</sup> ‰	AVS S <sup>d</sup> (mmol/g)	AVS fraction of total S increase
L1-R1	0.43	0.03	0.20	0.02	1.23	0.15	-39.31	0.38	-41.9	0.0016	0.008
L1-R2	0.33	0.02	0.09	0.02	0.98	0.26	-38.76	0.22	-43.0	0.0013	0.014
L1-R3	0.31		0.08	0.02	0.84	0.26	-38.49		-42.6	0.0009	0.011
L1-R4	0.30		0.06	0.02	0.69	0.27	-37.94		-41.0	0.0011	0.018
L1-R5	0.31		0.07	0.02	1.19	0.39	-38.86		-44.4	0.0013	0.018
L1 average			0.10								
L1 total					4.93	0.61					
L2-Ox1	0.30		0.07	0.02	0.87	0.30	-37.76		-38.6	0.0012	0.018
L2-Ox2	0.27		0.04	0.02	0.34	0.22	-37.68		-38.8	0.0004	0.011
L2-Ox3	0.30	0.01	0.06	0.02	0.87	0.33	-38.37	0.26	-41.6	0.0002	0.003
L2-Ox4	0.29		0.06	0.02	0.51	0.20	-38.28		-41.2	0.0006	0.009
L2-Ox5	0.30		0.07	0.02	0.70	0.26	-37.88		-39.2	0.0004	0.006
L2 average			0.06								
L2 total					3.28	0.59					
L5-1	0.19						-36.37				
L5-2	0.32						-39.65				
L5-3	0.27						-37.86				
L5-4	0.29						-38.93				
L5-5	0.23	0.02					-37.67				
L5 average	0.26	0.05					-38.10				
pre-column	0.23	0.01					-37.20	0.68		0.0003	0.0012

a. Standard deviation of replicate analyses propagated through calculation.

b. Total S increase for interval

c. Calculated  $\delta^{34}\text{S}$  of total S precipitated during biostimulation period

d. AVS is acid volatile sulfur concentration of sediment.

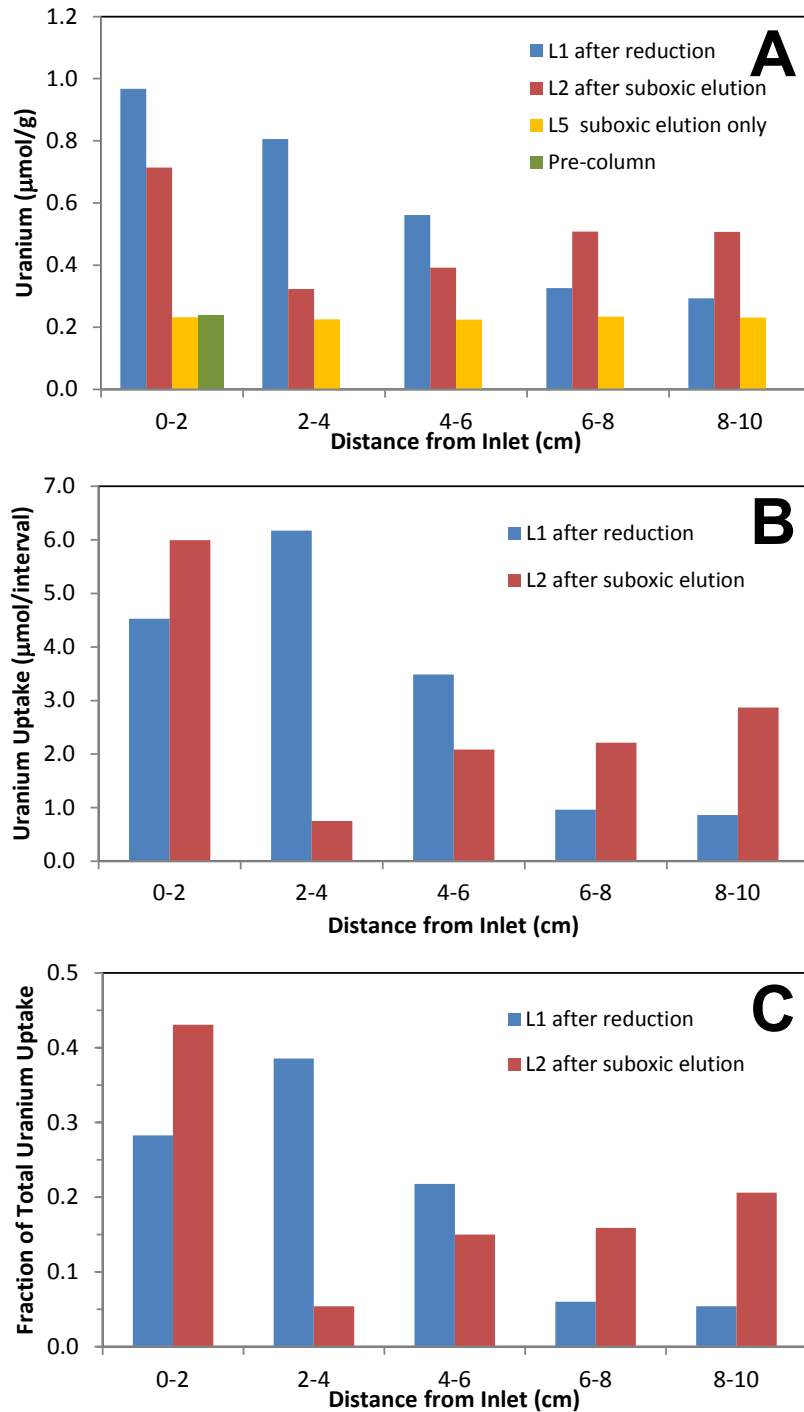


Figure 3.11 Solid phase uranium concentrations of sediments recovered after biostimulated reduction period (column L1) and after suboxic elution (column L2 and L5). (A) Uranium concentrations in columns L1, L2, and L5 by interval with pre-column sediment shown for comparison. (B) Mass distribution of uranium uptake by column interval in μmoles for columns L1 and L2 as the increase above initial total U of pre-column sediment. (C) Fraction of total uranium uptake in column by interval for columns L1 and L2.

### 3.3.3.2 Extractable ferrous and ferric iron

Extractable ferrous iron (Fe(II)) measured in 1 hour 0.5 N HCl extraction of column L1 sediments ranged from 8.1 to 10.5  $\mu\text{mol/g}$  compared to 3.3  $\mu\text{mol/g}$  Fe(II) in the pre-column sediment (**Figure 3.12A**; **Table 3.8B**). Fe(II) concentration was slightly higher at the inlet end. The increase in Fe(II) measured in the L1 column sediments indicates that either reduction of some of the Fe(III) occurs within the solid phase without mobilization of the Fe(II), or that mobilized Fe(II) precipitates within the column as a sulfide such as FeS or as siderite (FeCO<sub>3</sub>). The increase in ferrous iron for the whole column was calculated by subtracting the pre-column Fe(II) from the post biostimulation Fe(II), multiplying by the total weight of each interval and summing. This results in a total Fe(II) increase of 303  $\mu\text{mol}$  for column L1, which is about two times the integrated iron release measured in the effluent (164  $\mu\text{mol}$ ). The increase in sediment Fe(II) summed with effluent Fe(II) yields a total Fe reduction of 467  $\mu\text{mol}$  during the biostimulation, or 8.4  $\mu\text{mol/g}$ . The reducible iron fraction defined by the difference in 1 hour HH (ferrous and ferric iron) and 1 hour 0.5N HCl (ferrous only) extractions in the column L1 after biostimulation ranged from 0.7 to 1.4  $\mu\text{mol/g}$ . This range encompasses the pre-column sediment reducible Fe, 1.1  $\mu\text{mol/g}$ . The much greater observed Fe reduction (8.4  $\mu\text{mol/g}$ ) than the measured reducible Fe in the pre-column sediments (1.1  $\mu\text{mol/g}$ ) indicates that this measure of reducible iron is not representative of the ferric iron reduced during the biostimulation stage of the column experiment. A less labile or structural form of ferric iron that is reduced in place and/or solubilized as Fe(II) likely accounts for the difference in iron reduction. Reduction of Fe(III) in phyllosilicate minerals by dissimilatory microbial iron reduction can be significant in aquifer sediments (Wu et al, 2012; Lee et al, 2012; Komlos et al, 2007). The effectiveness of 0.5N HCl for extraction of Fe(II) produced by reduction of Fe(III) silicates is unknown.

After suboxic elution, sediment Fe(II) concentrations in column L2 ranged from 6.4 to 7.3  $\mu\text{mol/g}$ , about 20% lower on average than column L1 (**Figure 3.12B**; **Table 3.8B**), and varied little along the flow axis of the column. Fe(II) comprised most of the readily extractable iron from Column L2 sediments. The reducible iron concentration in column L2 had a similar range (0.2 to 1.5  $\mu\text{mol/g}$ ) as column L1, but on average was about 40% lower than the pre-column sediment. The HH minus HCl extractable Fe also represents labile ferric Fe, which is slightly higher in the effluent end of column L2 (**Figure 3.12**). The increase of Fe(II) over the initial or pre-column Fe(II) sediment concentration summed over the entire mass of sediment in column L2 was 197  $\mu\text{mol}$ , compared to 303 for column L1, indicating a decrease of 107  $\mu\text{mol}$ , or about 30% of the Fe(II), assuming a similar amount of reduction of iron in both columns. This 30% decrease in Fe(II) in column L2 is consistent with mobilization of iron from sediment and transport out of the column during the suboxic elution since there is no measurable increase in ferric iron in column L2 relative to L1. Low concentrations of dissolved Fe were measured in effluent during suboxic elution, with generally decreasing concentrations over time (**Figure 3.9**). Although, iron speciation was not measured, the effluent iron likely was predominantly Fe(II). Integrated Fe release from effluent (28.9  $\mu\text{mol}$ ), is much lower than the difference between total Fe(II) produced in columns L1 and L2 (107  $\mu\text{mol}$ ), suggesting that most of the iron (~75%) is not remobilized during oxidation. Instead, it is likely transformed to a form not soluble in 0.5N HCl or in HH. In column studies of biostimulated reduction and re-oxidation of iron in aquifer sediments,

Komlos et al (2007) found that the mineralogy of Fe silicates was largely the same after re-oxidation as before biostimulated reduction indicating that biogenic reduced Fe(II) is re-oxidized back to silicate Fe(III). These results are consistent with a component of re-oxidized Fe(III) that remains in silicate mineral structures and therefore does not contribute to extractable Fe reported here.

Sediment iron concentrations measured in the hot HNO<sub>3</sub> extraction and in HF total dissolution are shown in **Table 3.8B**. Higher iron is measured in HF dissolution than in hot HNO<sub>3</sub> digests consistent with a fraction of iron in silicate minerals that HNO<sub>3</sub> does not dissolve. The difference between HF and HNO<sub>3</sub> iron is smaller after biostimulation, consistent with reduction of Fe(III) in silicate to HNO<sub>3</sub> soluble form. Iron oxidation during suboxic elution resulted in no measurable change in this difference compared to after biostimulation.

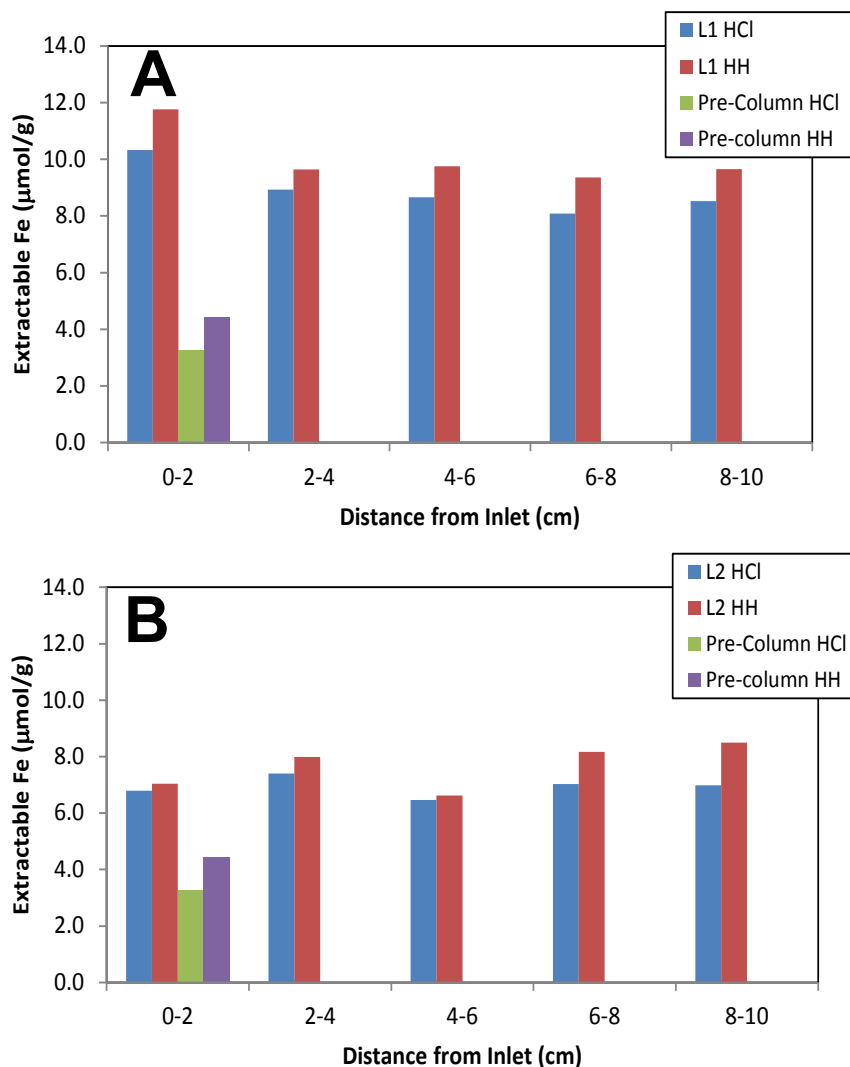


Figure 3.12 Extractable iron concentration in column sediments by interval for (A) column L1 after biostimulated reduction and (B) column L2 after suboxic elution, with pre-column sediment shown for comparison. HCl represents ferrous iron as defined by 1 hour 0.5 N HCl extraction in absence of oxygen, and HH represents both ferrous and ferric as defined by 1 hour room temperature hydroxylamine hydrochloride extraction.

### 3.3.3.3 Total and acid volatile sulfur

The total sulfur content of pre-column sediments was 0.75% or 0.24 mmol/g. Total S in column L1 after biostimulation ranged from 0.3 to 0.51 mmol/g, with highest S at the inlet end of the column (**Figure 3.13A**; **Table 3.8C**) Correcting for the pre-column S, assuming no loss during the experiment, a net increase of 0.06 to 0.18 mmol/g is calculated. A total S increase in column L1 of 4.65 mmol is calculated by summing the increase in S in each interval times its dry mass. This increase in S retained in column L1 is about 2.5 times greater than integrated effluent sulfide mass of 1.9 mmol. Combined these equal 6.5 mmol of S and represent the total sulfate reduced during biostimulation in column L1. The total S increase in column sediment is 15 times greater than the increase in sediment Fe(II) for the column (0.3 mmol Fe), and implies that most of the S retained is not precipitated as iron sulfides, such as FeS.

Stable sulfur isotopes measured during the total S analyses (**Figure 3.13B**) ranged from -37.91 to -39.74 per mil  $\delta^{34}\text{S}$  which represents a depletion in the heavier isotope,  $^{34}\text{S}$ , of -0.34 to -2.14 per mil (‰)  $\delta^{34}\text{S}$  relative to the pre-column sediment  $\delta^{34}\text{S}$  of -37.2 ‰. The most  $^{34}\text{S}$  depleted sample was at the inflow end of the column which had the greatest increase in total S. Microbial sulfate reduction typically results in isotope fractionation on the order -20 or more ‰  $\delta^{34}\text{S}$  (Habicht and Canfield, 1997). S isotope fractionation on this order is consistent with a microbial reduction process, which is expected in the biostimulation columns. The  $\delta^{34}\text{S}$  of the S retained or precipitated in the column was calculated based on two component mass balance,

$$\delta^{34}\text{S}_{\text{tot}} * \text{S}_{\text{tot}} = \delta^{34}\text{S}_{\text{ppt}} * \text{S}_{\text{ppt}} + \delta^{34}\text{S}_{\text{pre}} * \text{S}_{\text{pre}},$$

where,  $\delta^{34}\text{S}_{\text{tot}}$ ,  $\delta^{34}\text{S}_{\text{ppt}}$ ,  $\delta^{34}\text{S}_{\text{pre}}$  are the sulfur isotope ratios for the total S after biostimulation, the S precipitated in the column, and the S initially in the sediment prior to biostimulation, respectively, and  $\text{S}_{\text{tot}}$ ,  $\text{S}_{\text{ppt}}$ ,  $\text{S}_{\text{pre}}$  are the concentration of S in the sediment after biostimulation, S precipitated during biostimulation, and the initial total S in the sediment.

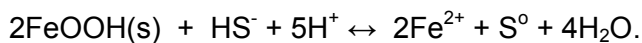
The  $\delta^{34}\text{S}$  of the precipitated S calculated from this equation ranges from -39.2 to -42.9 per mil, which indicates fractionation of about -40 ‰ relative to the AGW sulfate  $\delta^{34}\text{S}$  of -1.0 ‰ (Table 3.8). By comparison, the  $\delta^{34}\text{S}$  of the total S of the column sediment would range from -21.8 to -30.0 ‰ if no fractionation of the AGW sulfate S occurred during reduction. This was calculated using the above equation substituting the AGW sulfate  $\delta^{34}\text{S}$  (-1.0 per mil) for  $\delta^{34}\text{S}_{\text{ppt}}$  and solving for  $\delta^{34}\text{S}_{\text{tot}}$ . The observed S isotope fractionation of -38.2 to -41.9 ‰ is consistent with a microbial sulfate reduction process.

Total S in column L2 sediments ranged from 0.27 to 0.30 mmol/g, or an increase of 0.03 to 0.07 mmol/g, with no apparent trend along the flow path (**Figure 3.13**). The S increase summed for the whole of column L2 was 3.28 mmol. Assuming the same retention or precipitation of S occurred during biostimulation in column L2 as measured in column L1, the difference of 1.65 mmol is the loss of S during the suboxic elution, likely resulting from oxidation of reduced S species to soluble form. However, there was no measurable change in effluent sulfate during the course of elution of column L2 starting with bromide tracer through to the end of suboxic elution. During this period a total volume of 2.03 L of AGW was flowed through the column. If the apparent decrease in sediment S was from continuous transport of sulfate out of the column, this decrease in S divided by the total volume of flow an average would result in an

increase of 0.7 mM SO<sub>4</sub> in the effluent. Instead, average sulfate measured in the effluent was 10.75 mM which is much closer to the influent concentration of 10.65 mM.

The δ<sup>34</sup>S of the column L2 sediments ranged for -37.68 to -38.37 ‰ δ<sup>34</sup>S (**Figure 3.13B**), for a depletion of -0.08 to -0.77 ‰ δ<sup>34</sup>S. The calculated δ<sup>34</sup>S of the precipitated S in column L2 ranged from -38.2 to -41.3 ‰. Assuming the isotopic signature and concentration was the same in columns L2 and L1 at the end of the biostimulation, this lower apparent fractionation factor after suboxic elution suggests that the loss of sulfur, such as by oxidation and dissolution preferentially occurred for lighter isotopes.

Acid volatile sulfide (AVS) content of the pre-column sediment was 0.3 μmol/g, or about 0.1% of the total S content. The column L1 sediment intervals at the end of the biostimulation had AVS concentrations that ranged from 0.9 to 1.6 μmol/g, which accounts for less than 2% of the increase in total S (**Table 3.8C**). The column L2 intervals recovered after suboxic elution ranged from 0.2 to 1.2 μmol/g AVS, also a small percentage of the increase in total S. The lower AVS in column L2 suggests oxidation of part of the sulfide solid phases precipitated. The very low component of AVS suggests that the sulfide produced by sulfate reduction that was not transported out of the column had either transformed to FeS<sub>2</sub> if precipitated with ferrous iron (Mauer and Rittmann, 2004) or as elemental S resulting from reaction of free sulfide with ferric iron solids resulting in oxidation of S<sup>-2</sup> and reduction of ferric to ferrous iron (Li et al, 2009). These processes are illustrated in the following reactions:



Transformation of FeS to FeS<sub>2</sub> by reaction with H<sub>2</sub>S is the primary pathway for pyrite formation under anaerobic conditions in groundwater systems (Mauer and Rittmann, 2004).

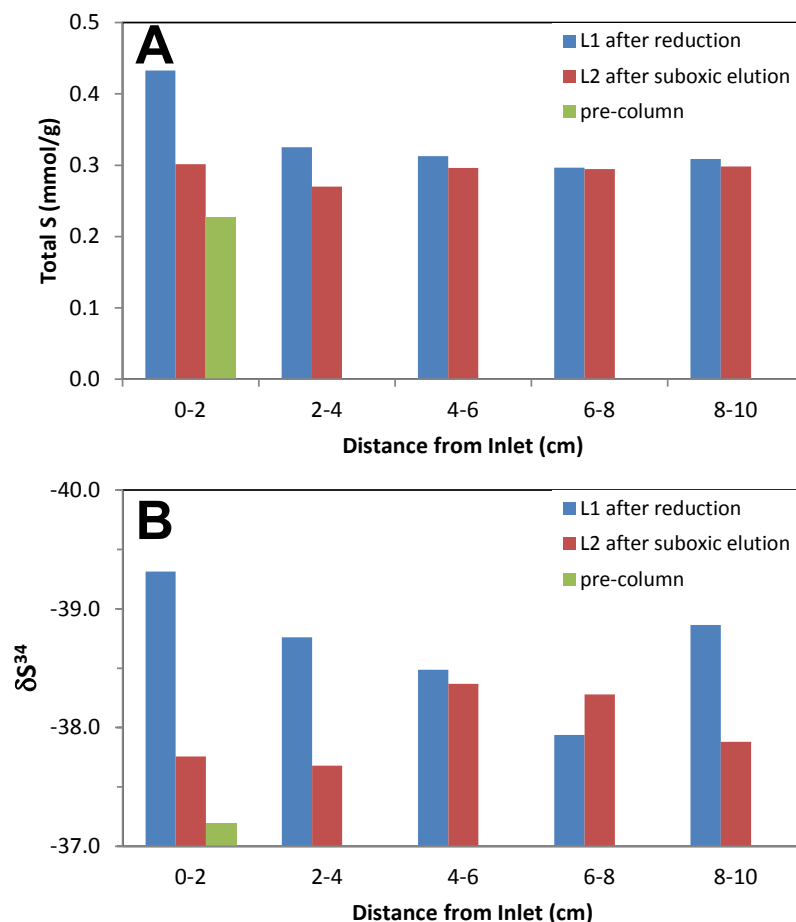


Figure 3.13 (A). Total sulfur concentration in column sediments by interval for column L1 after biostimulated reduction and column L2 after suboxic elution, with pre-column sediment shown for comparison. (B). S isotopic composition of total sulfur expressed as parts per thousand  $\delta^{34}\text{S}$  (‰).

### 3.3.3.4 Total solid phase carbonate

The total carbonate content of sediments from intervals of column L1 ( $19.7 \pm 0.9$  wt % as  $\text{CaCO}_3$ ), L2 ( $20.2 \pm 0.3$  wt % as  $\text{CaCO}_3$ ) and L5 ( $20.6 \pm 0.7$  wt % as  $\text{CaCO}_3$ ) were not significantly different than total carbonate measured in pre-column sediment ( $20.8 \pm 0.2$  wt % as  $\text{CaCO}_3$ ) indicating that precipitation and dissolution during biostimulation and suboxic elution were small.

## 3.3.4 X-ray Spectroscopy and $\mu\text{XRF}$ Mapping of Column Sediment

### 3.3.4.1 U oxidation state

XANES spectra of uranium in column L1, L2 and L5 sediments, and the pre-column ISR sediment as recovered from the field site, all are very similar to XANES spectra for a uraninite model compound with both the energy of the absorption maxima and near edge shoulder between 20960 and 20980 eV (Figure 3.14). In contrast, the U(VI) white line is at a higher

energy and the post edge shoulder is significantly more pronounced, as illustrated by a spectrum for andersonite U(VI) model (**Figure 3.14**). The oxidation state of uranium in sediments recovered from column L1 after biostimulated reduction with lactate and column L2 recovered after suboxic elution was quantified by linear combination fitting of the background corrected and normalized XANES spectra. The best fits were obtained using a synthetic crystalline uraninite for the U(IV) component and andersonite (a uranyl carbonate mineral) for the U(VI) component. Best fits were determined by the smallest residual chi squared ( $\chi^2$ ) value of difference between the sample spectra and the linear combination fit of the components in the least squares fitting routine of SIXPACK software. The sum of the fractions of each component in the fits may not equal exactly one owing to uncertainty in the fit. Fitting of U XANES spectra typically can distinguish components to 5% at best (Singer et al, 2009), such that a component  $\leq 5\%$  cannot be detected.

The U in all samples is dominated by U(IV) which comprises 85% or more of the total U in the sample (**Table 3.9**). The resulting fits are plotted along with sample spectra in **Figure 3.14**. Near equivalent fits to sample spectra were obtained using a single component uraninite U(IV) model resulting in slightly larger  $\chi^2$  values, and a U(IV) fraction of 0.95 to 1.01 (**Table 3.9**). These single component fits provide further evidence that U is predominantly in the U(IV) oxidation state. Column L1 interval R2 was measured both in December 2011 and July 2012. A small increase in the fraction of U(VI) was determined in later measurements suggesting that a small amount of oxidation occurred during storage. Samples were handled only in an anaerobic chamber, heat sealed in two layers of low permeability Mylar pouches containing oxygen scrubbers, and stored at  $-80^\circ\text{C}$ . No measurable difference in U oxidation state was observed for column L5 sediment compared to the pre-column sediment. Although about 5% of the initial total U was transported out of column L5 during suboxic elution, the change in U speciation is not detectable by XANES. The eluted U was assumed to be the result of either desorption of residual U(VI) remaining after the ISR process or represents a readily oxidized fraction of U(IV).

Overall, the U XANES indicate that the U uptake during biostimulation occurred primarily by reduction, and that U remaining after suboxic elution also was predominantly U(IV). In addition, little or no U(VI) produced during oxidation of bio-reduced U(IV) is retained in the column by surface complexation to sediments with a majority of the re-oxidized U(VI) transported out of the column. This suggests the concentration of sites for U(VI) adsorption, such as on ferric oxide surfaces, is not sufficient to retain a significant fraction of the U(VI) by surface complexation. Limited U(VI) sorption during elution is consistent with a sharp increase in effluent U(VI) concentrations observed in the later part of suboxic elution at about 180 days (170 PV).

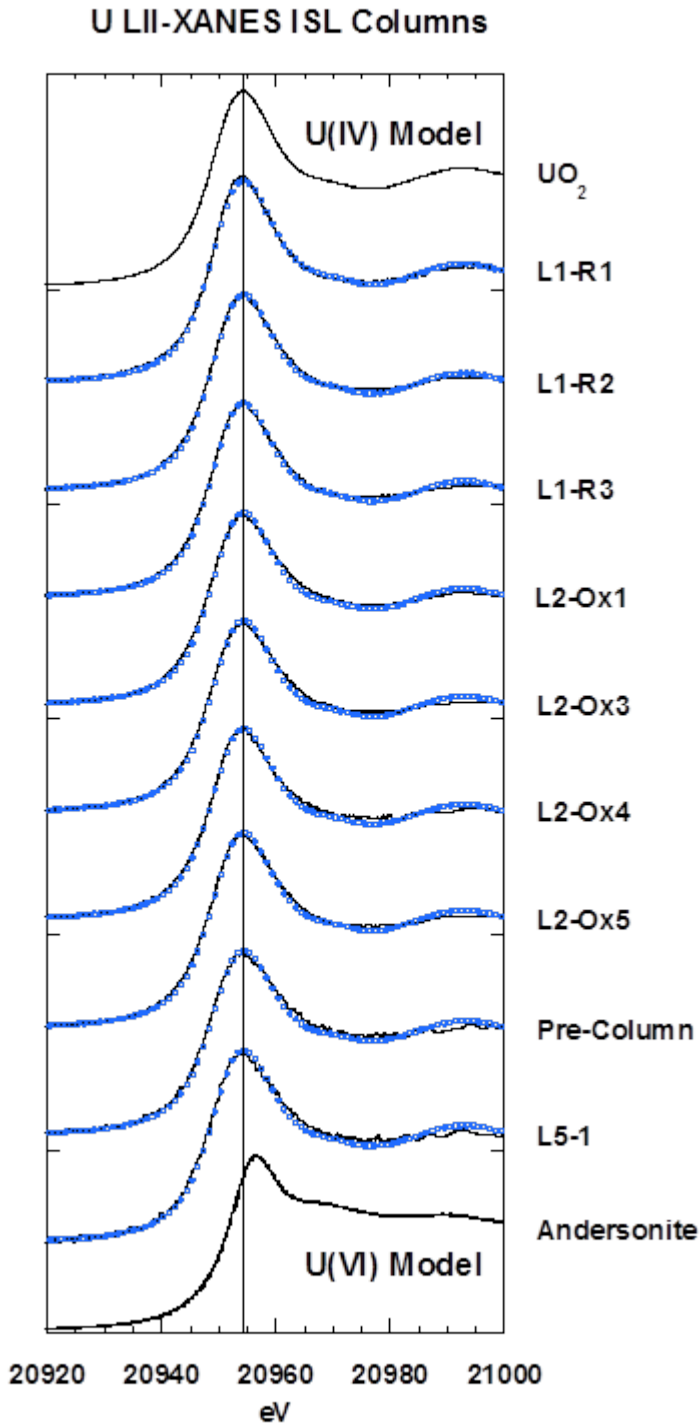


Figure 3.14 U LII XANES spectra of column sediments after biostimulated reduction with lactate (L1) and suboxic elution (L2). ISR pre-column background sediment, and after suboxic elution of the precolumn sediment (L5) are shown for comparison. Numbers (e.g R1) refer to column subsection interval with lower numbers closer to inlet. Sample spectra are shown in solid lines and fits in open symbols. Models for crystalline U(IV) (uraninite,  $\text{UO}_2$ ) and U(VI) (andersonite), are shown for comparison.

Table 3.9 Summary of uranium oxidation state from best fits of bulk U XANES spectra of column sediment samples. U(IV) and U(VI) are expressed as fractions of total uranium from linear combination fitting. UO<sub>2</sub> only represents fits to sample spectra using only crystalline uraninite model. UO<sub>2</sub> + Andersonite represents fit results using crystalline uraninite as U(IV) component and andersonite for U(VI) component. \* indicates measurement of second split of sample in July 2012, with first measurement in March 2010 for pre-column sediment, and December 2011 for L1-R2. All XANES were collected on U L<sub>II</sub> edge with the exception of the pre-column sample collected on the U L<sub>III</sub> edge in March 2010.  $\chi^2$  represents the sum of the square of difference between sample spectrum and the fit of the spectrum using the fraction of the components listed, and is specific to individual samples. Sample spectra and fits are shown in Figure 3.14.

Sample	UO <sub>2</sub> only		UO <sub>2</sub> + Andersonite		
	U(IV)	$\chi^2$	U(IV)	U(VI)	$\chi^2$
L1-R1	1.05	3.30E-4	1.12	-0.08	2.70E-4
L1-R2	1.01	4.22E-4	0.96	0.07	3.81E-4
L1-R2*	0.97	5.63E-4	0.85	0.15	3.73E-4
L1-R3	1.01	4.93E-4	0.96	0.06	4.61E-4
L2-Ox1	0.99	6.82E-4	0.90	0.13	5.59E-4
L2-Ox3	0.99	8.85E-4	0.88	0.13	7.46E-4
L2-Ox4	0.98	8.23E-4	0.84	0.18	5.61E-4
L2-Ox5	1.01	6.99E-4	0.94	0.09	6.29E-4
L5-1	0.99	1.48E-3	0.85	0.17	1.24E-3
Precolumn*	0.95	1.19E-3	0.84	0.13	1.02E-3
Precolumn	0.99	1.20E-3	0.86	0.14	1.10E-3

### 3.3.4.2 Speciation of column sediment uranium

Extended X-Ray Absorption Fine Structure (EXAFS) spectra can provide information on the local bonding environment of an element through analysis of the spectrum and by comparison to model compounds. The EXAFS spectra for the ISR column L1 and L2 sediments recovered after biostimulation and suboxic elution are presented in **Figure 3.15**. The reciprocal k-space  $k^3$ -weighted spectra of post biostimulated reduction column L1 samples are similar to spectra for nano-particulate and crystalline uraninite (UO<sub>2</sub>) between k of 2 and 6, for example the higher frequency oscillation that appears as a shoulder at about k of 4. The data quality above k of 6 degrades rapidly with a weak similarity to lower frequency oscillations in the model spectrum. The spectrum for the pre-column sediment shares the low frequency features of the uraninite model compounds. The possible presence of higher frequency oscillations are masked by noise. The post suboxic samples from column L2 also appear to be intermediate to the nanoparticulate UO<sub>2</sub> model and the pre-column sediment spectra. The comparison is more evident in the radial distribution function of the Fourier transform of the spectra (**Figure 3.15B**). All samples and the UO<sub>2</sub> model have a distinct U-O shell at about 1.8 Å indicative of the oxygen coordination shell of U(IV) which dominates all of the samples. A second shell at about 3 Å is present in the pre-column sediment, but is of unknown identity. The shell is present when the k range of the spectrum used for the transformation is limited to  $k < 7$ , below which the 3 Å feature

appears as a shoulder on U-O peak indicating that the 3 Å peak is representative of a longer distance neighbor and is not the result of noise in the higher k range of the spectrum. The pre-column sediment does not have the 3.8 Å U-U shell (Schofield et al, 2008) indicating that the background U is a non-uraninite U(IV) species. The Kingsville Dome ore body contained uraninite in addition to several other forms including U in clays and associated with iron disulfide replacing detrital Fe and Ti oxides (Arrendondo, 1991). The lack of a 3.8 Å U-U shell in the pre-column sediment is consistent with oxidation and mobilization of uraninite U during the ISR process. This suggests that the remaining U is atomically dispersed in the sediment, perhaps sorbed or coprecipitated with other minerals in a form that is relatively recalcitrant to oxidation and remobilization.

The 3.8 Å U-U shell is evident in the column L1 sample spectra and of similar magnitude to nano-particulate  $\text{UO}_2$  but is diminished in magnitude from the crystalline uraninite model. The decrease in intensity of this feature relative to the U-O shell may be the result of small particle size and/or low crystallinity of the U(IV) precipitated during the biostimulated reduction. However, its presence in column sample spectra but not in the pre-column sediment is consistent with formation of a uraninite ( $\text{UO}_2$ ) like U(IV) precipitate during reduction. The 3.8 Å shell also is present in the post suboxic elution samples from column L2, suggesting that U not remobilized during suboxic elution remains in this form and has not changed to another form. This observation is consistent with continued dominance of U(IV) in sediment after suboxic elution. The 3 Å shell observed in the pre-column sediment also is present in column samples but is of lower magnitude because of the contribution of the  $\text{UO}_2$ -like U(IV) formed in the column to the spectra of column samples.

Further analysis of the column sediment EXAFS spectra may provide information on the local bonding environment of U fitting of the spectrum. This process entails simulation of spectra through optimizing distance and coordination numbers of nearest and next nearest atoms in the element of interest's coordination sphere to obtain best fit to sample spectrum. This approach requires knowledge of the identity and structure of likely components comprising the element in a sample. The contribution of other U species evident in pre-column sediment need to be accounted for or subtracted prior to fitting. Clearly, the limited quality of spectra, which in part is a function of the low U concentration, severely restricts the ability to derive unique fits. Thus, shell by shell fits have not been attempted with the current data.

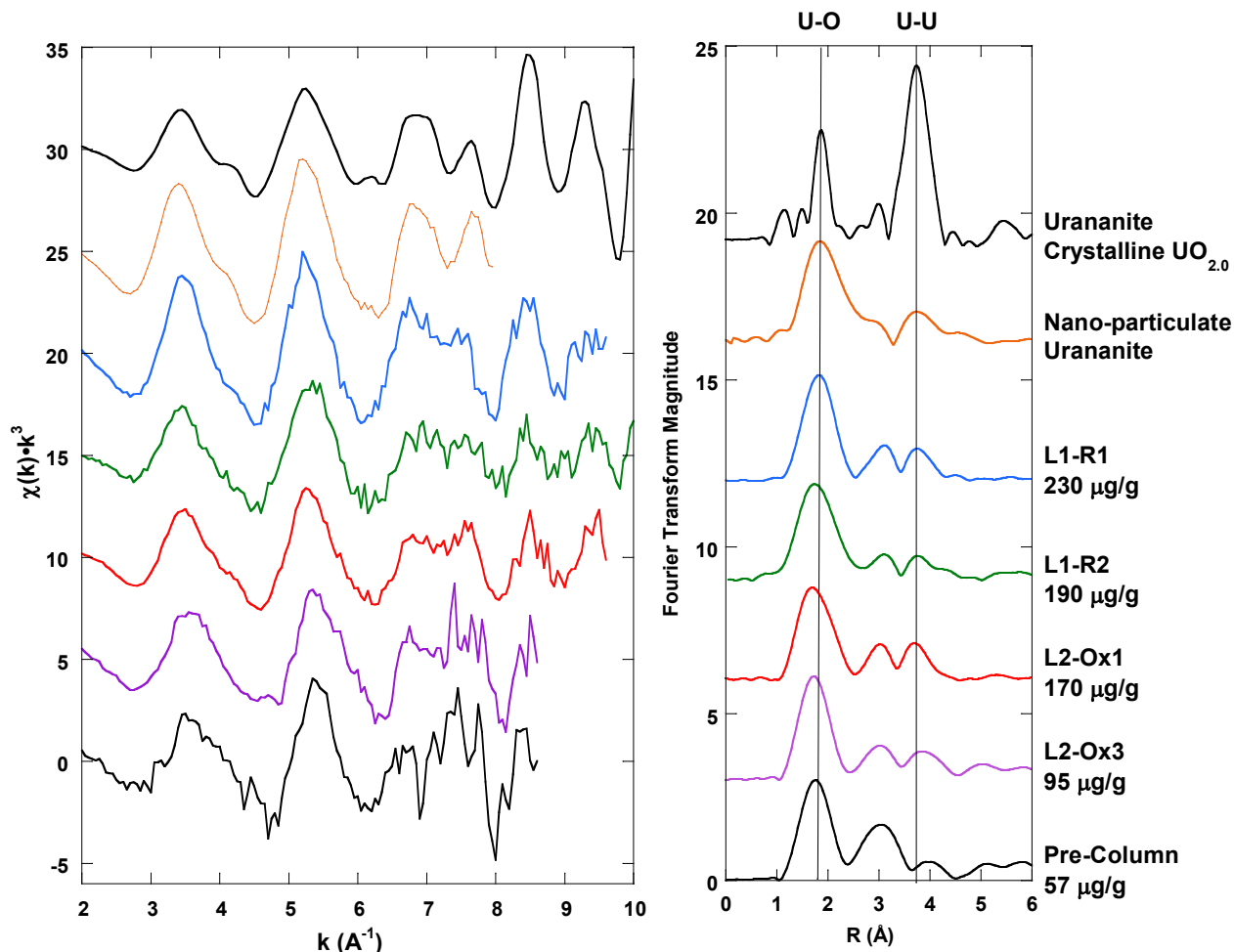


Figure 3.15 (A) U L<sub>II</sub>  $k^3$ -weighted EXAFS spectra and (B) Fourier transformed radial distribution of EXAFS spectra (not corrected for phase shift) for ISR column sediments after biostimulated reduction with lactate (L1) and suboxic elution following biostimulated reduction (L2). Pre-column experiment sediment and the crystalline urananite model are shown for comparison. Letters and numbers (e.g. R1) refer to column subsection interval with lower numbers closer to inlet. Uranium concentrations listed are total concentrations measured by hot nitric acid dissolution and include pre-column background U.

### 3.3.4.3 Distribution of U on sediments

Micro-focused synchrotron X-ray fluorescence ( $\mu\text{XRF}$ ) was used to map the distribution of uranium and other elements in thin sections of sediments recovered from the L1 and L2 column experiments and the pre-column sediments. This section describes the  $\mu\text{XRF}$  elemental maps of thin sections at 30  $\mu\text{m}$  step size (SSRL beam line 10-2 "mesoprobe"), and at subsequent finer resolution (2  $\mu\text{m}$  step size, SSRL beam line 2-3 microprobe). The distribution of U oxidation states was determined at selected locations using multi-energy imaging across the U L<sub>III</sub>-edge, or XANES imaging. Multi-energy maps were also collected across the Fe K-edge as an indicator of the distribution of iron phases. U L<sub>III</sub>-edge XANES spectra were collected at specific points ( $\mu\text{XANES}$ ) both to verify the XANES imaging approach and for comparison to bulk XANES measurements.

The pre-column sediment (57  $\mu\text{g/g}$  total U) has localized areas of U (**Figure 3.16**). The sediment contains some larger grains of up to about 1 mm in diameter that are optically dark. These grains are primarily iron. U does not appear preferentially associated with large iron bearing grains in this thin section. Calcium is widely distributed through the thin section in smaller grains and likely includes a large contribution from the abundant calcite and to a lesser degree from feldspars. Two of the areas with higher U content were imaged at higher resolution (**Figure 3.17**). In panel A (**Figure 3.17A**), the  $\mu\text{XRF}$  map shows a single grain ( $\sim 100 \times 200 \mu\text{m}$ ) containing U perhaps as a coating intermixed with Fe, along with other grains containing either Fe or Ca. The U content of this grain was not sufficient for  $\mu\text{XANES}$  data collection. The high U areas in panel B were of smaller size ( $< 10 \mu\text{m}$ ). The  $\mu\text{XANES}$  of one higher U spot (ISL Pre-column pt 1) indicates essentially all U(IV) (**Table 3.10, Figure 3.18**).

The content of U in the thin section of column L1 interval R1 (inlet end) was visually greater in the  $30 \mu\text{m}$  beam size  $\mu\text{XRF}$  map (**Figure 3.19**) than the pre-column sediment. Distributions of Fe and Ca were similar to pre-column sediment. An enlarged view of region 2 shows the presence of U in a large Fe grain ( $\sim 200 \times 400 \mu\text{m}$ ), along with smaller grains ( $< 100 \mu\text{m}$ ) with higher apparent U concentration (**Figure 3.19C and D**). Uranium oxidation state mapping of this large Fe grain (L1-R1B G2) and an adjacent high U grain showed U(VI) in localized areas with U(IV) distributed more diffusely within the iron grain (**Figure 3.20A and B**). On panel 2A of **Figure 3.20**, U  $\mu\text{XANES}$  at points within these grains show U is largely U(IV) (73 to 79% ) within grain L1-R1B G2 (pt 1 and pt 2), but is 57% U(IV) and 40%U(VI) in the smaller grain (**Table 3.10; Figure 3.18** L1-R1B 2 pt 1, 2, and 3). The Fe  $\mu\text{XANES}$  map of this area shows that the large grain is largely iron sulfide, with lower concentration areas of iron oxide adjacent to the grain (**Figure 3.20C**). **Figure 3.21** shows Fe XANES spectra of individual points on grains that are consistent with reduced Fe, such as iron sulfide (L1-R1 g2 pt1) and magnetite (L1-R1 g2 pt 2). The U oxidation state map of the smaller grains shown in **Figure 3.20** indicate that U is up to two-thirds U(VI) (**Figure 3.20D and E**) and the U in these grains is intermixed with (D) or surrounded by Fe (E). Fit of the U  $\mu\text{XANES}$  taken at a point within grain 2C show a mixture of 68% U(IV) and 34% U(VI) (**Table 3.10; Figure 3.18** L1-R1B 2C). It is unknown if the U(VI) is part of the residual U remaining after the ISR extraction of the ore body, or is the result of sorption of U(VI) during the column experiments.

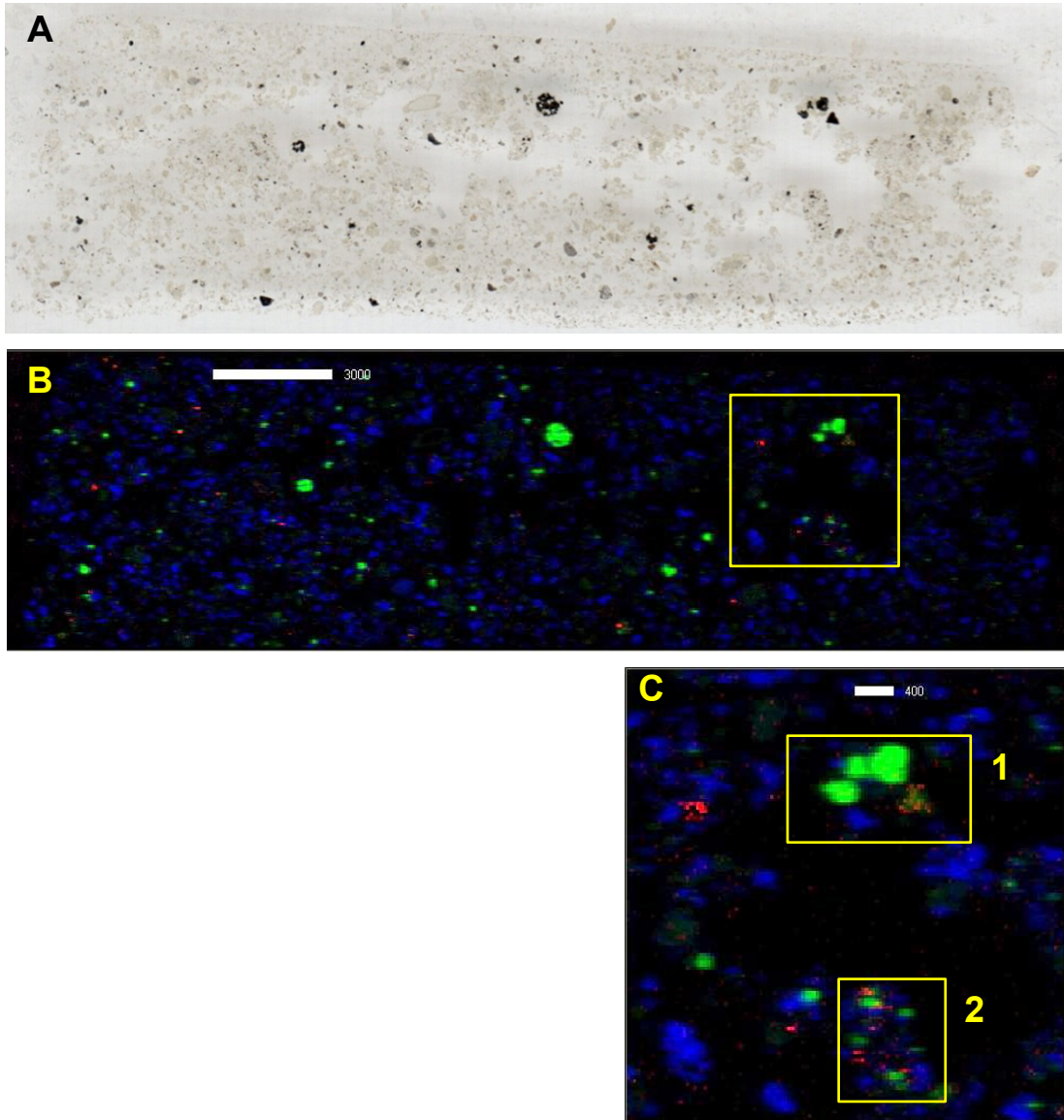


Figure 3.16 ISR pre-column sediment thin section: (A) Optical scan; (B) meso-scale XRF tri-color map of whole thin section panel at 30 x 30 um resolution with U shown in red, Fe in green, and Ca in blue. U is shown as difference between fluorescence above and below the U  $L_{III}$  edge to remove contribution from Rb fluorescence. (C) Area of interest for BL2-3 XRF mapping bounded by yellow. Scale bars are in units of microns.

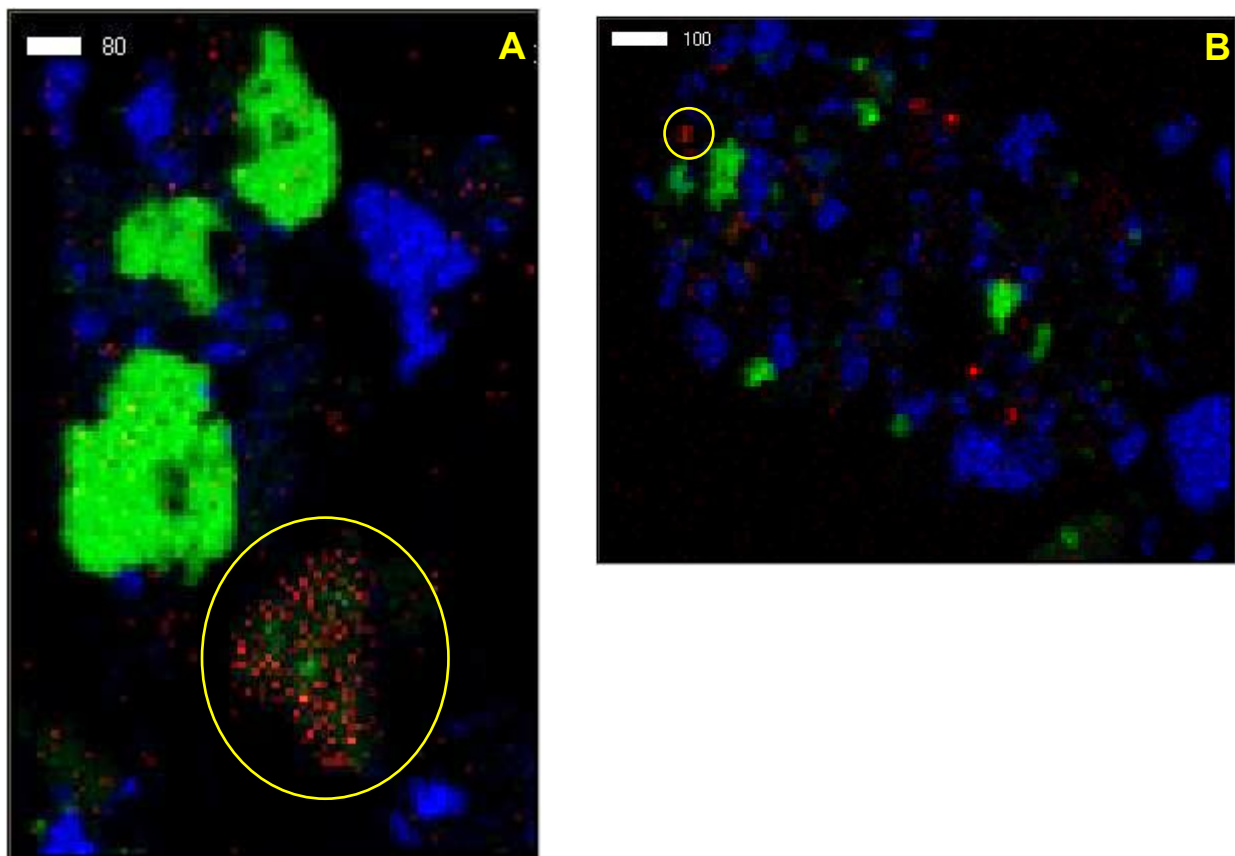


Figure 3.17 X-ray microprobe XRF maps of region 1 and 2 for ISR pre-column sediment thin section shown in Figure 3.16. (A)  $\mu$ XRF map of region 1 at 5 x 5  $\mu$ m resolution with iron shown in green, uranium in red and calcium in blue. Color brightness increases with concentration. (B) Region 2 scanned at 10 x 10  $\mu$ m resolution at a single energy with the image shown for iron in green, total U in red and calcium in blue. Images are mirror of Figure 3.16C and rotated 90° counter clockwise. Yellow circles mark grains where U L<sub>III</sub>  $\mu$ XANES spectra were attempted. The spectrum for the circled area in panel B is shown in Figure 3.18 (ISR Pre-column pt 1). Scale bars are in units of microns.

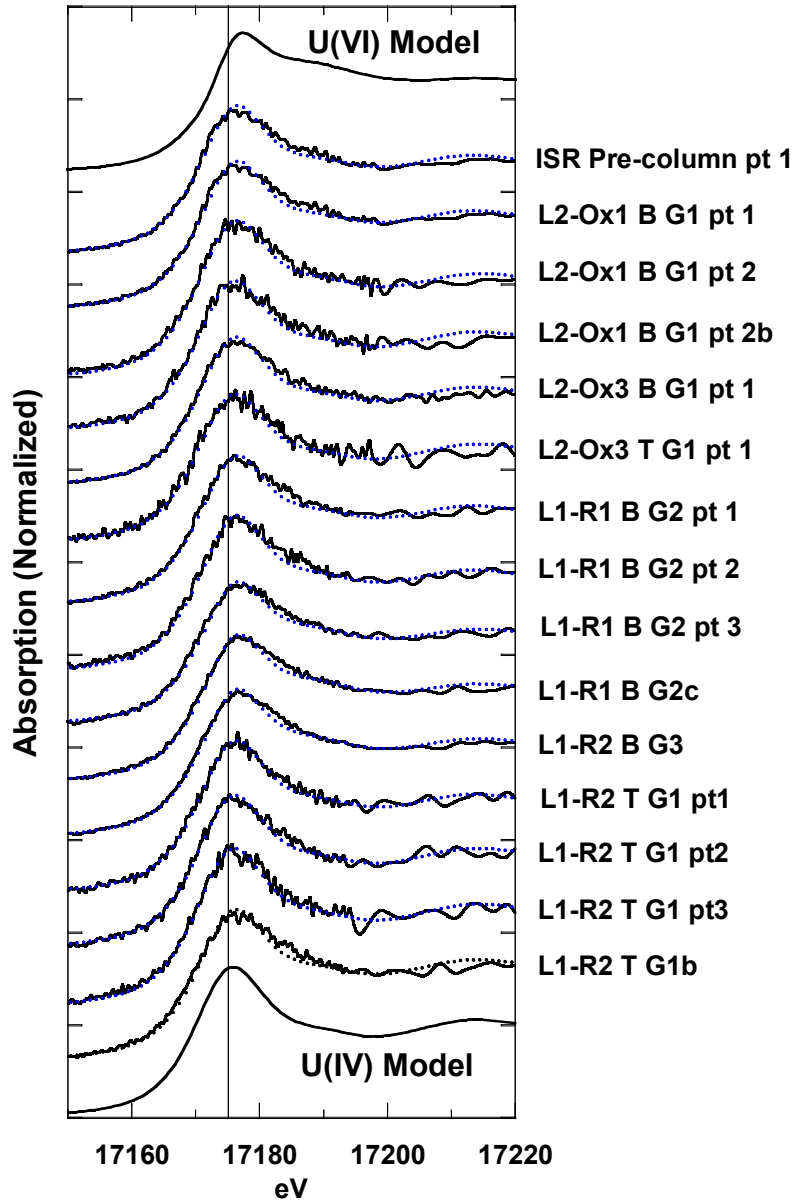


Figure 3.18 U L<sub>III</sub>  $\mu$ XANES spectra of points on thin sections of column sediments after biostimulated reduction with lactate (L1), suboxic elution (L2) and ISR pre-column background sediment. Letter and numbers (e.g R1) refer to column, subsection, interval with lower numbers closer to inlet (e.g. Ox1), thin section panel (B =bottom; T = top), grain, and point on grain within each thin section. Sample spectra are shown in solid lines and fits in open symbols. Models for U(IV) (crystalline uraninite, UO<sub>2</sub>) and U(VI) (andersonite, uranyl carbonate) are shown for comparison. Sample IDs and linear combination fits of percentage U(IV) and U(VI) are shown in Table 3.10. Locations of point XANES data collection are shown in Figures 3.17, 3.20B, 3.20E, 3.23A, 3.24A, 3.24B, 3.26, 3.28C, and 3.30.

Table 3.10 Summary of uranium oxidation state from best fits of individual point  $\mu$ XANES spectra on column sediment thin sections. U(IV) and U(VI) are expressed as fraction of total uranium from linear combination fitting of crystalline uraninite ( $\text{UO}_2$ ) for the U(IV) component and either andersonite (AND) or U(VI) sorbed to ferrihydrite (FHY) for U(VI) components. U  $L_{III}$  edge  $\mu$ XANES were collected using a 1- $\mu\text{m}$  beam size at SSRL BL 2-3.  $\chi^2$  represents the sum of the square of difference between sample spectrum and the fit of the spectrum using the fraction of the components listed, and is specific to individual samples. Sample spectra and fits are shown in Figure 20. Sample IDs represent column, interval section, thin section panel, grain and point on grain. Locations are shown on XRF maps of thin sections in Figures 3.17, 3.20, 3.23, 3.24, 3.26, 3.28 and 3.30. \* denotes U  $\mu$ XANES points on large iron sulfide grains.

Sample ID	Components	U(IV)	U(VI)	$\chi^2$
ISL Pre-column pt 1	UO <sub>2</sub> , AND	1.01	0.001	2.26E-3
L2-Ox1 B G1 pt 1	UO <sub>2</sub> , AND	0.71	0.32	1.17E-3
L2-Ox B G1 pt 2	UO <sub>2</sub> , AND	0.88	0.14	3.91E-3
L2-Ox1 B G1 pt 2b	UO <sub>2</sub> , AND	0.85	0.27	4.33E-3
L2-Ox3 B G1 pt 1	UO <sub>2</sub> , AND	0.81	0.21	1.48E-3
L2-Ox3 T G1 pt 1	UO <sub>2</sub> , AND	0.88	0.13	4.54E-3
L1-R1 B G2 pt1 *	UO <sub>2</sub> , AND	0.73	0.30	1.34E-3
L1-R1 B G2 pt2 *	UO <sub>2</sub> , AND	0.79	0.30	1.96E-3
L1-R1 B G2 pt3 *	UO <sub>2</sub> , FHY	0.57	0.42	1.45E-3
L1-R1 B G2c	UO <sub>2</sub> , FHY	0.68	0.34	1.61E-3
L1-R2 B G3	UO <sub>2</sub> , FHY	0.60	0.43	7.89E-4
L1-R2 T G1 pt1 *	UO <sub>2</sub> , AND	0.82	0.24	1.62E-3
L1-R2 T G1 pt2 *	UO <sub>2</sub> , AND	0.91	0.12	1.62E-3
L1-R2 T G1 pt3 *	UO <sub>2</sub> , AND	0.99	0.08	2.95E-3
L1-R2 T G1b	UO <sub>2</sub> , FHY	0.69	0.33	1.65E-3

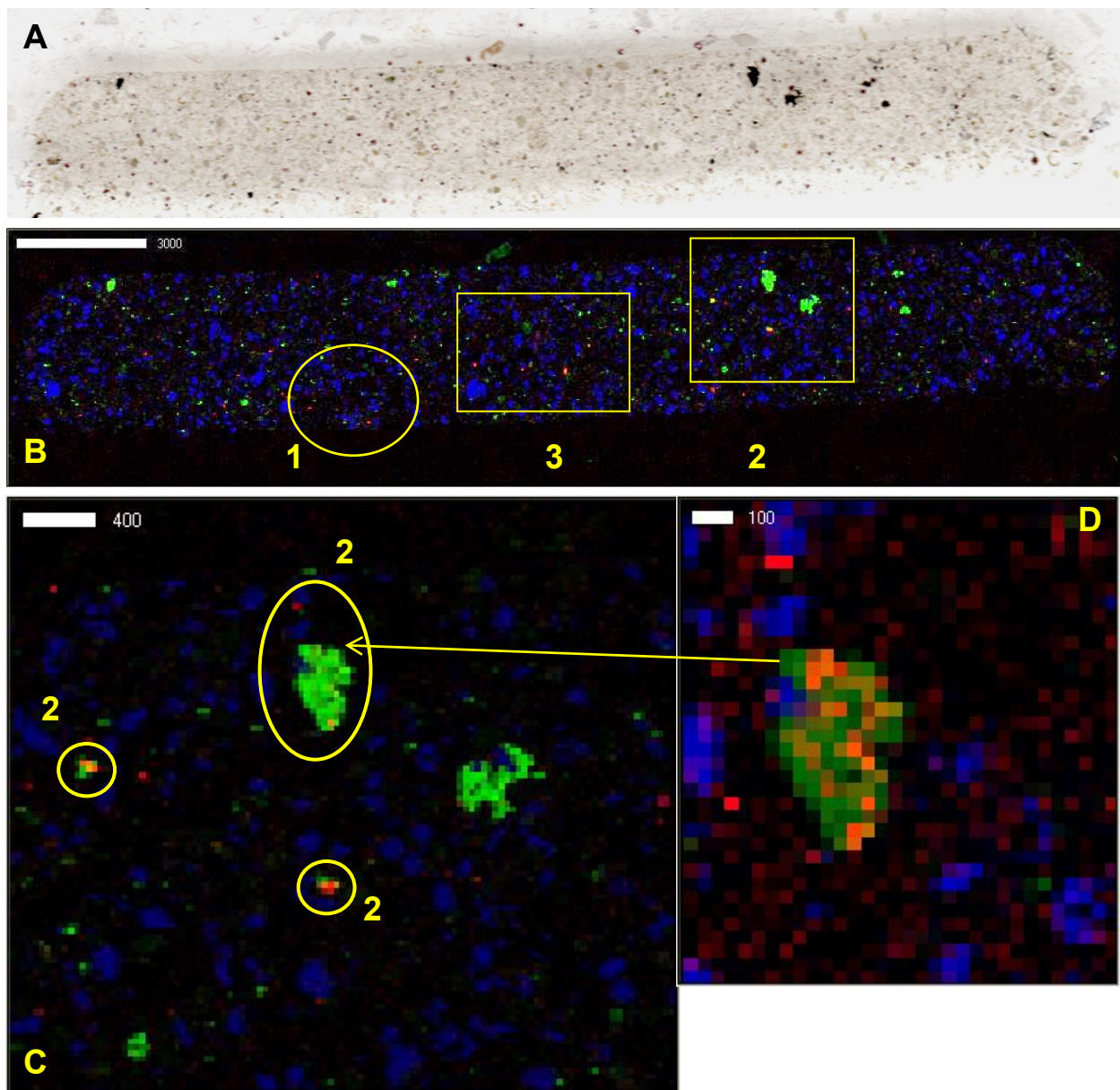


Figure 3.19 Column L1-R1 bottom panel of thin section: (A) Optical scan; (B) meso-scale XRF tri-color map of whole thin section panel with U shown in red, Fe in green, and Ca in blue, with areas of interest bounded by yellow. Scale bars are in units of microns. (C) is zoom of area 2 of meso-scale XRF map in B, with grains of interest denoted (e.g. 2A). (D) is a higher zoom of large iron grain (2A) in panel C bounded by yellow.

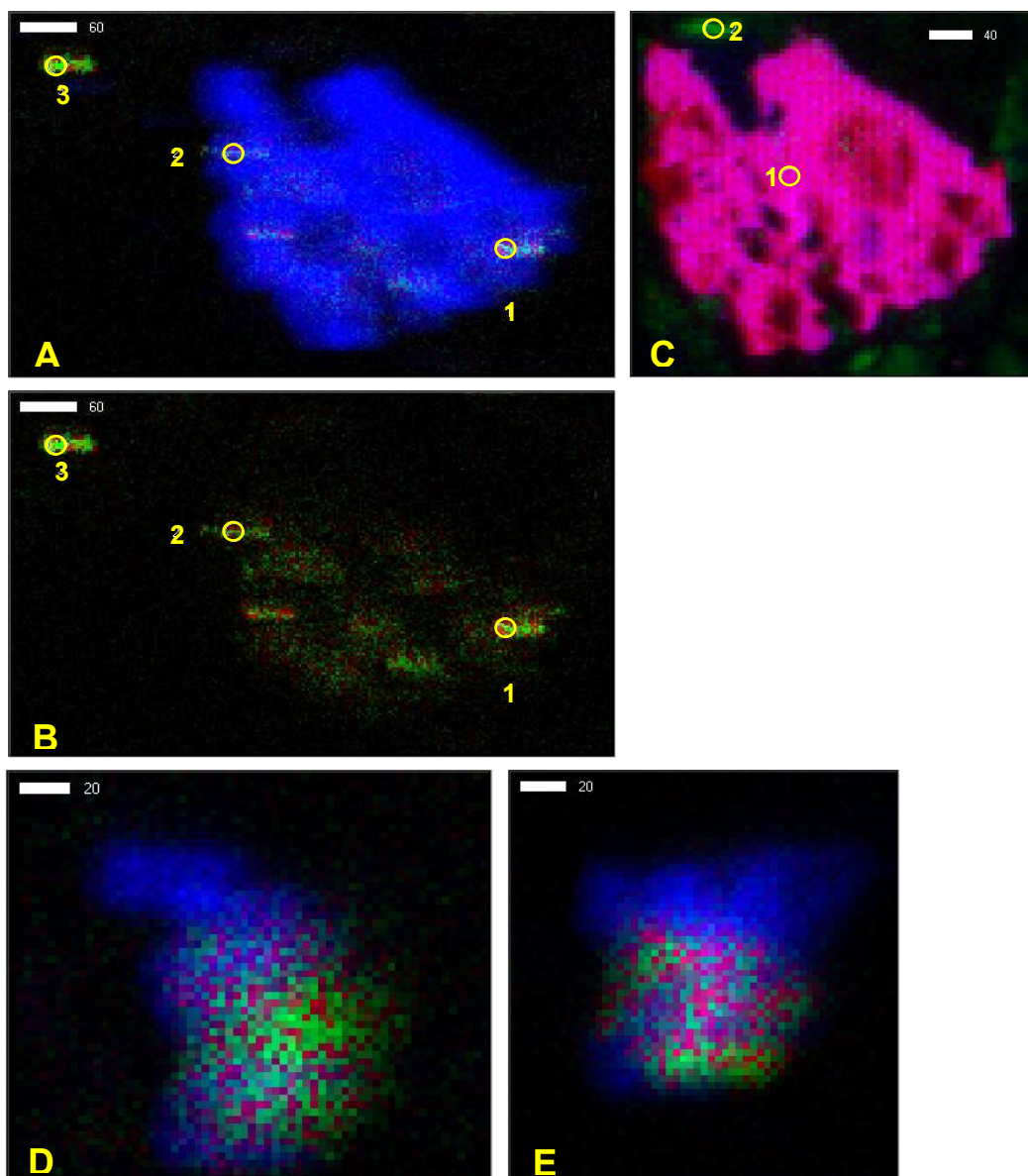


Figure 3.20 X-ray microprobe U oxidation state maps of grains 2A, 2B, and 2C in lactate column sample L1-R1 thin section shown in Figure 3.19. Panel A is a U oxidation state map of grain 2A where iron is shown in blue, U(VI) in green, and U(IV) in red. Panel (B) shows only U(IV) and U(VI). Total counts for small grain in upper left of 2A are 391 for U(IV) and 634 for U(VI). The total counts from the large grain are 5347 for U(IV) and 5962 for U(VI). Panel (C) is an iron  $\mu$ XANES map illustrating distribution of iron sulfide (red), iron oxide (green) and S (blue). These are mirror images of Figure 3.19 and rotated 90° counter clockwise. Points in panel B depict locations of U  $\mu$ -XANES spectra shown in Figure 3.18 (L1-R1 B G2 pt 1, 2, and 3), and in panel C locations of Fe  $\mu$ -XANES spectra shown in Figure 21 (L1-R1 g2 pt 1 and 2). Panels (D) and (E) are U oxidation state maps of smaller grains (2B and 2C) shown in enlarged area of Figure 3.19C, with U(IV) in red, U(VI) in green, and Fe in blue. Total counts are 2151 for U(IV) and 3252 for U(VI) for the area imaged in D, and 5850 for U(IV) and 6918 for U(VI) in E. The U  $\mu$ -XANES spectrum collected at the center of grain 2C is shown in Figure 3.18 (L1-R1 B G2c). Scale bars are in units of microns.

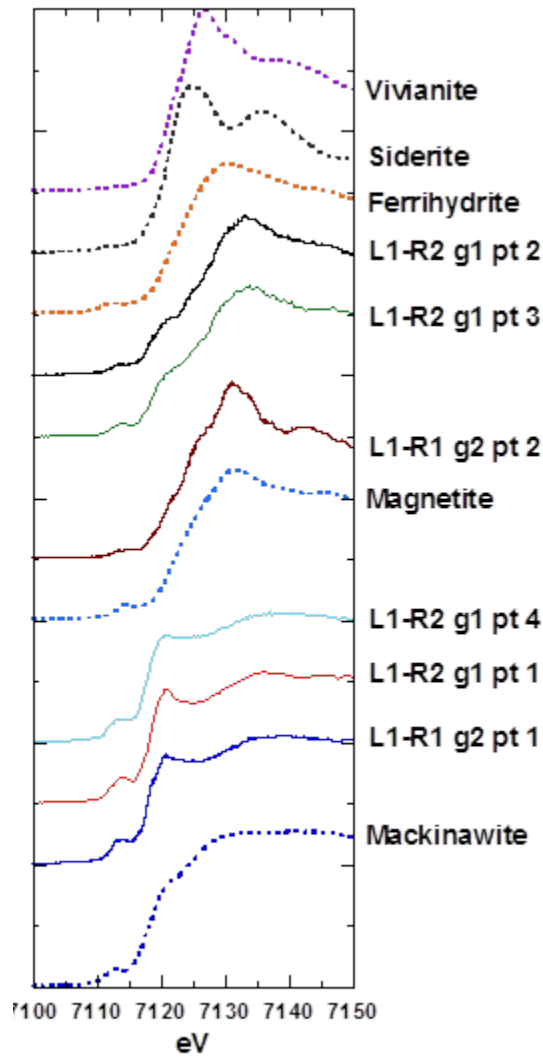


Figure 3.21 Fe XANES spectra of points on ISR column L1 sediment thin sections, and iron model reference mineral spectra. Points are shown in Figures 20C and 23B.

**Figure 3.22** is the 30- $\mu\text{m}$  resolution XRF image of column L1 section R2 thin section showing similar points of elevated U separate from Fe or Ca bearing grains as observed in L1-R1 (**Figure 3.22C** grain 1B), and a large Fe grain with U present on its exterior (**Figure 3.22C** grain 1). The 2- $\mu\text{m}$  resolution U  $\mu\text{XANES}$  oxidation state map of this grain (**Figure 3.23A**) shows that U is located primarily on the edges or surface of this iron grain and within voids or pores. Both U(IV) and U(VI) are intermixed at varying proportions depending on location. U  $\mu\text{XANES}$  at 3 points (**Figure 3.23A**) indicate 82 to 99% of the U is U(IV) (**Table 3.10**; **Figure 3.18**). This grain is mapped as iron sulfide by Fe  $\mu\text{XANES}$  imaging (**Figure 3.23 B**), with a diffuse area of iron oxide coating a large portion of the grain. Note that the brightness of the Fe oxide depicted in this figure is enhanced relative to iron sulfide since the Fe oxide color intensity is scaled to the maximum count rate for this component, which is about 20% of maximum FeS.

The Fe oxide would be barely visible if the maximum was set equal to the FeS maximum. The Fe  $\mu$ XANES spectra for points 1 and 4 (on **Figure 3.23B**) are consistent with spectra for reduced iron phases such as FeS with spectra for points 2 and 3 similar to the ferrihydrite model compound (**Figure 3.21**). XANES spectra of siderite, vivianite, and carbonate green rust are distinctly different than spectra from the samples.

The 2- $\mu$ m resolution U  $\mu$ XANES image of grain 1b (**Figure 3.24B**) maps as predominantly U(VI) with some U(IV) (**Figure 3.18**, L1 R2 T G 1b). In contrast, the fit to the point XANES spectrum collected at the center of this grain is 70% U(IV) and 30% U(VI) (**Figure 3.18**). Additional point XANES spectra would be needed to resolve this. The high concentration U grain in the lower panel of the L1-R2 thin section (**Figure 3.22E** grain 3) was mapped with near equal proportions of U(IV) and U(VI) (**Figure 3.24A**). The point XANES spectrum near the center of this  $\sim$ 120  $\mu$ m grain (L1 R2 B G3) yielded 60% U(IV) and 43% U(VI) (**Table 3.10**; **Figure 3.18**).

The 30- $\mu$ m resolution XRF image (**Figure 3.25B**) of the thin section of sediment from column L2 section Ox1, which was recovered after suboxic elution, also is similar in U distribution to the column L1 thin sections. None of the large Fe grains had significant U concentrations. The high concentration U grains depicted in the enlarged area in **Figure 3.25C** were imaged at 5- $\mu$ m resolution (**Figure 3.26A**), with grain 2B also imaged at 2- $\mu$ m resolution (**Figure 3.26B**). U  $\mu$ XANES indicate 88 and 85% U(IV) at two points on grain 2 (L2-Ox1 B pt 2 and 2b) and 71% U(IV) at grain 1 (L2-Ox1 B pt 1; **Table 3.10**; **Figure 3.18**). These higher resolution maps indicated little Fe associated with these U(IV)-bearing grains.

The 30- $\mu$ m resolution XRF image of the top panel of sediment from column L2 section Ox3 shows a lower abundance of U grains (**Figure 3.27B**) with no apparent U associated with large Fe grains. The higher resolution U  $\mu$ XANES oxidation state map of the high U grain (**Figure 3.28C**) show that this grain (L2-Ox3 T G1) is predominantly U(IV) consistent with U  $\mu$ XANES spectrum at the highest U concentration point within the grain that shows 88% U(IV) (**Table 3.10**, **Figure 3.18**). The bottom panel (**Figure 3.29B**) of the L2-Ox3 thin section also shows a lower U abundance than L2-Ox1 in the 30- $\mu$ m resolution XRF image. A 2- $\mu$ m resolution U  $\mu$ XANES image of the grain (L2-Ox3 B G1) circled in **Figure 3.29C** was predominantly U(IV) that was both intermixed with and in separate zones from Fe (**Figure 3.30**). The U  $\mu$ XANES spectrum at the highest U concentration point in the upper part of the grain yielded 81% U(IV) (**Table 3.10**; **Figure 3.18**).

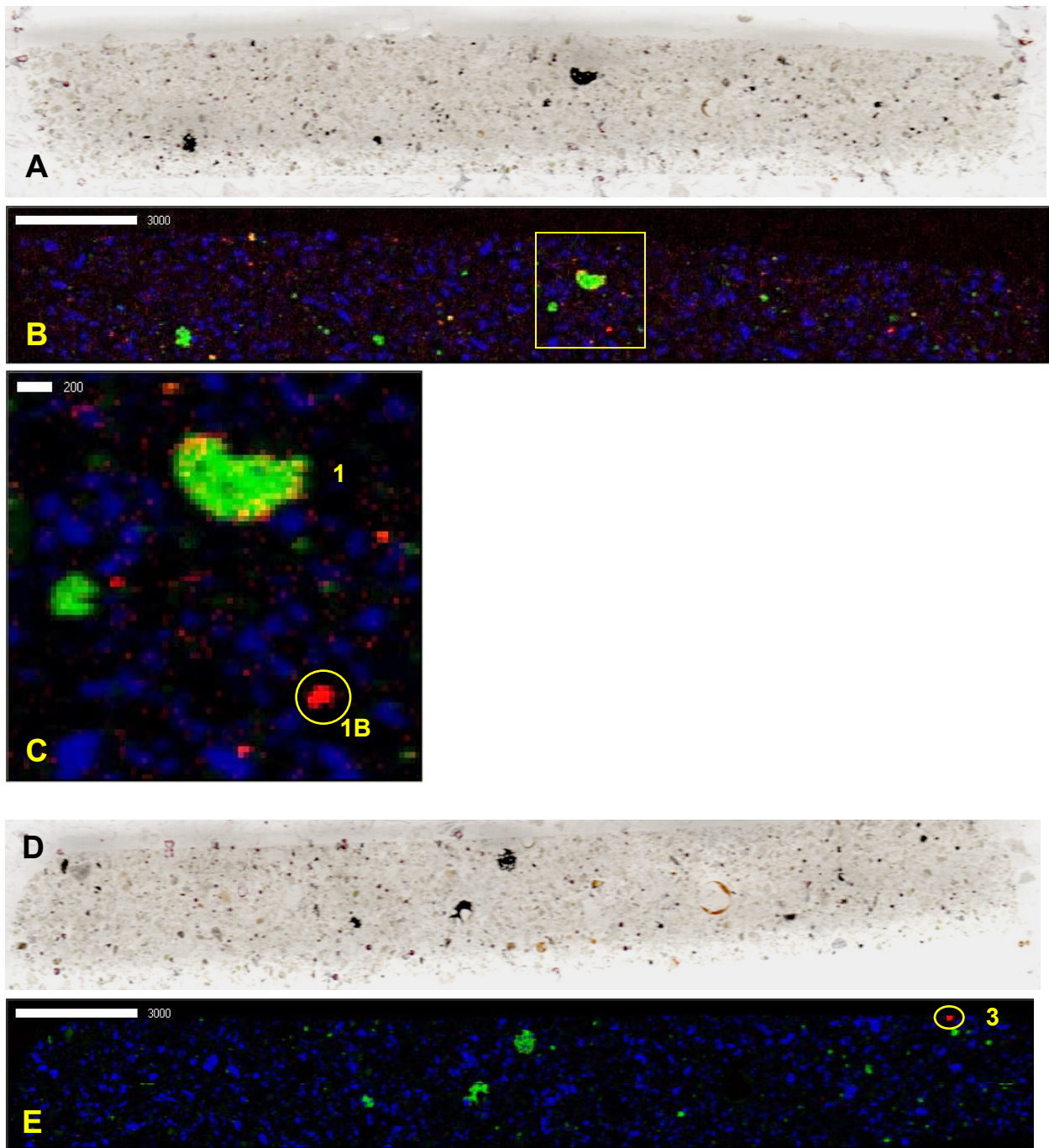


Figure 3.22 Column L1-R2 top panel of thin section: (A) Optical scan and (B) meso-scale XRF tri-color map with U shown in red, Fe in green, and Ca in blue. Area of interest is bounded by yellow and is enlarged in C. Bottom panel of thin section L1-R2: (D) optical scan, and (E) meso-scale XRF tri-color map of whole thin section panel with U shown in red, Fe in green, and Ca in blue. Area of interest (grain 3) is bounded by yellow. Scale bars are in units of microns.

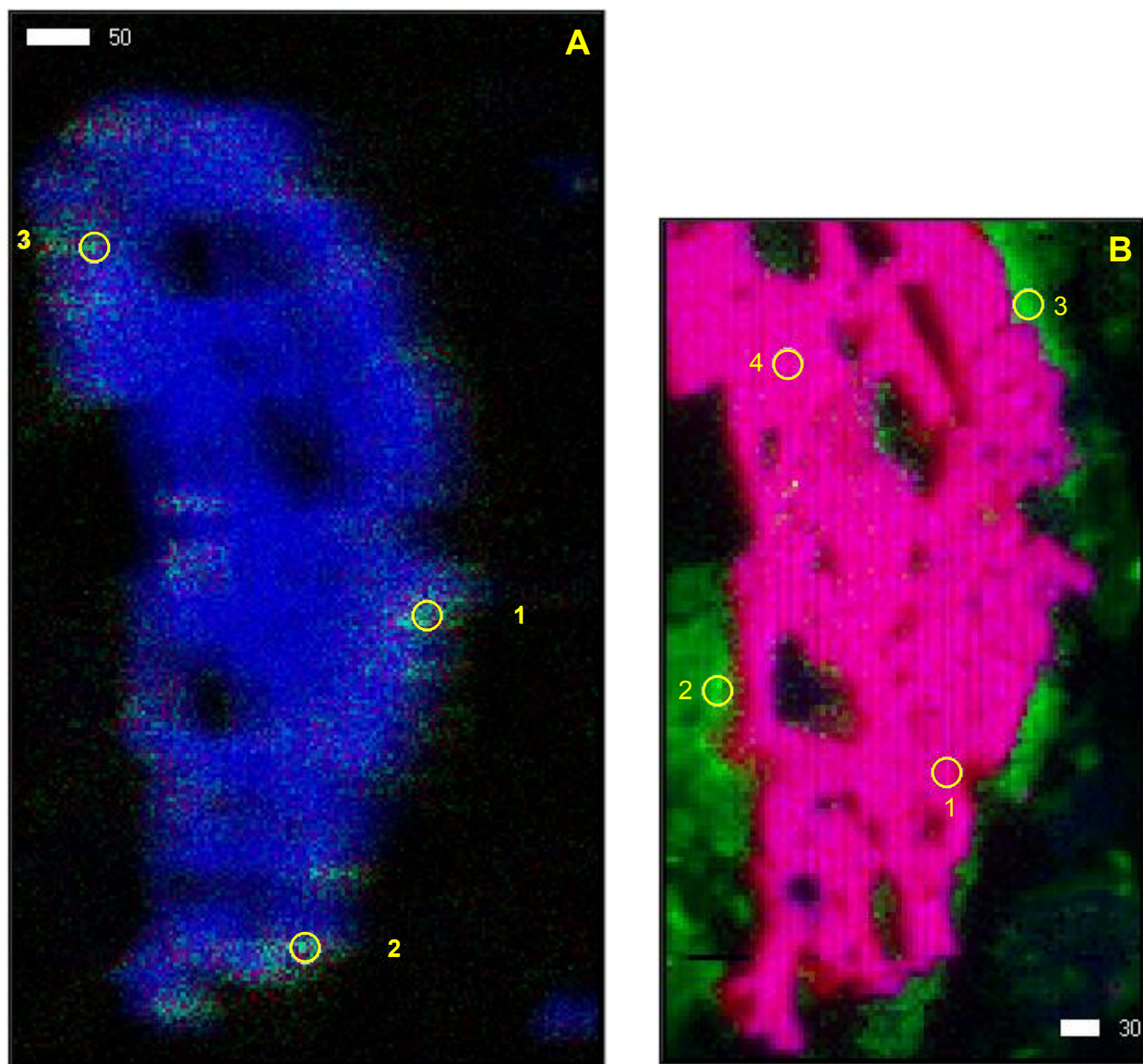


Figure 3.23 X-ray microprobe maps of thin section L1-R2 top panel, grain 1 of crescent shaped iron grain shown in Figure 3.22C, but rotated 90 counter clockwise, and mirror image. (A) is tricolor U oxidation state map U(IV) shown in red, U(VI) in green, and Fe in blue. Total counts in image area 12209 for U(IV) and 16374 for U(VI). (B) is iron phase map with iron sulfide shown in red, ferrihydrite (iron oxide) in green, and sulfur in blue. Sulfur and iron sulfide map together as purple. Points in A depict locations of U  $\mu$ -XANES spectra shown in Figure 3.18 (L1-R2 T G1 pt 1, 2, and 3), and in B locations of Fe  $\mu$ -XANES spectra shown in Figure 3.21 (L1-R2 T g1 pt 1, 2, 3, and 4). Scale bars are in units of microns.

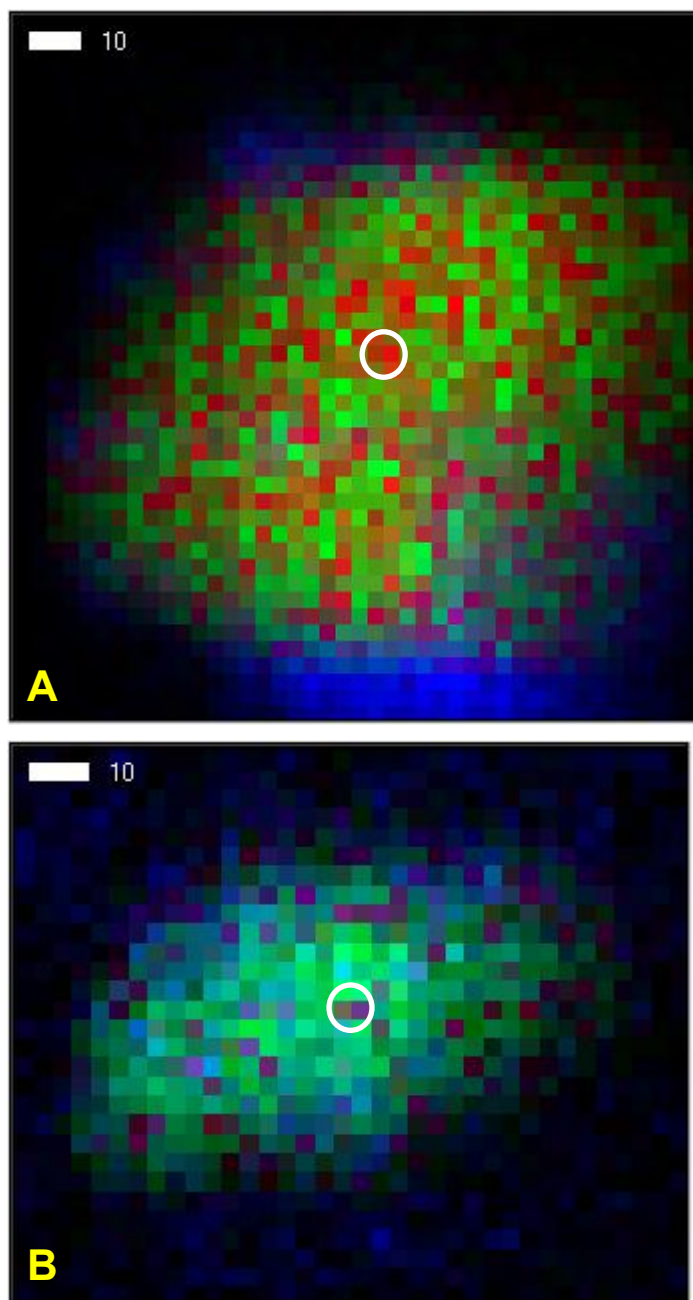


Figure 3.24 (A) X-ray microprobe U oxidation state map of L1-R2 bottom panel grain 3 in Figure 3.22E with U(IV) shown in red, U(VI) in green, and Fe in blue. Circle denotes the location of U  $\mu$ XANES spectrum L1-R2 B G3 shown in Figure 3.18. Total counts in imaged area are 21746 for U(IV) and 28354 for U(VI). (B) U oxidation state map of L1-R2 top grain 1B on Figure 3.22C with U(IV) in red, U(VI) in green, and Fe in blue. Circle denotes the location of the U  $\mu$ XANES spectrum L1-R2 T G1b. Total counts in imaged area are 694 for U(IV) and 3748 for U(VI). Scale bars are in units of microns.

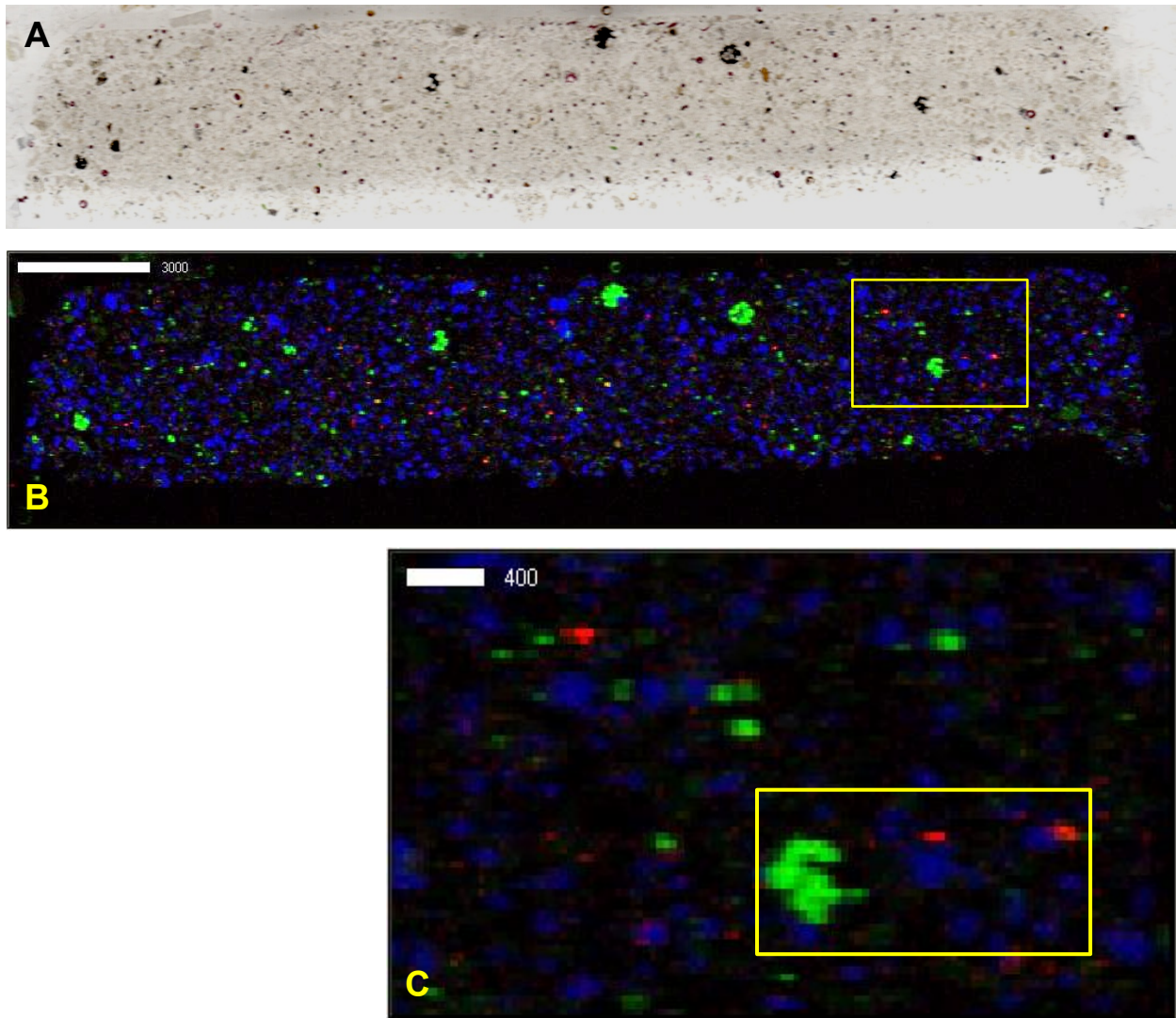


Figure 3.25 Column L2-Ox1 bottom panel of thin section: (A) Optical scan, and (B) meso-scale XRF tri-color map of whole thin section panel with U shown in red, Fe in green, and Ca in blue. (C) shows area of interest for BL 2-3 microprobe mapping bounded by yellow in B. Scale bars are in units of microns.

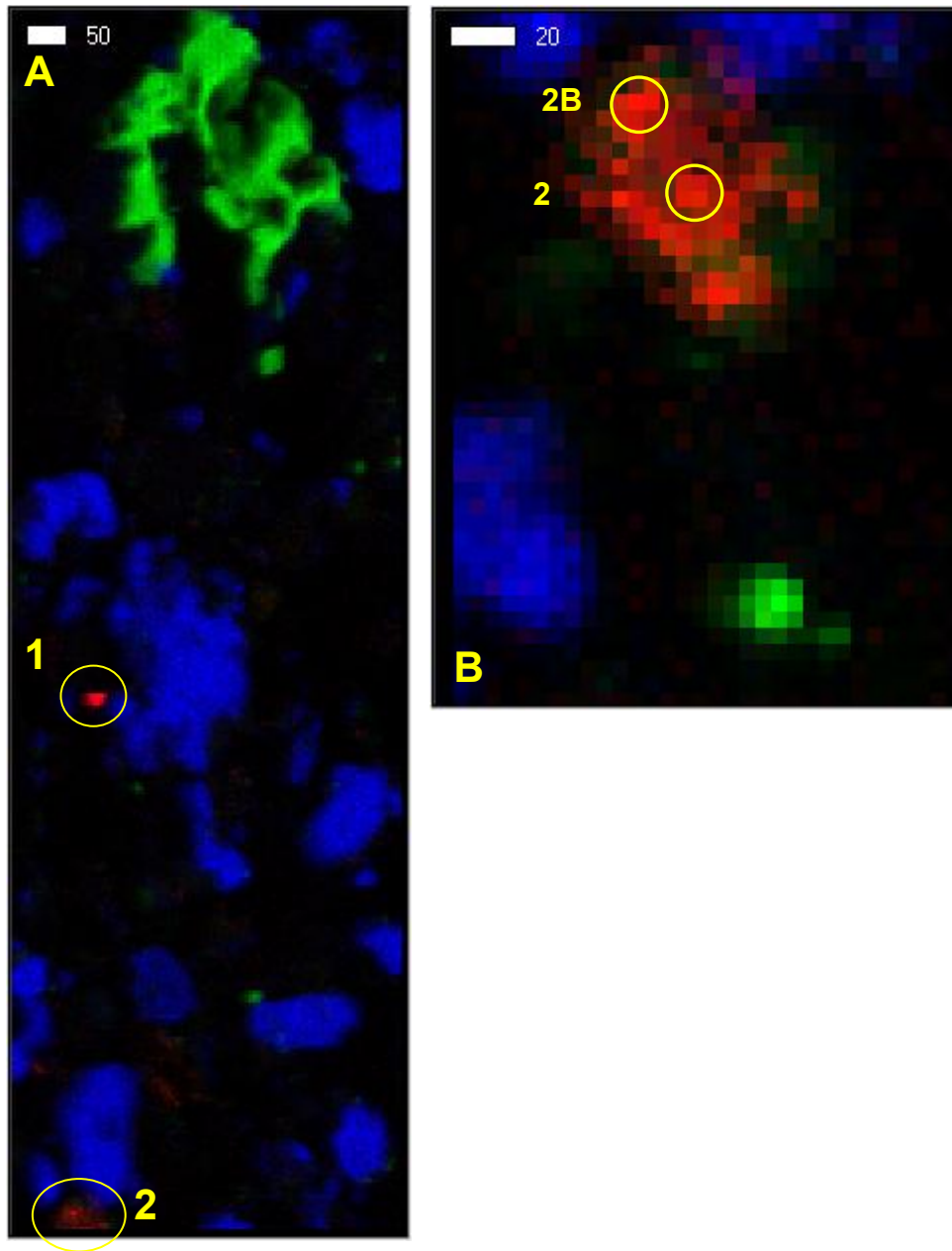


Figure 3.26 (A) X-ray microprobe XRF map of region thin section L2-Ox1 shown in yellow rectangle in Figure 3.25C. Fe is in green, U red and Ca blue. Color brightness increases with concentration. Images are mirror of Figure 3.25 and rotated 90° counter clockwise. Grains 1 and 2 are bounded by yellow ovals. (B) Detailed XRF map of grain 2 at 5 x 5  $\mu\text{m}$  resolution. U  $\mu\text{XANES}$  locations are bounded by yellow circles. U  $\mu\text{XANES}$  spectra for these points are shown in Figure 3.18 and denoted L2-Ox1 B G1 pt 1 for grain 1 in A, and L2-Ox1 B pt 2 and 2b in B. Scale bars are in units of microns.

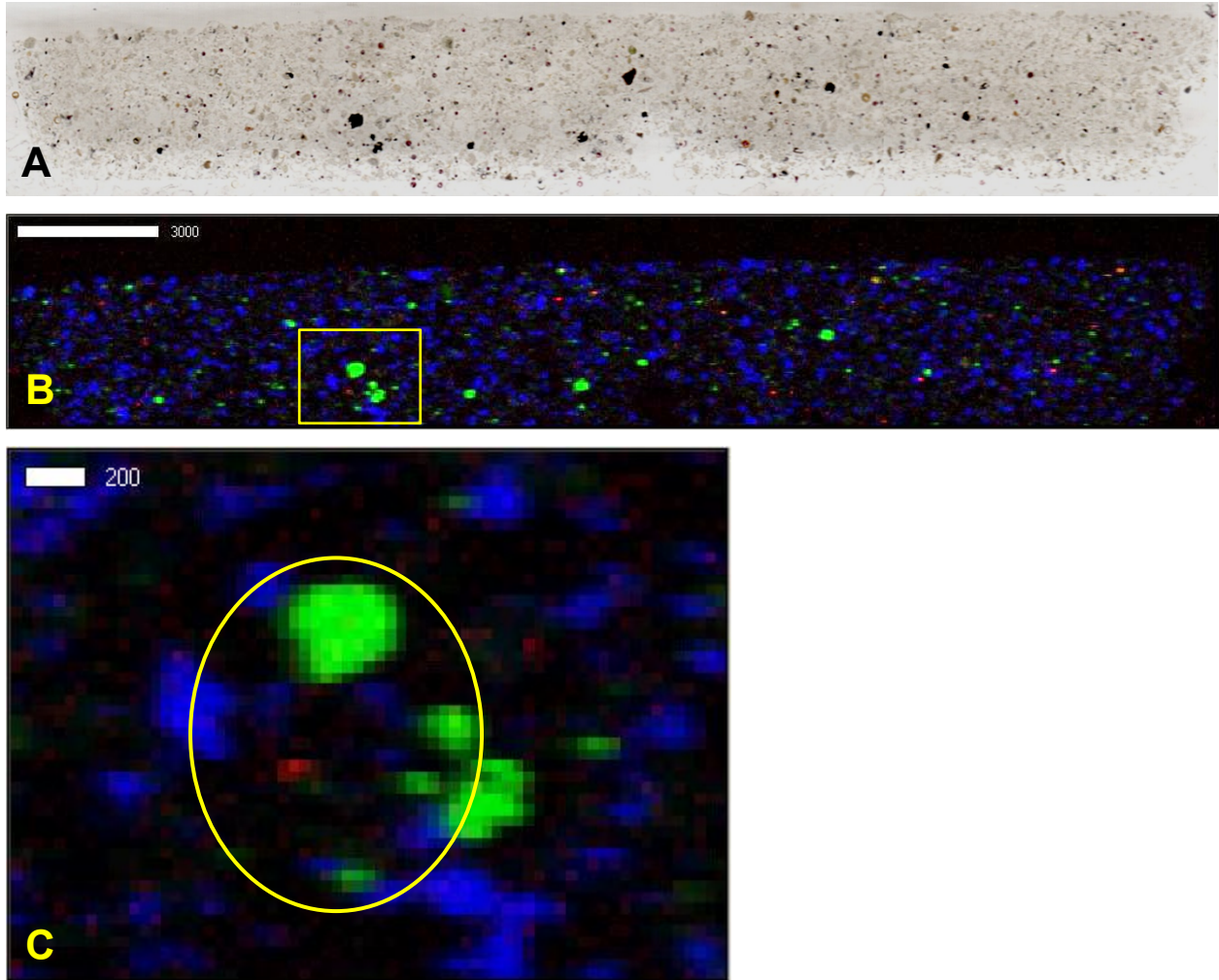


Figure 3.27 Column L2-Ox3 top panel of thin section: (A) Optical scan; (B) meso-scale XRF tricolor map of whole thin section panel with U shown in red, Fe in green, and Ca in blue. (C) is an enlargement of the area of interest for X-ray microprobe mapping bounded by yellow in B. Scale bars are in units of microns.

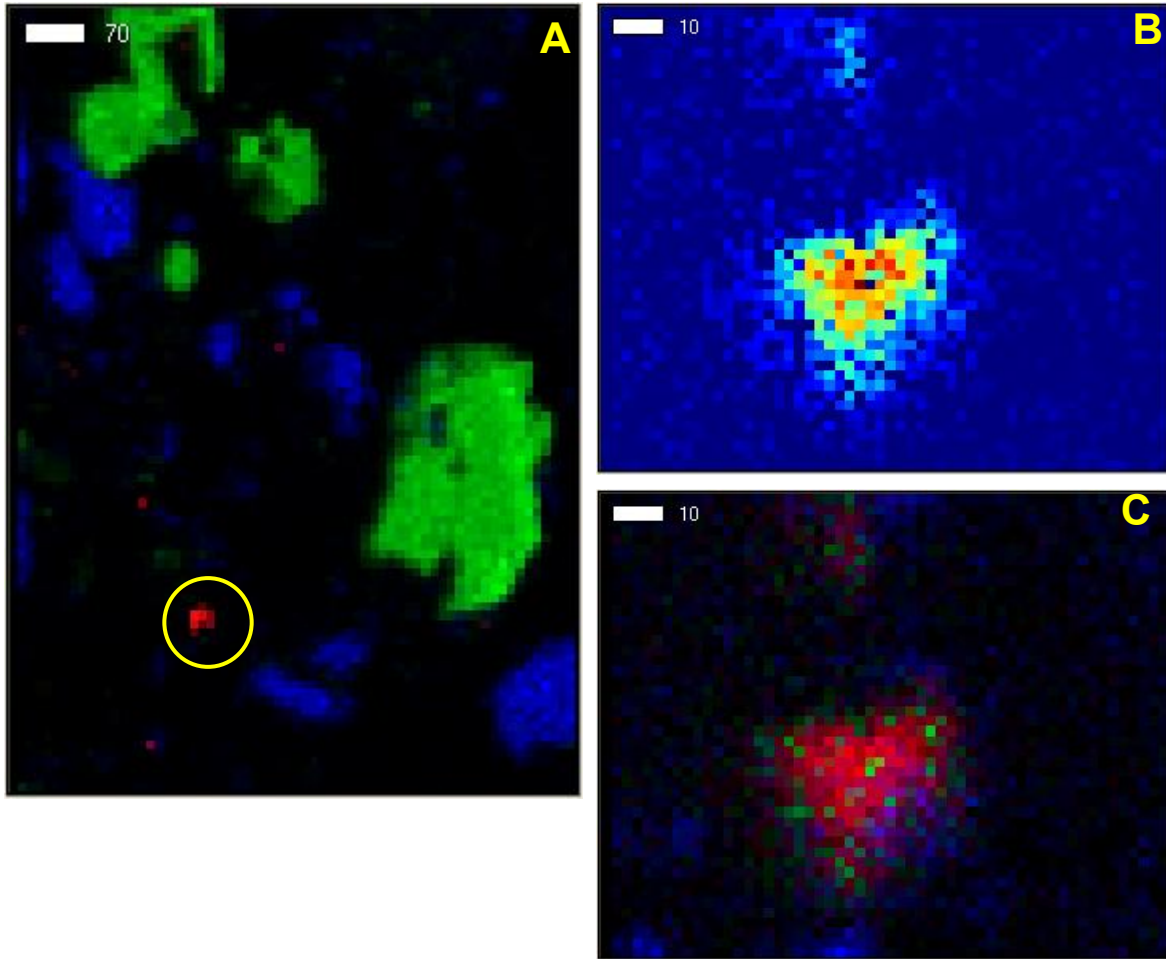


Figure 3.28 A) X-ray microprobe XRF map at 5 x 5 um resolution map of the area within yellow oval in Figure 3.27C thin section L2-Ox3 top, where U is shown in red, Fe in green, and Ca in blue. The map is a mirror image and rotated 90° counter clockwise of the area in Figure 3.27. (B) 2 x 2 um resolution map of the high U grain circled in A showing U(IV) distribution in high area concentration increasing with color warmth (blue to red). (C) is U oxidation state of the same area in B, where U(IV) is in red, U(VI) in green, and Ca in blue. Fe was not shown because of very low concentration relative to U(IV). U  $\mu$ -XANES spectrum was collected at center of highest U area of the grain and shown in Figure 3.18 (L2-Ox3 T G1 pt1). Total counts in imaged area are 2570 for U(IV) and 1049 for U(VI). Scale bars are in units of microns.

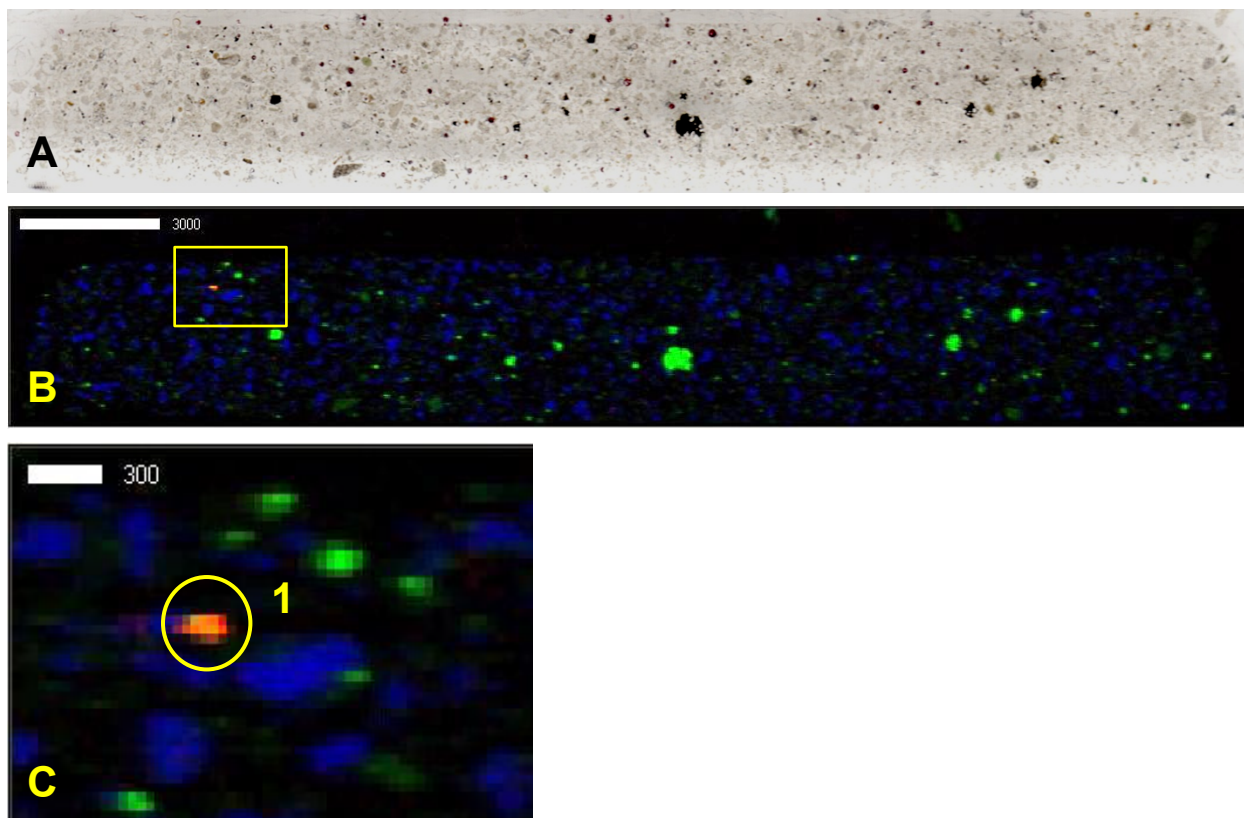


Figure 3.29 Column L2-Ox3 bottom panel of thin section: (A) Optical scan; (B) BL10-2 meso-scale XRF tri-color map of whole thin section panel with U shown in red, Fe in green, and Ca in blue. Area of interest for higher resolution  $\mu$ XANES imaging bounded by yellow is enlarged in C. Scale bars are in units of microns.

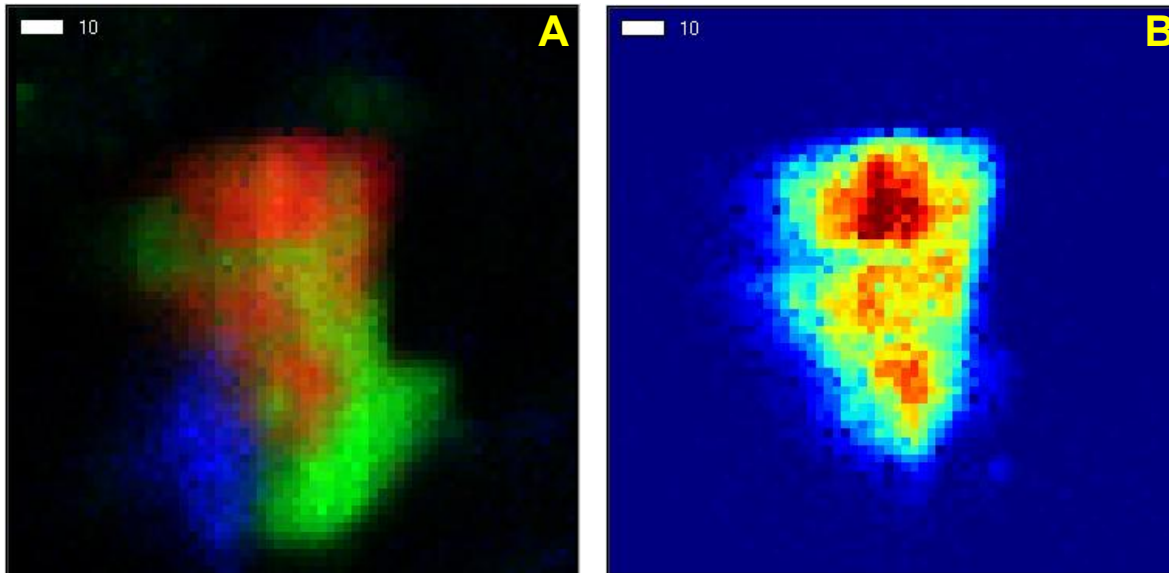


Figure 3.30 X-ray microprobe U oxidation state maps of L2-Ox3 bottom panel grain 1, the circled grain in Figure 3.29C. (A) U oxidation state at 2 x 2  $\mu\text{m}$  resolution where U(IV) in red, iron is shown in green and Ca in blue. U(VI) is not shown because of very low concentration relative to U(IV). (B) U(IV) distribution of the same grain where concentration increases with color warmth blue to red. U  $\mu$ -XANES spectrum was collected at center of highest U area in top part of the grain and is shown in Figure 3.18 (L2-Ox3 B G1 pt1). Total counts in XANES mapped area are 50078 for U(IV) and 2339 for U(VI).

Visual inspection of meso and microprobe XRF maps suggests that U is distributed widely over sediments in the thin sections, primarily on smaller grains ( $<100 \mu\text{m}$ ), with U often in particles of only a few pixels in size (e.g see Figures 3.17B, 3.19, 3.25, 3.26 and 3.27). Integrating U counts over the whole sample area indicates higher U contents of post-biostimulated reduction and post-suboxic elution column sediments than pre-column sediment that parallels the trend in total concentration. This observation suggests that biostimulated reduction results in distribution of U over many sediment grains instead of being concentrated in localized zones. The finer grains appeared to have much lower Fe content than large grains (see below). U  $\mu$ XANES spectra show that a majority of U is U(IV) with a slightly greater component of U(IV) in the post-suboxic elution samples (Table 3.10). The point U  $\mu$ XANES measurements for small grains measured in column L1 thin sections ranged from 60 to 99% U(IV) (average 74%) and L2 ranged from 71 to 88% U(IV) (average 83%). By comparison bulk XANES of column L1 and L2 samples averaged 97 and 89% U(IV), respectively, suggesting some oxidation may have occurred in the thin sections during sample processing and fabrication. In addition, only a limited number of these finer particles with sufficient zones of high U were located in the  $\mu$ XRF maps to allow for  $\mu$ XANES data collection. All of the grains analyzed had U distributed throughout the particles. It is unclear if the U in particles measured was in the sediment prior to biostimulation or precipitated during the column experiment. Coatings of U(IV) that may have formed on the finer grain sediments or as discrete particles during the column experiment were not observed in either the 2 or 30  $\mu\text{m}$  spatial resolution XRF

maps. Instead, data collection focused on higher concentration U areas, likely biasing measurements towards larger grain size fractions.

The sediment also contains some larger particles (>250  $\mu\text{m}$ ) that included grains comprised predominantly of iron sulfide minerals, some of which contain measurable U, either as coatings or within pores (see **Figures 3.19, 3.20, 3.22 and 3.23**). To test the contribution of the large iron grains to total U in a sample, the integrated total U, Ca, Fe counts in meso-probe XRF maps of the entire sample area of each thin section were compared with the integrated counts within 4 largest iron grains in each thin section. These grains ranged from 0.32 to 1.2 mm diameter and averaged 0.6 mm for 36 grains among nine thin section panels, and include grains L1-R1 B 2A (**Figures 3.19 and 3.20**), and L1-R2 T G1 (**Figures 3.22 and 3.23**). These large iron grains comprise 1.3% of the area of all thin sections but accounted for 12.5% of the Fe. In contrast, they accounted for only 1.8% of the total U counts indicating only a slight enrichment relative to the whole sample. Little difference was observed in this trend among the pre-column, post-reduction (L1) and post-suboxic elution sediments suggesting that the U present in these large grains is not preferentially precipitated or sorbed onto these large iron sulfide mineral grains during the biostimulated reduction, but that it is instead likely part of the U remaining after the ISR extraction. The U in the two large Fe grains measured ranged from 57 to 91% U(IV) (average 76%; Table 3.10), indicating a lower U(IV) component than measured in bulk samples, which may reflect either incomplete oxidation and leaching by the ISR process, or oxidation during thin section fabrication. No attempt was made to isolate sufficient mass of these large grains from the pre-column sediment for XANES data collection. Grain size separations and measurement of U content by gamma spectrometry indicate that >250  $\mu\text{m}$  fraction comprised 6% of mass of bulk sediment and contained 5% of total U in the pre-column sediment. The U distribution among grain size fractions was not measured after biostimulated reduction because of insufficient sample. Comparison of the integrated counts in coarse grains in pre- and post-column sediment thin section XRF maps suggest there was little change in U mass distribution during biostimulated reduction, and therefore do not contribute significantly to the total U measured by bulk XAS. Based on these observations, it is concluded that U in large iron grains likely is remnant uranium after ISR extraction of the ore body.

### 3.3.5 Microbial Assay

Biomass was very low in all ten aquifer sediment samples, which were recovered by drilling into the leached out ore bearing zone of the Kingsville ISR site. Because only sample 3712 B-C 580-590 was retrieved as an intact core, and subsequently used for batch and column experiments, results for this material are presented.

PCR products could not be obtained from this sample from the 30 cycle bacterial 16S rRNA gene in order to generate TRFLP profiles. However, the qPCR 40 cycle assays have higher sensitivity, and sulfate reducing bacteria (SRB) were detected by this method in all core samples. *Geobacter* was not detected in any of this core sample by qPCR. Cloning of the *dsrB* gene PCR product revealed a high diversity of SRB at this site despite the low biomass, and representatives were from most families of SRB, but dominated by *Desulfobulbaceae* and *Desulfobacteraceae*. Closest sequences in the database tended to be uncultured organisms from contaminated environments such as oil field, petroleum contaminated sediment, aquifers

impacted by landfill leachate, and a uranium mill tailings site, as well as estuarine and deep sea sediments (Table 3.11). Tentative genus identifications based on closest similarity to named organisms are *Desulfotomaculum*, *Desulfosalina*, *Desulfofustis*, *Desulfobulbus*, *Desulfatibacillum*, *Syntrophobacteriaceae*, *Desulfosarcina*, *Desulfobacter*, and *Desulfonema*.

Biomass was very low in the batch experiments sediments, even after amendment with electron donors for the 60 day duration of the experiment. As a result, no data were obtained from the H<sub>2</sub> or acetate treatments. However, the lactate amended sample did contain *Geobacter* and SRB at low concentrations, 1.47 x 10<sup>3</sup> gene copies /gm SRB, and 2.6 x 10<sup>2</sup> gene copies/gm *Geobacter*. As this is the only Kingsville Dome sample with *Geobacter* detected, *Geobacter* endpoint PCR was performed and followed by cloning and sequencing. *Geobacteraceae* sequences detected were most closely related to subsurface clade 1 of *Geobacteraceae*, as well as *Pelobacter propionicus* (Table 3.12).

Biomass also was too low in column sediments to provide sufficient DNA in extractions for microbial assay. Because of the small column size only 0.5 – 1 g of sediment was available for extraction. However, bacterial amplifications were obtained for TRFLP fingerprinting in the 2 effluent filter samples, though not in the sediment column samples. Only faint amplification occurred with the column sediment DNA extractions, which were not sufficient for fingerprinting. One of these filters was taken during the Fe(III) reduction stage before sulfate reduction, as indicated by high dissolved iron and no measureable sulfide in effluent (days 40 to 60). The other was taken after onset of sulfate reduction evidenced by measurable effluent sulfide (days 60 to 74). The TRFLP fingerprints were very simple with 2 main peaks, but the proportion of each peak is different in the samples. Bacterial 16S rRNA gene clone libraries were constructed for these 2 samples, and showed that during the Fe reduction phase, the dominant organism was *Rhizobium sp.*, representing 76% of the sequences. Several sequences from the *Clostridiales*, including one most closely related to *Desulfotomaculum acetoxidans*, represented 17% of the clone library, with several other minor groups (Table 3.13a).

Results for qPCR detected *Geobacter* only in the first effluent filter collected at the end of the Fe reduction phase, but with a low abundance of 5 x 10<sup>3</sup> copies contained on the filter (Table 3.13). SRB also were detected at very low concentration also in this filter with 8.9 x 10<sup>2</sup> copies contained on the filter. Community shifts are evident in the second effluent filter collected after the onset of sulfate reduction. *Rhizobium sp.* GN33-3 is still dominant, but the other *Rhizobium* (sp. 49) is now a minor part of the community. A *Synrhizobium* has increased and represents 22% of the clone library. Known sulfate reducers have become more abundant, with the sequence most closely related to *Desulfotomaculum* which only represented 2.4% of the sequences during Fe(III) reduction, now representing 12.2%. Also, a *Desulfosporosinus sp.* which was not detected in the first clone library now represents 7.3% of the clone library (Table 3.13b). Results for qPCR detected *Geobacter* only in the filter taken during the Fe reduction phase, and the abundance was low, with 5 x 10<sup>3</sup> copies contained on the filter. SRB were detected at very low concentrations also in the Fe(III) reduction phase filter with 8.9 x 10<sup>2</sup> copies contained on the filter.

Sulfate reducers appear to be numerically dominant at Kingsville dome relative to *Geobacter*, and the diversity of SRB is high at Kingsville dome compared to Rifle, CO samples. Perhaps *Geobacter* are more sensitive to the ISR process (introduction of large quantities of

oxygen to the ore zone) that this sample set had undergone, relative to SRB. If so, the remediation post ISR may rely more heavily on SRB than at a uranium mill tailings site. It is also possible that sulfate reduction is the more dominant terminal electron accepting process here for another reason. The *Geobacteraceae* types that were detected in the lactate treated microcosm, were dominated by the subsurface clade 1 that Holmes et al. (2007) found to be important in many subsurface environments. Sequences very closely related to *Pelobacter propionicus* in the *D. acetoxidans* clade were also abundant, though not as dominant as the subsurface clade1. This suggest that although *Geobacter* may be impacted by ISR processes or otherwise is less competitive with sulfate reducers, the *Geobacteraceae* that are there are consistent with those expected to have the ability to reduce U(VI). Although the total biomass is low in the Kingsville Dome samples, the diversity of sulfate reducers along with their numerical dominance over *Geobacter* imply that these organisms are important “microbial players” at the Kingsville dome site.

The column experiment had too low biomass to characterize bacteria in the small mass of sediment available, but it was possible to characterize the bacteria from the filters taken at 2 time points, at the end of Fe(III) reduction during the decline of effluent dissolved Fe, and after the onset of sulfate reduction. The dominant organisms were in the nitrogen fixing genus *Rhizobium* in both cases, but there is evidence of community shift favoring sulfate reducers consistent with the onset of sulfate reduction, as the sequence close to the sulfate reducing member of the family *Clostridiales*, *Desulfotomaculum acetoxidans*, increases in proportion, and a sequence close to the sulfate reducing *Desulfosporosinus* is also detected. *Desulfosporosinus* is known to be capable of reducing U(VI) (Suzuki et al. 2004). Members of the *Clostridiales* are also evident in both samples and the second most dominant group after *Rhizobium*.

It is not surprising that *Geobacter* qPCR abundances were higher than SRB abundance in the effluent filter sample taken during Fe(III) reduction, and not detectable in the filter taken after the onset of sulfate reduction; however, it is surprising that given this result, that the clone library during Fe(III) reduction did contain SRB but no *Geobacteraceae*. Although only one SRB sequence in the Fe(III) reduction filter was detected, it is possible that if more clones had been sequenced, a *Geobacteraceae* may have been detected, better reflecting its importance at that time during the experiment.

Table 3.11 Microbial assay of Kingsville Dome ISR pre-column sediment sample 3712 BC 580-59 showing microbial phylotypes, relative abundance, and closest BLAST hits.

Group #	Clones	#	Relative Abundance %	Closest Blast Hit	% Identity	Source	Tentative Identity
1	D06	1	1.3	<a href="#">AY337048.1</a>	76	continental margin sediment	
2	E11	1	1.3	<a href="#">FJ748851.1</a>	84	estuarine sediment	
3	B07,C04	2	2.6	<a href="#">EF065047.1</a>	89	landfill leachate groundwater	Desulfosarcina
4	G08,H03,F07	3	3.9	<a href="#">AY337204.1</a>	94	continental margin sediment	Desulfosarcina
5	A11,A12,A05,	3	3.9	<a href="#">FM212324.1</a>	91	petroleum contaminated sediment	Desulfobacter
6	C11,A09,H06,H10,F10,D03,G01,G02,D08,F02,H11,F09	12	15.6	<a href="#">CP001147.1</a>	77	Thermodesulfovibrio	Thermodesulfovibrio
7	A08,D04	2	2.6	<a href="#">GU127914.1</a>	80	Peatland	Thermodesulfovibrio
8	A07,H07,E12	3	3.9	<a href="#">AY953397.1</a>	84	mudflat estuary	Desulfobulbus
9	D02,G06,A03,F04	4	5.2	<a href="#">EF065071.1</a>	80	landfill leachate groundwater	Desulfotomaculum
10	G05,E10,C01,A04,D09,C10	6	7.8	<a href="#">HQ690093.1</a>	90	Old Rifle aquifer	Desulfobulbus
11	D07,B05,B08,B04,B09,C08,C06,C07	8	10.4	<a href="#">HQ690093.1</a>	89	Old Rifle aquifer	Desulfobulbus
12	B02,B10	2	2.6	<a href="#">AY953400.1</a>	94	mudflat estuary	Desulfobulbus
13	C02,B03,B06	3	3.9	<a href="#">AY953397.1</a>	84	mudflat estuary	Desulfobulbus
14	E08,E04,E07,H08,E01,F03,C09,	7	9.1	<a href="#">AY741574.1</a>	85	estuary sediment	Desulfobulbus
15	A10	1	1.3	<a href="#">DQ250779.1</a>	84	landfill leachate groundwater	Desulfosalina
16	C05	1	1.3	<a href="#">AF244995.1</a>	82	oligochaete worm symbiont	Desulfatibacillum
17	A02	1	1.3	<a href="#">AB263169.1</a>	84	deep sea sediment	Moorella
18	D05	1	1.3	<a href="#">EF065047.1</a>	87	landfill leachate	Desulfosarcina

19	F05,E09,G09,G03,F01	5	6.5	<a href="#">AF360646.1</a>	93	groundwater	Desulfosarcina
20	B12,A06,E03,D11	4	5.2	<a href="#">FR689594.1</a>	89	desulfosarcina	Desulfosarcina
21	C03	1	1.3	<a href="#">AB263171.1</a>	92	steel corrosion	Desulfohalobium
22	C12	1	1.3	<a href="#">FR689565.1</a>	92	deep sea sediment	Desulfarculus
23	F11,H09,F08	3	3.9	<a href="#">CP002364.1</a>	87	steel corrosion	Desulfobulbus
24	D12	1	1.3	<a href="#">FR689554.1</a>	78	propionicus	Desulfobacterium
25	E02	1	1.3	<a href="#">EU725482.1</a>	94	steel corrosion	Desulfotomaculum
						anaerobic granular sludge bed	

Table 3.12 Geobacter clones from sediments recovered at the end of the lactate amendment batch uranium uptake experiment using the 3712 BC580-590 sediment.

Phylotype #	Relative Abundance (%)	Closest Genbank relative (Blast)	Blast source description	Sequence similarity %
1	12.5	HQ875511	Geobacter from paddy soil	95
2	12.5	<a href="#">EF668602.1</a>	Riflegeoclone 24	100
3	25.0	<a href="#">X70954.1</a>	Pelobacter propionicus	99
4	43.8	<a href="#">CP002479.1</a>	Geobacter M18	100
5	6.3	<a href="#">EF668503.1</a>	uncultured Geobacter M16clone	89

Table 3.13A Sequences obtained from effluent filter collected during later stages of Fe(III) reduction.

Phylotype #	Relative abundance (%)	Closest Genbank relative (Blast)	Blast source description	Sequence similarity (%)	Tentative Identity
1	45.2	<a href="#">GU994887.1</a>	uranium contaminated groundwater	100	Rhizobium sp. GN33-3
2	31.0	<a href="#">HQ652582.1</a>	magnetite drainage sample	100	Rhizobium sp. 49(2011)
3	7.1	<a href="#">HQ133178.1</a>	hexadecane degrading methanogenic consortium	98	Sedimentibacter sp. (Clostridiales)
4	7.1	<a href="#">FJ938130.1</a>	agricultueal compost waste	94	Clostridia
5	2.4	<a href="#">CP001720.1</a>	Desulfotomaculum acetoxidans	95	Desulfotomaculum (Closridia)
6	2.4	<a href="#">EU331405.1</a>	Anaeromyxobacter dehalogens	99	Anaeromyxobacter dehalogens
7	2.4	<a href="#">JN247803.1</a>	Pseudoxanthomonas sp.	98	Pseudoxanthomonas sp.
8	2.4	<a href="#">HM057106.1</a>	Pseudomonas sp.Y3-3	92	Pseudomonas sp.Y3-3

**Table 3.13B Sequences obtained from effluent filter collected during onset of sulfate reduction.**

Phylotype #	Relative abundance (%)	Closest Genbank relative (Blast)	Blast source description	Sequence similarity (%)	Tentative Identity
1	48.8	<a href="#">GU994887.1</a>	uranium contaminated groundwater	100	Rhizobium sp. GN33-3
2	22.0	<a href="#">AM084031.1</a>	Synorhizobium sp.	100	Synorhizobium sp.
3	2.4	<a href="#">HQ652582.1</a>	magnetite drainage sample	98	Rhizobium sp. 49(2011)
4	7.3	<a href="#">NR_042202.1</a>	Desulfosporosinus lacus STP12	99	Desulfosporosinus lacus STP12
5	2.4	<a href="#">FN689722.1</a>	Sporotalea propionica	99	Sporotalea propionica
6	12.2	<a href="#">CP001720.1</a>	Desulfotomaculum acetoxidans	95	Desulfotomaculum (Clostridia)
7	2.4	<a href="#">HQ133178.1</a>	hexadecane degrading methanogenic consortium	98	Sedimentibacter sp. (Clostridiales)
8	2.4	<a href="#">HQ384240.1</a>	Acetobacterium wieringae	99	Acetobacterium wieringae

### 3.4 Discussion of Experimental Findings

#### 3.4.1 Biogeochemical Processes During Biostimulation

The integrated column effluent concentrations for lactate, acetate, total dissolved CO<sub>2</sub>, sulfate, sulfide, iron, and uranium combined with “whole-column” changes in content of iron, S, and uranium (**Table 3.5**) are used in this section to provide insight on the biogeochemical processes occurring during the biostimulated reduction stage of the column experiments. Some of these processes are incorporated into model simulation of biostimulated reduction presented in Section 4.0, specifically sulfate, iron and uranium reduction.

Complete consumption of lactate was occurring by day 18, with concurrent appearance of acetate in the effluent reaching a steady state concentration between 14 and 55 days of 3 to 3.5 mM. Lactate consumption, presumably by oxidation to acetate, and subsequent oxidation of acetate by microbial processes requires equivalent reduction of other constituents to balance electron transfer from these electron donors. Likely terminal electron accepting processes (TEAP) under anaerobic conditions in aquifer sediments are sulfate, iron, manganese, and uranium reduction. An electron balance for electron donors (lactate and acetate oxidation) and TEAPs was constructed using the integrated column effluent data and solid phase analyses (**Table 3.14**). Oxidation of lactate to acetate produces 4 electrons per lactate molecule oxidized. Subsequent oxidation of acetate to CO<sub>2</sub> produces 8 electrons, but could result in formation of formate as an intermediate step (Sharp et al, 2011), although no formate was detected during HPLC analysis of column effluent for lactate and acetate. Reduction of sulfate to sulfide (S<sup>-2</sup>) requires an 8 electron transfer, 1 electron for reduction of Fe(III) to Fe(II), 2

electrons for U(VI) reduction to U(IV), and 2 electrons for Mn(IV) reduction to Mn(II). Total sulfate reduction was estimated from the sum of the integrated effluent dissolved sulfide and the increase in solid phase S, assuming that solid phase S increase is all  $S^{2-}$ . This estimated amount of sulfate reduction requires 52.4 mmol of electrons, which is similar to the total electrons donated in integrated loss of lactate (49.6 mmol, **Table 3.14**) assuming all of the lactate consumption results in acetate production. The net consumption of acetate is defined as the production of acetate from lactate minus transport of acetate out of the column and equals 5.94 mmol. Oxidation of this amount of acetate produces 47.5 mmol of electrons during the experiment if acetate is oxidized completely to  $CO_2$  and requires a TEAP other than sulfate, since sulfate reduction equals lactate oxidation.

Ferric iron reduction estimated from the integrated effluent iron and the increase in 1-hour 0.5N HCl extractable Fe(II) from the sediment accounts for 0.47 mmol of electrons, with 0.51 mmol of electrons if the 24-hour 0.5N HCl extractable Fe(II) is used instead to represent iron reduction. Both estimates account only for a small fraction of the electron balance for acetate oxidation (**Table 3.14**). Reduction of Fe(III) in phyllosilicate minerals by dissimilatory microbial iron reduction can be significant in aquifer sediments (Wu et al, 2012; Lee et al, 2012; Komlos et al, 2007). However, ferrous iron produced by reduction of Fe(III) silicates may not be quantitatively extracted by 0.5 N HCl since silicate phases likely are not dissolved by HCl. The iron concentration in hot  $HNO_3$  digest of column L1 sediments was on average 23% higher than iron in pre-column and column L5 sediments. Since  $HNO_3$  also does not dissolve silicates and since the influent did not contain significant dissolved Fe, the increase may be attributed to Fe(II) from reduction of Fe(III) in phyllosilicate minerals, if this Fe(II) component is soluble in hot nitric acid. If so, the estimated total iron reduction in column L1 increases to 1.95 mmol. Alternatively, the Fe(III)-silicate reduction can be estimated from the difference between Fe measured in hot  $HNO_3$  digest and in the total HF dissolution. The difference between HF and  $HNO_3$  iron was less for column L1 sediments after biostimulated reduction than in pre-column sediments. Assuming this change is the result of reduction of Fe(III)-silicate to a  $HNO_3$ -soluble Fe(II) form, 1.0 mmol of Fe(III)-silicate reduction is estimated that did not result in dissolved Fe transport out of the column, for a total reduction of 1.16 mmol when including effluent Fe. Both of these estimates of Fe(III)-silicate reduction are insufficient to account for electrons produced during acetate oxidation (**Table 3.14**). In fact, if the total iron in column L1 determined by HF dissolution (14 mmol) was initially Fe(III) and was all reduced to Fe(II) during the biostimulation, the total Fe accounts at most for one third of total electron transfer needed to close the electron balance for acetate oxidation to  $CO_2$ .

Uranium and manganese reduction combined account for less than 1% of electrons produced by 97.1 mmol acetate oxidation (**Table 3.14**). The total uranium retained by the column (17.0  $\mu$ mol), if assumed all is reduced to U(IV), accounts for 0.034 moles of electrons. The integrated effluent Mn was 7.7  $\mu$ mol (0.015 mmol electrons). The total initial sediment Mn in column L1 was 0.40 mmol. If all Mn were reduced during biostimulation, it would result in only a small fraction of the electron balance (0.8 mmol or 1.8%).

Combined, the measured total sulfate, iron, uranium and manganese reduction at most account for 54.4 moles of the 97.1 mmol (58%) of the electrons produced during lactate and acetate oxidation. The deficit in the electron transfer mass balance indicates there must be

either some other TEAP or transformation of acetate pathway that doesn't consume electrons such as methanogenesis (Lovley and Klug, 1986). Dissolved oxygen entering the column cannot be ruled out completely but is insufficient to close the balance. Although the influent reservoir was continuously purged and the inlet tubing was jacketed with the anaerobic gas mixture, the peristaltic pump tubing was in the air. The 43 moles of electrons remaining in mass balance (**Table 3.10**) is equivalent to reduction of 10.7 mmol of oxygen. This would require a 6.6 mM influent dissolved oxygen concentration, which is more than 25 times saturation with respect to air.

Since no other products of terminal electron accepting processes can be invoked or measured, fermentation of lactate to hydrogen, acetate to methane and/or biomass growth likely account for the remaining acetate consumption since electron transfer to a TEAP is not required (Lovley and Klug, 1986). However, the very low biomass present in post column sediments limited DNA extractions making bioassay unfeasible. Therefore, biomass growth is unlikely to account for the remaining consumption of lactate and/or acetate. Alternatively, syntrophic growth of methanogens with sulfate reducing bacteria such as many of the *Disulfotomaculum* and *Desulfotomaculum* species has been reported in which methanogens utilize the acetate produced by sulfate reducing bacteria (Muyzer and Stams, 2008).

Table 3.14 Summary of electron transfer during biostimulated reduction in column L1. Lactate and acetate consumed are from integrated column effluent concentrations (see Table 3.5). Reduction of U is from integrated increase in sediment recovered from column L1. Sulfate reduction is the sum integrated dissolved sulfide in effluent and the increase in total sulfur in column sediments. Iron reduction is the sum integrated dissolved iron in the effluent and the extracted iron from column sediments (see footnotes). Manganese reduction is the sum of the integrated effluent dissolved Mn and the total sediment Mn, assuming that it is all reduced.

Constituent	Total during biostimulation mmoles	HCO <sub>3</sub> produced mmoles	Number of electrons transfer	mmoles electrons	Electrons accepted from donor (%)
Electron donors:					
$C_3H_6O_3^- + 2H_2O \rightarrow C_2H_3O_2 + HCO_3^- + 6H^+ + 4e^-$					
Lactate → acetate	12.4	12.4	4	49.6	51
$C_2H_3O_2^- + 2H_2O \rightarrow 2CO_2 + 7H^+ + 8e^-$					
Acetate → CO <sub>2</sub>	5.94	11.92	8	47.5	49
Total electrons from donors				97.1	
Electron acceptors:					
$SO_4^{2-} + 8e^- \rightarrow S^{2-}$	6.55	13.1	-8	-52.4	54
Fe(III) + e <sup>-</sup> → Fe(II) (a)	0.47		-1	-0.47	0.48
Fe(III) + e <sup>-</sup> → Fe(II) (b)	0.51		-1	-0.51	0.52
Fe(III) + e <sup>-</sup> → Fe(II) (c)	1.95		-1	-1.95	2
Fe(III) + e <sup>-</sup> → Fe(II) (d)	1.16		-1	-1.16	1.2
U(VI) + 2e <sup>-</sup> → U(IV)	0.017		-2	-0.034	0.04
Mn(IV) + 2e <sup>-</sup> → Mn(II)	0.008		-2	-0.016	0.016
Total TEAP				-53 to -54.4	54.5 to 57.7
Unaccounted e <sup>-</sup>				43	42
Dissolved CO <sub>2</sub> effluent	5.1				
HCO <sub>3</sub> produced (e)		24.3			
Missing CO <sub>2</sub>		19.2			

- (a) Fe(II) sediment from increase in 1 hr 0.5 N HCl extraction compared to pre-column sediment plus effluent Fe
- (b) Fe(II) sediment from increase in 24 hr 0.5 N HCl extraction plus effluent Fe
- (c) Fe(II) sediment from increase in hot HNO<sub>3</sub> extraction plus effluent Fe
- (d) Fe(II) sediment from change in (HF total - hot HNO<sub>3</sub> extraction) plus effluent Fe
- (e) Assumes 1 mole CO<sub>2</sub> produced during lactate oxidation to acetate; and 2 moles CO<sub>2</sub> acetate to CO<sub>2</sub>

Since methane production was not anticipated it was not analyzed in the column effluent. In addition, because effluent sampling was not designed for methane collection, headspace measurement of sample bottles used would likely have been compromised by diffusional loss of methane through PTFE effluent tubing and loss during equilibration with effluent bottle headspace and subsequent venting during filling. Since methane was not measured, the extent of methane production was estimated by assuming that methane production results from consumption of the remaining acetate. In contrast to acetate, no methanogens have been described that utilize lactate (Muyzer and Stams, 2008). The near steady state acetate concentration of about 3.5 mM between 30 and 55 days (**Figure 3.7B**), requires consumption of 7.5 mM acetate. Lactate is fully consumed during this period. Combined, iron reduction and sulfate reduction, in excess of lactate consumption, account for at most 10% of the 7.5 mM acetate. Thus, some other process is required to utilize the remaining 6.8 mM acetate. Fermentation of acetate produces 0.5 mole CO<sub>2</sub> and 0.5 mole methane per mole of acetate. Therefore, if fermentation is assumed, this steady state acetate concentration would produce 3.4 mM methane, a concentration that is above saturation for methane (2 mM, Martens and Klump, 1980) at which point bubble formation occurs. An equilibrium partial pressure of 2.3 atmospheres in the column apparatus is calculated for this dissolved methane concentration using Henry's law. The partial pressure resulting from production of methane to account for the remaining acetate is consistent with the back pressure increase observed during the biostimulation experiment (**Figure 3.31A**), which exceeded 25 PSI (1.7 atmospheres) at day 60, the limit of the pressure gage. Methane production has been shown to reduce hydraulic conductivity in sand columns as a resulting of induced pressure and bubble formation limiting flow (Sanchez de Lozada et al, 1994; Ye et al, 2009). Comparison of bromide tracer breakthrough for column L2 conducted after lactate was removed from the influent, with column L5 that did not undergo biostimulation shows faster initial tracer breakthrough in L2 but increased tailing (**Figure 3.31B**). Both are consistent with a decrease in permeability and preferential flow paths which can result either from gas pressure or biomass clogging (Baveye et al, 1998). Additionally, the back pressure in the column apparatus relaxed to the initial condition within three pore volumes after influent lactate ended. The rapid change suggests a decrease in gas pressure with cessation of production and flushing.

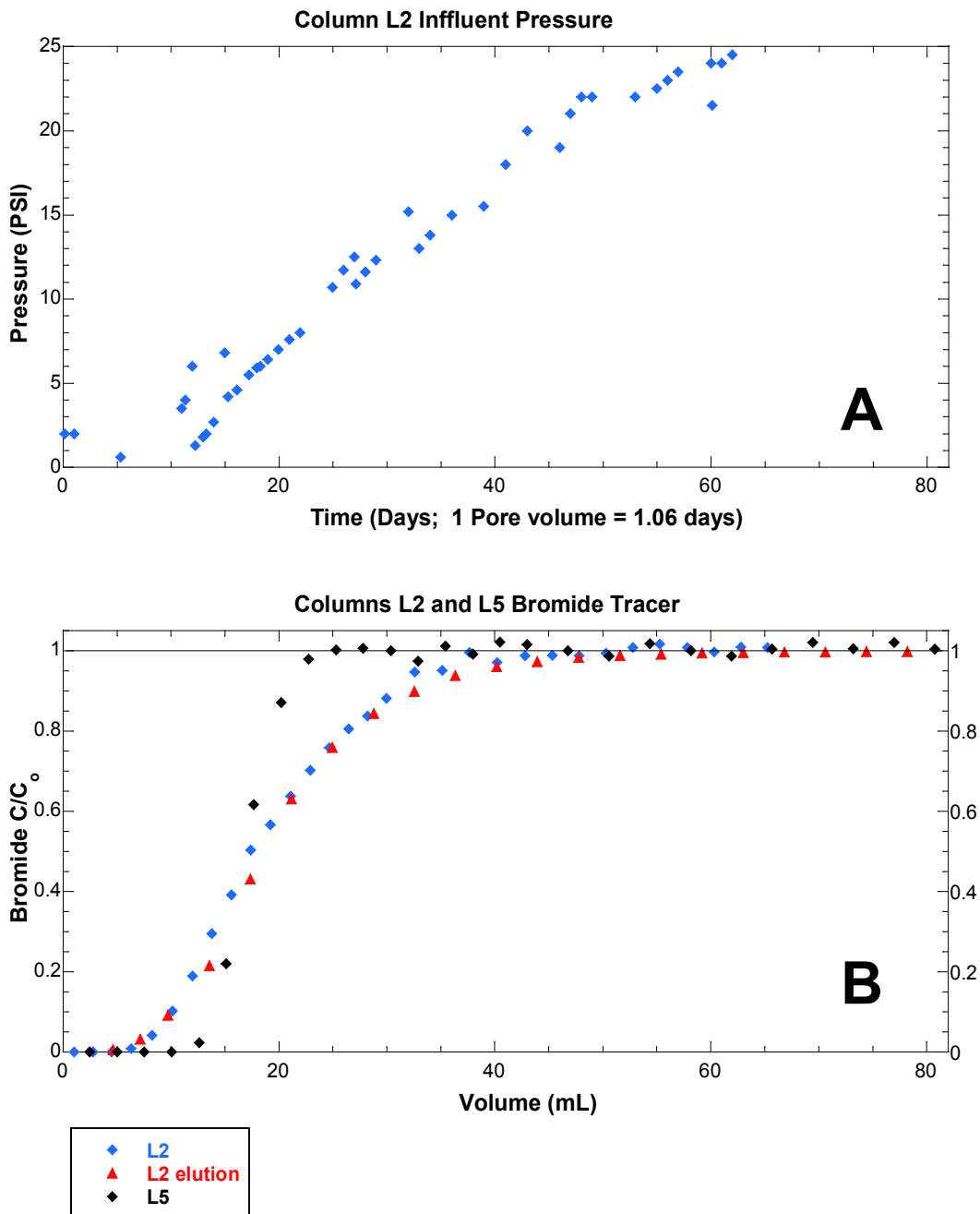


Figure 3.31 (A) Column L2 backpressure at influent end of column versus time. Pressure is in pounds per square inch above atmospheric pressure. (B) Bromide tracer versus volumes of tracer influent for column L2 at the end of biostimulated reduction, and for column L5 with no biostimulation to represent initial condition of columns, plotted as the ratio of effluent to influent bromide concentration. Bromide elution for column L2 is plotted as one minus the ratio of measured bromide to the initial influent concentration.

An alternative pathway to fermentation of acetate to methane is the production of H<sub>2</sub> and acetate from lactate by acetogenic microbes, with H<sub>2</sub> subsequently used by methanogens to produce methane by reduction of dissolved CO<sub>2</sub>. In this case, acetate is consumed by sulfate and iron reducing bacteria. The required methane and/or hydrogen production by these pathways is consistent with column back pressures and may account for consumption of remaining acetate (Muyzer and Stams, 2008). Based on changes in cell counts and presence of methanogens in biostimulation column experiments with Rifle aquifer sediments at low sulfate concentrations, Komlos et al (2008) invoked methanogenesis to account for consumption of acetate since SO<sub>4</sub>, Fe and U reduction accounted for only 1.5% of electrons from the acetate donor. However, because sulfate concentrations were high throughout the ISR column experiment, sulfate reducing microbes should outcompete methanogens for acetate and hydrogen (Oremland et al, 1982). As a result, methanogenesis would be limited based on the frequently observed sequence of sulfate reduction continuing until sulfate decreases to low levels prior to methanogenesis (Lovley and Klug, 1986) and the spatial separation of sulfate reduction from methanogenesis in sediments (Kuivila et al, 1989). However, since excess electron donor is present (continuous 10 mM lactate input) this hierarchy of electron accepting processes may not apply since the electron donor is not limiting (Komlos et al, 2008a). Unfortunately, the low concentrations of DNA prevented assay of microbial communities in column sediments after the experiments. Thus, further description of microbial processes to account for observed consumption of lactate and acetate during biostimulation is not possible.

A net increase of 5.1 mmol total dissolved CO<sub>2</sub> was estimated by integrating effluent sample concentrations (**Table 3.5**). Total consumption of lactate and acetate for the duration of the column experiments would result in 24.1 mmol of CO<sub>2</sub> produced, 12.4 from lactate oxidation and 11.9 mmol from acetate, assuming complete oxidation to CO<sub>2</sub>. Since there was no measurable increase in solid phase inorganic carbonate, a large fraction of CO<sub>2</sub> by complete oxidation of lactate and acetate could not be accounted for. However, loss of CO<sub>2</sub> exceeding the initial 15% pCO<sub>2</sub> from outlet tubing by diffusion and from sample bottles during re-equilibration and headspace displacement as effluent bottles filled may have occurred. The amount of lactate and acetate utilized for cell growth resulting in an increased biomass is assumed to account for the increased rate of lactate consumption during the first 20 days of biostimulation, but cannot be calculated.

### **3.4.2 Stability of Immobilized Uranium**

The near complete removal of dissolved U(VI) from the influent over the course of the biostimulation stage with the resulting sequestered U primarily as U(IV) suggests that stimulation and growth of ambient microbial populations in the Kingsville Dome aquifer after ISR extraction by addition of electron donor and carbon source may be an effective means of removing dissolved uranium from groundwater following the ISR process.

Previous studies have reported oxidative remobilization of U(IV) under anaerobic conditions resulting from continued reduction of Fe and Mn oxides which serve as terminal electron acceptors for U oxidation coupled with increased dissolved carbonate shifting the redox state to more favorable conditions for U oxidation (Wan et al, 2005). The remobilization of U was studied following biostimulated reduction in column experiments with aquifer sediments from the Old

Rifle, CO, site inoculated with *Geobacter metallireducens* under low sulfate conditions. These experiments showed near 88% and 97% remobilization within 54 days when 0.27 mM dissolved oxygen (saturation with respect to air) or 1.6 mM nitrate were added to the influent, respectively (Moon et al, 2007). After 200 days of biostimulated reduction in similar column experiments under low sulfate conditions, re-oxidation of U(IV) resulted in the increase of effluent [U] to over 150  $\mu\text{M}$  within 10 days of exposure to dissolved oxygen at saturation with air, with 60% of U remobilized after 60 days and nearly all by 120 days (Komlos et al, 2008b). The extent of U remobilization in these experiments suggested little adsorption of U(VI) by iron oxides or other surfaces on the column sediments and that oxidation of ferrous iron provided negligible buffering of U(IV) oxidation. Cell decay and ferrous iron oxidation accounted for 43% and 23% of oxygen consumption, respectively, with U accounting for 12% (Komlos et al, 2008b). In contrast, Sharp et al (2011) found little remobilization of biologically reduced U in columns with Rifle sediments with no added sulfate upon exposure to oxygen. Instead, the increase in the relative proportion of U(VI) in the middle and outflow end of the column was attributed to retention of U(VI) by sorption following re-oxidation of U(IV) near the inflow end of the column.

The presence of iron sulfides has been proposed to limit re-oxidation of U(IV) by serving as a redox buffer or armoring the U(IV) precipitate (Abdelouas et al, 1999). The timing and extent of U remobilization following prolonged biostimulated reduction of sulfate, iron and U in column experiments with inoculated Rifle sediments show significantly less U re-oxidation and a delay in release of U upon addition of oxygen or nitrate to column influent (Moon et al, 2009), compared to low sulfate experiments which had little or no iron sulfide precipitation. The iron sulfides formed during biostimulation served to partially limit biogenic U(IV) oxidation by competing for dissolved oxygen. Less than 1% of U was remobilized by 0.27 mM dissolved oxygen and no oxidation at 0.03 mM dissolved oxygen was observed through 50 days of elution. Sulfide oxidation accounted for 85% of oxygen consumption. Mackinawite (FeS) has been shown to inhibit  $\text{UO}_2$  oxidation provided that it is in physical proximity to the U(IV) phases and is in sufficient quantity to effectively scavenge oxygen to act as a redox buffer (Bi et al, 2013).

In the present study, the time dependence of the suboxic elution of U in column L2 provides a measure of the stability of the bioreduced U. Prior to introduction of dissolved oxygen to the column influent stream, effluent [U] averaged 0.01  $\mu\text{M}$  over 30 pore volumes after U(VI) and lactate were removed from the influent. Because other processes, such as adsorption of U(VI) by sediment, can change (lower) the effluent dissolved [U], rates calculated from column effluent data are considered net rates. A net rate of U release of  $9.8\text{E}-10$   $\mu\text{mol}/\text{sec}$  is calculated for the whole column by multiplying this near steady state [U] by the flow rate. Previous studies of remobilization or oxidation of reduced U report rates in terms of  $\text{mol g}^{-1} \text{sec}^{-1}$ , where g is the mass of reduced (or total) uranium (in grams) in flow through or batch reactors (Bi et al, 2013; Sharp et al, 2011; Ulrich et al, 2009). Following this approach, dividing the net rate by the mass of U attenuated during biostimulation yields a remobilization rate of  $2.4\text{E}-13$   $\text{mol g}^{-1} \text{sec}^{-1}$  which is four orders of magnitude slower than rates measured for synthetic and biogenic  $\text{UO}_2$  (Ulrich et al, 2009). The very low effluent [U] prior to introduction of dissolved oxygen combined with the predominance of U(IV) (>95%) in the sediment following biostimulation are consistent with negligible release of sorbed U(VI) from sediments, assuming there is no oxidation during this period.

Pre-operational dissolved oxygen concentrations are not well known in groundwater of roll front U ore deposits targeted for ISR extraction, with most reported values below the lower end of the working range of dissolved oxygen meters (0.5 mg/L). A lower value of 0.2 mg/L (6  $\mu\text{M}$ ) was chosen to test suboxic conditions typically found in these deep aquifers. Column L2 was eluted with 19 pore volumes of AGW containing 6  $\mu\text{M}$  dissolved oxygen (20 days), followed by 62 PV at 12  $\mu\text{M}$  (67 days). During this period a total of about 27% of the total U uptake during biostimulation was remobilized, likely the result of oxidation. The small increase in the fraction of U(VI) in column L2 sediments following suboxic elution (13% U(VI), see **Table 3.9**) compared to before introduction of oxygen (9% U(VI) for column L1) further suggests transport of [U] out of the column is largely the result of oxidation of U reduced during biostimulation.

During the first 35 days of suboxic elution, effluent [U] increased linearly from 0.07 to 0.63  $\mu\text{M}$  (**Figure 3.9**). The corresponding instantaneous net U release rates increased from  $3.5\text{E-}12 \text{ mol g}^{-1} \text{ sec}^{-1}$  during the first 5 days following introduction of  $\text{O}_2$  to  $2.5\text{E-}11 \text{ mol g}^{-1} \text{ sec}^{-1}$  after 35 days. The rate of U release then began to increase as illustrated by the change in slope of effluent [U], with a constant rate of increase between 52 and 82 days after introduction of oxygen (**Figure 3.9**). During this second period of linear increase in [U] the net instantaneous rate of U remobilization increased from  $1.7\text{E-}10 \text{ mol g}^{-1} \text{ sec}^{-1}$  after 55 days (52 PV) to  $7.9\text{E-}10 \text{ mol g}^{-1} \text{ sec}^{-1}$  by the end of the experiment. These rates are more than an order of magnitude slower than rates for synthetic abiotic and biogenic  $\text{UO}_2$  (Ulrich et al, 2009), for synthetic  $\text{UO}_2$  in the presence of mackinawite (Bi et al, 2013), and more than 4 orders magnitude slower than U(IV) release rates from biogenic  $\text{UO}_2$  produced during biostimulation of Rifle aquifer sediments (Sharp et al, 2011). Although the rates from those studies are from batch and flow through reactors, the rates calculated here from column data are likely more indicative of release rates expected in an aquifer following biostimulation since the column rates include reactive processes that would occur during transport in an aquifer. Overall, the rate of U remobilization increased by more than a factor of 200 during the 81 PV suboxic elution, with full mobilization of bioreduced U projected to occur after 150 PV.

The observed increase in mobilization rate may be the result of depletion of other components that compete for dissolved oxygen. Oxygen consumption was attributed primarily to cell decay and iron oxidation in oxic elution in low sulfate biostimulation column experiments with U (Komlos et al, 2008b). In this study, oxidation of 0.11 mmol ferrous iron occurred based on the difference between whole column extractable ferrous iron before and after suboxic elution, represented by columns L1 and L2 (**Table 3.5**). Based on the cumulative effluent concentration of iron during suboxic elution, about 70% of the Fe release during the suboxic elution had occurred before the change in the rate of U remobilization occurred 35 days after introduction of suboxic AGW, with 84% total iron release at 52 days. The transport of iron out of column L2 during suboxic elution accounts for about 26% of the total decrease in sediment Fe(II) concentration measured (the difference between column L1 and L2). It is unclear if the re-oxidized iron that remains in the column precipitates as iron oxides and provides sufficient sites for adsorption of remobilized U(VI) since there was only a small increase in U(VI) in the sediment following suboxic elution. However, Komlos et al (2007) reported that re-oxidation of bioreduced Fe silicates resulted in oxidized iron in silicates with similar structure to before reduction. This finding suggests that a large component of the re-oxidized iron remaining in the column likely is phyllosilicate Fe. Adsorption of U(VI) onto silicate minerals likely is minimal

compared to iron oxides forming on sediment surfaces since no measurable loss of [U] was observed in columns without biostimulation activity (columns H1 and H2).

Solid phase total sulfur decreased by 1.6 mmol in column L2 at the end of suboxic elution compared to column L1 (Table 3.8C). Very little change in effluent sulfate was measured during the suboxic elution indicating that sulfides did not oxidize completely to sulfate and/or the contribution of sulfate from sulfide oxidation was insufficient to result in a measurable change in effluent sulfate. In either case, net decrease in sediment sulfur after biostimulation (column L1) and suboxic elution (L2) had to result in net transport of dissolved S out of the column. Since total S measurements were only made at the end of each experimental stage no information on the rate or timing of sulfur oxidation during suboxic elution is available.

The estimated oxidation of Fe from the change in sediment Fe(II), 0.11 mmol, is less than 10% of the decrease in total S, indicating a large fraction of sulfur reduced during biostimulation did not form iron sulfides. This is consistent with the negligible fraction of acid volatile sulfide measured in column L1 sediments at the end of the biostimulation (**Table 3.8C**). Thus, it is unclear which competing oxidation processes provided redox buffering prior to the change in U remobilization rate occurring after about 50 pore volumes in column L2.

### 3.4.3 Comparison to Model Simulation of Biostimulated Reduction

The following chapter (4) presents simulations of column effluent during biostimulation based on the reactive transport models for biostimulated U reduction in groundwater (Yabusaki et al. 2011, Fang et al, 2009, Yabusaki et al, 2007). The model assigns sulfate reduction to occur primarily through lactate oxidation, which is reasonable since the electron transfer for the total sulfate reduction is equivalent to electron transfer required from oxidation of all lactate consumed to form acetate. For the modeled reduction to equal electron transfer from acetate oxidation, the model also assigns a pool of Fe(III) oxide and one pool of phyllosilicate Fe(III), along with minor contributions from U reduction and biomass growth. A second pool of phyllosilicate Fe(III) is invoked to account for lactate not consumed during sulfate reduction based on the change in effluent sulfate, which as discussed above, likely underestimates sulfate reduction. The total of the solid phase Fe(III) pools used in the model simulations, 240 millimoles for the entire column (4.2 mmol/g times mass of sediment in the column, 57 g), greatly exceeds the 15 millimoles total iron present in each column initially based on HF dissolution of pre-column sediment (0.25 mol/g). This large iron pool was required in model simulation to balance electron transfer because no other microbial processes involving electron transfer or fermentation were included. Nonetheless, the simulations are able to capture the rate and extent of iron and uranium reduction in the column which may allow upscaling for prediction of biostimulated reduction at the field scale.

The modeling effort did not simulate the remobilization of U(VI) in response to the introduction of oxygen to suboxic levels. A more thorough understanding of mechanisms resulting in oxidation and remobilization of U reduced during biostimulation is required to develop reactive transport simulation for remobilization of bioreduced U(IV). Moreover, remobilization of U following bioremediation of a roll front ISR site will be a function of groundwater dissolved O<sub>2</sub> concentrations. This will depend on the ambient dissolved O<sub>2</sub>

concentrations in the surrounding aquifer as well as on how effectively oxygen from the ISR process can be eliminated throughout the system, including low permeability zones that may bleed out dissolved O<sub>2</sub> for long times.

### 3.5 Summary of Experimental Findings

The laboratory column experiments with Kingsville Dome aquifer sediment recovered following ISR extraction under conditions geochemically relevant to the aquifer described in this chapter demonstrate the ability of the indigenous microbial population during biostimulation with lactate to reduce uranium resulting in precipitation of U(IV). The results provide a basis for evaluating the feasibility and design of field scale tests of biostimulated remediation of elevated groundwater uranium resulting from in situ leaching and recovery of uranium from sandstone uranium roll front ore deposits. The biostimulated reduction by lactate lowered dissolved uranium from 10 μM to <0.1 μM within 45 days. Near complete uptake of the influent 20 μM U(VI) continued through 82 days principally by reduction to U(IV). Slow release of U occurred in response to return to suboxic conditions with dissolved U increasing to 0.13 μM (<30 μg/L) over 10 days (~10 PV) of elution with suboxic groundwater (6 μM dissolved oxygen). U remobilization occurred at a linearly increasing rate with effluent [U] increasing to 0.63 μM by 35 days (33 PV). The rate and extent of U remobilization subsequently increased with [U] >13 μM after 87 days (81 PV) of suboxic elution at the end of the experiment. Analyses of sediments recovered from columns at end of the biostimulation and re-oxidation stages showed that the sequestered uranium was primarily U(IV) in the form of a uraninite-like phase. Significant findings are highlighted below.

1. The indigenous microbes in the Kingsville Dome sediment after ISR extraction were capable of reducing uranium in batch tests in the absence of dissolved oxygen when amended with electron donors. The timing and rate of reduction proceeded in order for the following electron donors: H<sub>2</sub> > lactate > acetate.
2. Hydrogen amended AGW (pH<sub>2</sub>= 0.05) was not sufficient to cause measurable attenuation of influent uranium in flow-through column experiments, likely because there was no added carbon source to promote biomass growth required for bioreduction of uranium, iron or sulfate.
3. Effluent concentrations from the two identical lactate amended columns (L1 and L2) were comparable throughout the biostimulated reduction stage. The summary below thus applies to both with differences noted.
4. Consumption of 10 mM influent lactate was observed starting at 5 days with effluent concentrations approaching 0 by 18 days. Complete consumption of lactate continued through to the end of the biostimulation period (82 days). Concomitant with lactate consumption, effluent acetate increased from 0 to 3 mM over the first 18 days and was relatively constant between 3 and 3.5 mM through 55 days, suggesting steady state production and consumption of acetate, with the production rate from lactate oxidation exceeding acetate consumption.
5. Effluent dissolved Fe increased starting at about 10 days indicating the onset of iron bioreduction with maximum concentrations exceeding 300 μM at 20-25 days, followed by

decrease in effluent [Fe] to  $<10 \mu\text{M}$  by 45 days. The decrease in [Fe] was coincident with the appearance of measurable dissolved sulfide, indicating that the rate of sulfate reduction was producing sufficient dissolved sulfide to result in iron sulfide precipitation therefore limiting effluent Fe. A total of 0.16 mmol Fe was transported out of column L1 during biostimulation. An increase of 0.3 mmol of extractable Fe(II) was measured for column L1 with sediment Fe(II) concentrations increasing 4.8 to  $7 \mu\text{mol/g}$ .

6. Dissolved sulfate in effluent decreased slightly from the influent concentration of 10.65 mM throughout biostimulation with an integrated loss of 1.4 mmol for column L1. Sediment total S increased by 0.06 to 0.2 mmol/g in column L1 intervals during biostimulation for a total retention of 4.9 mmol. The calculated decrease in  $\delta^{34}\text{S}$  isotopic signature ( $-40$  to  $-43.2 \text{‰}$ ) of total S increase is consistent with microbial reduction of sulfate. Effluent dissolved sulfide increased to measurable concentrations after day 40, coincident with decrease in effluent dissolved Fe. Combined, effluent sulfide and solid phase S increase was 6.6 mmol.

7. In anaerobic column experiments with ISR sediment the introduction of 10 mM lactate resulted in a decrease in the  $20 \mu\text{M}$  influent dissolved U(VI) by 8 days (7.5 PV). Uptake of U occurred somewhat coincident to increase in effluent iron suggesting iron reduction may be the result of the same microbial process. Dissolved U decreased to  $<0.1 \mu\text{M}$  by 45 days (42 PV) with near complete uptake over the next 35 days that continued through the remainder of biostimulation. The cumulative uranium uptake of  $16 \mu\text{mol}$  resulted in increasing the sediment U concentration by  $0.3 \mu\text{mol/g}$  ( $70 \mu\text{g/g}$ ) over the initial sediment U of  $0.24 \mu\text{mol/g}$ . U uptake occurred preferentially near the column inlet with total U concentrations of up to  $0.97 \mu\text{mol/g}$ .

8. Very low dissolved uranium ( $0.01 \mu\text{M}$ ) was observed in the effluent for 30 PV after the electron donor and U(VI) were removed from the influent and prior to introduction of dissolved oxygen.

9. Upon introduction of  $6 \mu\text{M}$  dissolved oxygen to the influent, effluent [U] increased linearly from  $0.07$  to  $0.63 \mu\text{M}$  over 35 days (33 PV). The overall rate of U remobilization increased rapidly from this point with effluent [U] increasing to  $5 \mu\text{M}$  by 55 days (52 PV) and was greater than  $13 \mu\text{M}$  after the end of the experiment at 87 days (81 PV), with about 27% of bio-reduced uranium being released. Effluent dissolved iron decreased somewhat linearly from  $20$  to  $8 \mu\text{M}$  during the suboxic elution. No measurable difference was observed between influent and effluent sulfate throughout suboxic elution.

10. Suboxic elution resulted in release of  $2.1 \mu\text{moles}$  of uranium, which is about 27% of the solid phase U uptake that occurred during biostimulation. Sediment Fe(II) decreased by about 30% as a result of suboxic elution. Little change in reducible Fe(III) was measured over the course of biostimulation and suboxic elution compared to the pre-column sediment, suggesting the reduction and re-oxidation of iron occurred largely in phyllosilicate Fe(III) minerals. Solid phase total S decreased 1.65 mmol (33%) during suboxic elution.

11. XANES measurements showed that  $>95\%$  of the U uptake occurred as the result of reduction and precipitation. EXAFS spectra of column sediments indicate that bio-reduction of uranium may result in the formation of a uraninite phase. The low amount of sequestered

uranium combined with the pre-existing U(IV) of a different form in pre-column sediments limited more conclusive structural determination of the U(IV) formed in the columns. Little change in the column sediment U(IV) fraction was measured after suboxic elution indicating that U(VI) was largely transported out of column as dissolved uranyl species with a negligible fraction of the re-oxidized U(VI) adsorbed to sediments.

12. Microfocused synchrotron XRF imaging showed that U is largely distributed among smaller grain sizes of sediment. Large iron sulfide grains were present and contain U which may be remnant U not leached during ISR process, and included both U(IV) and U(VI). These grains comprised a small fraction of the total U.

13. Microbial assay of ISR sediment used for the column experiment showed that despite low biomass there was a high diversity of sulfate reducing bacteria (SRB) in the sediment recovered from the aquifer that included representatives from most families of SRB, but dominated by *Desulfobulbaceae* and *Desulfobacteraceae*. *Geobacter* was not detected, suggesting an important role of SRB for reduction of iron and uranium, as well as sulfate, as previously observed (Lovley et al, 1993; Beyenal et al, 2004). Bioassay of an effluent filter collected on the falling limb of the dissolved Fe peak show presence at low abundance of both *Geobacter* and sulfate reducing bacteria during iron reduction. Another effluent filter, collected during sulfate reduction, showed a community shift toward increasing SRB and a concomitant decrease in the iron reducing *Geobacter*. Biomass in sediments recovered from columns was too low to provide sufficient DNA for community identification.

14. Geochemical mass balance for the biostimulation period indicates other processes are required to account for 42% of electron transfer resulting from the observed consumption of lactate and acetate in excess of sulfate, iron and uranium terminal electron accepting processes.

15. Suboxic elution of Kingsville ISR sediment that had not been subjected to biostimulated reduction showed that 4.6% of the sediment-associated U was mobilized after 44 pore volumes, which included more than 30 pore volumes of low oxygen (~6-12  $\mu\text{M}$ ) influent solution.

## 4 Simulation of Uranium Bioremediation in ISR Sediment Columns

We describe the modeling of transport and uranium biogeochemistry during biostimulated reduction in a laboratory column experiment that was performed by the USGS using the post-ISR sediments from Kingsville Dome (Chapter 3). Recent investigations in shallow uranium-contaminated aquifer systems (Anderson et al., 2003; Vrionis et al., 2005; Williams et al., 2011; Wu et al., 2006a; Wu et al., 2006b) have demonstrated that the stimulation of indigenous dissimilatory metal-reducing bacteria, via the addition of an electron donor (i.e., ethanol, lactate, acetate), can reduce soluble hexavalent uranium [U(VI)] to immobile solid-phase U(IV) (Anderson et al., 2003; Vrionis et al., 2005; Williams et al., 2011). While the bioremediation principle is common to both the shallow uranium groundwater plumes and the relatively deep uranium ISR aquifers, there is an important conceptual difference. In the shallow sites, the conditions favorable for the bioreduction of U(VI) need to be artificially maintained; whereas at the post-ISR sites, the intent of the engineered biostimulation is considered a temporary action that is designed to return the geochemical conditions to the naturally low redox potential associated with the uranium roll front deposit.

We use the systematic and quantitative coupling of process models to describe the interplay between the saturated flow, microbiology, and geochemistry during lactate biostimulation of the Kingsville Dome sediment column experiments. Modeling of these experiments is used to understand and quantify uranium behavior in the context of 1) biostimulation with lactate electron donor, 2) functional microbial groups representing Fe(III)-reducing bacteria (FeRB), which are also responsible for the bioreduction of U(VI), and sulfate-reducing bacteria (SRB) responding to the biostimulation, and 3) geochemical response to the biostimulation products.

While both columns, L1 and L2 in the laboratory study described in Chapter 3 experienced 83 days of lactate biostimulation, Column L2 was subsequently used to investigate non-reactive tracer transport and the impact of suboxic conditions on uranium behavior following biostimulated reduction. In this chapter, the focus of the column experiment modeling is on the engineered uranium bioreduction and immobilization in Column L1. The effluent profiles of both columns were very similar throughout the biostimulated reduction stage.

### 4.1 Uranium Bioremediation Modeling Studies

A particularly relevant reactive transport modeling study is NUREG/CR-6870 (Davis and Curtis, 2007), which described the use of the PHREEQC computer code (Parkhurst and Appelo, 1999) to analyze the geochemistry during groundwater restoration at the Ruth ISL (Schmidt, 1987) in Wyoming. In this case, models that consider groundwater flow, solute transport, and geochemical reactions are used to estimate the number of pore volumes and therefore costs associated with groundwater restoration. One finding was that slow desorption from the sediments resulted in the persistence of U, Se, and V above baseline concentrations despite tens of pore volumes of groundwater flushing.

Saturated flow and multicomponent biogeochemical reactive transport modeling studies were also performed to simulate uranium bioremediation in shallow contaminated groundwater plumes. These include the 2002, 2003, 2007 and 2008 field biostimulation experiments at the Rifle IFRC site (Fang et al., 2009; Li et al., 2010; Li et al., 2009; Yabusaki et al., 2007; Yabusaki et al., 2011). A comprehensive reaction network was developed from these studies that included biologically-mediated TEAPs for solid phase Fe(III), aqueous U(VI), and aqueous sulfate; aqueous and (nonelectrostatic) surface complexation for Fe(II) and U(VI); calcite, siderite, FeS, S secondary minerals; sulfide promoted dissolution of Fe(III) minerals, cation exchange, protonation/deprotonation of Fe(III) surfaces, and major ion chemistry. In this case, the integration of the abiotic chemistry with the TEAPs in the modeling is necessary to account for the impact of biostimulation products on uranium behavior. In laboratory and field experiments, the bulk of the bicarbonate and reduced phases (e.g., Fe(II), sulfide) produced by the biologically-mediated reactions are not observed in solution. This underscores the importance of accurately representing the solid phase reactions (e.g., mineral reactions for carbonates, iron, and sulfur; iron and uranium surface complexation) that control the pH, Eh, alkalinity, and aqueous components of interest.

An important challenge identified in these uranium bioremediation modeling studies (Fang et al., 2009; Williams et al., 2011) is the impact of biologically-mediated reaction products (e.g., biomass, bicarbonate, Fe(II), U(IV), H<sub>2</sub>S) on the behavior of uranium (Englert et al., 2009; Li et al., 2010; Li et al., 2009). In particular, the sensitivity of uranium mobility to pH, Eh, alkalinity, calcium, and reactive surface area requires detailed biogeochemical process modeling to mechanistically simulate changes to the aqueous and solid phase chemistry induced by acetate biostimulation (Davis et al., 2006; Dong et al., 2005; Li et al., 2009; Liu et al., 2005; Luo et al., 2007). Biologically-mediated oxidation of acetate produces a large amount of bicarbonate that directly affects the alkalinity, and indirectly affects the pH, calcium and reactive surface area through precipitation of carbonate minerals (Li et al., 2009). The reductive dissolution of Fe(III) minerals and the precipitation of sulfides and elemental sulfur affects pH and reactive surface area (Poulton et al., 2004). CaUO<sub>2</sub>(CO<sub>3</sub>)<sub>3</sub><sup>2-</sup> and Ca<sub>2</sub>UO<sub>2</sub>(CO<sub>3</sub>)<sub>3</sub><sup>0</sup>(aq) complexes (Dong and Brooks, 2006), which are predicted to be predominant for the Kingsville Dome post-ISR geochemical conditions, have been shown to affect U(VI) bioreduction (Brooks et al., 2003) and adsorption (Zheng et al., 2003). Thus, the inclusion of a reaction network that accounts for uranium, terminal electron-accepting processes (TEAPs), biomass, major ion chemistry (Ca, Mg, K, Na, carbonate, sulfate, Cl), reduction products [Fe(II), U(IV), H<sub>2</sub>S], aqueous complexation (e.g., Ca-UO<sub>2</sub>-CO<sub>3</sub>), surface complexation [Fe(II), U(VI)], and precipitation/dissolution (goethite, calcite, FeS, S, UO<sub>2</sub>) is critical to capturing important biogeochemical interactions during bioremediation of a uranium ISR site.

## **4.2 Findings from Column Experiments using Kingsville Dome ISR Sediments**

The column experiments in Chapter 3 were designed to investigate the potential for stimulating indigenous microorganisms in post-ISR Kingsville Dome aquifer sediments. The findings from the biostimulation stage of column L1 were the following:

- After 14 days, the column effluent indicated that the continuous influx of 10 mM lactate was completely consumed during transport through the column (**Figure 4.1**). At this point in the experiment, the nonreactive transport travel time through the length of the column was 1.1 days.
- Acetate, produced by the lactate oxidation reaction(s), increases from 0 and plateaus at 3 mM at day 14 in the column effluent. From day 55 to 83 (end of the bioreduction phase of the experiment), the effluent acetate concentration increases to ~10 mM. This means that before the end of the experiment, nearly all the acetate produced by lactate oxidation leaves the column unreacted.
- Fe(II) increases to a peak of ~320  $\mu\text{M}$  after 30 days, after which it decreases to less than 10  $\mu\text{M}$  at day 45 (**Figure 4.2**). There are two minor peaks at 4 and 15 days.
- Continuous influx of 20  $\mu\text{M}$  U(VI) was transported through the column with negligible attenuation until the lactate was being completely consumed at day 14. After day 14, aqueous U(VI) in the column effluent began to decrease. The rate of U(VI) reaction progressively increased until day 40 when essentially none of the continuously influent 20  $\mu\text{M}$  U(VI) was found in the column effluent (**Figure 4.3**), indicating complete attenuation of dissolved U.
- Sulfate consumption during transport through the column was ~1 mM from the continuous influx of 10.65 mM sulfate (**Figure 4.4**). The sulfate consumed in the column was relatively small despite influent lactate and produced acetate concentrations that were ~10 mM.

Over the first 14 days of the column experiments, the rate of microbially-mediated oxidation of the continuously influent 10 mM lactate progressively increases. After 14 days, lactate transported through the column is completely consumed. At this point, 31 and 35 pore volumes of influent solution have passed through columns L1 and L2, respectively. Assuming one mole of acetate is produced for each mole of lactate reacted with no other microbial process consuming lactate, 10 mM acetate is being generated in the column at this time. From day 14 to day 55, effluent acetate is ~3 mM, meaning that 85% of the electron donors available to the column were consumed (i.e., 10 mM lactate and 7 mM acetate). From that point in time to the end of the experiment at 83 days, effluent acetate increases and approaches 10 mM, while lactate is fully consumed. This implies that at the end of the experiment, nearly all of the acetate produced is unreacted.

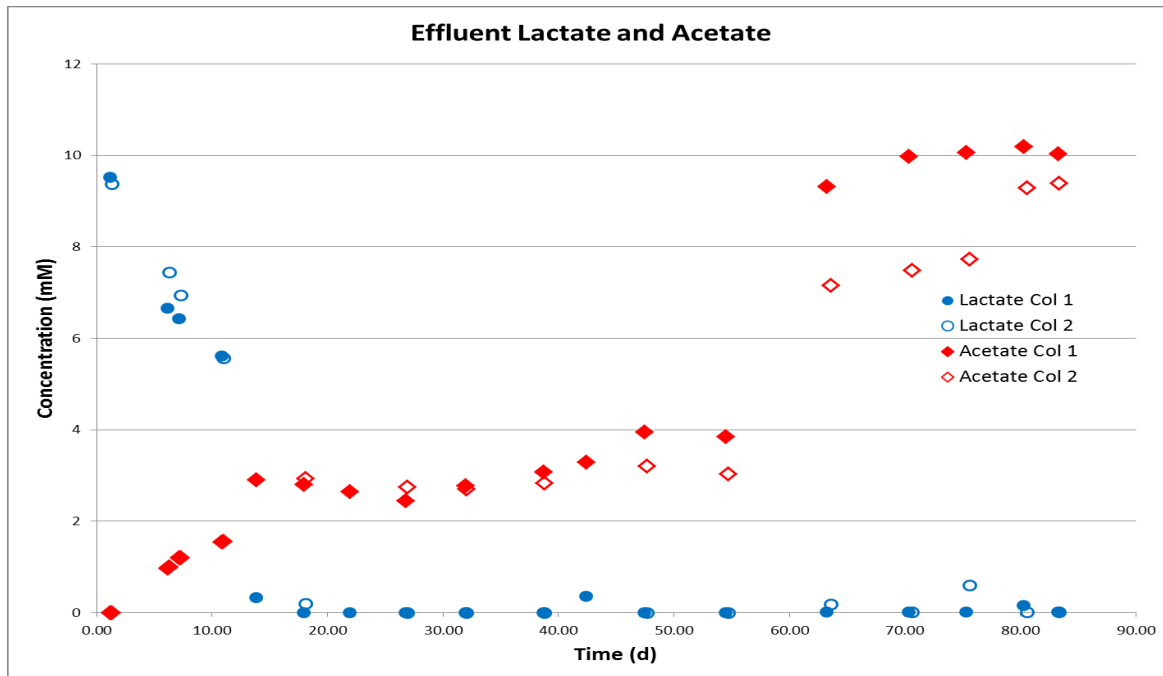


Figure 4.1 Effluent lactate (blue symbols) and acetate (red symbols) concentrations from column 1 (solid symbols) and column 2 (open symbols).

The increase in aqueous Fe(II) during the first 30 days of biostimulation followed by a decline to near zero is similar to observations in shallow aquifer sediments. The increase is consistent with the initial activity of the Fe(III) TEAP reactions, while the decrease from day 30 to 45 is consistent with the production of sulfide via sulfate bioreduction that reacts with the aqueous Fe(II) to form FeS, effectively titrating Fe(II) from solution.

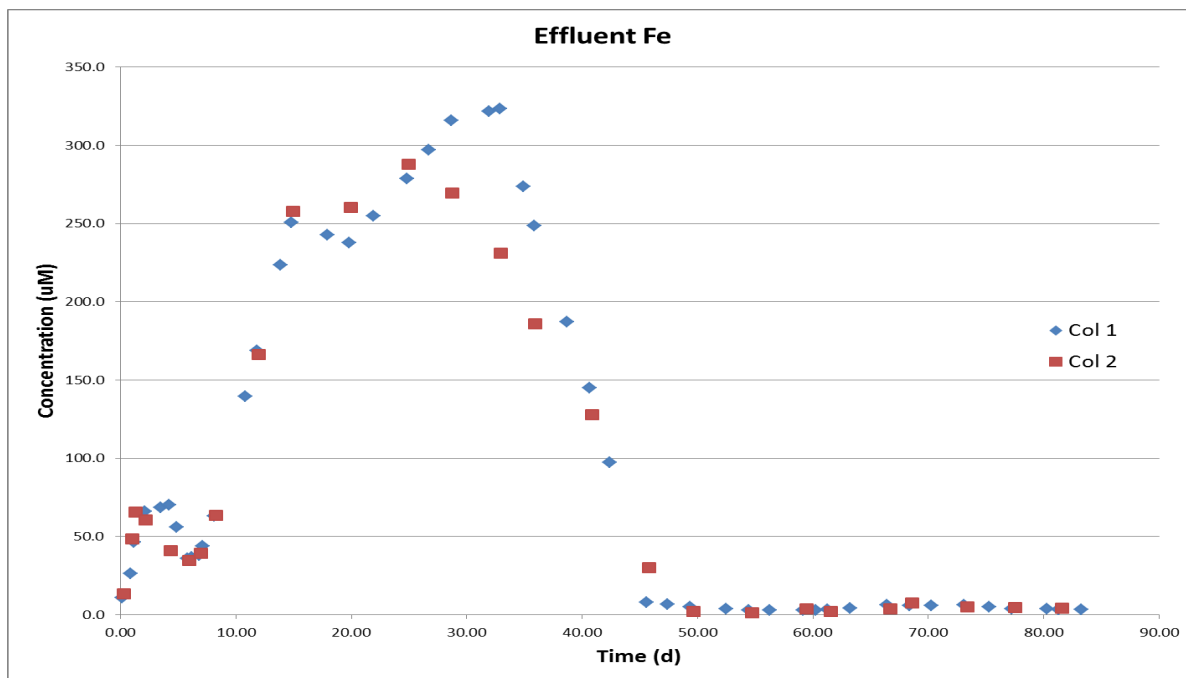


Figure 4.2 Effluent Fe(II) concentrations from column 1 (blue diamonds) and column 2 (red squares).

Other behaviors exhibited by the Kingsville sediment column experiments are not similar to observations in biostimulation experiments with shallow aquifer sediments. For the first 10 days, effluent uranium is generally at influent concentrations as opposed to the rapid uranium bioreduction exhibited for acetate biostimulation in shallow aquifers. Only until half or more of the influent lactate is consumed (> 10 days) is a measurable decrease in effluent U(VI) concentration observed. At day 20, ~2.5 mM of the 20 mM influent U(VI) has been removed. By Day 40, nearly all the influent U(VI) has been removed. Thus, the most effective U(VI) removal occurred after the point in time when the influent lactate was being fully consumed during the 1.1 day transit of column L1.

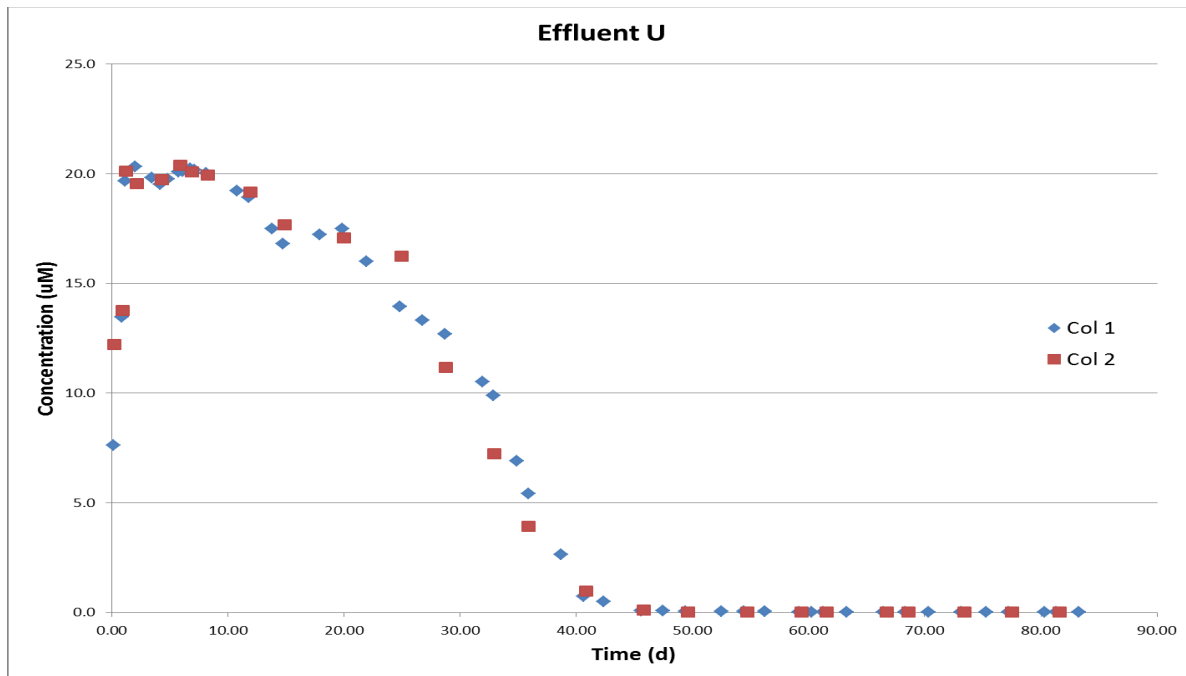


Figure 4.3 Effluent U(VI) concentrations from column 1 (blue diamonds) and column 2 (red squares).

In the shallow aquifer system, extensive sulfate bioreduction appears to interfere with the efficiency of U removal through SRB competition for electron donor and the production of bicarbonate which favors desorption of U. While the sulfate concentrations, ~10 mM, are similar to the Rifle shallow aquifer, only 10 to 20% is removed during the experiment, putatively by bioreduction to sulfide. While the sulfide generated is still more than sufficient to completely react the ~300 µM Fe(II) generated by Fe(III) bioreduction, the persistence of sulfate in the presence of lactate and excess acetate is unlike the Rifle biostimulation behavior.

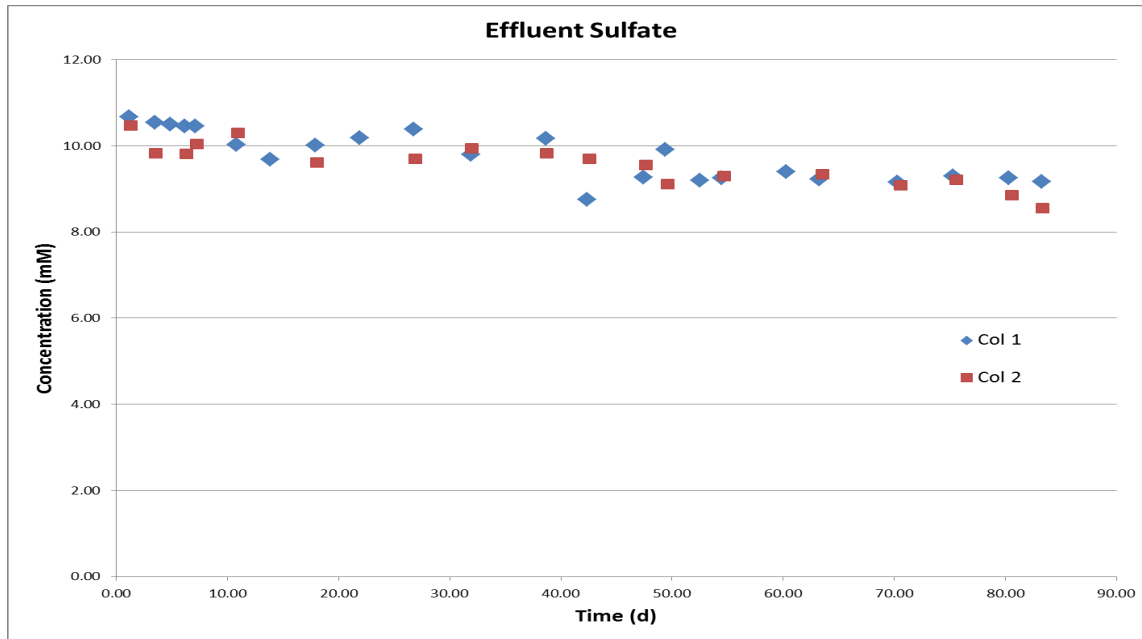


Figure 4.4 Effluent sulfate concentrations from column 1 (blue diamonds) and column 2 (red squares).

### 4.3 Conceptual Bioresorption Model

Based on these observations, a conceptual model of processes controlling the Fe(III), U(VI), and sulfate TEAPs during lactate biostimulation in the column experiments was postulated. A preliminary assumption is that the lactate and acetate electron donors are principally consumed in TEAP reactions involving Fe(III), sulfate, and U(VI).

- Sulfate bioreduction occurs principally through lactate oxidation. This is consistent with the situation at the end of the column experiment when the removal of 1-2 mM sulfate occurs while acetate is largely unreacted. Based on the stoichiometry of the sulfate TEAP reaction with biomass in Fang et al. (2009), this means that 3 to 6 mM lactate is being consumed.
- Two pools of phyllosilicate Fe(III) are used in the model, one pool that is bioavailable for the lactate reaction, and one pool that is bioavailable for the acetate reaction. As only a relatively small amount of lactate is consumed for sulfate bioreduction, the only other TEAP capable of continuously consuming the remainder of the 10 mM influent lactate is through the Fe(III) terminal electron acceptor, which motivated the use of an Fe(III) TEAP reaction that was exclusive to lactate.

Assuming stoichiometric oxidation of lactate to acetate, the absence of lactate in the column effluent after 14 days means that the equivalent of 10 mM acetate is continuously being generated by the lactate oxidation. From day 14 to day 55, effluent acetate concentrations are fairly constant at ~3 mM, after which it increases to ~10 mM by the end of the 83 day experiment. That means that ~7 mM acetate is consumed continuously between 15 and 55 days. Once again, the Fe(III) TEAP was

the most straightforward process capable of continuously consuming ~7 mM acetate. The increase in effluent acetate concentrations to ~10 mM after day 55, however, is consistent with the depletion of the Fe(III) pool. Since Fe(III) must not be limiting to account for the continuous oxidation of the influent lactate, the assumed pool of Fe(III) that is bioavailable for acetate-based reaction must be finite.

- Most of the biogenic Fe(II) is solid-associated. The effluent aqueous Fe(II) concentrations, which peak at ~300  $\mu\text{M}$  after ~30 days represent a small fraction of the biogenic iron. In the Fe(III) TEAP reactions, 4 and 8 moles of Fe(II) are produced for every mole of lactate and acetate oxidized, respectively. Thus, nearly all of the Fe(II) produced through TEAP reactions is not in the effluent. While there are multiple pathways for Fe(II) to be associated with the solid phases, the bioreduction of phyllosilicate Fe(III) (iron-containing clays) in which Fe(III) is reduced in place without the release of aqueous Fe(II) is the simplest. Phyllosilicate Fe(III) has also been shown to be more bioavailable than the crystalline Fe(III) pool (Komlos et al., 2008b).
- Uranium and goethite bioreduction are acetate-based and inhibited by lactate. Unlike the relatively rapid increase in effluent Fe(II) concentrations, U(VI) concentrations do not decrease until lactate is almost completely consumed. This lag in the onset of uranium bioreduction is consistent with lactate inhibition. In the U(VI) TEAP reaction with biomass from Fang et al. (2009), one mole of acetate can bioreduce three moles of U(VI). Thus, only ~7  $\mu\text{M}$  acetate is needed to catalyze the conversion of the 20  $\mu\text{M}$  influent U(VI) concentrations. This is negligible and probably impossible to discern in comparison to the millimolar acetate concentrations.

The reductive dissolution of bioavailable crystalline Fe(III), represented by goethite in the model, is assumed to be the largest source of dissolved Fe(II) in the column. Its contribution to the effluent Fe(II) peak at ~30 days is also consistent with a lagged response from lactate inhibition. As identified in Fang et al. (2009), the amount of goethite reduced to Fe(II) is much greater than the observed aqueous Fe(II) in solution. This means that most of the Fe(II) produced by the acetate-promoted goethite reduction becomes solid associated through adsorption and secondary mineral formation (e.g., FeS, FeCO<sub>3</sub>).

- The progressive increase in the uranium bioreduction rate over time is consistent with a biomass dependent rate. From day 10 to day 40, the progressive U(VI) decrease in the column effluent is consistent with a bioreduction rate that is dependent on the biomass, which is increasing with continuous acetate stimulation. This requires the direct incorporation of biomass into the reaction rate law, i.e., augmenting the dual monod approach with a biomass term.
- The specification of initial Fe(III) concentrations is critically important to match the timing of the effluent acetate behavior. The relatively rapid increase in effluent acetate concentrations to ~8-10 mM after day 55 is consistent with the depletion of

the crystalline and phyllosilicate Fe(III) pools that are bioavailable to the acetate-promoted bioreduction reactions.

We consider this conceptual model a preliminary attempt that should be updated as more details of the biologically-mediated processes become available. While the postulated processes are based on our experience in biostimulation field experiments in shallow aquifers, it should be noted that the hydrobiogeochemistry exhibited in these column experiments using post-ISR sediments from the Kingsville Dome uranium deposit is distinctly different (e.g., lag in U(VI) bioreduction, low sulfate bioreduction in the presence of excess acetate). Thus, alternative conceptual models for the column behaviors are possible.

#### **4.4 Simulator Description**

In order to model how the microbial community will respond in subsurface environments undergoing bioremediation, the microbially-mediated reactions are specified in a reactive transport model that can define the spatial and temporal variability in the biogeochemical environments. We used the HYDROGEOCHEM code (Yeh et al., 2004) to resolve the detailed coupled processes and model the large number of reactive components in the column experiments with the Kingsville Dome post-ISR sediments. HYDROGEOCHEM is a comprehensive simulator of coupled fluid flow, hydrologic transport, heat transfer and biogeochemical reactions under variably saturated conditions in two or three dimensions. It uses a finite element method based on unstructured grids, iteratively solving fluid flow, heat transfer and reactive chemical transport equations. The numerical model incorporates advection, diffusion with Fick's law modified for the inclusion of dispersion, and mixed kinetic and equilibrium reactions. An operator splitting solution method is used for flow, transport, and reactions, each of which employs implicit time-stepping schemes. A general reaction-based approach to biogeochemical processes was implemented in the code so that it can be applied to a wide range of problems (Fang et al., 2003; Fang et al., 2006). Programmed reaction types include aqueous complexation, adsorption-desorption, ion-exchange, oxidation-reduction, precipitation / dissolution and microbially mediated reactions.

HYDROGEOCHEM provided the framework for incorporating and coupling the flow and reactive transport process models for this column study. In particular, the multicomponent biogeochemical solver technology (Fang et al., 2006; Fang et al., 2003) addressed the complexity of mixed kinetic and equilibrium reactions that described the aqueous and surface complexation, redox, mineral precipitation and dissolution, and microbially mediated transformations that were characterized from these experiments.

#### **4.5 Simulation Description**

The modeling of the uranium bioremediation column experiments requires a specification of the hydrologic parameters (e.g., flow rates, porosity, dispersivity), initial solid phase concentrations (terminal electron acceptors, surface complexation sites, adsorbed components, biomass), dissolved initial and inlet concentrations (including lactate, U(VI), Fe(II), sulfate, pH, alkalinity, major ions), and the biogeochemical reaction network.

The conceptual model described in Section 4.3 is translated into a quantitative specification for the simulation of the column experiment. For the 83-day simulation period, the two column experiments are operationally identical with similar behaviors (see previous effluent concentration plots). We chose to model Column L1 but include observations from Columns L1 and L2 in the model comparisons. **Table 4.1** summarizes the hydrologic model attributes including the change in flow rate at day 14.

Table 4.1 Hydrologic parameters for Column 1: Darcy flux, pore velocity, residence time, porosity, and dispersivity. The flow rate to the column changed at day 14; thus, the multiple values represent those before and after that time point.

Parameter	Value
Darcy Flux (pre/post 14 d)	0.47/0.17 cm/h
Pore Velocity (pre/post 14 d)	1.1/0.39 cm/h
Residence Time (pre/post 14 d)	9.9/27 h
Porosity	0.44
Dispersivity	2.0 cm

**Table 4.2** summarizes the solid phase model specification including the initial goethite and phyllosilicate Fe(III) pools. As described previously, the specification of the initial concentrations of the goethite and phyllosilicate Fe(III) are important controls on the rise in unreacted acetate over the last 30 days of the column experiment. The goethite represents the crystalline Fe(III) whereas the phyllosilicate Fe(III) represents the structural iron in clays. The simplest conceptualization was to have (1) one non-limiting phyllosilicate Fe(III) pool (i.e., pool 1) associated exclusively with the lactate-based TEAP reaction and (2) a second phyllosilicate Fe(III) pool (i.e., pool 2) and goethite mineral that are bioavailable exclusively to acetate-based TEAP reactions. The initial mineral concentrations were calibrated to match the timing of the continuous and complete consumption of lactate, the initial consumption of about 70% of the acetate, followed by an increase in unreacted effluent acetate concentrations. The calibrated initial phyllosilicate Fe(III) concentrations appear to be high compared to the iron extractions performed on the pre- and post-biostimulation sediments. Possible explanations range from limitations in characterizing phyllosilicate iron to uncharacterized processes consuming lactate and acetate.

Surface complexation reactions for the adsorption of U(VI), Fe(II), and H<sup>+</sup> are associated with a generic >FeOH surface complex. In the absence of characterization studies for these reactions and initial site density, we use reactions and parameters from a previous study (Yabusaki et al., 2011). The oxidation of lactate and acetate during the biostimulation will produce high bicarbonate concentrations that favor the formation of aqueous uranium complexes over surface complexes, i.e., desorption. The expectation, based on uranium bioremediation field experiments in shallow aquifers is that the combination of U(VI) desorption and bioreduction to solid associated U(IV) will eventually deplete the adsorbed U(VI).

Table 4.2 Initial concentrations of solid phases: goethite, initial phyllosilicate Fe(III) pools, and initial surface complexation site concentrations. Pools 1 and 2 are associated with the lactate- and acetate-based TEAP reactions, respectively. In the model, the goethite and silicate iron in Pool 2 are eventually depleted resulting in the increase in effluent acetate concentration.

Solid Phase Component	Concentration
Goethite	1.3E-5 mol/g
Fe(III)-phyllosilicate (Pool 1)	2.8E-3 mol/g
Fe(III)-phyllosilicate (Pool 2)	1.4E-3 mol/g
>FeOH surface complex	1.0E-5 mol/g
Biomass lactate-based FeRB	3.1E-11 mol/g*
Biomass acetate-based FeRB	3.1E-10 mol/g*
Biomass SRB	3.1E-11 mol/g*
Sorbed U(VI)	3.0E-9 mol/g
Sorbed Fe(II)	1.5E-11 mol/g
Sorbed H+	9.6E-6 mol/g

\*biomass moles based on molecular formula C<sub>5</sub>H<sub>7</sub>O<sub>2</sub>N

Initial aqueous conditions for the modeling are based on measured concentrations in the column experiment (**Table 4.3**).

Table 4.3 Initial dissolved concentrations in the column.

Component	Total Concentration
pH	6.42
carbonate	12.5 mM
Ca	20.2 mM
Fe	26.4 μM
Mg	4.87 mM
Na	32.2 mM
sulfate	11.35 mM
U(VI)	13.5 μM
K	0.558 mM

The initial flow rate for column L1 was ~0.029 ml/min before being lowered to 0.011 ml/min at 14 days. At 0.44 porosity, the residence time increased from less than 10 h to over 1 day; corresponding pore velocities were 1.06 cm/h and 0.39 cm/h before and after day 14 (**Table 4.1**). The average influent concentrations are the same for columns 1 and 2 (**Table 4.4**).

Table 4.4 Average influent concentrations from the reservoir for both column experiments.

Component	Concentration
U	20.2E-6 M
Al	67.0E-6 M
Ca	20.1E-3 M
Mg	5.05 E-3 M
Fe	2.34E-6 M
K	0.785E-3 M
Na	30.5E-3 M
S	10.6E-3 M
Lactate	9.84E-3 M
pH	6.26
Alkalinity	6.28 meq/L
CO <sub>2</sub>	10.6E-6 M

#### 4.6 Biologically-Mediated Processes: Shallow Groundwater Plume versus Deep ISR

The biologically-mediated transfer of electrons to solid phase Fe(III) by FeRB and to aqueous sulfate by SRB provides the energy for cell maintenance, activity, and growth. Introducing lactate and, implicitly, acetate electron donor in solutions passing through the Kingsville Dome sediments stimulates FeRB that catalyze the reduction of Fe(III) mineral but also opportunistically catalyze the reduction of the trace amounts of aqueous U(VI) that are present (Lovley et al., 1991). Reduced uranium [U(IV)] becomes part of the solid phase, most likely as adsorbed surface coatings or uraninite forming on existing grains.

As in the shallow aquifer sediments, aqueous Fe(II) increases very soon after biostimulation is initiated and is attenuated only after sulfide from the bioreduction of sulfate by SRB reacts with Fe(II) to form FeS mineral. This effectively removes Fe(II) from solution. Based on the timing of the decrease in Fe(II) at ~30 days, there is commonality with the shallow aquifer SRB in this lagged appearance of sulfate bioreduction, which is attributed to initially low abundance and a slow growth rate.

There are, however, fundamental differences between the shallow and ISL sediments. The first is the 10-15 day lag in U(VI) bioreduction in the Kingsville Dome column experiment. In the shallow aquifer sediments, U(VI) bioreduction occurs rapidly in tandem with the Fe(III) bioreduction. The model accounts for this lag by 1) limiting U(VI) bioreduction to acetate electron donor (acetate is an intermediate product of lactate oxidation) and 2) using lactate concentration in an inhibition term such that U(VI) bioreduction is active only when lactate concentrations are diminished. Another difference is the very small fraction of sulfate (10-20%) that is bioreduced in the Kingsville Dome sediments in the presence of large excesses of acetate. In the shallow aquifer sediments, the bulk of acetate consumption was attributed to sulfate conversion by SRB. One consequence of the largely unreacted acetate in the system is

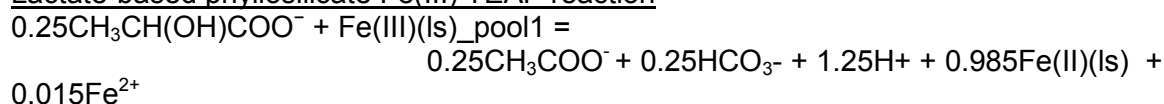
that there is less bicarbonate production. This may be why there is no obvious impact to the U(VI) concentrations due to complexation with bicarbonate that favors U(VI) desorption.

In the presence of elevated alkalinity, Fe(II), and sulfide; and lowered redox potential, calcite and iron sulfide secondary mineral formation are thought to be the most important volumetrically (Li et al., 2009). Lesser amounts of elemental sulfur, from the sulfide promoted dissolution of Fe(III) minerals (Fang et al., 2009), and siderite should also form.

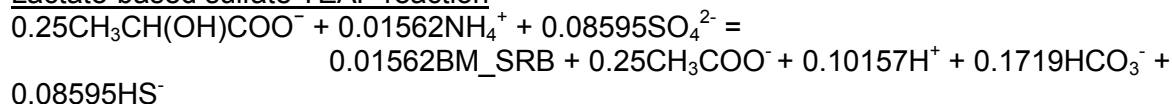
## 4.7 Model Implementation

The simulation of the 83-day lactate biostimulation for column L1 used variable time stepping with a maximum time step of 30 min. The 1-D model domain used to represent the column experiment was 10.5 cm long, comprised of 10 grid cells with uniform 1.05 cm spacing. The influx of lactate was based on the flow rate and influent concentrations. The reactive transport modeling of biostimulated reduction is an adaptation of the reaction network developed for the 2008 field experiment at the Rifle IFRC site (Yabusaki et al., 2011). The principal departure from this reaction network is the addition of the lactate-based TEAP reactions for Fe(III) and sulfate.

### Lactate-based phyllosilicate Fe(III) TEAP reaction



### Lactate-based sulfate TEAP reaction



In this case, the system of equilibrium and kinetic reactions addressed 2 distinct functional microorganisms (i.e., FeRB and SRB), 4 TEAPs (i.e., phyllosilicate Fe(III), poorly crystalline Fe(III), U(VI), and sulfate), 7 minerals (i.e., FeOOH, Fe<sub>3</sub>O<sub>4</sub>, FeS, S, calcite, siderite, uraninite), ~100 biogeochemical species (including surface complexes).

Key assumptions included: 1) acetate-oxidizing FeRB are solely responsible for the bioreduction of aqueous U(VI), 2) SRB are present and active throughout the biostimulation, 3) abiotic uranium reduction is negligible, and 4) geochemistry, including uranium surface complexation, is fully operative during biostimulation (e.g., biomass does not significantly alter geochemical reactivity).

The aqueous initial and boundary conditions were lactate, U(VI), pH, bicarbonate, calcium, magnesium, sodium, potassium, chloride, Fe(II), and sulfate. The initial sorbed U(VI) and Fe(II) were assumed to be in equilibrium with their aqueous counterparts through their respective surface complexation models. U(VI) minerals were not included in the reaction network as they have not been identified in sediment analyses and are undersaturated with respect to the solution chemistry. Other nonaqueous initial conditions include FeRB and SRB biomass,

goethite, 2 pools of phyllosilicate iron and surface complexation sites (**Table 4.2**). Both functional microbial groups, FeRB and SRB, are present and active during the initial period of biostimulation (Callister et al., 2010). The kinetics of the microbially mediated TEAP reactions is of the Monod type with thermodynamic control. The electron donor (i.e., lactate, acetate) consumption rate,  $R_C^{bio}$ , is:

$$R_C^{bio} = - \sum_{eA}^{N_{eA}} \mu_{m,eA} s_C B \left( \frac{C_C}{K_{s,C} + C_C} \right) \left( \frac{C_{eA}}{K_{s,eA} + C_{eA}} \right) f(\Delta G_r)$$

where

- $N_{eA}$  = number of terminal electron acceptors
- $s_C$  = stoichiometric coefficient of electron donor in the TEAP reaction
- $C_C$  = electron donor concentration
- $B$  = biomass concentration of microorganism mediating the TEAP reaction
- $C_{eA}$  = terminal electron acceptor concentration
- $\mu_{m,eA}$  = electron donor oxidation rate for the terminal electron acceptor
- $K_{s,C}$  = half-saturation coefficient for electron donor
- $K_{s,eA}$  = half-saturation coefficient for the terminal electron acceptor
- $f(\Delta G_r)$  =  $1 - \exp[(\Delta G_r - \Delta G_{min})/RT]$ 
  - $\Delta G_r$  = free energy change of the corresponding TEAP reaction
  - $\Delta G_{min}$  = minimum free energy change required to drive ATP synthesis
  - $R$  = gas constant
  - $T$  = absolute temperature

The FeRB and SRB are assumed to be attached populations whose biomass is a control on the rates of the TEAP reactions they catalyze. The initial FeRB and SRB biomass amounts are initially low (**Table 4.2**). As the FeRB and SRB biomass grow, the respective TEAP reaction rates increase commensurately. A first-order decay model ( $dB/dt = -kB$ ) is used to describe the loss of biomass via decay. A maximum rate is used to limit the biomass-dependent reduction rates.

#### 4.7.1 Uranium Speciation

Table 4.5 Uranium aqueous complexation reactions and formation constants.

Reaction	logK (I = 0) <sup>(a)</sup>
<b>Aqueous Species</b>	
$\text{UO}_2^{2+} + \text{H}_2\text{O} = \text{UO}_2\text{OH}^+ + \text{H}^+$	-5.25
$\text{UO}_2^{2+} + 2\text{H}_2\text{O} = \text{UO}_2(\text{OH})_{2(\text{aq})} + 2\text{H}^+$	-12.15
$\text{UO}_2^{2+} + 3\text{H}_2\text{O} = \text{UO}_2(\text{OH})_3^- + 3\text{H}^+$	-20.25
$\text{UO}_2^{2+} + 4\text{H}_2\text{O} = \text{UO}_2(\text{OH})_4^{2-} + 4\text{H}^+$	-32.40
$2\text{UO}_2^{2+} + \text{H}_2\text{O} = (\text{UO}_2)_2\text{OH}^{3+} + \text{H}^+$	-2.70
$2\text{UO}_2^{2+} + 2\text{H}_2\text{O} = (\text{UO}_2)_2(\text{OH})_2^{2+} + 2\text{H}^+$	-5.62
$3\text{UO}_2^{2+} + 4\text{H}_2\text{O} = (\text{UO}_2)_3(\text{OH})_4^{2+} + 4\text{H}^+$	-11.90
$3\text{UO}_2^{2+} + 5\text{H}_2\text{O} = (\text{UO}_2)_3(\text{OH})_5^+ + 5\text{H}^+$	-15.55
$3\text{UO}_2^{2+} + 7\text{H}_2\text{O} = (\text{UO}_2)_3(\text{OH})_7^- + 7\text{H}^+$	-32.20
$4\text{UO}_2^{2+} + 7\text{H}_2\text{O} = (\text{UO}_2)_4(\text{OH})_7^+ + 7\text{H}^+$	-21.90
$\text{UO}_2^{2+} + \text{CO}_3^{2-} = \text{UO}_2\text{CO}_3(\text{aq})$	9.94
$\text{UO}_2^{2+} + 2\text{CO}_3^{2-} = \text{UO}_2(\text{CO}_3)_2^{2-}$	16.61
$\text{UO}_2^{2+} + 3\text{CO}_3^{2-} = \text{UO}_2(\text{CO}_3)_3^{4-}$	21.84
$3\text{UO}_2^{2+} + 6\text{CO}_3^{2-} = (\text{UO}_2)_3(\text{CO}_3)_6^{6-}$	54.00
$2\text{UO}_2^{2+} + \text{CO}_3^{2-} + 3\text{H}_2\text{O} = (\text{UO}_2)_2\text{CO}_3(\text{OH})_3^- + 3\text{H}^+$	-0.85
$3\text{UO}_2^{2+} + \text{CO}_3^{2-} + 3\text{H}_2\text{O} = (\text{UO}_2)_3\text{CO}_3(\text{OH})_3^+ + 3\text{H}^+$	0.66
$\text{UO}_2^{2+} + \text{Cl}^- = \text{UO}_2\text{Cl}^+$	0.17
$\text{Ca}^{2+} + \text{UO}_2^{2+} + 3\text{CO}_3^{2-} = \text{CaUO}_2(\text{CO}_3)_3^{2-}$	25.40 <sup>(b)</sup>
$2\text{Ca}^{2+} + \text{UO}_2^{2+} + 3\text{CO}_3^{2-} = \text{Ca}_2\text{UO}_2(\text{CO}_3)_3^0(\text{aq})$	30.55 <sup>(b)</sup>
$\text{UO}_2^{2+} + 2\text{Cl}^- = \text{UO}_2\text{Cl}_2(\text{aq})$	-1.10
$\text{Mg}^{2+} + \text{UO}_2^{2+} + 3\text{CO}_3^{2-} = \text{MgUO}_2(\text{CO}_3)_3^{2-}$	26.11 <sup>(c)</sup>
$\text{UO}_2^{2+} + \text{SO}_4^{2-} = \text{UO}_2(\text{SO}_4)\text{aq}$	3.15
$\text{UO}_2^{2+} + 2\text{SO}_4^{2-} = \text{UO}_2(\text{SO}_4)_2^{2-}$	4.14

<sup>a</sup> Values from Guillaumont et al. (2003), unless otherwise indicated.

<sup>b</sup> Bernhard et al. (2001).

<sup>c</sup> Dong and Brooks (2006).

Table 4.6 Uranium surface complexation reactions and formation constants.

Reaction	logK (estimated*)
<b>Surface Species</b>	
$\text{SSOH} + \text{UO}_2^{2+} = \text{SSOUO}_2^+ + \text{H}^+$	12.28
$\text{SOH} + \text{UO}_2^{2+} = \text{SOUO}_2^+ + \text{H}^+$	6.95
$\text{WOH} + \text{UO}_2^{2+} = \text{WOUO}_2^+ + \text{H}^+$	2.74
$\text{SSOH} + \text{UO}_2^{2+} + \text{H}_2\text{O} = \text{SSOUOOH} + 2\text{H}^+$	0.033
$\text{SOH} + \text{UO}_2^{2+} + \text{H}_2\text{O} = \text{SOUOOH} + 2\text{H}^+$	-2.12
$\text{WOH} + \text{UO}_2^{2+} + \text{H}_2\text{O} = \text{WOUOOH} + 2\text{H}^+$	-5.01
SSOH denoting very strong binding sites: 0.01% of total sites	
SOH denoting strong binding sites: 0.1% of total sites	
WOH denoting weak binding sites: 99.89% of total sites	

\*Values from Fang et al. (2009)

## 4.7.2 Major Ion Reactions

Table 4.7 Major ion reactions and formation constants

Reaction	LogK
$\text{CH}_3\text{COO}^- + \text{H}^+ = \text{AcH}$	4.76
$\text{Ca}^{2+} + \text{H}_2\text{O} = \text{CaOH}^+ + \text{H}^+$	-12.60
$\text{Ca}^{2+} + \text{CH}_3\text{COO}^- = \text{CaCH}_3\text{COO}^+$	1.18
$\text{Ca}^{2+} + \text{CO}_3^{2-} + \text{H}^+ = \text{CaHCO}_3^+$	11.33
$\text{Ca}^{2+} + \text{CO}_3^{2-} = \text{CaCO}_3$	3.15
$\text{Ca}^{2+} + \text{SO}_4^{2-} = \text{CaSO}_4$	2.31
$\text{CO}_3^{2-} + 2\text{H}^+ = \text{H}_2\text{CO}_3$	16.68
$\text{CO}_3^{2-} + \text{H}^+ = \text{HCO}_3^-$	10.33
$\text{Fe}^{2+} + \text{H}_2\text{O} = \text{FeOH}^+ + \text{H}^+$	-9.50
$\text{CH}_3\text{COO}^- + \text{Fe}^{2+} = \text{FeCH}_3\text{COO}^+$	1.82
$\text{Fe}^{2+} + \text{CO}_3^{2-} + \text{H}^+ = \text{FeHCO}_3^+$	12.33
$\text{Fe}^{2+} + \text{CO}_3^{2-} = \text{FeCO}_3(\text{aq})$	5.50
$\text{Fe}^{2+} + 2\text{CO}_3^{2-} = \text{Fe}(\text{CO}_3)_2^{2-}$	7.10
$\text{Fe}^{2+} + \text{SO}_4^{2-} = \text{FeSO}_4$	2.25
$\text{Fe}^{2+} + \text{Cl}^- = \text{FeCl}^+$	0.90
$\text{Fe}^{2+} + 2\text{HS}^- = \text{Fe}(\text{HS})_2(\text{aq})$	8.95
$\text{Fe}^{2+} + 3\text{HS}^- = \text{Fe}(\text{HS})_3^-$	10.99
$\text{HS}^- + \text{H}^+ = \text{H}_2\text{S}(\text{aq})$	6.99
$\text{HS}^- = \text{H}^+ + \text{S}^{2-}$	-12.92
$\text{K}^+ + \text{SO}_4^{2-} = \text{KSO}_4^-$	0.85
$\text{Mg}^{2+} + \text{H}_2\text{O} = \text{MgOH}^+ + \text{H}^+$	-11.79
$\text{CH}_3\text{COO}^- + \text{Mg}^{2+} = \text{MgCH}_3\text{COO}^+$	1.14
$\text{CO}_3^{2-} + \text{Mg}^{2+} + \text{H}^+ = \text{MgHCO}_3^+$	11.40
$\text{CO}_3^{2-} + \text{Mg}^{2+} = \text{MgCO}_3(\text{aq})$	2.98
$\text{Mg}^{2+} + \text{SO}_4^{2-} = \text{MgSO}_4(\text{aq})$	2.25
$\text{Na}^+ + \text{CH}_3\text{COO}^- = \text{NaCH}_3\text{COO}$	-0.18
$\text{Na}^+ + \text{CO}_3^{2-} + \text{H}^+ = \text{NaHCO}_3(\text{aq})$	10.08
$\text{CO}_3^{2-} + \text{Na}^+ = \text{NaCO}_3^-$	1.27
$\text{Na}^+ + \text{SO}_4^{2-} = \text{NaSO}_4^-$	0.70
$\text{NH}_4^+ = \text{NH}_3(\text{aq}) + \text{H}^+$	-9.25
$\text{NH}_4^+ + \text{SO}_4^{2-} = \text{NH}_4\text{SO}_4^-$	1.11
$\text{SO}_4^{2-} + \text{H}^+ = \text{HSO}_4^-$	1.99
$\text{H}_2\text{O} = \text{OH}^- + \text{H}^+$	-14.00
$>\text{FeOH} + \text{H}^+ = >\text{FeOH}_2^+$	7.47
$>\text{FeOH} = >\text{FeO}^- + \text{H}^+$	-9.51
$>\text{FeOH} + \text{Fe}^{++} = >\text{FeOFe}^+ + \text{H}^+$	-5.00
$>\text{FeOH} + \text{Fe}^{++} + \text{H}_2\text{O} = >\text{FeOFeOH} + 2\text{H}^+$	-11.96
$\text{CO}_2(\text{aq}) = \text{CO}_2(\text{g})$	2.1

## 4.7.4 Kinetic Reactions

Table 4.8 Kinetic reactions, rate laws, and reaction parameters.

Kinetic Reactions	Rate Laws*	Parameters
$\text{Ca}^{2+} + \text{HCO}_3^- = \text{Calcite(s)} + \text{H}^+$	$r_i = \begin{cases} k_i (\Omega_i - 1) & \text{for } \Omega_i \geq 1 \\ k_{-i} [Q_i] (\Omega_i - 1) & \text{for } \Omega_i < 1 \end{cases}$	$K_i = 1.644 \times 10^{-7} \text{ Md}^{-1}$ $k_i = 1.37 \times 10^{-6} \text{ d}^{-1}$ $K_{\text{sp}} = 71.48$
$\text{Fe}^{2+} + \text{HCO}_3^- = \text{Siderite(s)} + \text{H}^+$	$r_i = \begin{cases} k_i (\Omega_i - 1) & \text{for } \Omega_i \geq 1 \\ k_{-i} [Q_i] (\Omega_i - 1) & \text{for } \Omega_i < 1 \end{cases}^b$	$k_i = 1.37 \times 10^{-6} \text{ Md}^{-1}$ $k_{-i} = 1.37 \times 10^{-7} \text{ d}^{-1}$ $K_{\text{sp}} = 0.6504$
$\text{Fe}^{2+} + \text{HS}^- = \text{FeS(s)} + \text{H}^+$	$r_i = \begin{cases} k_i (\Omega_i - 1) & \text{for } \Omega_i \geq 1 \\ k_{-i} [Q_i] (\Omega_i - 1) & \text{for } \Omega_i < 1 \end{cases}$	$k_i = 5.11 \times 10^{-6} \text{ Md}^{-1}$ $k_{-i} = 6.85 \times 10^{-6} \text{ d}^{-1}$ $K_{\text{sp}} = 2.25\text{e-}4$
$0.125 \text{ CH}_3\text{COO}^- + \text{Fe(III)(ls)}_{\text{pool2}} + 0.5 \text{ H}_2\text{O} = 0.25 \text{ HCO}_3^- + 1.0 \text{ Fe(II)(ls)} + 1.125 \text{ H}^+$	$r = \mu_i [\text{acetate}] [\text{lactate}]$	$\mu_i = 1.6 \times 10^4 \text{ M}^{-1} \text{ d}^{-1}$
$0.125 \text{ CH}_3\text{COO}^- + \text{FeOOH(s)} + 1.875 \text{ H}^+ = \text{Fe}^{2+} + 1.5 \text{ H}_2\text{O} + 0.25 \text{ HCO}_3^-$	$r = \mu_i [\text{FeOOH}] [\text{Ac}] \frac{K_i}{K_i + [\text{lactate}]}$	$\mu_i = 40.0 \text{ M}^{-1} \text{ d}^{-1}$ $K_i = 1.3 \times 10^{-3} \text{ M}$
$0.125 \text{ CH}_3\text{COO}^- + 0.3538 \text{ H}_2\text{O} + 0.0113 \text{ NH}_4^+ + 0.3875 \text{ UO}_2^{2+} = 0.0113 \text{ BM}_{\text{iron}} + 0.855 \text{ H}^+ + 0.1938 \text{ HCO}_3^- + 0.3875 \text{ UO}_2(\text{s})$	$r = \mu_{m,eA} B \left( \frac{C_c}{K_{s,C} + C_c} \right) \left( \frac{C_{eA}}{K_{s,eA} + C_{eA}} \right) \left( \frac{K_i}{K_i + [\text{lactate}]} \right)$	$\mu_{m,eA} = 0.8 \text{ Md}^{-1}$ $K_{s,C} = 1 \times 10^{-9} \text{ M}$ $K_{s,eA} = 5.0 \times 10^{-5} \text{ M}$ $K_i = 3.0 \times 10^{-5} \text{ M}$
$0.25 \text{ CH}_3\text{CH(OH)COO}^- + 0.01562 \text{ NH}_4^+ + 0.08595 \text{ SO}_4^{2-} = 0.01562 \text{ BM}_{\text{lac}} + 0.25 \text{ CH}_3\text{COO}^- + 0.10157 \text{ H}^+ + 0.1719 \text{ HCO}_3^- + 0.08595 \text{ HS}^-$	$r = \mu_{m,eA} B \left( \frac{C_c}{K_{s,C} + C_c} \right) \left( \frac{C_{eA}}{K_{s,eA} + C_{eA}} \right)$	$\mu_{m,eA} = 2.0 \times 10^{-2} \text{ Md}^{-1}$ $K_{s,C} = 5.0 \times 10^{-4} \text{ M}$ $K_{s,eA} = 1.0 \times 10^{-5} \text{ M}$
$0.25 \text{ CH}_3\text{CH(OH)COO}^- + \text{Fe(III)(ls)}_{\text{pool1}} = 0.25 \text{ CH}_3\text{COO}^- + 0.25 \text{ HCO}_3^- + 1.25 \text{ H}^+ + 0.985 \text{ Fe(II)(ls)} + 0.015 \text{ Fe}^{2+}$	$r = \mu_i [\text{Fe}_{\text{ls}}] [\text{lactate}] [\text{BM}_{\text{lac}}]$	$\mu_i = 2.0 \times 10^2 \text{ M}^{-2} \text{ d}^{-1}$

\*Reaction-rate formulations for calcite, siderite, and iron sulfide are functions of the saturation state follow Hunter et al. (1998).

### Nomenclature

- $i$  = the  $i$ -th mineral phase
- $r_i$  = the rate of the mineral reaction
- $k_i$  = the mineral precipitation rate [ $\text{ML}^{-3}\text{T}^{-1}$ ]
- $k_{-i}$  = the mineral dissolution rate [ $\text{ML}^{-3}\text{T}^{-1}$ ]
- $Q_i$  = the concentration of the  $i$ -th mineral phase [ $\text{ML}^{-3}$ ]
- $\Omega_i$  = the saturation index of the  $i$ -th mineral phase
- $K_{\text{sp}}$  = saturation constant

$r$	=	the rate of bioremediated reaction
$C_c$	=	electron donor concentration
$C_{eA}$	=	terminal electron acceptor concentration
$\mu_{m,eA}$	=	electron donor oxidation rate for the terminal electron acceptor
$K_{s,C}$	=	half-saturation coefficient for electron donor
$K_{s,eA}$	=	half-saturation coefficient for the terminal electron acceptor
$\mu_i$	=	rate coefficient
$k_i$	=	Inhibition constant [M]
$[Ac]$	=	Acetate concentration [M]
$[FeOOH]$	=	Goethite concentration [M]
$[Fe_{ls}]$	=	Layer silicate iron (III) concentration [M]
$[lactate]$	=	Lactate concentration [M]
$[BM_{lac}]$	=	Lactate related biomass concentration [M]

## 4.8 Biostimulation Modeling Approach for the Column Experiments

The goal of the modeling is to interpret the observed behavior of the Kingsville Dome sediment column experiments by developing a reaction network and parameterization to simulate the bioreduction of sulfate, Fe(III), and U(VI) in the lactate biostimulation column experiments using Kingsville Dome sediments. While column experiments typically use a finer-grained subset of the field particle size distribution, the sediments recovered from the Kingsville Dome drilling were sand size and smaller (see Table 3.6), which allowed direct use in the column studies.

In the absence of a well-instrumented bioremediation field experiments at an ISR site, the column experiments were intended to provide basic information on the potential for bioremediation of uranium ISR sites. The recognition here and stated in Chapter 2 is that laboratory conditions are not necessarily representative of the field conditions that control the behavior of uranium and other components of interest at ISR sites. In this case, preserved post-ISR sediments recovered from the Kingsville aquifer are used in column experiments where indigenous microorganisms are stimulated with lactate to catalyze the conversion of aqueous U(VI) to immobile U(IV). While lactate is commonly used as an electron donor, it should be recognized that the specific electron donor – terminal electron acceptor – microorganism – geochemistry combination yields specific behaviors. The first degradation product of lactate is acetate, which is also a commonly used electron donor. So in general, there will need to be two sets of microbially-mediated TEAP reactions, one for lactate and one for acetate (**Table 4.8**).

## 4.9 Column Simulation Results

In the model, lactate is consumed in the sulfate and phyllosilicate Fe(III) TEAP reactions. The continuously influent 10 mM lactate is rapidly consumed over the first 14 days at an

increasing rate (**Figure 4.5**). The rapid drop in effluent lactate concentrations between 12 and 14 days is due to a decrease in the influent flow rate from 0.03 ml/min to 0.011 ml/min. The increase in residence time from 10 to 27 h allowed nearly complete lactate consumption by day 14. From day 14 to the end of the 83-day biostimulation stage of the experiment, the continuously influent 10 mM lactate is essentially completely consumed during the 1.1 day transit through the column.

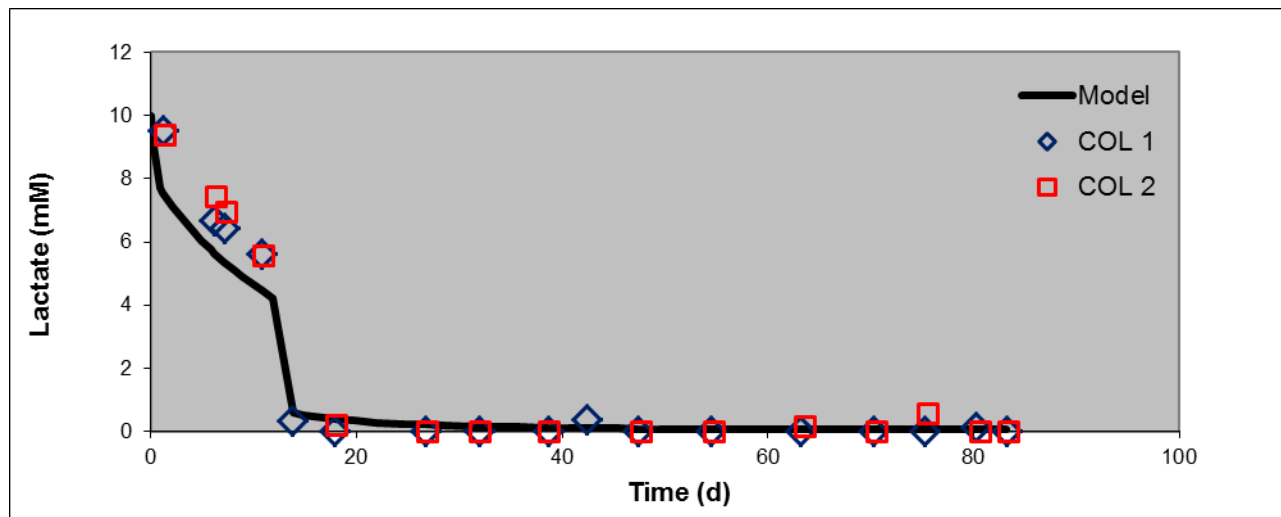


Figure 4.5 Lactate concentrations in column effluent: comparison of model and observations from columns 1 and 2.

Acetate is being progressively produced within the column as lactate is transported by the flow and oxidized by FeRB and SRB via the lactate-based phyllosilicate Fe(III) and sulfate TEAP reactions, respectively. From day 15 to 55, effluent acetate concentrations are ~3 mM. This implies that ~7 mM acetate, of the 10 mM acetate produced by the complete oxidation of the influent 10 mM lactate, was being consumed. In the model, there are three acetate-based TEAP reactions. Two are Fe(III) reactions: goethite (representative of the bioavailable crystalline Fe(III) terminal electron acceptor) and phyllosilicate Fe(III) (iron containing clays). The third is for the U(VI) TEAP reaction. All three modeled TEAP reactions are mediated by FeRB. After day 55, acetate concentrations rapidly rise to 9 to 10 mM in column L1 and 7-8 mM increasing to over 9 mM in column L2 (**Figure 4.6**). The model accomplishes this behavior through the sequential depletion of the bioavailable phyllosilicate Fe(III) and goethite. In this case, the acetate-based phyllosilicate Fe(III) TEAP reaction rate is faster resulting in progressive depletion of bioavailable Fe(III) from the front end of the column as compared to the acetate-based goethite TEAP reaction which is slower resulting in higher depletion at the effluent end of the column.

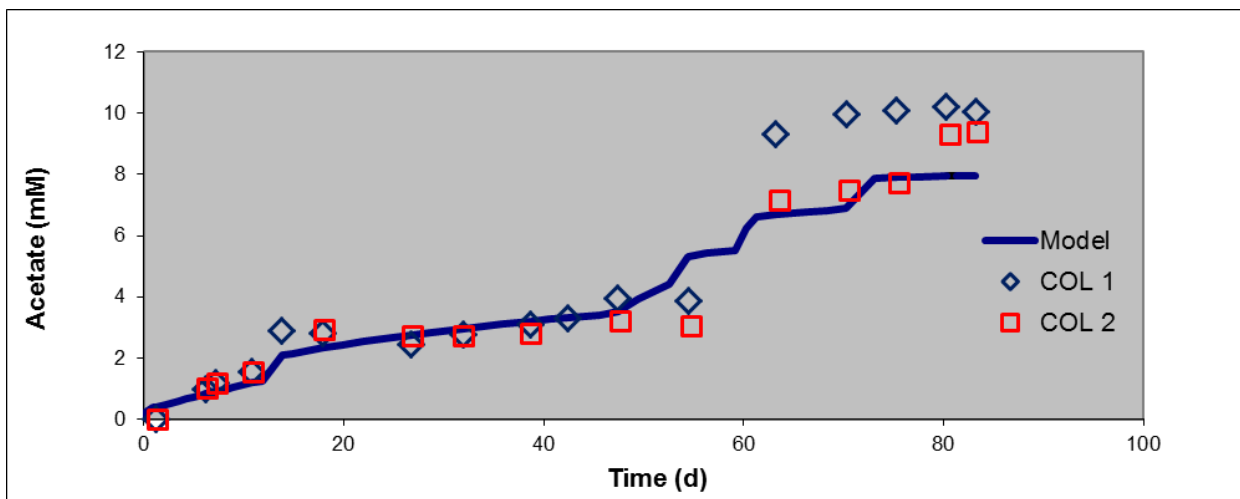


Figure 4.6 Acetate concentrations in column effluent: comparison of model and observations from columns 1 and 2.

There is an initial transient pulse of effluent  $\sim 60 \mu\text{M}$  Fe(II) at 2 days that is not captured by the model (**Figure 4.7**). This can occur when sediments are first exposed to flowing solution and is observed in column L5 (Figure 3.10) which did not undergo bioreduction. The column experiment observations appear to settle down after 4 days whereupon the effluent Fe(II) steadily increases with the rate of increase slowed by the drop in flow rate from 0.03 ml/min to 0.011 ml/min at day 14. Peak Fe(II) is  $\sim 300 \mu\text{M}$  occurring at 30 days for column L1 and 25 days for column L2. Prior to the drop in flow rate, the modeled effluent Fe(II) increases relatively slowly to  $34 \mu\text{M}$ . After the drop in flow rate the additional residence time allows a higher rate of Fe(III) bioreduction resulting in a relatively rapid climb in predicted effluent Fe(II) to  $\sim 300 \mu\text{M}$  after 22 days. The decline in the Fe(II) after the peak is attained occurs during a period of steady consumption of 10 mM lactate and 7 mM acetate (15 to 55 days). During this period, the principal pools of bioavailable terminal electron acceptors (i.e., goethite, phyllosilicate Fe(III) and sulfate) in the model are not limiting. The progressive increase in SRB biomass has resulted in an increasing amount of sulfide being produced through the sulfate TEAP reaction to react with the Fe(II) to form FeS mineral. This is because the sulfate TEAP reaction rate law has a biomass dependent term. As more and more sulfide is produced, more and more Fe(II) is removed from solution until day 45, when the Fe(II) is largely removed from solution. While the model does reproduce the general trend of the observed Fe(II) breakthrough, including the peak effluent Fe(II) concentration, the temporal width of the simulated pulse is not as wide as observed in columns L1 and L2. In the model, there is a trade-off between capturing the peak, which is the net result of the three Fe(III) (goethite and 2 phyllosilicate pools) TEAP reactions and rates and one sulfate TEAP reaction and rate; and capturing the total amount of Fe(II) liberated by bioreduction. This is further constrained by the eventual depletion of the bioavailable acetate-based goethite and Fe(III) terminal electron acceptor pools.

In the model there is significantly more Fe(II) produced than is observed in solution. The Fe(III) TEAP reactions reduce 4 moles and 8 moles of Fe(III) for every mole of lactate and acetate consumed, respectively. That means that the equivalent of at least  $\sim 75 \text{ mM}$  Fe(II) is being produced at the height of lactate and acetate consumption. The phyllosilicate Fe(III) is generally considered to be reduced in place in the layer silicate clay structure. Conversely, the

goethite in the acetate-based Fe(III) TEAP reaction is assumed to be reductively dissolved, liberating Fe(II) in solution. Solid phase reactions involving the formation of secondary minerals (e.g., FeS, siderite) and Fe(II) surface complexation effectively remove the bulk of Fe(II) liberated into solution.

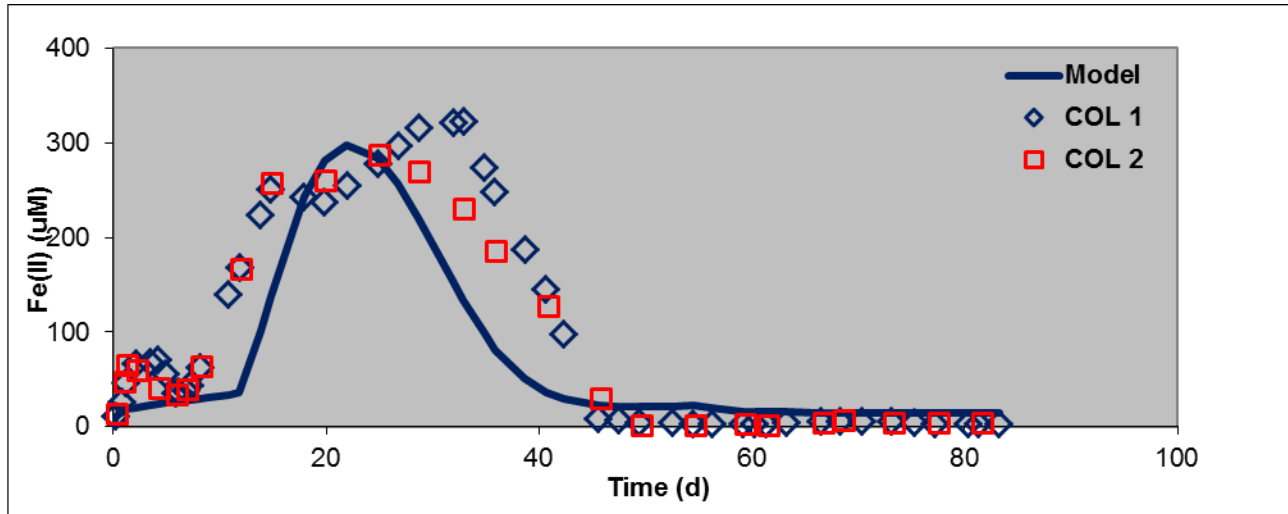


Figure 4.7 Fe(II) concentrations in column effluent: comparison of model and observations from columns 1 and 2.

In the model, the bioreduction of sulfate is lactate-based and active from the beginning of the biostimulation. Prior to the drop in the flow rate, the modeled sulfate bioreduction removed a nearly constant 0.75 mM sulfate from the influent solution. The modeled sulfate removal increased to ~1.5 mM after the drop in flow rate, which allowed more reaction time. However, the modeled sulfate removal slowly decreased to ~1.0 mM by the end of the experiment, due to slowly increasing lactate consumption in the Fe(III) TEAP which made less lactate available for the sulfate TEAP reaction. Over the course of the experiment, the removal of sulfate is always less than 2 mM of the 10.65 mM influent sulfate concentration (**Figure 4.8**). As the bioreduction of one mole of sulfate results in one mole of sulfide, even 1-2 mM of sulfide is sufficient to react with essentially all of the aqueous Fe(II) in the column. The stoichiometry of the sulfate TEAP reaction consumes nearly 3 moles of lactate for every mole of sulfate reduced. That means that 3 to 6 mM of the 10 mM influent lactate is consumed in the sulfate TEAP. The remainder of the lactate is consumed in the phyllosilicate Fe(III) TEAP.

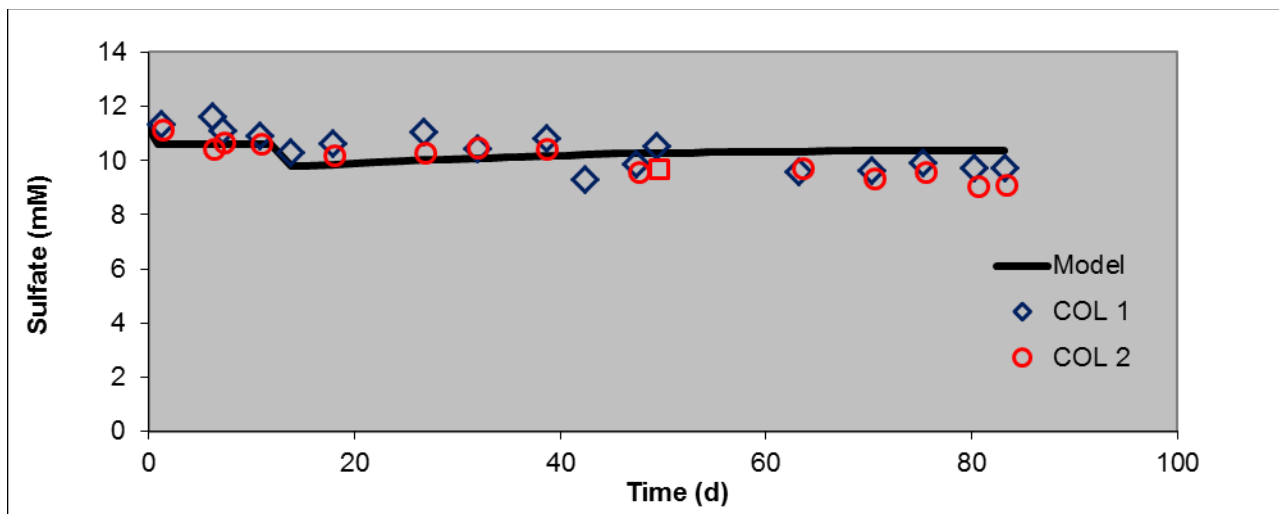


Figure 4.8 Sulfate concentrations in column effluent: comparison of model and observations from columns 1 and 2.

The continuous influent 20  $\mu\text{M}$  U(VI) is attenuated by precipitation and adsorption. In the model, U(VI) bioreduction via the acetate-based TEAP reaction is the dominant removal mechanism. Until day  $\sim 14$ , effluent U(VI) exhibits little attenuation from the influent 20  $\mu\text{M}$  concentration. The onset of U(VI) attenuation corresponds to the time when lactate becomes largely depleted (**Figure 4.9**). The model accomplishes this lag in U(VI) removal by using the presence of lactate to inhibit the U(VI) bioreduction. Thus, U(VI) bioreduction will be significant only where lactate has been sufficiently oxidized. The rate of U(VI) bioreduction increases with time until  $\sim$ day 40, when U(VI) in the effluent becomes negligible. In the model, the increasing rate of U(VI) bioreduction is the result of a biomass-dependent rate law for the acetate-based U(VI) TEAP reaction. FeRB biomass increases with the continuously influent lactate. In the model, uraninite is produced throughout the column and can account for up to 99.98% of the solid phase uranium. This is because of 1) the reduction kinetics, which allow more reaction in a transported fluid parcel with longer residence time (equivalently deeper transport into the column), and 2) the removal of U(VI) from solution via bioreduction lowers aqueous concentrations, which drives more U(VI) desorption.

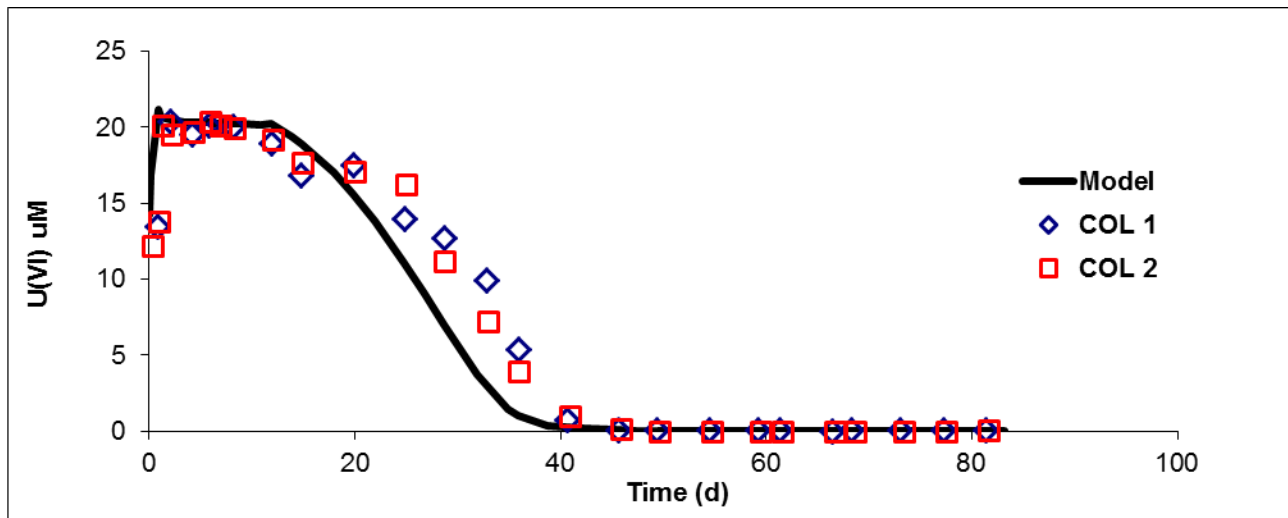


Figure 4.9 U(VI) concentrations in column effluent: comparison of model and observations from columns 1 and 2.

Model-predicted spatial distributions of solid-associated components at the end of the 83-day biostimulation period are shown in Figures 4.10-4.13. There is considerable spatial variation in these concentrations that reflects the microbial reaction kinetics. The introduction of lactate allows the lactate-based bioreduction reactions to consume phyllosilicate Fe(III) and sulfate, with the highest rates nearer the influent end of the column where the lactate concentrations are the highest. Consequently, the lactate-based phyllosilicate Fe(III) is progressively consumed from the influent end of the column. As lactate is transported through the column these biologically-mediated lactate oxidation reactions produce acetate. As a result, the acetate-based bioreduction of goethite and U(VI) occurs deeper into the column away from the column inlet. In this case, goethite is progressively depleted beginning at the column outlet.

At the end of the 83-day simulation, FeS mineral has precipitated throughout the column with the highest abundance nearer the column inlet (**Figure 4.10**). At this location, the lactate-based sulfate bioreduction has produced high concentrations of sulfide which react with the aqueous biogenic Fe(II) to form the FeS mineral. This result is qualitatively consistent with the Table 3.8B trend of higher solid phase Fe(II) and Table 3.8C trend of higher solid phase S concentrations near the influent end of the column.

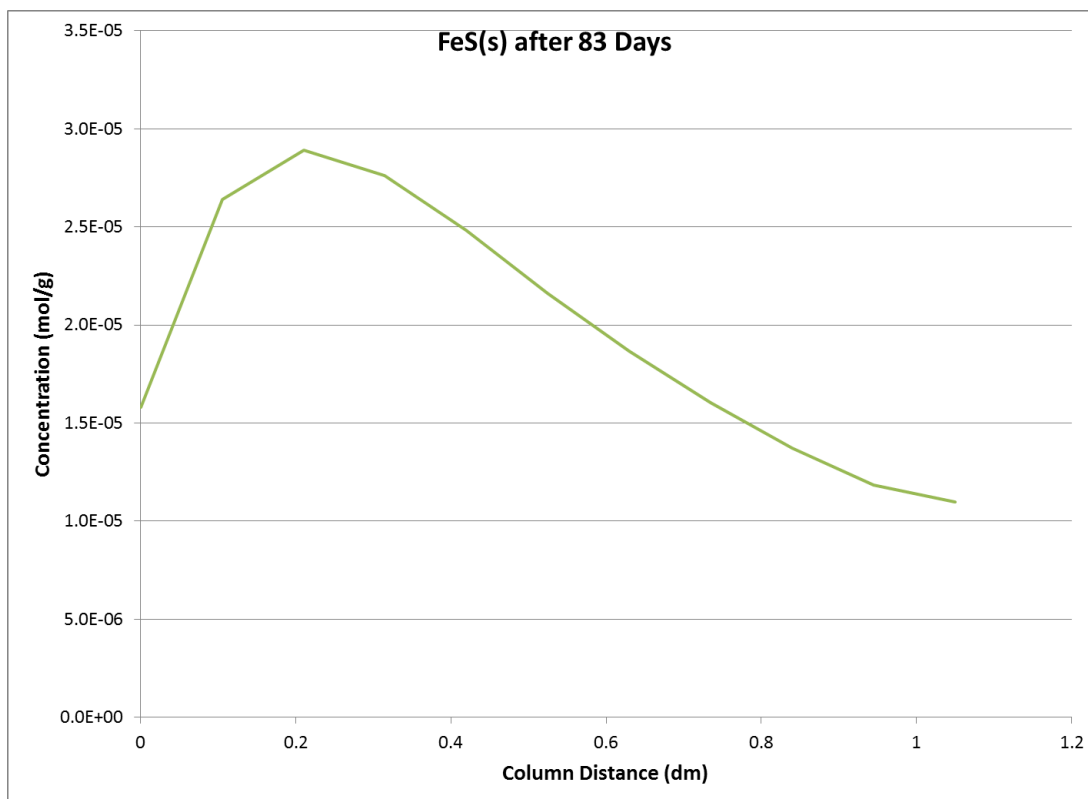


Figure 4.10 FeS(s) abundance as a function of distance from column entrance at the end of the 83-day biostimulation. (1 dm = 10 cm)

During the 83-day simulation, adsorbed U(VI) desorbs from sediments throughout the column but is preferentially desorbed beginning from the effluent end of the column (**Figure 4.11**). This is due to 1) the progressive increase in bicarbonate concentrations as lactate and acetate continuously oxidize while being transported through the column, and 2) the acetate-based bioreduction of aqueous U(VI). In the first case, the elevated bicarbonate concentrations thermodynamically favor the formation of U(VI) aqueous complexes over surface complexes. In the second case, the bioreduction of aqueous U(VI) to solid-associated U(IV) effectively removes U(VI) from solution, which also drives further desorption of adsorbed U(VI). Note that towards the end of the experiment when goethite and phyllosilicate Fe(III) pools for acetate bioreduction are being depleted, acetate oxidation is limited, which decreases the bicarbonate production and U(IV) conversion.

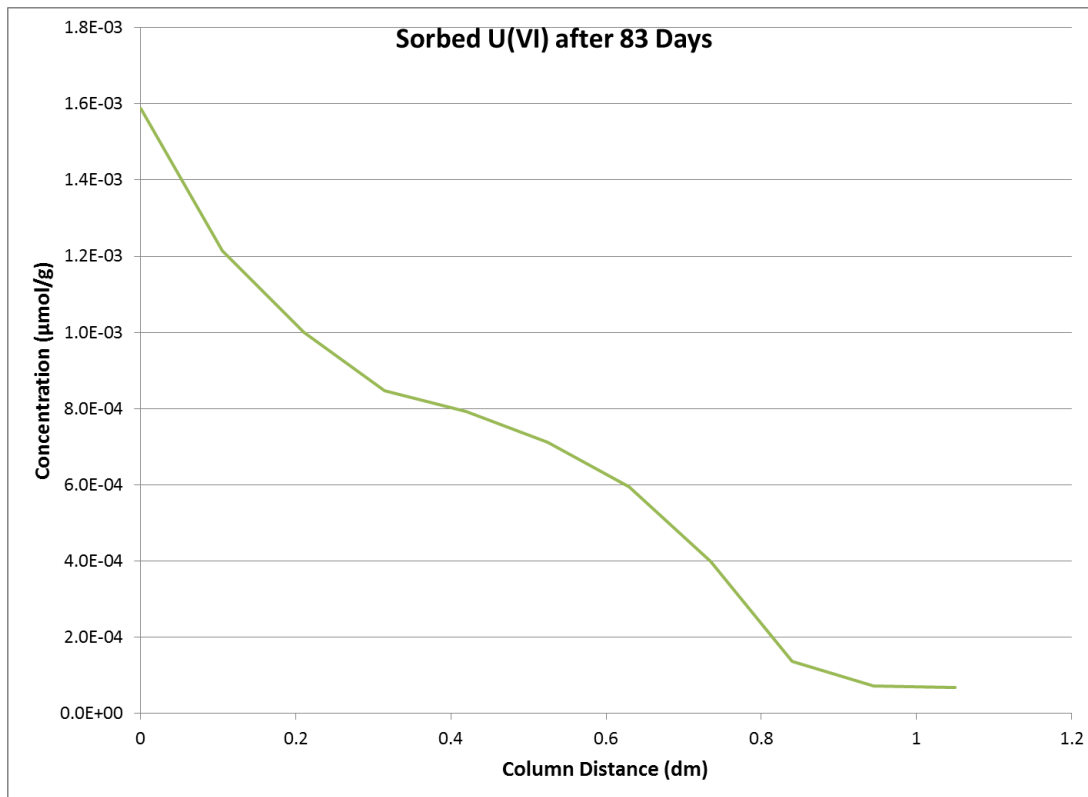


Figure 4.11 Sorbed U(VI) abundance as a function of distance from column entrance at the end of the 83-day biostimulation.

At the end of the 83-day simulation, solid-associated U(IV) has a peak concentration 2 cm from the effluent end of the column (**Figure 4.12**). Since effluent acetate concentrations at this time are approaching the stoichiometric conversion from lactate (i.e., acetate is largely unreacted), the U(IV) peak away from the column outlet is the result of limited availability of aqueous U(VI) beyond this location. This is consistent with the depletion of sorbed U(VI) towards the end of the column (**Figure 4.11**). The solid phase analyses of the post-biostimulation column sediments in Table 3.8A identified the peak U(IV) concentrations in the upgradient half of the column. This can happen if the U(VI) bioreduction rate is higher than in the model.

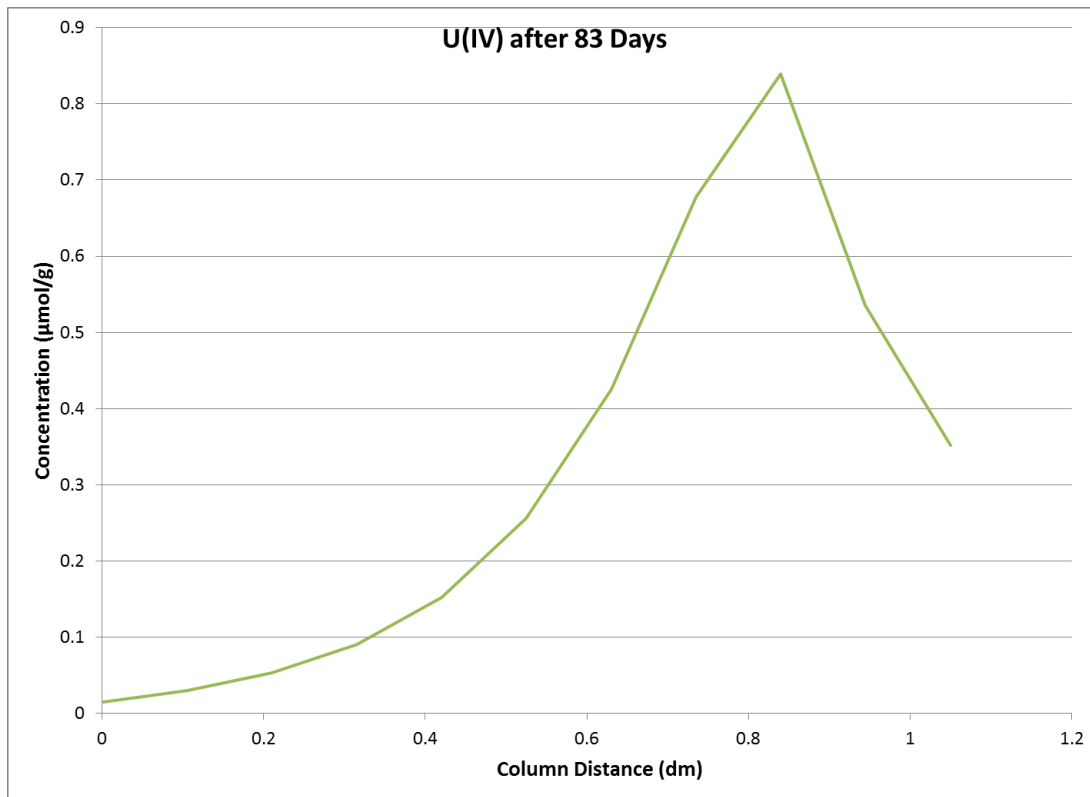


Figure 4.12 U(IV) concentration as a function of distance from column entrance at the end of the 83-day biostimulation.

The bioreduction of phyllosilicate Fe(III) leads to biogenic Fe(II) that largely remains in the layer silicate structure. **Figure 4.13** shows the near linear decrease in phyllosilicate Fe(II) from the beginning to the end of the column at the end of the 83-day simulation. This generally reflects the lactate-based phyllosilicate Fe(III) TEAP reaction rate which is fastest at the column inlet where the highest lactate concentrations are found and becomes progressively lower as lactate is consumed as it is transported through the column. The Fe(II) in Table 3.8B was also higher at the inlet but generally flat after that. Concentration magnitude based on the extractions was generally lower in the post-biostimulation solid phase extractions than in the model simulations. Possible explanations range from difficulty extracting phyllosilicate iron to the consumption of electron donor by processes other than the modeled TEAPs.

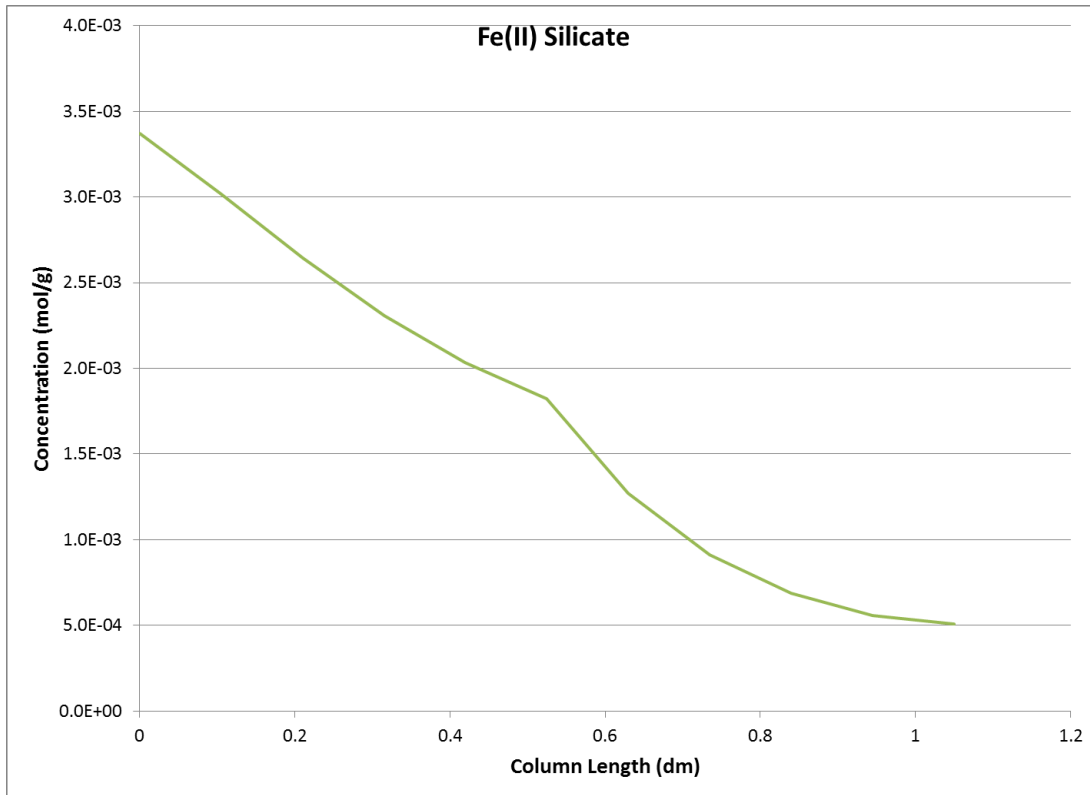


Figure 4.13 Fe(II) silicate abundance as a function of distance from column entrance at the end of the 83-day biostimulation.

#### 4.10 Biostimulation Studies: Deep ISR vs Shallow Aquifer

The most important findings from the studies of the biostimulation column experiments using the preserved Kingsville Dome post-ISR sediments were

1. The microbial community in the post-ISR sediment column could be stimulated with lactate resulting in essentially complete removal of continuously influent 20  $\mu\text{M}$  U(VI) over the  $\sim$ 1-day column transit time. The viability of the anaerobe populations putatively responsible for the bioreduction of U(VI) to immobile, sediment associated U(IV) is significant in light of the prolonged exposure to oxygen and other components of the lixiviant during ISR operation. Oxygen inhibits the activity of these organisms and can, in some cases, be toxic. Thus, the ability to respond within the experimental time scales to biostimulation after the disruption imparted by ISR extraction is notable.
2. The response of the microbial community in the Kingsville Dome sediments to lactate biostimulation is distinctly different from that observed in shallow aquifer sediments. In the biogeochemical modeling, these differences were addressed with inhibition terms, biomass-dependent reaction rates, and electron donor-specific (a) TEAP reactions and (b) bioavailable terminal electron acceptor pools.

**Acetate.** The first oxidation product in the lactate-based TEAP reactions is acetate, which is another electron donor that can also drive the microbially-mediated reactions. After 14 days of continuous biostimulation, the complete continuous consumption of the 10 mM influent lactate electron donor produces 10 mM of acetate according to the stoichiometry in the modeled TEAP reactions. Initially, 70% of the acetate is consumed in TEAP reactions but by the end of the experiment, nearly all the acetate leaves the column unreacted. This is a complete departure from the shallow alluvial continuous acetate biostimulation experiments where acetate initially drives Fe(III) and U(VI) bioreduction but then is nearly completely consumed mole for mole by sulfate bioreduction. The diminishing ability of the microbial community in the Kingsville Dome sediments to utilize acetate was modeled as the progressive depletion of Fe(III) pools of limited size that are bioavailable only to acetate-based TEAP reactions.

**Sulfate.** When sulfate reduction is the dominant TEAP in the Rifle shallow aquifer system, the acetate electron donor will continue to be consumed as long as sulfate is not limiting. While the ambient sulfate concentrations ( ~10 mM) in the ISR sediment column experiments are comparable to the Rifle aquifer, only a small amount (1-2 mM) of sulfate is removed from solution via bioreduction despite the presence of excess acetate electron donor. In the model, this insensitivity of sulfate reduction to acetate is addressed by limiting the TEAP reaction mediated by sulfate reducing bacteria to lactate electron donor. Since much less sulfate is reduced to sulfide, less electron donor is consumed, and less biomass is produced. This could be viewed as a benefit, in that more of the electron donor is being used by the microorganisms responsible for catalyzing the reduction of U(VI). Conversely, there is less sulfide produced by sulfate reducing bacteria, which decreases the solid phase reservoir of lowered redox potential that contributes to the restoration and maintenance of baseline conditions.

**Fe(III) Minerals.** The bioreduction of iron (oxy)hydroxide (i.e., goethite) and phyllosilicate Fe(III) (iron-bearing clays) account for the bulk of the electron donor consumed in the modeled experiments. The rise and fall of Fe(II) in the first 40 days of column effluent is similar to the biostimulation of iron-reducing bacteria in shallow alluvial aquifer systems where the initial increase in aqueous Fe(II) is eventually attenuated by the formation of FeS from reaction with increasing sulfide concentrations. In the model, Fe(II) is liberated by the reductive dissolution of the crystalline Fe(III), whereas the Fe(III) in the clays is reduced in place with minimal release of Fe(II) into solution. In this case, the iron-bearing clays are the dominant Fe(III) TEAP. Solid phase iron characterization indicated less electron donor consumption via TEAP reactions and more consumption by undetermined non-TEAP processes than simulated. While this does not alter the principal conceptual processes simulated, it does underscore a need to further explore alternative conceptual models for the column behaviors.

**U(VI).** Unlike the shallow alluvial aquifers in which the bioreduction of U(VI) (and Fe(III)) responds almost immediately to the biostimulation, there is a 14-day lag in the Kingsville Dome sediment columns that is coincident with complete lactate consumption. In the model, the presence of lactate inhibits the U(VI) bioreduction which is attributed to acetate. Thus, U(VI) bioreduction is 1) acetate-based, despite acetate being largely unreacted by day 60, and 2) inhibited by the presence of lactate. U(VI) removal from solution progressively increased after the 14-day lag period until negligible amounts of U(VI) were present in the column effluent after 40 days of lactate biostimulation.

## 5 Field-Scale Flow and Transport Modeling

### 5.1 Overview

The conceptualization of processes identified for the laboratory columns using Kingsville Dome sediments was extended to the field scale using a hypothetical confined aquifer. The general attributes of the site were selected from a range of values based on ISR sites and are listed in **Table 5.1**. The scenario being modeled is that this section of the confined aquifer was previously the subject of uranium ISR. In this scenario, the elevated uranium concentrations and major ion chemistry (see **Tables 4.2** and **4.3**) are based on field observations of groundwater during the drilling of the post-ISR sediments used in the column experiments.

Table 5.1 Hypothetical sand-sandstone aquifer attributes.

Parameter	Value
Thickness	10 m
Hydraulic conductivity	1.4 m/d
Specific storage	1.0E-5 1/m
Porosity	0.15
Depth below water table	104 m
Water pressure	10 atm/103 mH <sub>2</sub> O

Restoration is based on the delivery of 10  $\mu\text{M}$  lactate to the 10 m thick confined aquifer interval using multiple injection wells coordinated with a single central production well. The most common injection/pumping patterns are five- and seven-spot (Lusher, 2003), although ore body geometry and/or surface topography may give rise to other patterns such as direct line. For this hypothetical scenario, we chose a five-spot well pattern with 4 injection wells on the corners of a 30.5 m square with a central recovery well in the middle of the square. Distance between the center extraction well and corner injection wells was 21.6 m. This 5-spot scenario is a highly simplified and idealized problem geometry designed to focus on the basic interplay between flow and reaction processes in a field setting. In a typical ISR well field, the well network will be much larger and more complex, with distances between wells varying as a function of the size of the mineralized zone, permeability, pumping rates and drawdown. Spacing between injection wells is generally 40 to 150 feet. Our single 5-spot analysis can be considered a “building block” element of a larger network of 5-spot patterns (see **Figure 1.3**) that are typically used to cover the zone of economic uranium extraction. **Table 5.2** contains the modeled 5-spot well specifications, including pumping rates and drawdown.

Table 5.2 Well attributes for 5-spot pattern.

Parameter	Value
Well diameter	6 inches
Injection wells	4
Production wells	1
Injection rate	10 gpm
Production rate	40.4 gpm
Drawdown	54 feet

The flow modeling used a two-dimensional, depth-averaged model domain to analyze the drawdown, time to near steady-state, capture zone, and sensitivity to gradient and dispersion. While the idealized conditions for the modeling do not include the impact of spatially variable material properties, some insights on potential impacts of heterogeneities were identified through the dispersivity tests.

The conceptualization of the ISR-mined region is based on an idealized spatial distribution of chemical species (including uranium, iron, sulfur), biological species (including initial FeRB and SRB biomass, and mineralogy (including the crystalline and phyllosilicate iron terminal electron acceptors, as well as the >FeOH surface complexation sites). In this case, the 2-D depth-averaged domain is for a confined aquifer with Dirichlet hydraulic head boundary conditions. These boundary conditions drive a linear uniform regional gradient. The 5-spot pattern of injection wells is a set of hydrologic sources and sinks that perturb the plane of the regional piezometric surface. The porosity, hydraulic conductivity, and dispersivity are uniformly assigned to the entire model domain. As in the modeling of the column experiment, the initial aqueous solute speciation and chemical reactions are used to assign the adsorbed U(VI), Fe(II), and H<sup>+</sup> concentrations. The system is assumed to be initially anaerobic. While the use of oxygen in the lixiviant may have left residual amounts in the aquifer, it takes less than 1 mM of electron donor to remove all the accessible oxygen (Yabusaki et al., 2010). The assumption here is that biostimulated removal of oxygen is sufficiently efficient to deal with parts of the aquifer that are less accessible to the primary flow paths. The use of pumping and injection wells complicates the concept of a pore volume that works so well with column experiments. While the zone of influence for the 5-spot pattern certainly has a pore volume associated with it, the amount of water transported through any part of the zone is location-dependent. Thus, we use the time it takes for the longest travel time to reach the pumping well as a measure of cycle time. The amount of groundwater that must be pumped is a significant component of the overall cost of decommissioning a site.

## 5.2 Field-Scale Coupled Process Simulator

eSTOMP, the scalable parallel processing version of the STOMP subsurface simulator (White and Oostrom, 2006), was used to model the coupled saturated flow and transport processes and the large number of reactive components for the two-dimensional field-scale

simulations of uranium ISR site restoration. eSTOMP was selected for the field scale coupled process simulations because the high-resolution reaction dominated computations could be executed on massively parallel computers. In this case, the operator splitting reaction solver is identical to the one employed in HYDROGEOCHEM. The eSTOMP simulator solves transient flow and multicomponent biogeochemical reactive transport problems in the subsurface environment in any dimensionality. The governing flow and transport equations are the partial differential equations (PDEs) for the conservation of water and solute mass. All boundary conditions, sources, and sinks can be time variant and applied selectively over the boundary surfaces. The water mass conservation equation, shown below, equates the time rate of change of water mass within a control volume with the flux of water mass crossing the control volume surface. Flow of fluid phases is computed from Darcy's law.

$$\frac{\partial}{\partial t} \left[ \sum_{\gamma=\ell,g,i} (n_D \omega_\gamma^w \rho_\gamma s_\gamma) \right] = - \sum_{\gamma=\ell,g} (\nabla \mathbf{F}_\gamma^w + \nabla \mathbf{J}_\gamma^w) - \nabla \mathbf{F}_\ell^S + \dot{m}^w$$

where,

$$\mathbf{F}_\gamma^w = - \frac{\omega_\gamma^w \rho_\gamma k_{r\gamma} \mathbf{k}}{\mu_\gamma} (\nabla P_\gamma + \rho_\gamma g \mathbf{z}_g) \text{ for } \gamma = \ell, g$$

$$\mathbf{J}_\gamma^w = - \tau_\gamma n_D \rho_\gamma s_\gamma \frac{M^w}{M_\gamma} D_\gamma^w \nabla \chi_\gamma^w \text{ for } \gamma = \ell, g$$

$$\mathbf{F}_\ell^S = D_\ell^S \nabla S_\ell$$

The solute conservation equation, shown below, equates the time rate of change of solute within a control volume with the flux of solute crossing the control volume surface. In the eSTOMP simulator, solute is partitioned among the fluid and solid phases assuming thermodynamic and geochemical equilibrium conditions. Solute transport occurs by advection and diffusion-dispersion through the aqueous phase.

$$\begin{aligned} \frac{\partial C}{\partial t} = & - \sum_{\gamma=\ell,g,n} (\nabla [C_\gamma \mathbf{V}_\gamma]) + \dot{m}^C - \dot{R}^C C \\ & + \sum_{\gamma=\ell,g,n} \left( \nabla \left[ (\tau_\gamma s_\gamma n_D D_\gamma^C + s_\gamma n_D \mathbf{D}_{h\gamma}) \nabla C_\gamma \right] \right) \end{aligned}$$

where,

$$\mathbf{V}_\gamma = - \frac{k_{r\gamma} \mathbf{k}}{\mu_\gamma} (\nabla P_\gamma + \rho_\gamma g \mathbf{z}_g) \text{ for } \gamma = \ell, g, n$$

Equilibrium reactions (i.e., mass action equations relating species activities through an equilibrium constant) are represented as

$$(C_j) = K_{eqj} \prod_{N_{eqj}^s} (C_i)^{e_i} (i \neq j); \text{ for } j = 1, N_{eq}^{eq}$$

Kinetic equations define kinetic components where a stoichiometrically weighted sum of species concentrations vary in time according to a weighted sum of kinetic rates:

$$\frac{d \sum_{N_{tkj}^s} (b_i C_i)}{dt} = \sum_{N_{tkj}^r} (c_k R_k); \text{ for } j = 1, N_{kn}^{eq}$$

A variety of popular reaction rate models are available including those based on simple first order reactions, transition state theory, and Monod kinetics.

eSTOMP uses one-sided communication and a global shared memory programming paradigm from the Global Array Toolkit (GA) library (Nieplocha et al., 2006) for scalability, performance, and extensibility on massively parallel processing computers. The approach is compatible with the more commonly used Message Passing Interface (MPI) (Message-Passing-Interface-Forum, 2009) that is used by the PETSc (Balay et al., 2010) global implicit solver in eSTOMP. The principal benefit to this parallel processing approach is that simulations with highly resolved process and property detail can be performed on a massively parallel computer in hours instead of weeks on a desktop computer. These efficiencies enabled rapid turnaround of the multiple test scenarios that were simulated.

Written in Fortran-90, eSTOMP solves the conservation equations for compressible flow and multicomponent reactive transport based on finite-volume discretization. A Newton-Krylov solution procedure is used for the nonlinear global implicit formulation of the governing flow and transport PDEs. Solute mass conservation and reactions are sequentially solved following the solution of the flow equations. Kinetic and equilibrium reactions are represented as a system of ordinary differential and algebraic equations (DAEs). The nonlinear system of DAEs is formulated with the backward Euler method and Gauss-Jordan matrix decomposition. Newton-Raphson iteration is used to solve the reaction system of equations.

### 5.2.1 Physical System

Attributes of the model used in this study were chosen to be representative of typical ISR sites with sandstone formations containing uranium roll front deposits. The single, 10 m thick layer aquifer was confined by no-flow lower and upper boundaries to represent the bottom- and top-confining geology, respectively. The 2-D plan view model constrains all flow to the horizontal. Hydraulic conductivity was specified at 1.4 m/d, porosity at 0.15, and the specific storativity (meters of water released per m decrease in head) was 1.0E-5 1/m. Background pressure was set at 10 atm, or about 340 feet of hydraulic head. A typical pumping rate of 10 gpm was used for each injection well, and 40.4 gpm (4 injection wells x 10 gpm +1%) was used for the center extraction well. A conservative (non-reacting, unretarded) tracer with a nominal concentration of 1.0 was included in the injectate of the four injection wells.

A sensitivity analysis was conducted on this baseline specification to evaluate the significance of model grid resolution and extent, regional hydraulic gradient magnitude and direction, and dispersion. **Tables 5.3** and **5.4** list these inputs for the sensitivity analysis. The east-to-west and southwest-to-northeast flow directions represent the possible extremes of background flow in relation to this well field. Because of well field symmetry, no other flow directions are needed.

Table 5.3 Model domain and sensitivity parameters.

Parameter	Test A	Test B
Regional hydraulic gradient magnitude	5e-3	5e-4
Regional hydraulic gradient direction	West to east	Southwest to northeast
Diffusivity and dispersivity	Diff = Disp = 0	Diff=water, Disp = 10 m

Table 5.4 Grid testing attributes for Grid 1 and 2.

Attribute	Grid 1	Grid 2
Extent	195.75 m x 195.75 m	395.75 m x 395.75 m
Dimensions in Grid Cells	161 x 161	277 x 277
Total Cells	25921	76729

## 5.2.2 Model Flow System

The five-spot well pattern forms a square, and the entire model domain was also a square, with the objective of having enough buffer area around the well field such that boundary conditions would not unduly influence the water flow and transport in the vicinity of the wells. Cell size was variable to reduce the number of computational nodes in the model and save runtime. Model cells (each centered on a computational node) ranged in size from 0.15 m (~6 in) to 40 m on a side. The minimum cell size of 0.15 m is similar to the diameter of typical ISR production wells in the field. Cell size was set to increase with distance from the wells so that the grid was fine in the dynamic and high gradient regions of the flow system, and relatively coarse in the other regions of the flow system.

**Grid Testing.** Two grids were used to assess 1) the adequacy of the domain size (i.e., minimize boundary effects on the flow field around the five-spot well pattern), 2) grid resolution (i.e., capture spatially variable flow and transport features), and 3) convergence of the simulated field variables. The larger grid used more nodes (smaller growth in spacing) in the vicinity of the wells, as well as having more cells to make a wider buffer away from the well field. The smaller grid was 195.75 m on a side, and had 161 nodes in the x- and y-directions, for a total of 25,921 nodes (**Figures 5.1** and **5.2**). The larger grid was 395.75 m on a side, and had 277 nodes in

each direction, for a total of 76,729 nodes (**Figures 5.3 and 5.4**). In both grids the well field was placed at the center of the model. Grid 1 (smaller) was the primary grid used in production runs. Grid 2 served as a check on the adequacy of grid 1; if the larger extent and greater number of nodes in grid 2 do not yield significantly different results from grid 1, then grid 1 should be adequate.

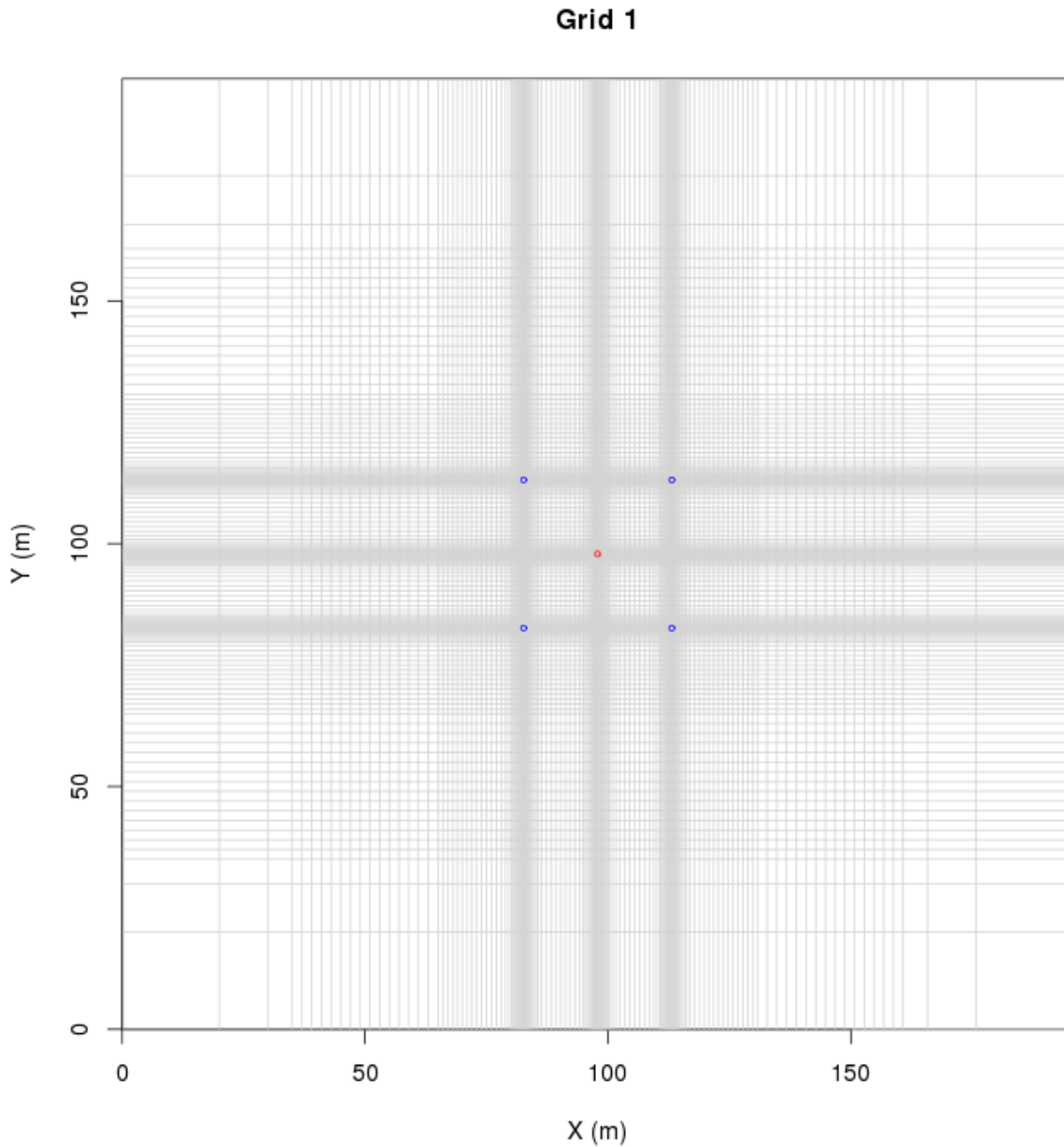


Figure 5.1 Model grid 1. The square domain is 196 m on a side, has the same spacing in the x- and y-directions, and contains 25,921 nodes. Blue dots are injection wells, red dot is extraction well.

**Grid 1 Region Close to Wells**

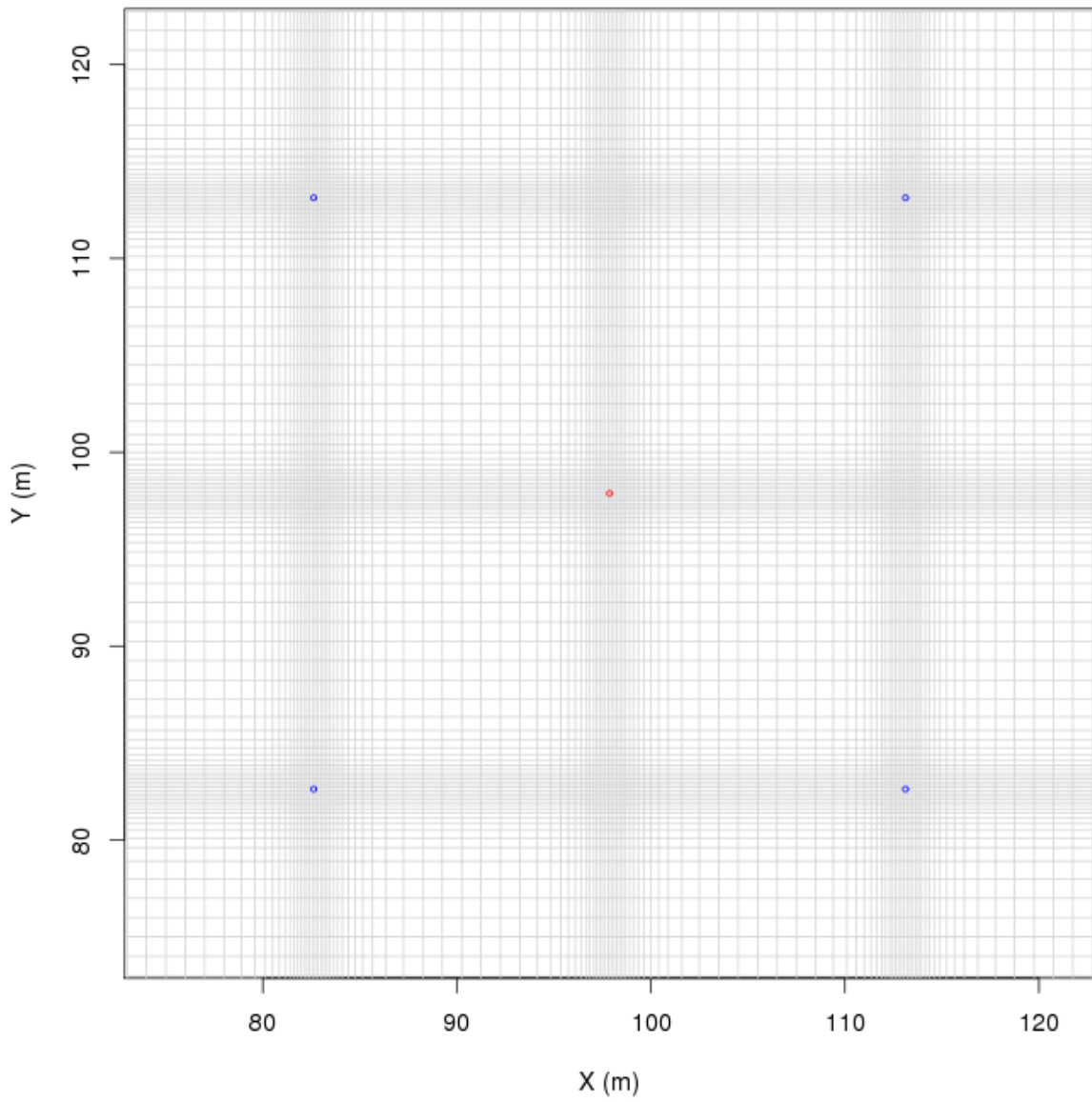


Figure 5.2 Model grid 1 center area, showing small cells used in the vicinity of the wells.

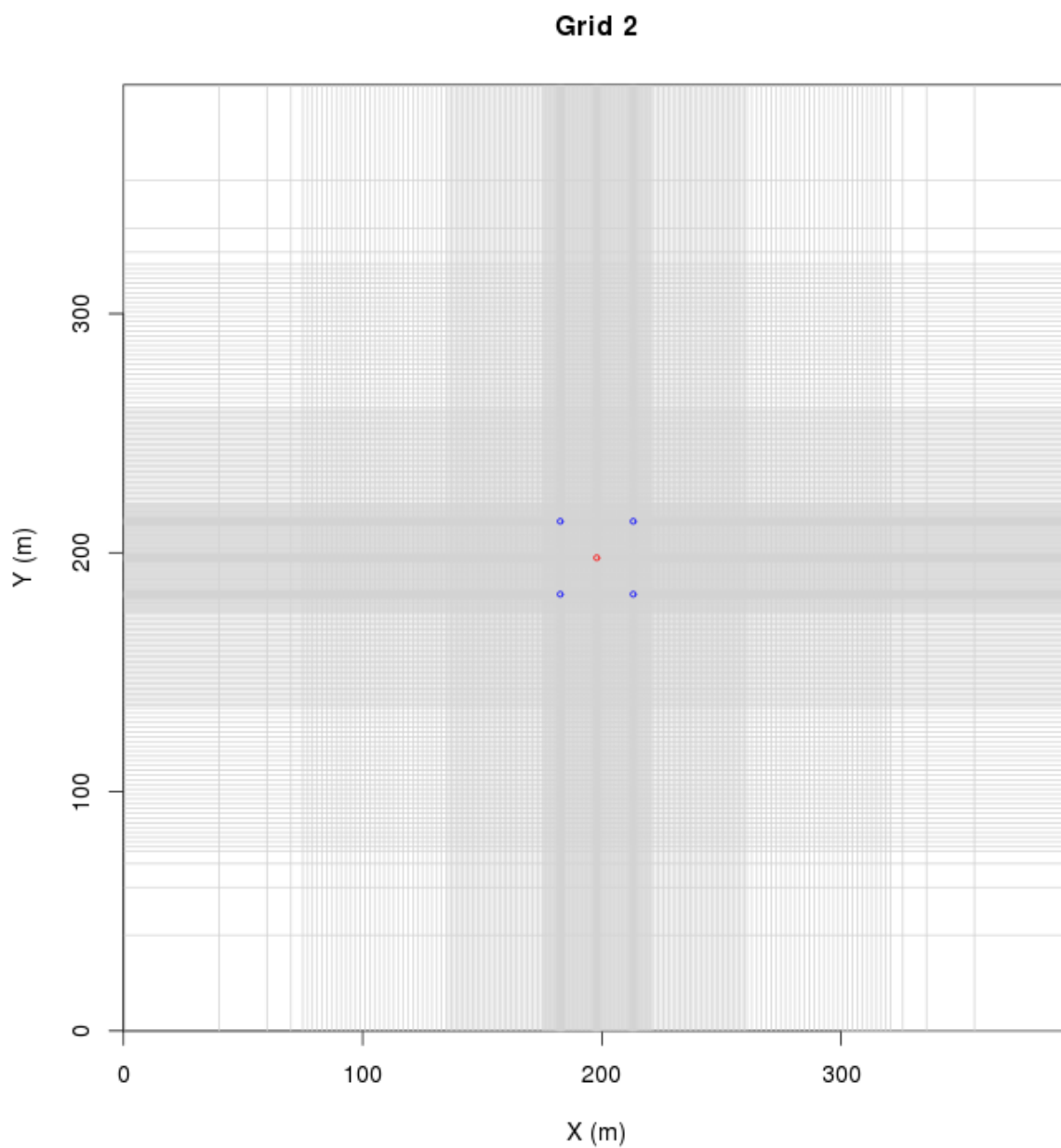


Figure 5.3 Model grid 2. The square domain is 396 m on a side, has the same spacing in the x- and y-directions, and contains 76,729 nodes. Blue dots are injection wells, red dot is extraction well.

**Grid 2 Region Close to Wells**

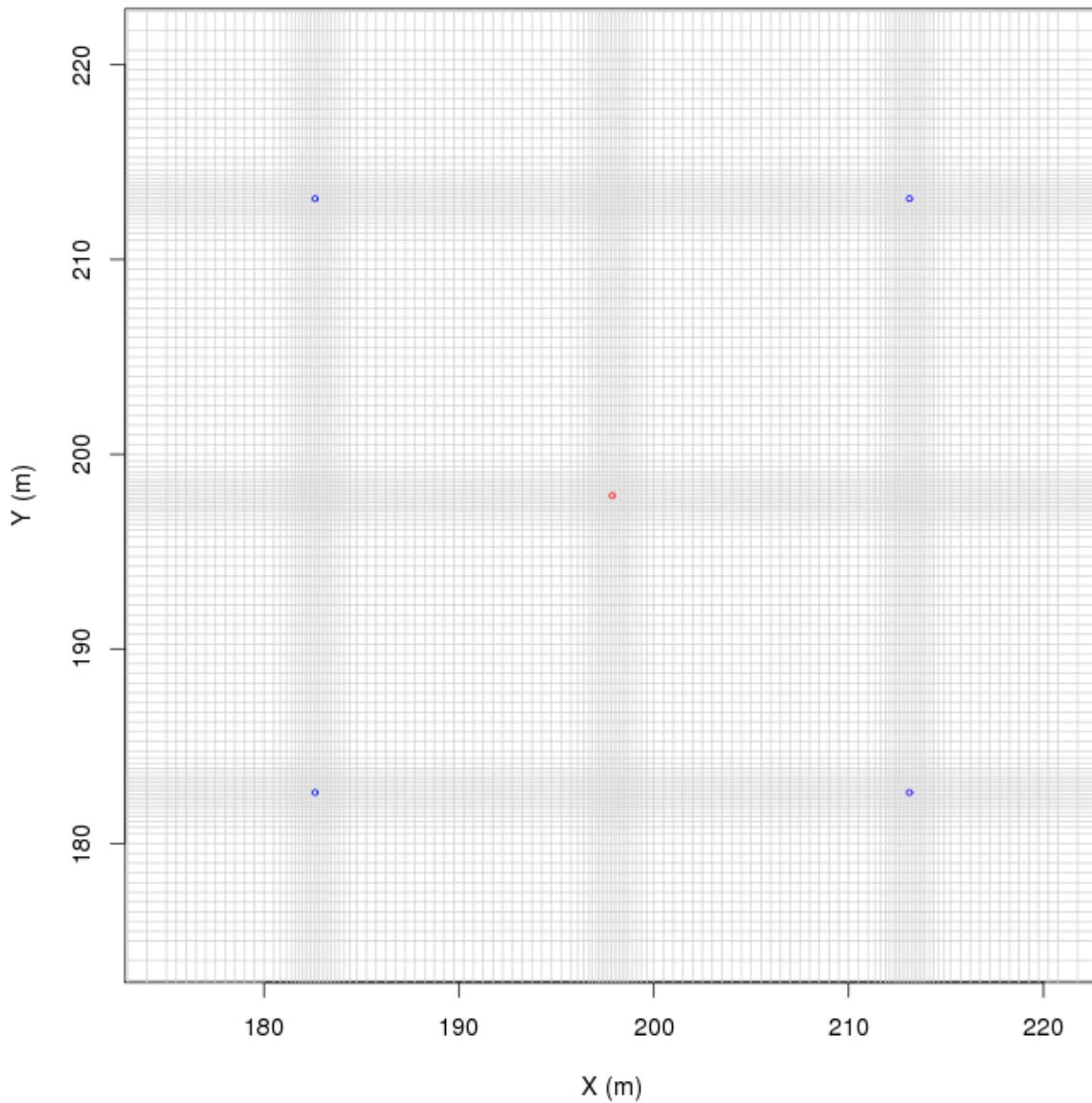


Figure 5.4 Model grid 2 center area, showing small cells used in the vicinity of the wells.

Boundary conditions were constant head type for groundwater (i.e., Dirichlet), and advection outflow type for the tracer. These respective conditions defined a steady and uniform background hydraulic gradient and allowed the tracer to leave the model in the pumped groundwater. In the two-dimensional, depth-averaged model, the injection wells were designated point sources of injectate with tracer concentration of 1.0, and the extraction well was a designated sink where groundwater and tracer were removed. Each source or sink was represented by a single node in the model, having the smallest cell size, 0.15 m x 0.15 m. Two versions of "spinup" or attainment of a steady state in water flow prior to tracer injection, were

tried. The first one involved running the model to 20 years with just the background, regional flow. The second one included well pumping (water only) in addition to the background regional flow. In both versions, most of the change in the flow field occurred in the first two days, and all change in groundwater velocities was zero within 200 days. Since the time period of interest for evaluating tracer transport was a year or more, either version was sufficient for the modeling objectives.

### **5.2.3 Flow and Transport Results**

The operation of the five-spot wells results in local perturbations from the regional gradient of the piezometric head surface. For both grids, these perturbations are shown in **Figure 5.5** for the 4 combinations of the 1) 0.005 and 0.0005 regional hydraulic gradients and 2) gradient direction parallel and diagonal to the five-spot square. Within a given grid, the head change is identical, indicating proper model execution, i.e., consistency with the principle of superposition in a linear PDE. Away from the well field, there will be head differences between the two grids because of the different distances between the five-spot wells and the model boundaries. These differences, however, are very small and the spatial patterns of head change are essentially the same in both grids.

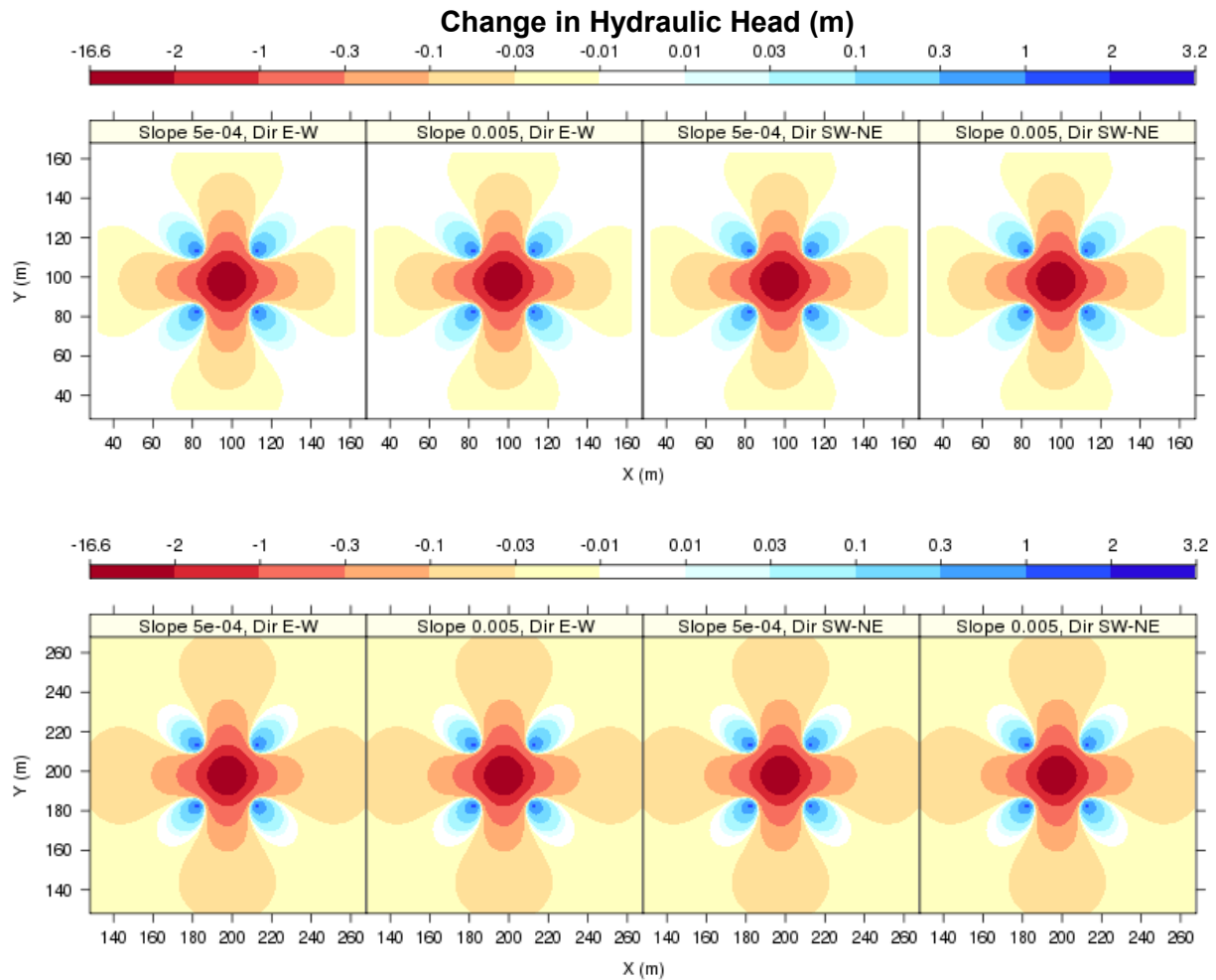


Figure 5.5 Top: change in hydraulic head in meters caused by pumping wells, in comparison to the background flow state, grid 1. Bottom: change in hydraulic head caused by pumping wells, in comparison to the background flow state, grid 2.

As a first check on the transport away from the injection wells, the paths of released particles were computed and plotted in **Figure 5.6**. Routing was based on advection by the steady-state velocity field with the five-spot well pattern in operation. Sixty particles were placed in a circle around each injection well, spaced 6 degrees apart, at a radial distance of 0.32 meters from the well node. From these initial positions, the particles were moved in small increments according to the groundwater velocity field. Particles were either captured by the central extraction well, transported out of the model domain at the boundaries, or in a few special cases, stagnated in zones where the regional flow and 5-spot operations canceled. **Figure 5.6** shows that all particles were captured by the extraction well in cases with the smaller ( $5e-4$ ) background gradient. However, the larger background gradient resulted in some particles escaping the well field and moving to the model boundaries. These particle excursions occur where initial movement caused by injection puts the particles out in areas where the background flow has more influence than the extraction. Such particles are initially pushed in a direction away from the extraction well, and in a direction close to that of the background flow. These results were the same for both grids. It should be emphasized that these flowlines

represent the effects of advection only--that is, movement according to the bulk groundwater flow, and with no dispersion.

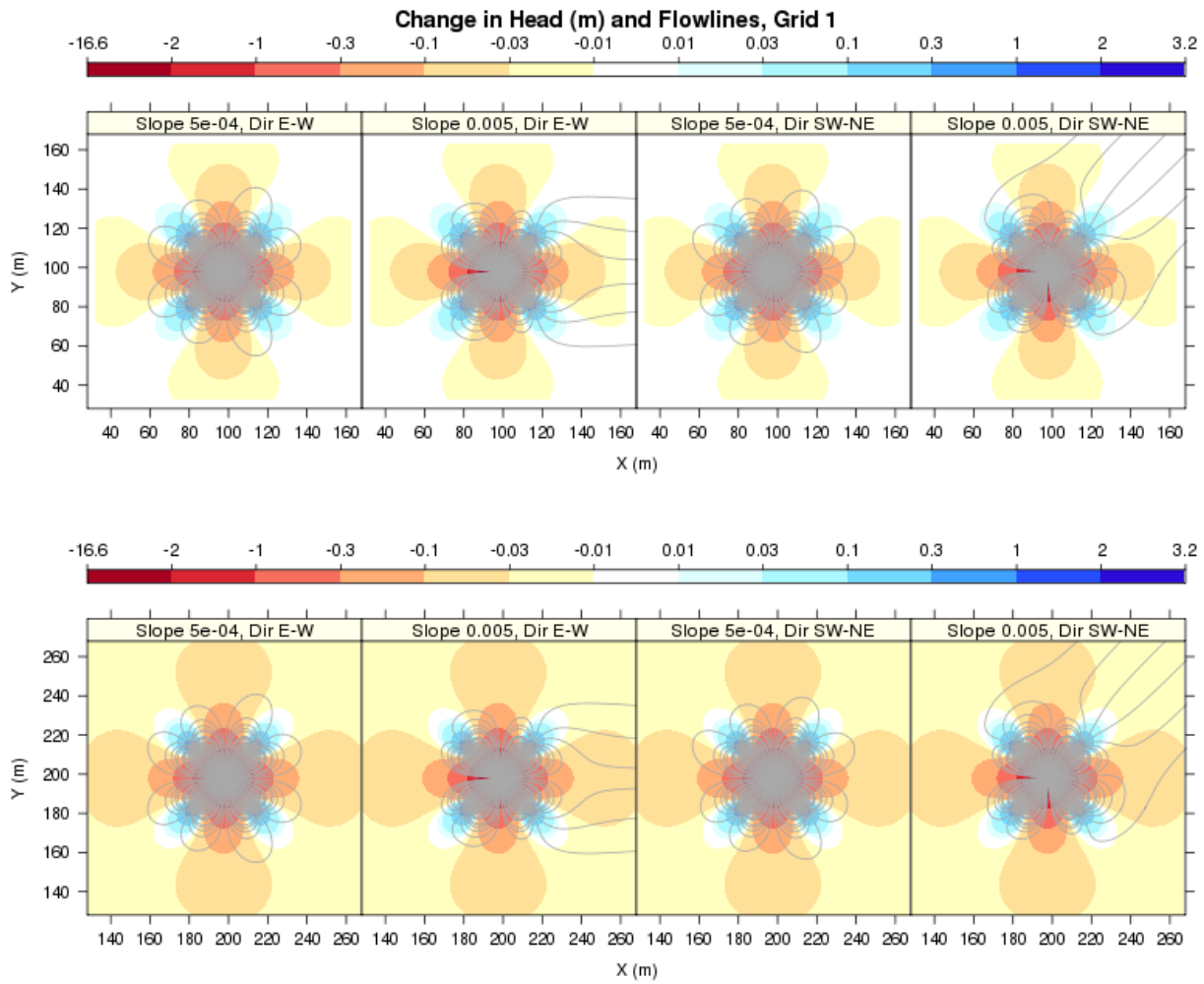


Figure 5.6 Top: paths of particles initially placed around injection wells, and color contours of head change, grid 1. Bottom: paths of particles initially placed around injection wells, and color contours of head change, grid 2.

The distribution of travel times for the 60 particles initially placed around each injection well is large because of the different particle paths with spatially variable velocities. In this model, hydrologic properties are homogeneous; thus, the spatially variable velocities are due to the 5-spot well pattern operation. Travel time statistics are summarized in **Table 5.5**. Along the direct path from the injection well to the pumping well, particle travel time is slightly less than 1 week. However, the mean particle travel time is nearly 4 weeks for the high gradient (i.e., 0.005) case and ~6.5 weeks for the low gradient (i.e., 0.0005) case. The longest particle capture times, ~3 years or more, were associated with the low gradient case. While the spatial delineation of the capture zone pore volume in **Figure 5.6** is definitive, the injection of one pore volume will definitely not access the entire capture zone. This is because the mass flux of injectate will be

location-dependent and there are a few particle trajectories that will take well over two orders of magnitude more time to be captured than the fastest particles. This will become even more significant when the time scales of reaction are similar to some of the time scales of transport. Spatially dependent electron donor delivery will lead to preferential depletion of solid phase electron acceptors.

Table 5.5 Particle travel time statistics.

Case	Particles Recovered / Particles Released	Particle Travel Time in Days			
		Minimum	Median	Mean	Maximum
Grid 1 Grad 0.0005 E-W	240/240	6.7 d	10.2 d	46.0 d	1250 d
Grid 1 Grad 0.005 E-W	234/240	6.6	10.0	25.5	351
Grid 1 Grad 0.0005 SW-NE	240/240	6.7	10.2	46.0	1050
Grid 1 Grad 0.005 SW-NE	234/240	6.6	10.0	27.3	556
Grid 2 Grad 0.0005 E-W	240/240	6.7	10.2	47.4	1280
Grid 2 Grad 0.005 E-W	234/240	6.6	10.0	25.3	337
Grid 2 Grad 0.0005 SW-NE	240/240	6.7	10.2	46.5	1080
Grid 2 Grad 0.005 SW-NE	234/240	6.6	10.0	27.2	548



Figure 5.7 Travel time histograms for particles released from the perimeter of the injection wells. The travel time intervals are in days: < 10, 10 to 30, 30 to 100, 100 to 300, 300 to 1000, and > 1000. Results are presented for the four combinations of flow (east to west, and southwest to northeast) and regional groundwater gradient (0.0005, 0.005).

The second method of evaluating well field performance in the model was to consider transport of an inert tracer that is continuously released from each injection well. Concentrations at successive times up to 1000 days are contoured in **Figures 5.8-5.14**. A characteristic cloverleaf pattern forms, where concentrations are naturally greatest near the injection wells, and least in the four areas where flow is able to go directly from the distal aquifer to the extraction well. The area containing tracer grows over time, more rapidly in early time and more slowly later, but never stops increasing. This growth occurs even in simulations where diffusion and dispersion are set to zero because of numerical dispersion. Although numerical dispersion is caused by the discrete rather than continuous nature of the model grid and is a type of model error, it can be regarded as one approximation of the dispersion that happens in the real system. The real system will have a more complex variation in flowpaths and travel times that are caused by the natural variability in hydraulic conductivity and porosity.

**Figures 5.8** and **5.9** show the minor effect of grid choice on tracer concentrations, particularly near the well field. Grid 2 involves a larger number of smaller cells near the well field, and results in somewhat sharper plume edges visible in later time. However, the patterns are essentially the same.

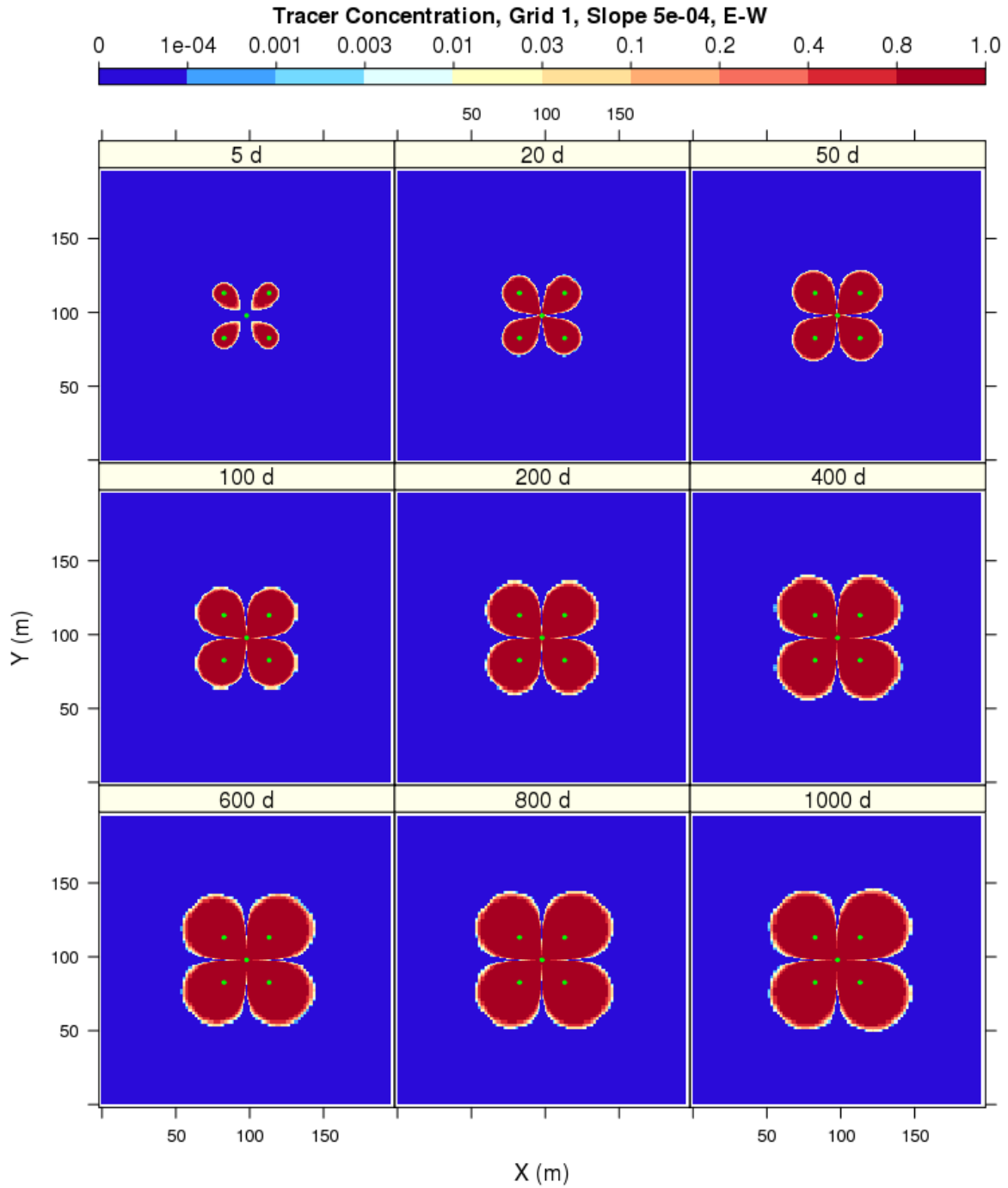


Figure 5.8 Grid 1, Gradient 5e-04 E-W, D=0, tracer concentrations over time. Green dots are well locations.

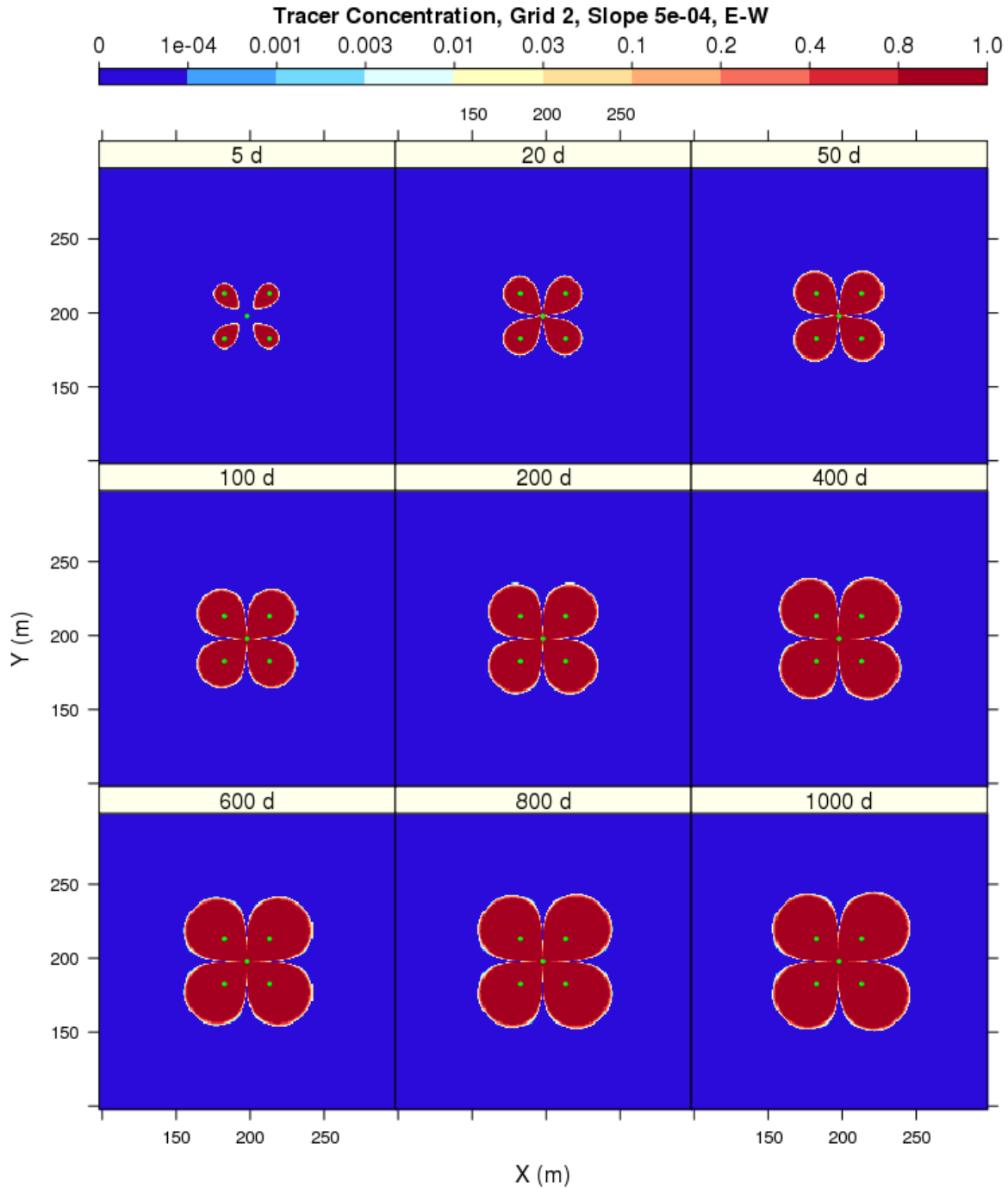


Figure 5.9 Grid 2, Gradient 5e-04 E-W, D=0, tracer concentrations over time.

In addition to the cases where diffusion and dispersivity were both set to zero ( $D=0$ ), cases were also run with diffusion coefficient =  $2.5e-5 \text{ cm}^2/\text{sec}$  (molecular diffusion in water), longitudinal dispersivity = 10.0 m, and transverse dispersivity = 1.0 m ( $D=10$ ). This magnitude of dispersivity is somewhat large though not uncommon in nature, and in theory the numerical model could accommodate dispersivity up to 10% of the domain extent because of the choice of

uniform material property distribution across the domain. **Figure 5.10** shows the same case as **Figure 5.9**, except for having  $D=10$ . The tracer is much more spread out and, in this case, the lower grid resolution outside the primary zone five-spot well pattern is creating some angular features in the contours.

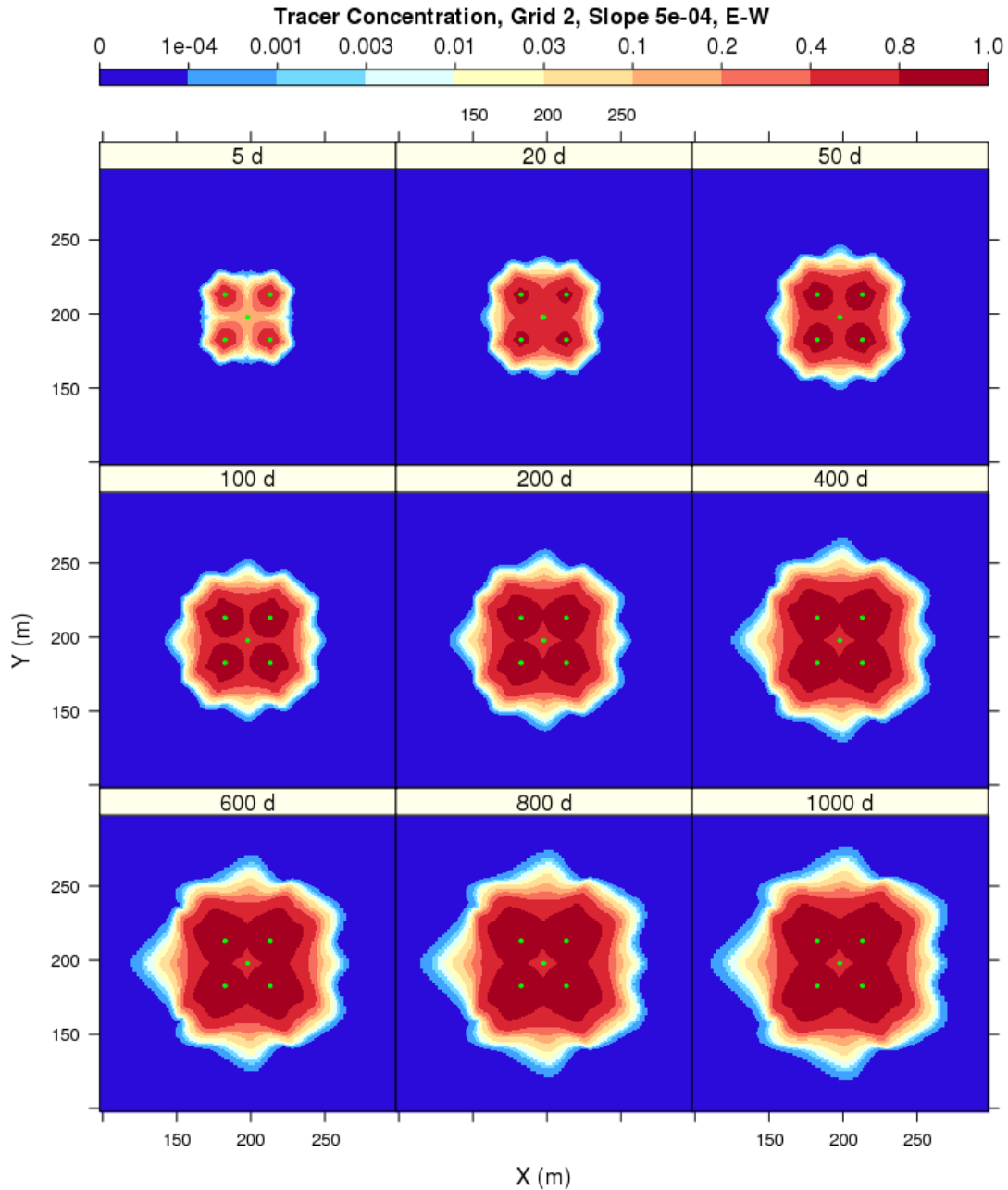


Figure 5.10 Grid 2, Gradient 5e-04 E-W,  $D=10$ , tracer concentrations over time.

Cases with the steeper background gradient and flow from southwest to northeast are shown in **Figures 5.11-5.13**. It is evident in **Figure 5.13** that the stronger regional flow field leads to greater skewing of the cloverleaf pattern in the downgradient direction, and some tracer reaches

the model boundaries even with  $D=0$ . This case is stressing the ability of the grid 1 specification to capture the central behavior without numerical artifacts.

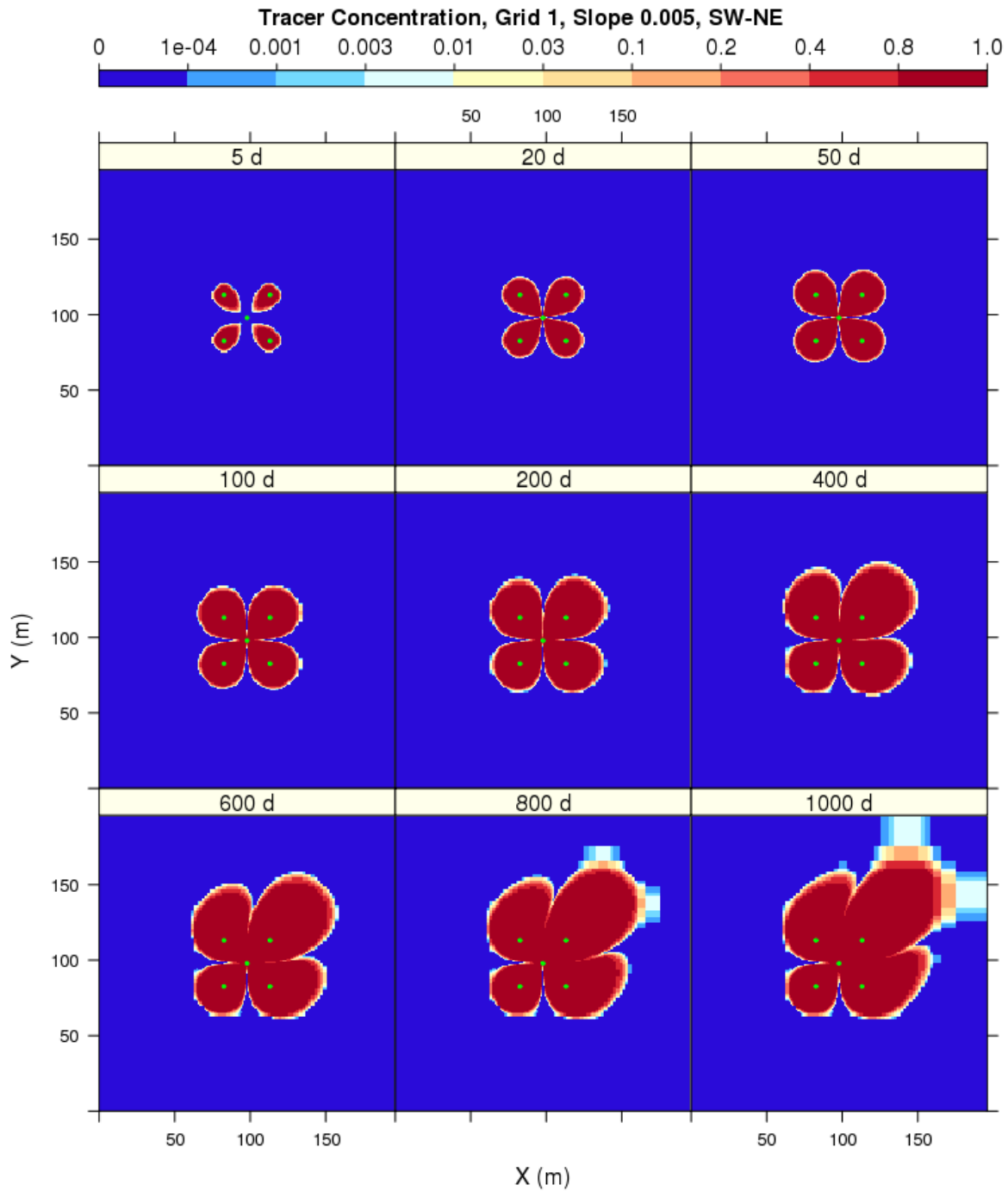


Figure 5.11 Grid 1, Gradient 0.005 SW-NE,  $D=0$ , tracer concentrations over time.

For the remaining tests only the grid 2 results are presented. **Figure 5.12** is the grid 2 version of the previous 0.005 SW-NE gradient with the  $D=0$  specification. This clearly demonstrates that for the higher regional flow cases, using a larger grid can keep the tracer plume in a region where resolution is adequate.

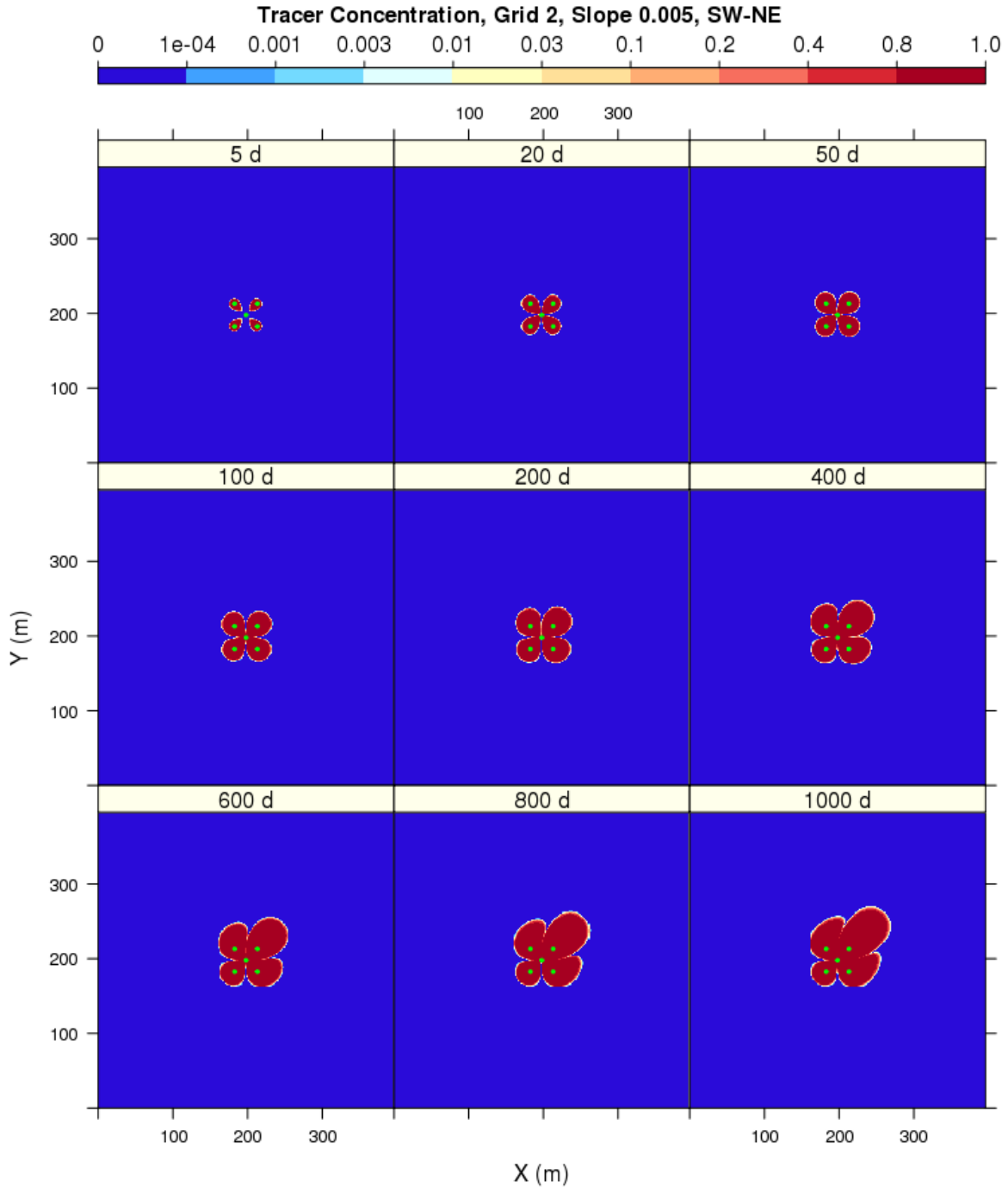


Figure 5.12 Grid 2, Gradient 0.005 SW-NE,  $D=0$ , tracer concentrations over time.

The high SW-NE gradient, high dispersion case (**Figure 5.13**) shows significant downgradient migration away from the capture zone of the central pumping well.

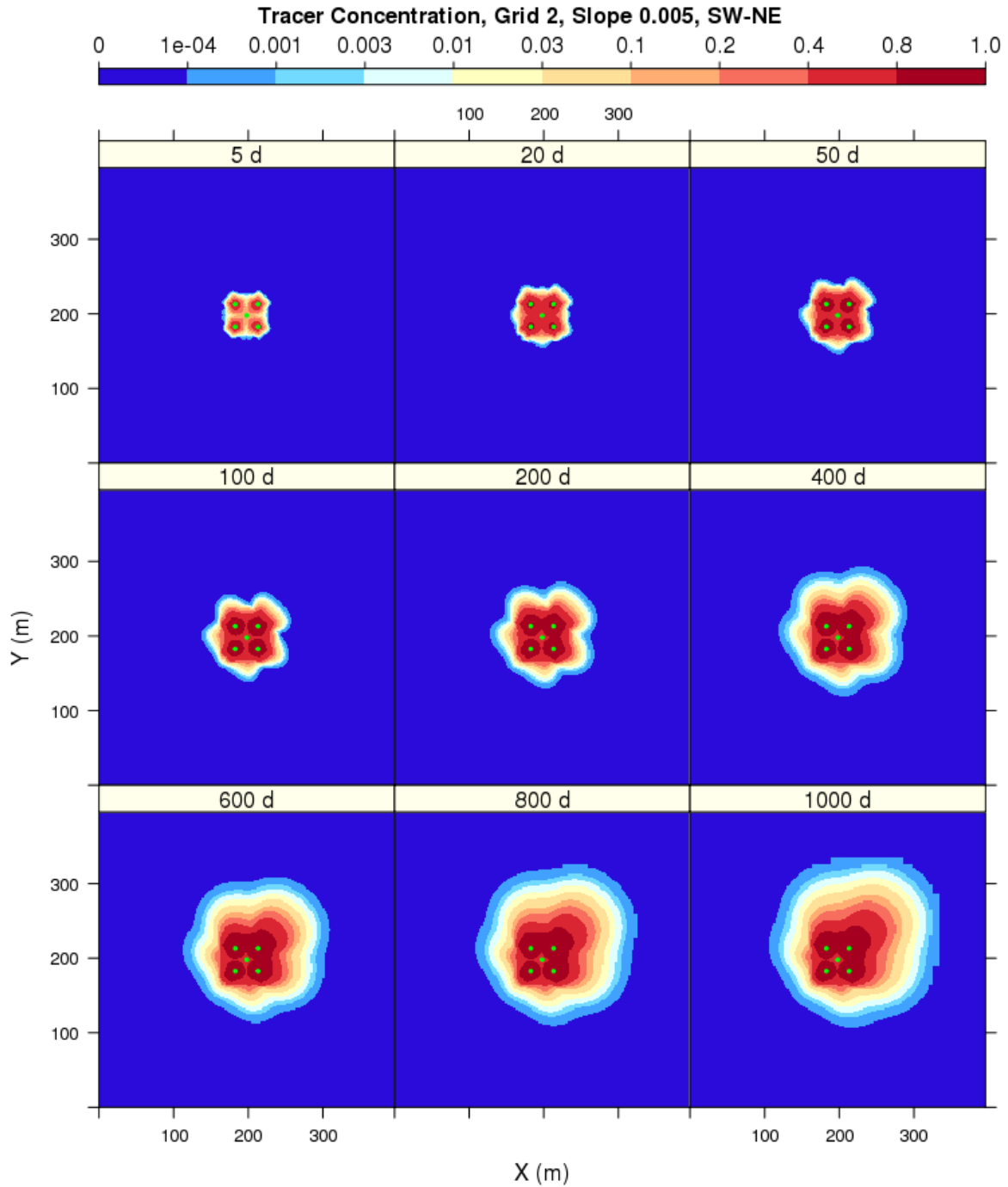


Figure 5.13 Grid 2, Gradient 0.005 SW-NE, D=10, tracer concentrations over time.

The final method for evaluating the well field was to track particles initially placed throughout the model domain, and delineate the zone where particles were captured by the extraction well. Here the goal was not to evaluate the fate of injected water, but rather to see the relationship between the area of advection towards the extraction well, and the area of tracer presence caused by dispersion as well as advection. If the advection capture zone does not contain the tracer plume, then tracer will almost certainly be lost from the well field. **Figure 5.14** shows the capture zone as a contour line overlaid on the 1000 day tracer concentrations. The most favorable cases with respect to tracer capture are those with the lower background gradient and  $D=0$ . However, even in those two cases, there is a portion of the tracer plume at high concentrations that lies outside the advective capture zone. Increasing the background gradient or dispersivity decreases the amount of capture, and indicates that more tracer will escape the extraction well.

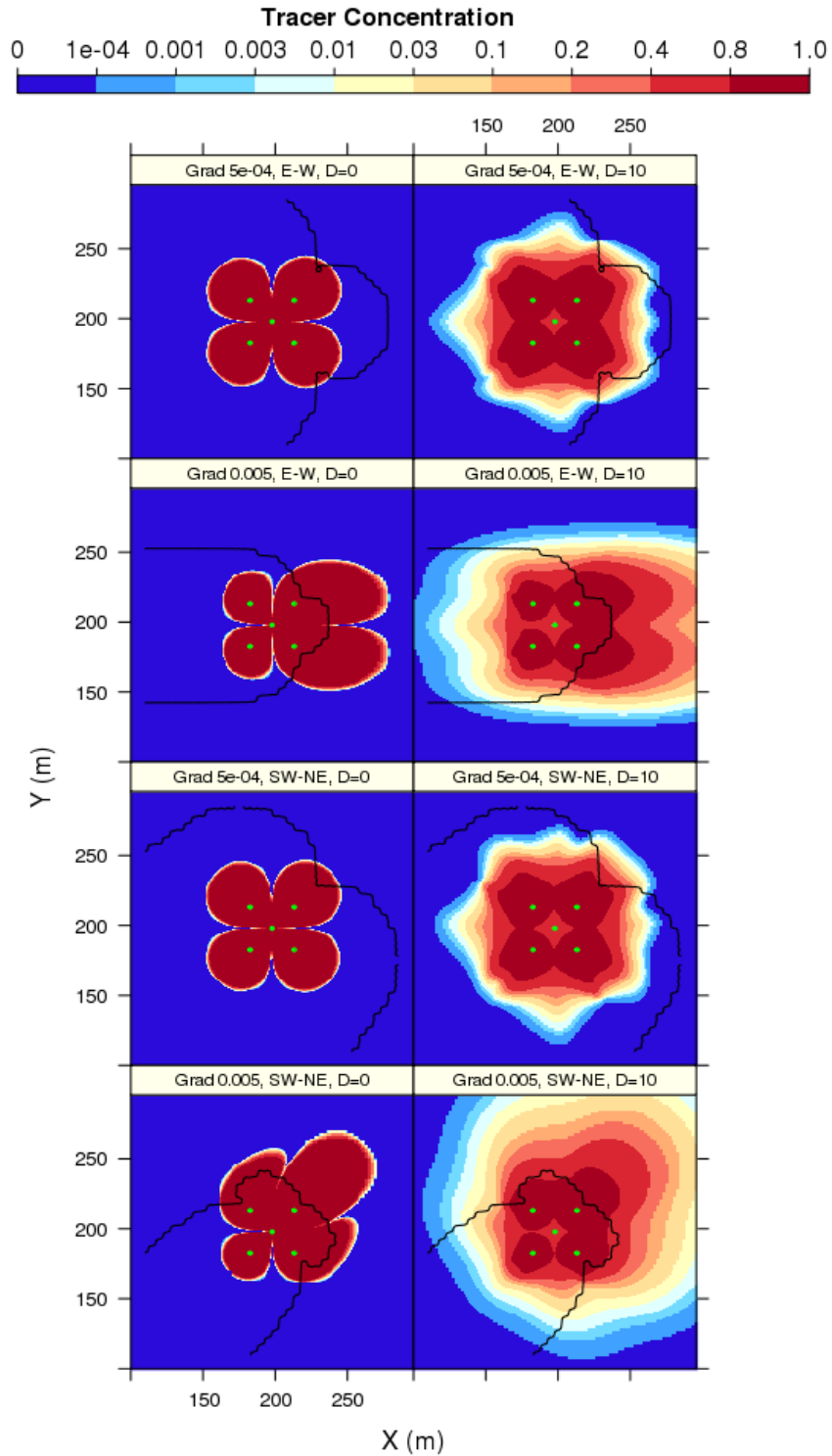


Figure 5.14 Tracer concentrations at 1000 days for 4 base cases ( $D=0$ ) and 4 dispersion cases ( $D=10$ ), grid 2. Black lines delineate capture zones, wherein particles within contour line are captured by the extraction well in advective transport.

### 5.3 Findings

The general findings from the field-scale simulations are the following:

- In the comparison of the steady-state and transient flow modeling approaches, it was found that most of the change in the flow field occurred in the first two days of the five-spot well operation. All changes in groundwater velocities were zero within 200 days. Although the analyses used transient velocity fields, these results justify steady-state flow fields for scoping and scenario comparisons.
- Flow modeling on both the small and large grids was numerically consistent with the linear PDEs being solved and satisfied the principle of superposition. For the flow phenomena of interest, the smaller grid (smaller domain, lower resolution, and fewer grid cells) performed very similarly to the larger more detailed grid. The larger grid was necessary to resolve the transport of a conservative tracer when the regional gradient or the dispersivity was high.
- Operation of the 5-spot well pattern results in a nonuniform flow field even though the material properties are homogeneous. Travel time for particles released near the injection well ranged from less than a week to 3.5 years. Mean particle travel time is nearly 4 weeks for the high regional gradient (i.e., 0.005) case and ~6.5 weeks for the low regional gradient (i.e., 0.0005) case. This has implications for characterizing treatment in terms of injected pore volumes. While the pore volume of the capture zone is definitive, the time it takes to access the entire pore volume is much longer than the time it takes to inject one pore volume. This is because transport in the low flow rate regions (i.e., away from the axis between the pumping and injection wells) is slower and exposed to less injectate than other regions. This variability in advective travel time from the injection well to the pumping well results in a range of residence times within the capture zone that will affect the extent of kinetically controlled reactions.
- While most of the material injected in the perimeter wells of the five-spot pattern will be captured by the central pumping well, higher regional gradients increase the opportunity for excursions of injectate beyond the capture zone. This will be exacerbated by heterogeneities in the hydraulic conductivity that alter the idealized flow paths examined in this study.



## 6 Field-Scale Post-ISR Bioremediation Modeling

### 6.1 Bioremediation Concepts

The general approach for the bioremediation of uranium ISR sites is to return the roll front to the low pre-operational redox potential that maintained the baseline conditions. The fundamental assumption is that the introduction of lixiviant and duration of ISR operations has not irreversibly altered the mineral assemblages in a way that would prevent restoration of the low redox potential. In this respect, the solid phases are the largest and most important reservoirs for redox capacity in the subsurface. For the bioremediation technology to succeed, the post-ISR sediments must be returned to a redox potential that is sufficient to restore and sustain the baseline redox conditions.

The objective of the field-scale simulations is to gain insight on the potential for ISR bioremediation and issues of performance. We use the results of the modeling of the column experiments in Chapter 4 to inform the field-scale modeling approach. The column experiments and associated modeling are not considered substitutes for well- instrumented field experiments that address site-specific conditions. Consequently, these hypothetical simulations of the field implementation of lactate bioremediation are essentially scoping analyses to identify insights and potential issues with the field implementation.

As mentioned in Chapter 4 (modeling of the column experiments), the poorly consolidated sand and silt dominated sediments that were recovered from the Kingsville Dome drilling were used directly without having to exclude larger size fractions. The column diameter was 2.22 cm which was appropriate for the sediments, which were < 1 mm. Ostensibly, the use of the full field particle size distribution eliminates or at least minimizes the need to upscale the reactive phases that are typically associated with smaller size fractions. For this reason, no upscaling of the reactivity is performed for the field scale simulations.

In U.S. ISR operations, oxygen is commonly used in the injected lixiviant. The oxidation of reduced minerals in the sandstone aquifer sediment is presumed to be a key factor in the longer time scales associated with post-ISR restoration. The re-establishment of the low redox potential baseline is based on diminishing the effects of oxidants in the system using biostimulation of indigenous organisms to catalyze the reduction of key terminal electron acceptors such as U(VI).

Sparging with oxygen gas would increase the electron donor requirements by the ratio of oxygen partial pressures. At ~100 m below the water table, the hydrostatic water pressure is nearly 10 atm. This will increase the dissolved oxygen saturation capacity by an order of magnitude. Using 25° C Henry's Law coefficients for oxygen with atmospheric gas composition, the dissolved oxygen concentration could be 2.6 mM. Based on the stoichiometry of lactate and acetate oxidation coupled with oxygen reduction, about 2 moles of oxygen can be reduced for each mole of lactate reacted. Thus, a little more than 1 mM lactate will completely consume the accessible oxygen assuming that dissolved oxygen is at saturation at end of the ISR process. The 10 mM lactate injectate should stimulate sufficient bioreduction to deplete the oxygen. Thus, the expectation is that the groundwater brought to the surface by the production

well will be anaerobic after bioremediation is implemented. In fact, oxygen in groundwater sampled about two years after ISR processes stopped was  $< 0.015$  mM, Table 3.1, suggesting that this evaluation is very conservative.

In the handling of the produced groundwater at the surface before re-injection, a potentially important consideration is the maintenance of the anaerobic conditions. The issue is whether greater than suboxic levels of oxygen adversely affect the microorganisms that accomplish the intended bioreduction of terminal electron acceptors. It also may be important to keep the oxygen levels as low as possible to drive the diffusion of oxygen out of intra- and inter-particle zones that have limited transport access to the bulk groundwater flow. Anaerobic groundwater will also deplete oxygen from entrapped gas bubbles through partitioning with the aqueous phase. If oxygen sparging was used during the ISR process, exsolution of oxygen as the pumped groundwater reaches the ground surface is possible but only in the initial pore volume(s). The electron donor should stimulate microorganisms that will use dissolved oxygen as a terminal electron acceptor, resulting in the conversion of oxygen to water.

## 6.2 Modeling Approach

The specification of the field-scale simulation is based on the reaction network, initial and boundary condition geochemistry developed in the Chapter 4 modeling of the column experiments and the Chapter 5 flow and transport studies. The bioremediation simulation assumes the 0.0005 west to east regional gradient case where the flow field is aligned with the grid (i.e., not the southwest to northeast flow field that was diagonal to the grid). The initial and upgradient influent boundary condition chemistry for the regional system is the boundary condition chemistry in **Table 4.4** without lactate. The solid phases are based on **Table 4.2**.

The assumption here is that the production well in the center of the five-spot pattern will be initially operated alone as a groundwater sweep. This can be run until the initial transient of elevated metals concentrations decreases and begins to approach a steady state. Typically, this can require 1-2 pore volumes. After the groundwater sweep, the biostimulation will be initiated by introducing groundwater amended with 10 mM lactate in each of the 4 perimeter wells of the 5-spot pattern at the 10 gpm groundwater injection rate. The assumption is that the injected groundwater is from a background well with no elevated metals concentrations. In this case, we assume a baseline uranium concentration of 0.075 mg/L (0.315  $\mu$ M). All other background groundwater components are as listed in **Table 4.4**. The pumping rate for the central production well in the 5-spot pattern can be operated at the summation of the injection rates at the 4 wells. Unlike the ISR operation where excursions of lixiviant and metals cannot be tolerated, minor injectate excursions of lactate are not considered a threat to the water quality. Consequently, the produced water can all be recycled, provided the water quality is satisfactory. If treatment is necessary, standard ion exchange and reverse osmosis techniques described in Chapter 2 can be employed.

Two injectate formulations are modeled. The first case, presented in **Section 6.3**, uses lactate amendment in the injectate under the assumption that recycling of bioreduced water from the production well effectively removes the U(VI) and sulfate terminal electron acceptors.

The second case, presented in **Section 6.4**, uses injectate based on lactate amendment of groundwater from a background well with the terminal electron acceptors present.

### **6.3 Field-Scale Bioremediation Modeling Results**

As in the modeling of the column experiment, the injected lactate is consumed in two microbially-mediated TEAP reactions, phyllosilicate Fe(III) and sulfate, whereas the acetate produced by these reactions is consumed in TEAP reactions involving crystalline (i.e., goethite) and phyllosilicate forms of Fe(III) as well as aqueous U(VI). The solid phase phyllosilicate Fe(III) is immobile with 98.5% of the biogenic iron remaining in the clay structure. Note that aqueous phase components will be physically displaced and mixed by the injected water. Relative to the column experiment, the magnitudes and time scales of the TEAP reaction products are profoundly affected by the pumping rates and well configuration. For example, the rate of electron donor delivery to the sediments near the well bore is three orders of magnitude more than the column experiment. Consequently, a parcel of injectate will react with considerably more than 10 cm of sediment and sediments near the well bore will be exposed to 3 orders of magnitude more electron donor.

After 2 days of biostimulation, lactate is largely unreacted and within a 5 m radius of the injection wells (**Figure 6.1**). From Table 5.5, the median residence time is on the order of 10 days. Thus, the bulk of the injectate is still in the vicinity of the injection well. At this point, the pumping well has only a minor impact on the geometry of the lactate distribution. The outermost fringe of the lactate distribution, which contains the lactate that has been in the system the longest is approximately half of the initial lactate concentration. While lactate is being consumed in TEAP reactions, dispersion also contributes to the lower concentrations on the outer fringe of the injectate.

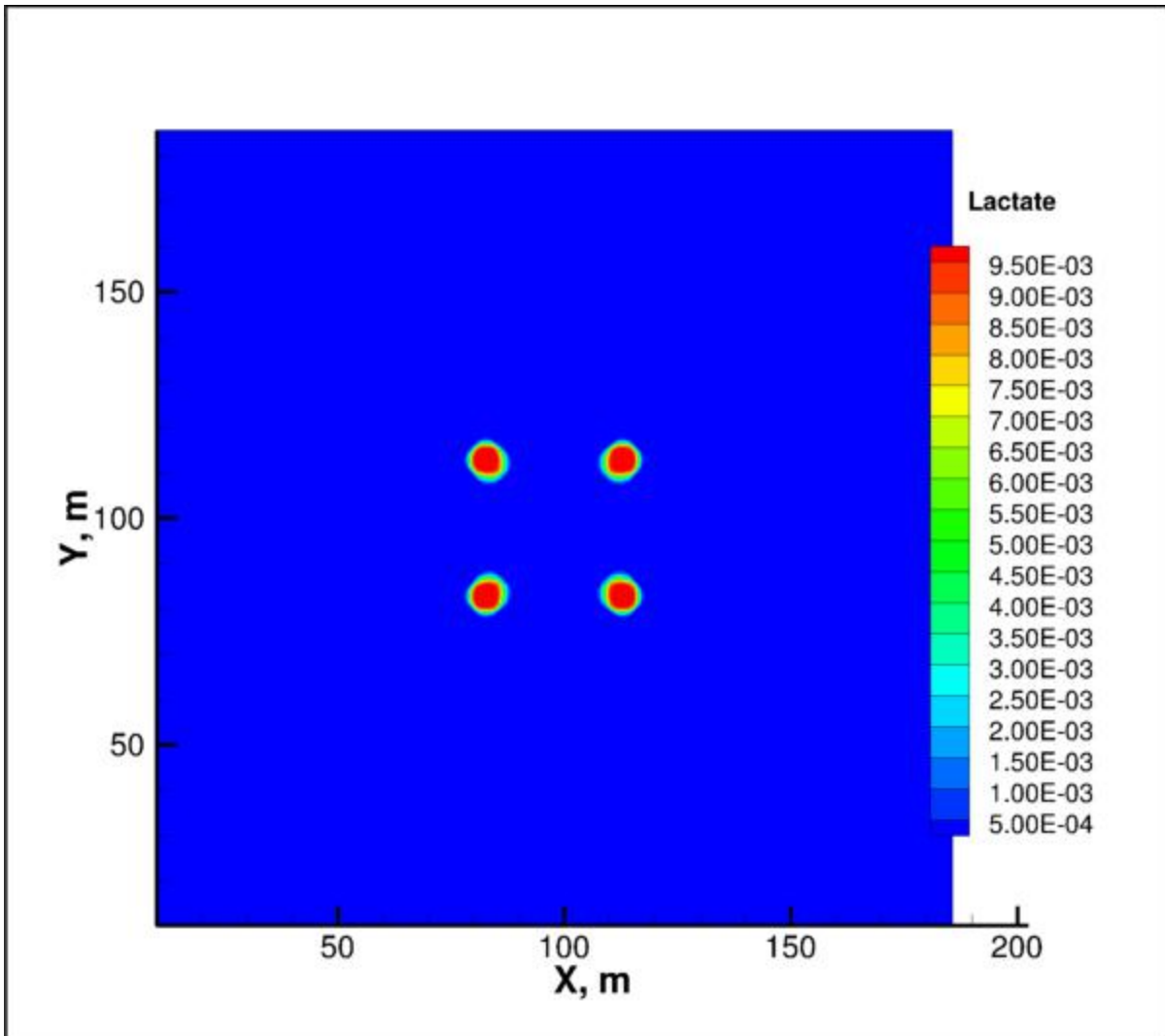


Figure 6.1 Lactate concentration (M) distribution after 2 days of injection from perimeter wells.

After 2 days, the acetate concentrations near the injection well are essentially zero corresponding to where the lactate reaction kinetics are slow relative to the high transport rates near the injection well (**Figure 6.2**). The highest acetate concentrations, ~3 mM, are in a central band of the injectate fringe. Lower concentrations are found inside and outside of this band. This represents the radius where the transport time scales and TEAP kinetics are of the same order. In this case, the lower acetate concentrations just inside the ring of peak concentrations are due to less lactate being oxidized. Conversely, outside this ring, the lower concentrations are due to consumption of acetate by Fe(III) TEAP reactions and the dispersive transition across the acetate front. Slightly more skewing in the geometry of the acetate distributions is due to the pumping well drawing injectate towards the middle of the 5-spot well pattern.

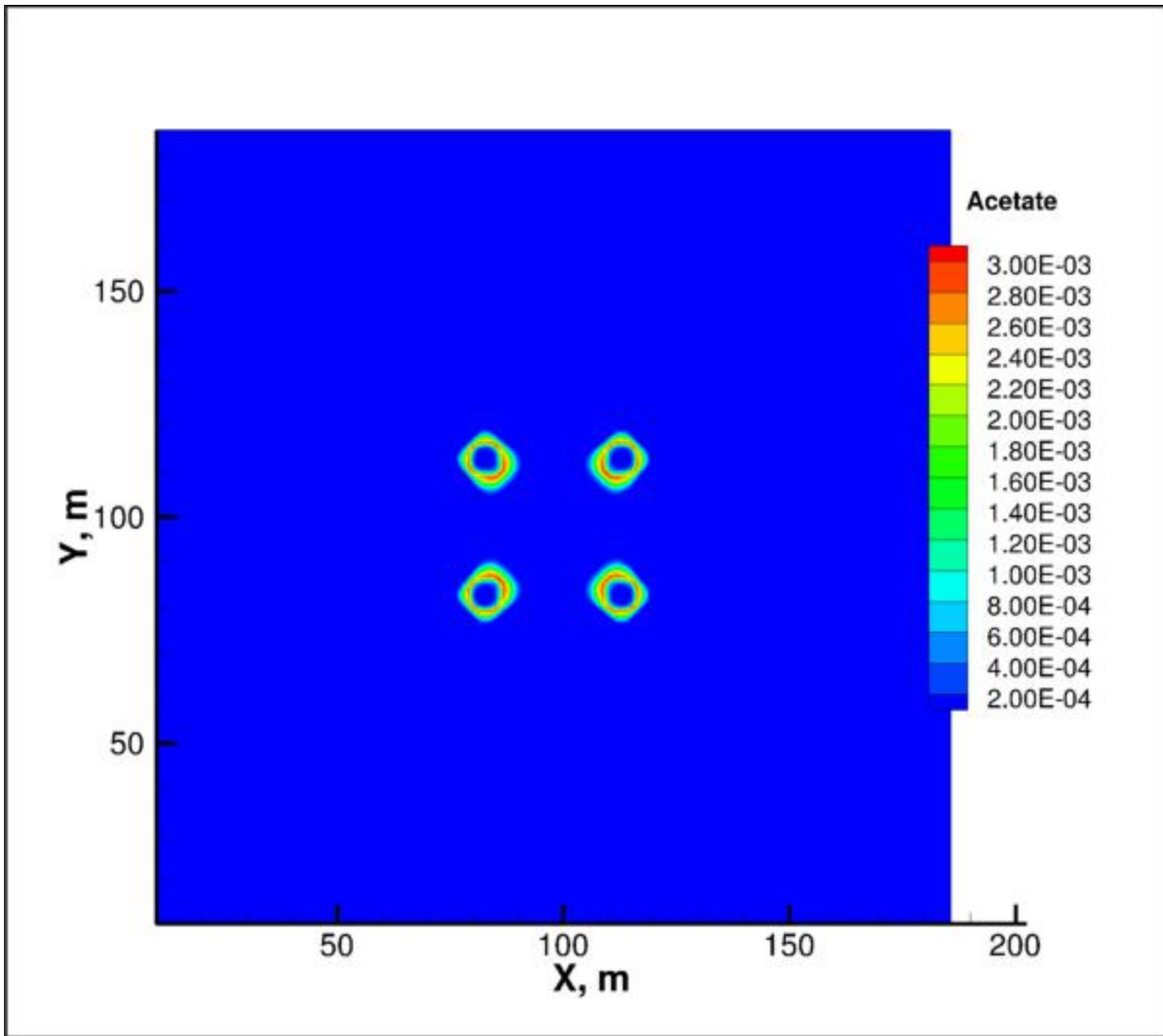


Figure 6.2 Acetate concentration (M) distribution after 2 days of injection from perimeter wells.

Aqueous Fe(II) concentrations are very similar in character to the acetate concentrations with a maximum  $\sim 1$  mM concentration (**Figure 6.3**). This implies that the acetate-driven Fe(III) bioreduction is controlling the dissolved Fe(II) behavior. In the model, lactate participates in the phyllosilicate Fe(III) TEAP reaction but not the crystalline Fe(III) TEAP reaction. This is an important distinction since most of the biogenic Fe(II) from the reduction of phyllosilicate Fe(III) is reduced in place (i.e., not liberated into solution); whereas the bioreductive dissolution of crystalline Fe(III) (i.e., FeOOH), which is only associated with acetate electron donor, liberates all bioreduced iron into solution.

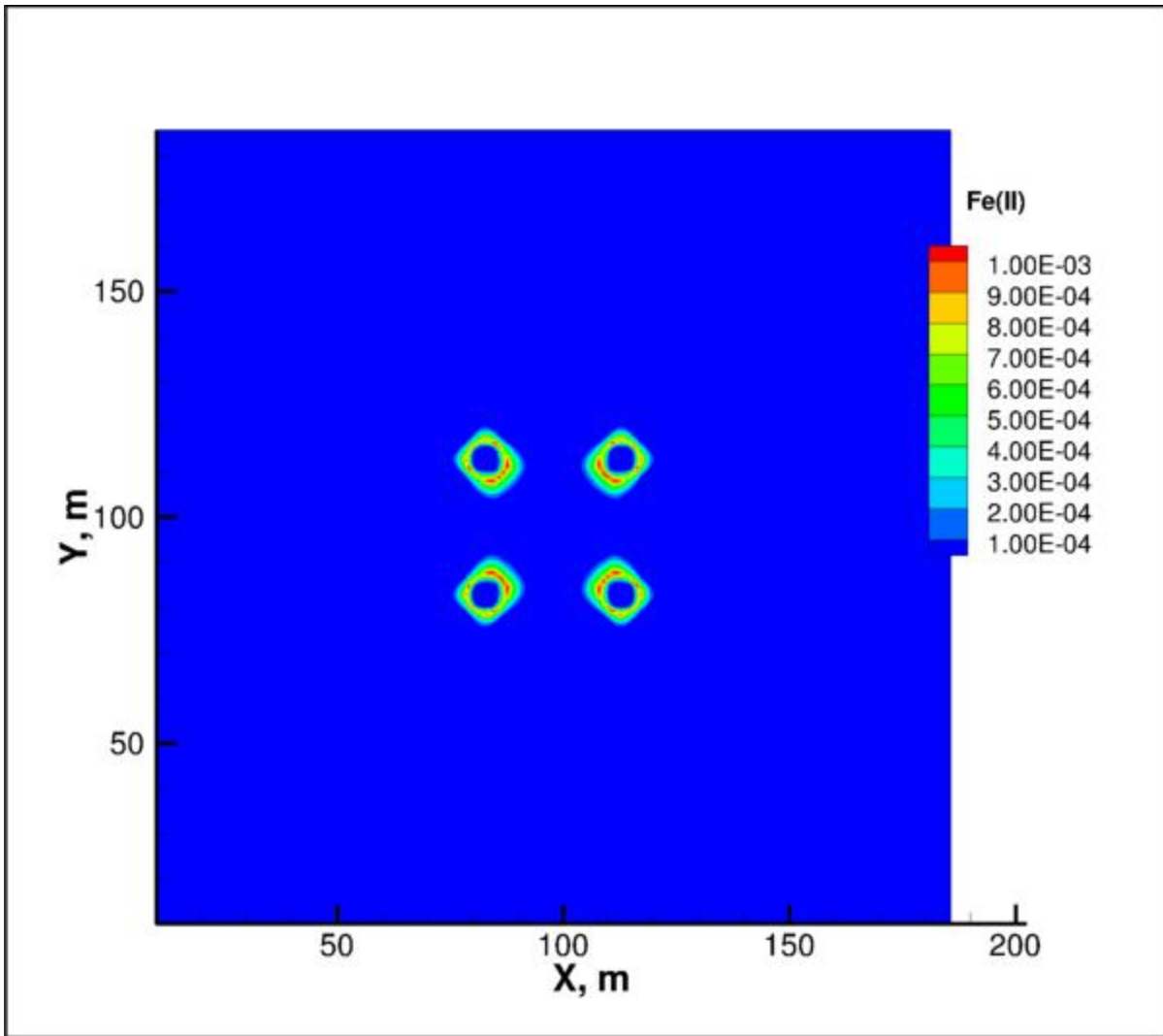


Figure 6.3 Aqueous Fe(II) concentration (M) distribution after 2 days of injection from perimeter wells.

**Figure 6.4** illustrates the situation if we assume sulfate is progressively removed from solution by reinjecting and reformatting the injectate with lactate. In this case, the low sulfate injectate is displacing the background sulfate resulting in very low concentrations near the well. On the fringes of the impacted zone, sulfate concentrations between the ambient and injectate concentrations are the result of dispersion and sulfate bioreduction.

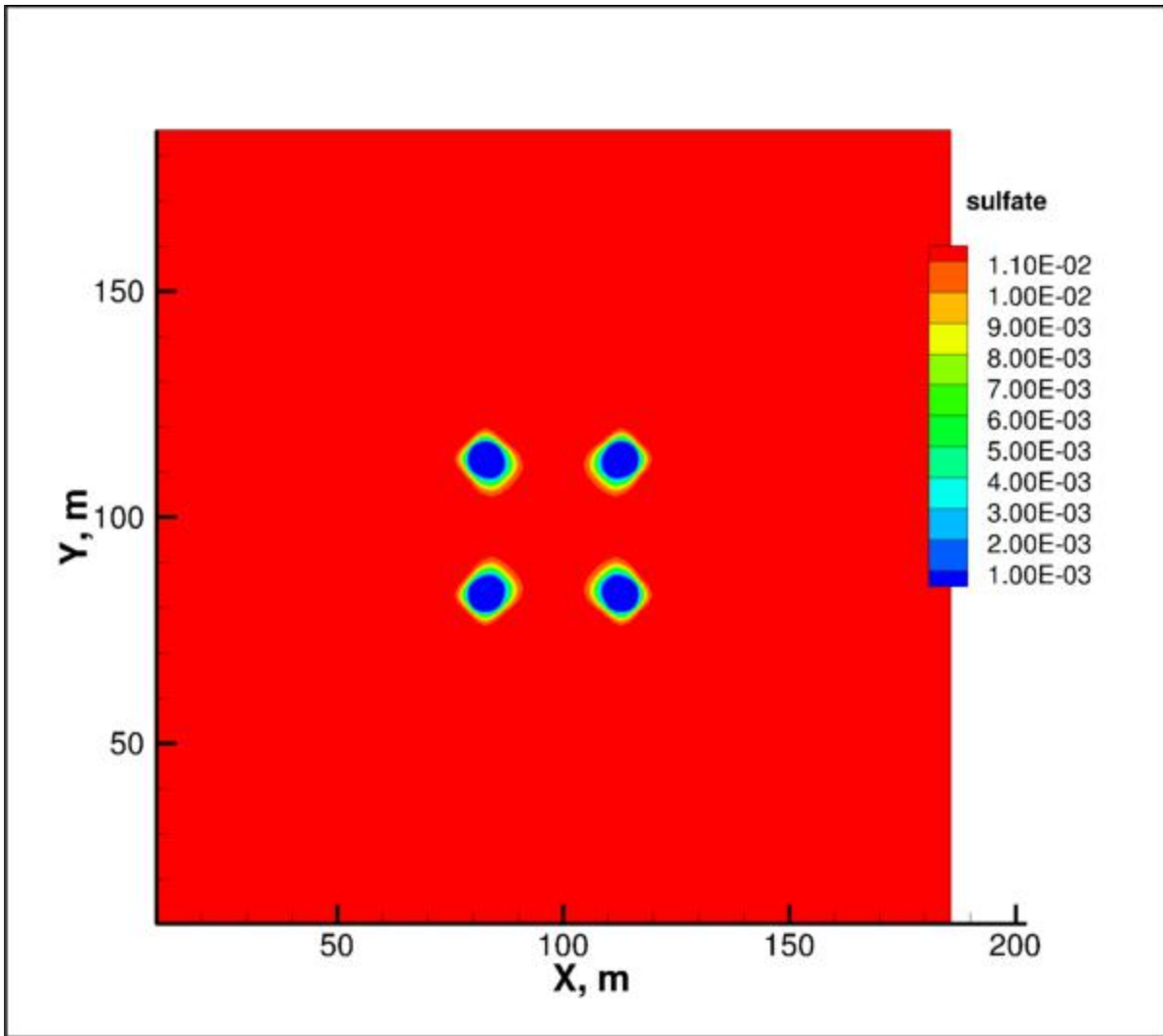


Figure 6.4 Sulfate concentration (M) distribution after 2 days of injection from perimeter wells.

The aqueous U(VI) concentration distribution after 2 days of lactate biostimulation displays complex behavior (**Figure 6.5**). While aqueous U(VI) is being displaced by the injectate, the low bicarbonate injectate is also favoring less aqueous uranium complexation and more uranium surface complexation. This results in more adsorbed U(VI) in the presence of the injectate as it moves outward. Within the outer fringe of the injectate migration, we see a ring of elevated aqueous U(VI) concentrations,  $\sim 5 \mu\text{M}$ , which is still lower than the ambient  $20 \mu\text{M}$  concentrations. On either side of this ring are lower U(VI) concentrations. The ring represents the point where the displaced aqueous U(VI) has been pushed out. The lower concentrations on the outside of the ring are the result of U(VI) TEAP bioreduction reactions with acetate from the oxidation of lactate. In this case, the kinetics of lactate consumption are sufficiently slow to limit the highest acetate to injectate that has been in the aquifer the longest, i.e., the fringe extent of the injectate migration.

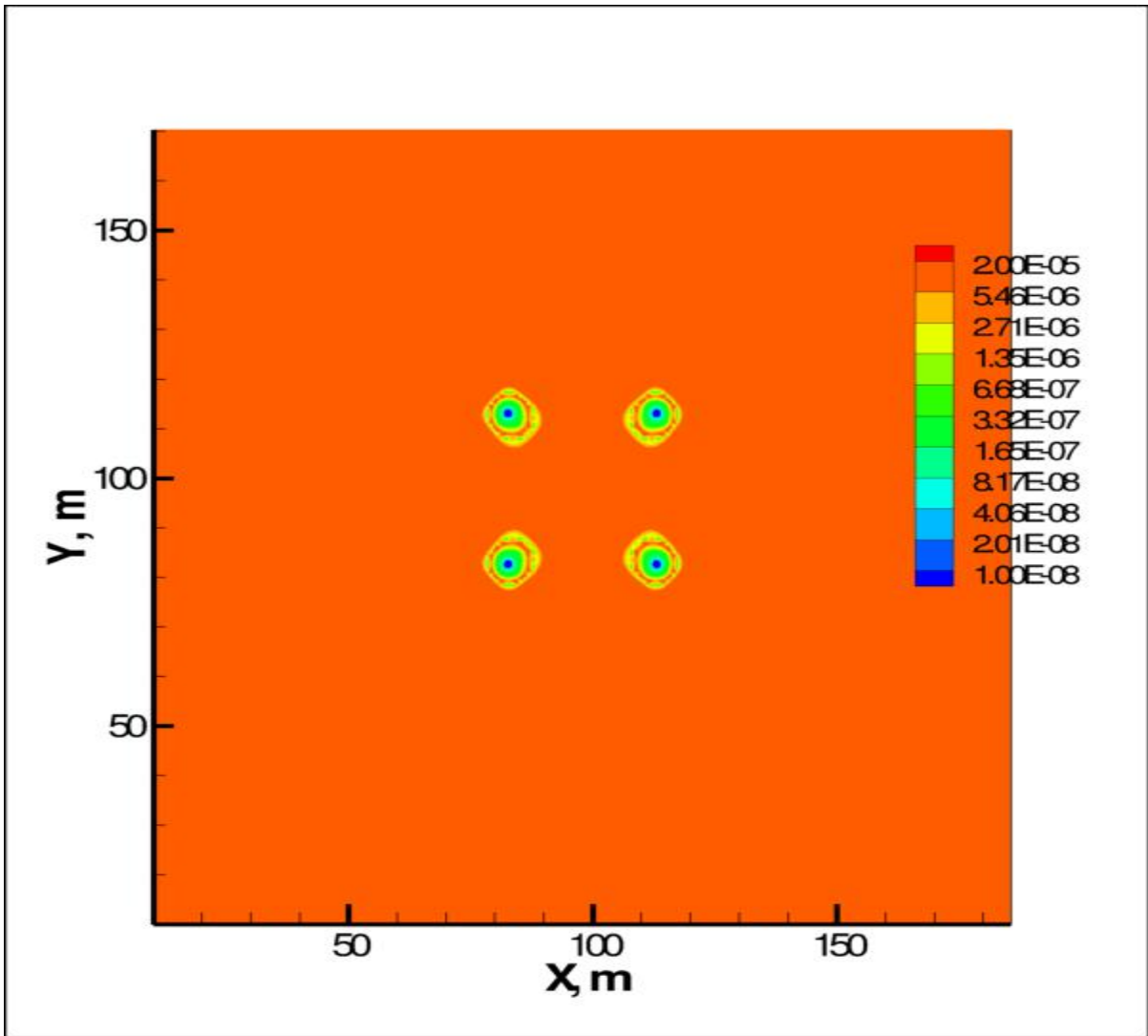


Figure 6.5 Aqueous U(VI) concentration (M) distribution after 2 days of injection from perimeter wells.

### 6.3.1 10 Days

The modeling results after 10 days of lactate biostimulation from the four corner injection wells show that injectate has just arrived at the central production well. This corresponds with the mean advection travel time from the injection wells to the pumping well. Aqueous U(VI) initially in each injectate lobe is being displaced by the injectate. The bulk of the U(VI) is initially adsorbed to the sediments. In **Figure 6.6**, adsorbed U(VI) concentrations are decreasing due to desorption in response to the displacement of the aqueous U(VI).

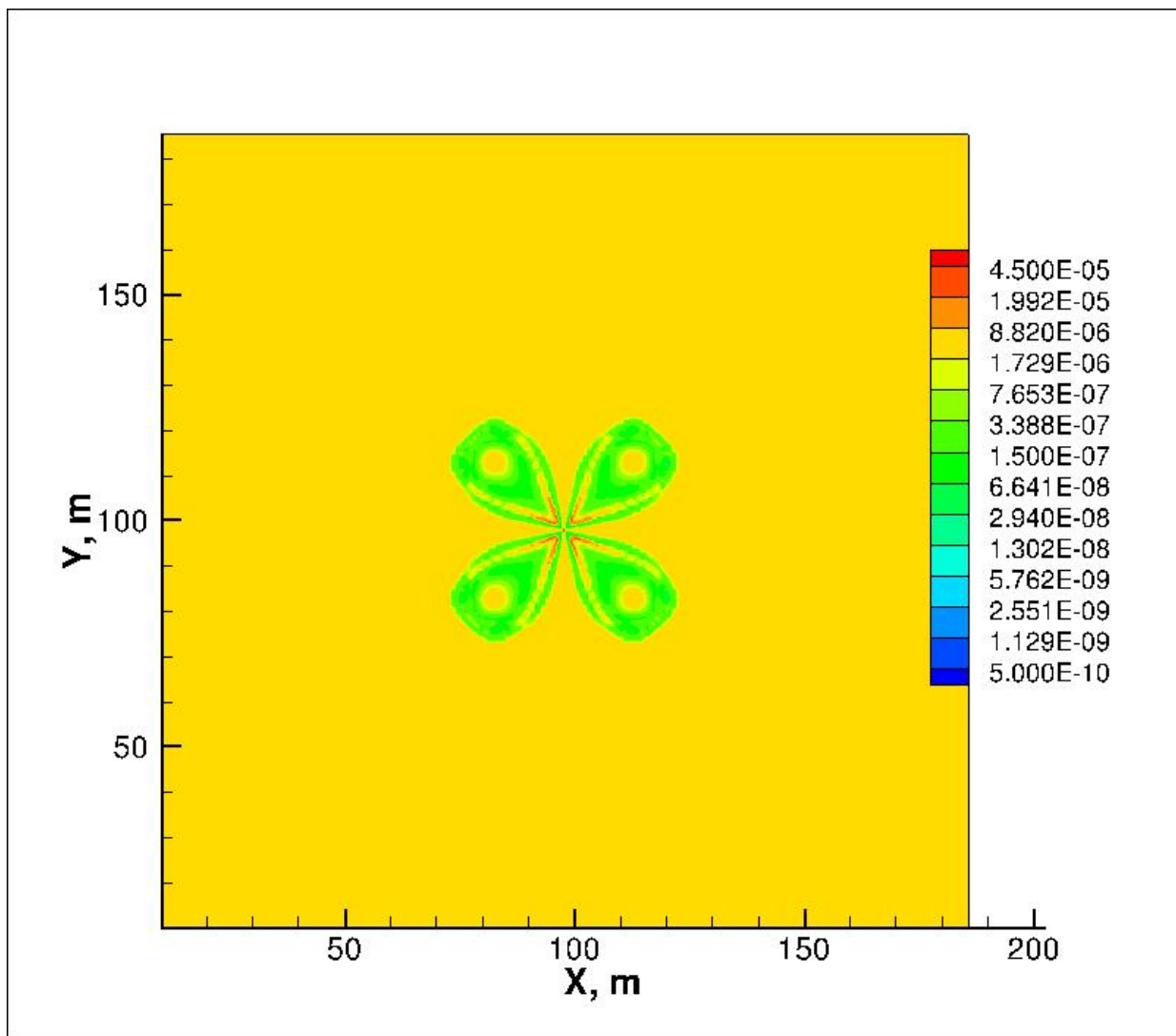


Figure 6.6 Adsorbed U(VI) concentration (M) distribution after 10 days of biostimulation from injection wells.

The bioreduction of aqueous U(VI) in the acetate-based TEAP reaction is also taking place. Thus, desorbed U(VI) is decreased subject to the availability of acetate and the U(VI) TEAP reaction kinetics. **Figure 6.7** shows that the areas of highest desorption are correlated with the areas of highest precipitation of U(IV) mineral. Once again, the lactate oxidation kinetics controlling acetate production are sufficiently slow relative to the near-injection well transport rates that acetate-based TEAP reactions (e.g., FeOOH and U(VI)) are not significant in the vicinity of the injection well. The highest U(IV) concentrations occur intermediate between the injection well and the lobe edges. This is where the displaced U(VI) is most available. U(IV) concentrations drop off near the lobe edges with the depletion of aqueous U(VI) and acetate as well as dispersive mixing across the injectate front. The implication here is that the interplay of transport, desorption, and U(VI) bioreduction will dictate how much aqueous U(VI) reaches the pumping well.

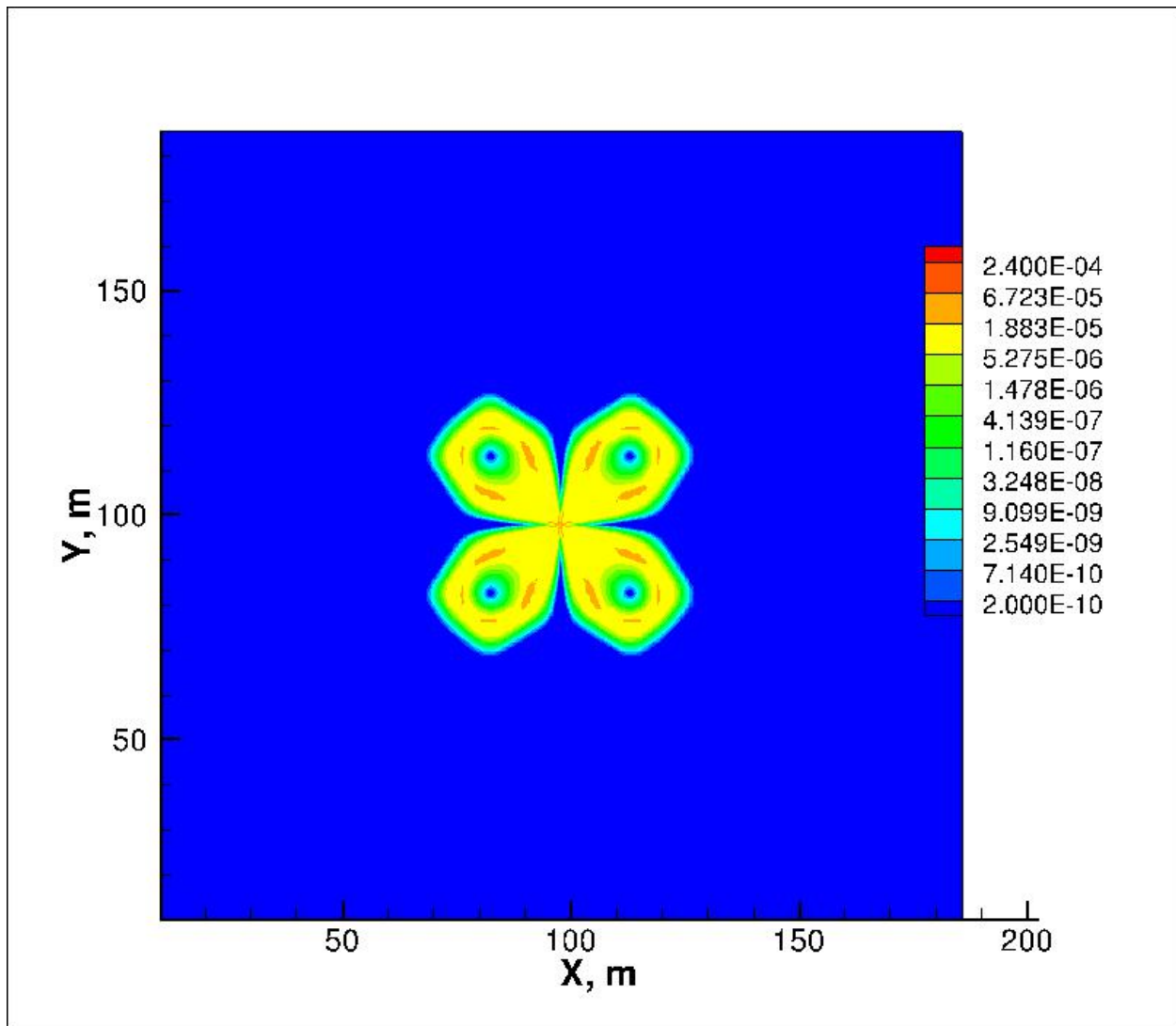


Figure 6.7 U(IV) concentration (M) distribution after 10 days of biostimulation from injection wells.

The bulk of the Fe(II) in solution after 10 days originated in the FeOOH (goethite) crystalline Fe(III) pool. With the exception of the near-injection well zone where little acetate was produced, FeOOH is depleted throughout the injectate impacted zone (**Figure 6.8**).

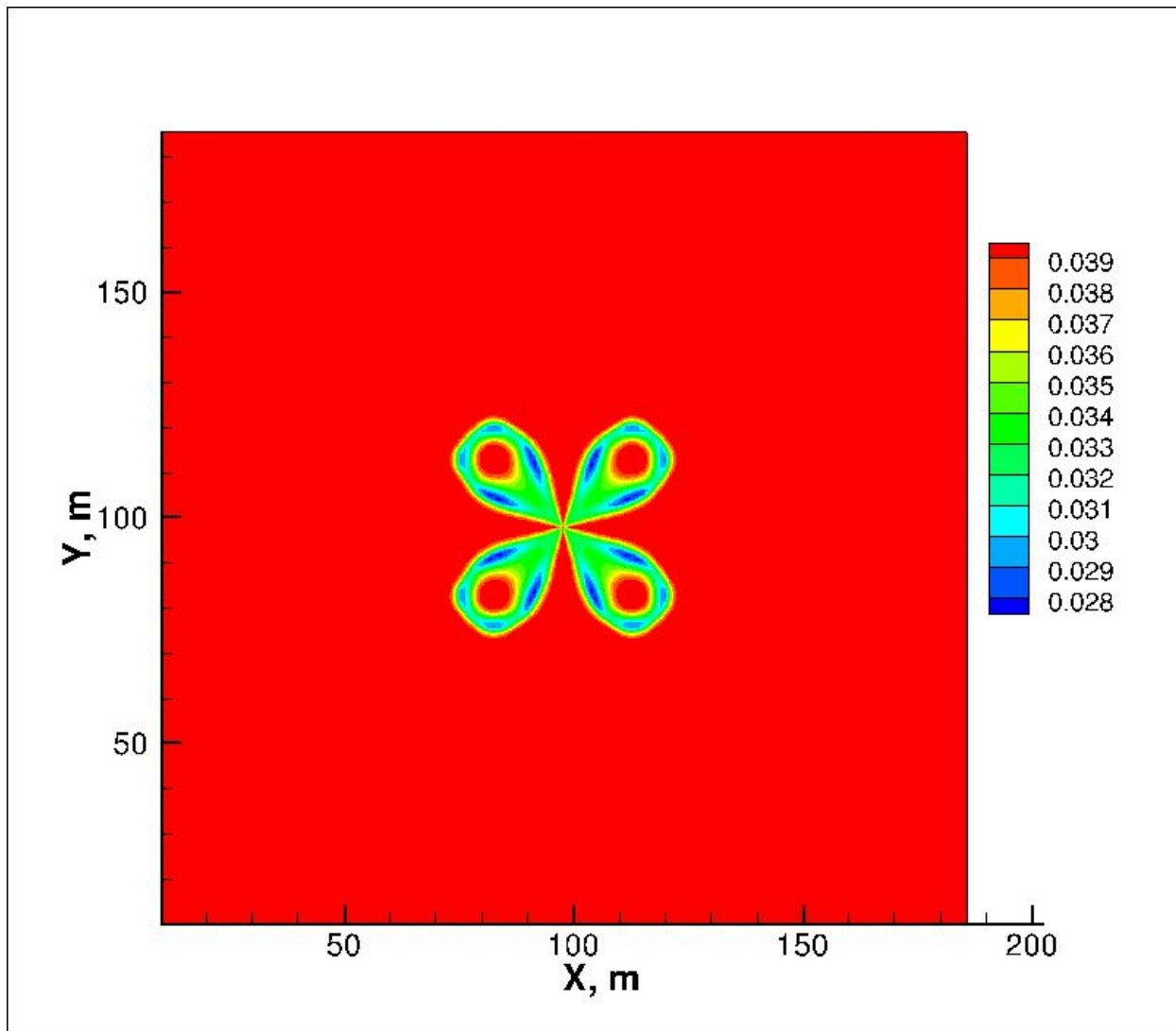


Figure 6.8 FeOOH (goethite) concentration (M) distribution after 10 days of biostimulation from injection wells.

The production of aqueous Fe(II) from the bioreductive dissolution of FeOOH is not apparent from the distribution of aqueous Fe(II) concentrations. Most illuminating is the distribution of FeS, which is similar in character to the FeOOH (**Figure 6.9**). This implies that sufficient sulfide is available to react with the aqueous Fe(II) in the injectate lobe(s) to form FeS.

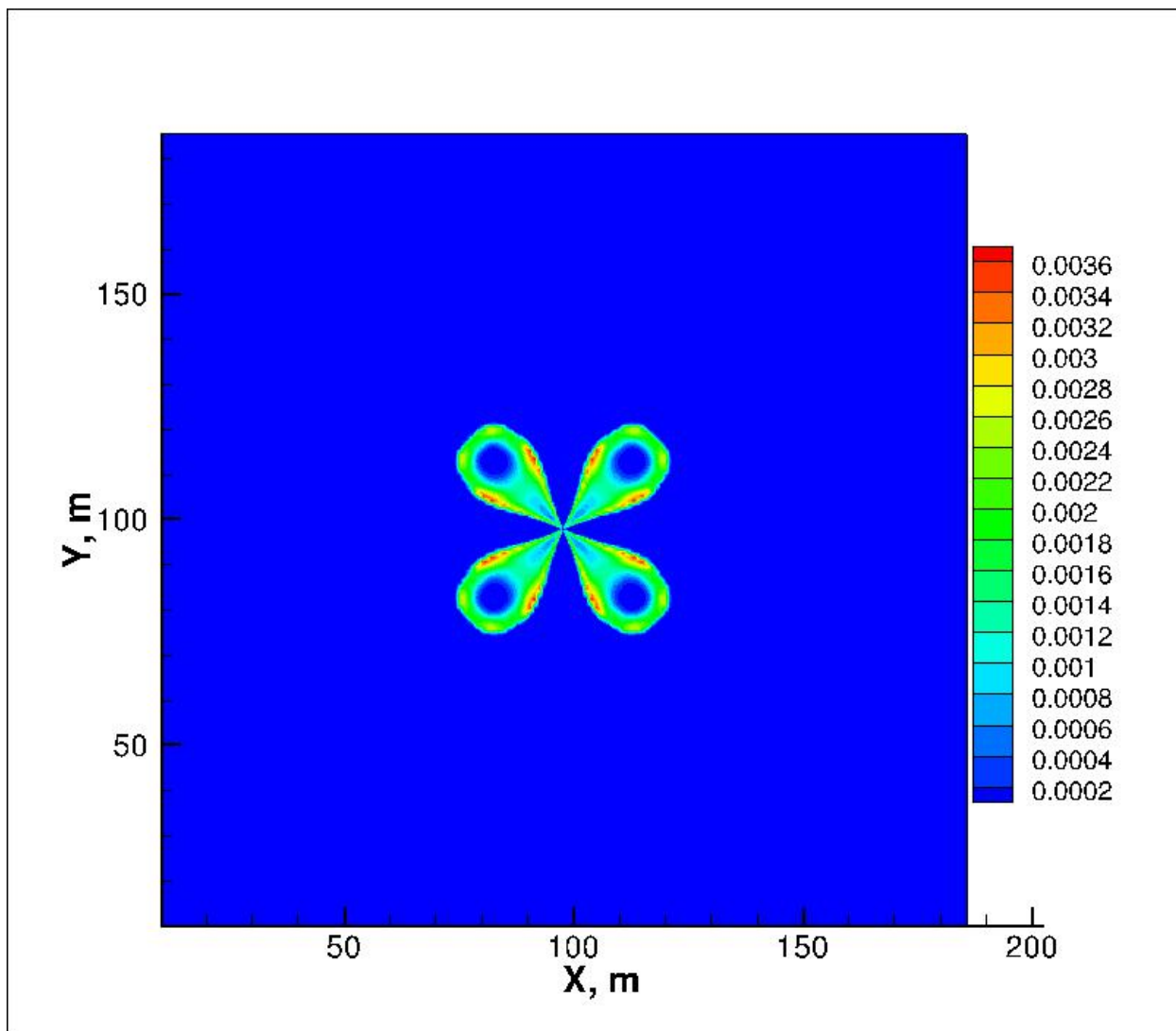


Figure 6.9 FeS concentration (M) distribution after 10 days of biostimulation from injection wells.

Another potential solid phase sink for Fe(II) is through adsorption. In this case, relatively small amounts of Fe(II) are sorbed along a narrow fringe outside of the areas of primary FeOOH dissolution and FeS precipitation (**Figure 6.10**).

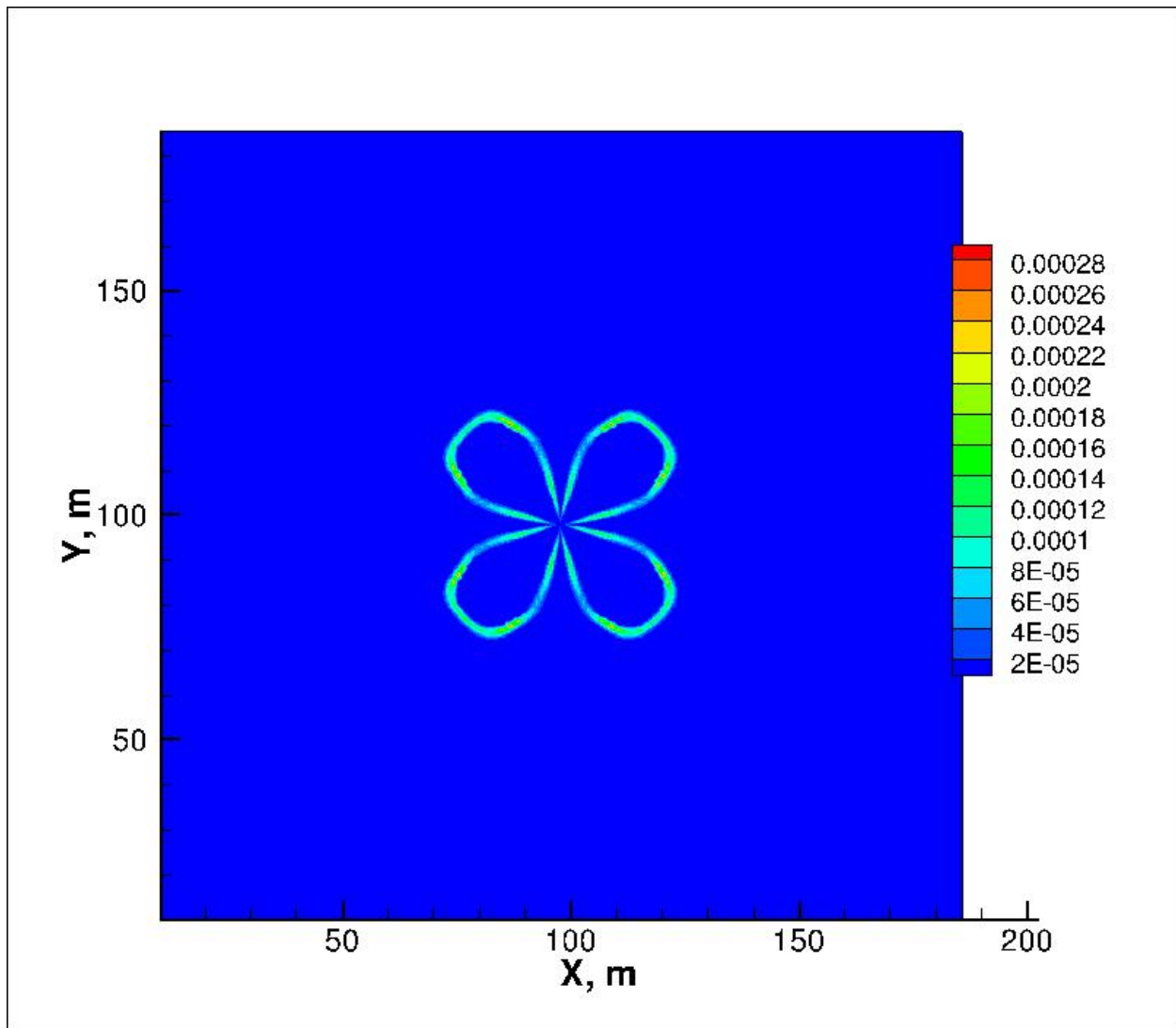


Figure 6.10 Adsorbed Fe(II) concentration (M) distribution after 10 days of biostimulation from injection wells.

The lactate-based phyllosilicate Fe(III) consumption is approximately  $3 \times 10^{-4}$  M over the injectate lobe(s) (**Figure 6.11**). This relatively small change implies that the bulk of lactate oxidation is due to the sulfate TEAP. In part, this is due to the reaction stoichiometry where almost 3 moles of lactate are oxidized to reduce 1 mole of sulfate. Thus, the approximately  $1.5 \times 10^{-3}$  M increase in FeS concentration across the injectate lobes results from the reduction of  $1.5 \times 10^{-3}$  M sulfate in which  $4.5 \times 10^{-3}$  M lactate was consumed.

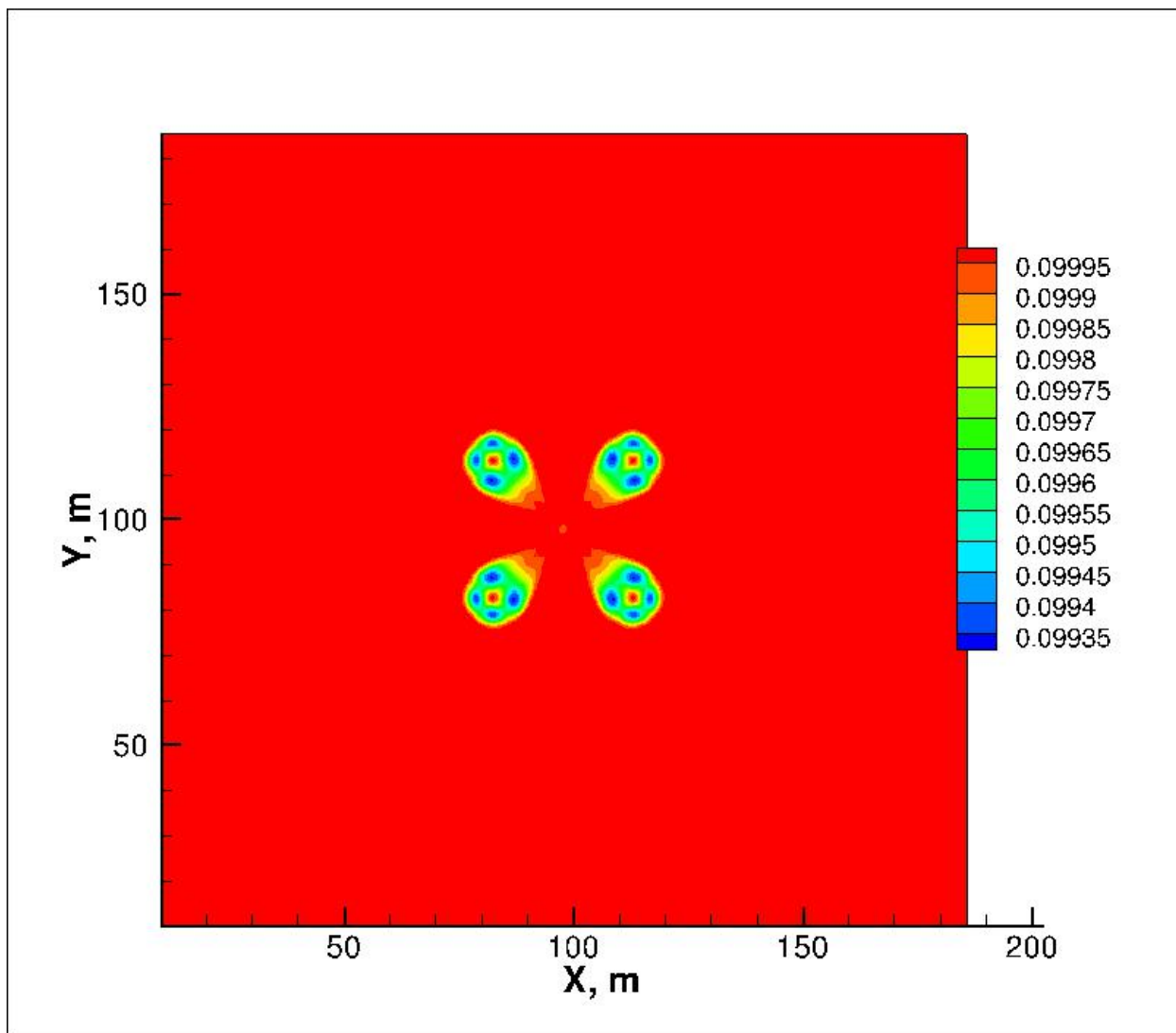


Figure 6.11 Lactate-driven phyllosilicate Fe(III) concentration (M) distribution after 10 days of biostimulation from injection wells.

The reduction of phyllosilicate Fe(III) in the injectate lobe via acetate-based TEAP reaction is approximately  $1.5 \times 10^{-2}$  M after 10 days of lactate biostimulation (**Figure 6.12**). This compares to  $5 \times 10^{-3}$  M of FeOOH. Thus, the bulk of acetate is consumed in the phyllosilicate Fe(III) TEAP reaction. This is consistent with the reaction rate, which is faster than for FeOOH.

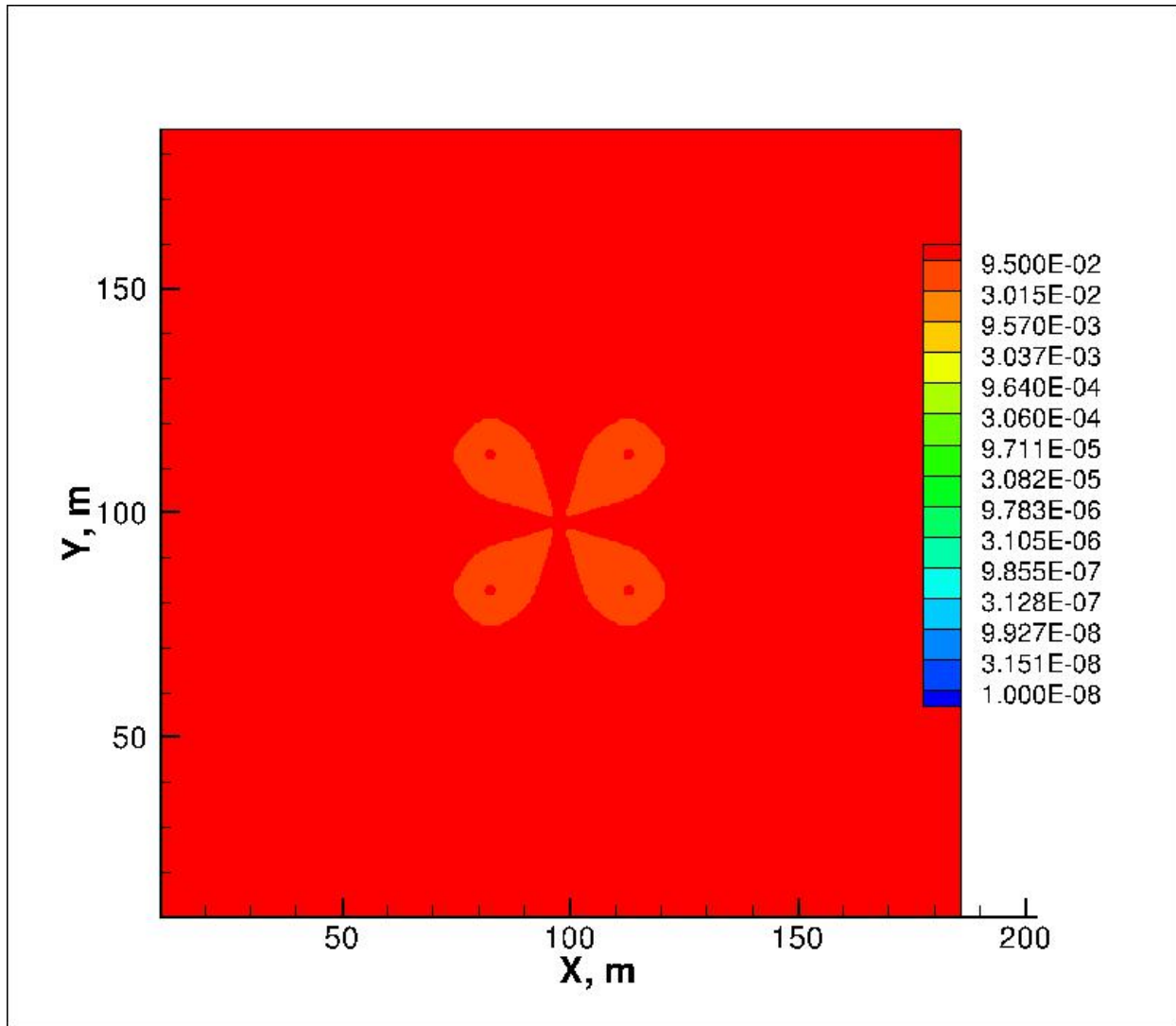


Figure 6.12 Acetate-driven phyllosilicate Fe(III) concentration (M) distribution after 10 days of biostimulation from injection wells.

After 10 days of lactate biostimulation, aqueous sulfide is found primarily in a narrow zone inside the outer edge of the injectate lobe (**Figure 6.13**). The relative absence of aqueous sulfide in the lobe interior is due, in part, to removal from solution via FeS mineral precipitation (**Figure 6.9**). As indicated by the sorbed Fe(II) distribution (**Figure 6.10**), there is a fringe of Fe(II) outside of the aqueous sulfide edge. At this location, lactate has been consumed, which precludes sulfide production. Acetate and Fe(III), however, are present resulting in the production of Fe(II) from the bioreduction of Fe(III) minerals.

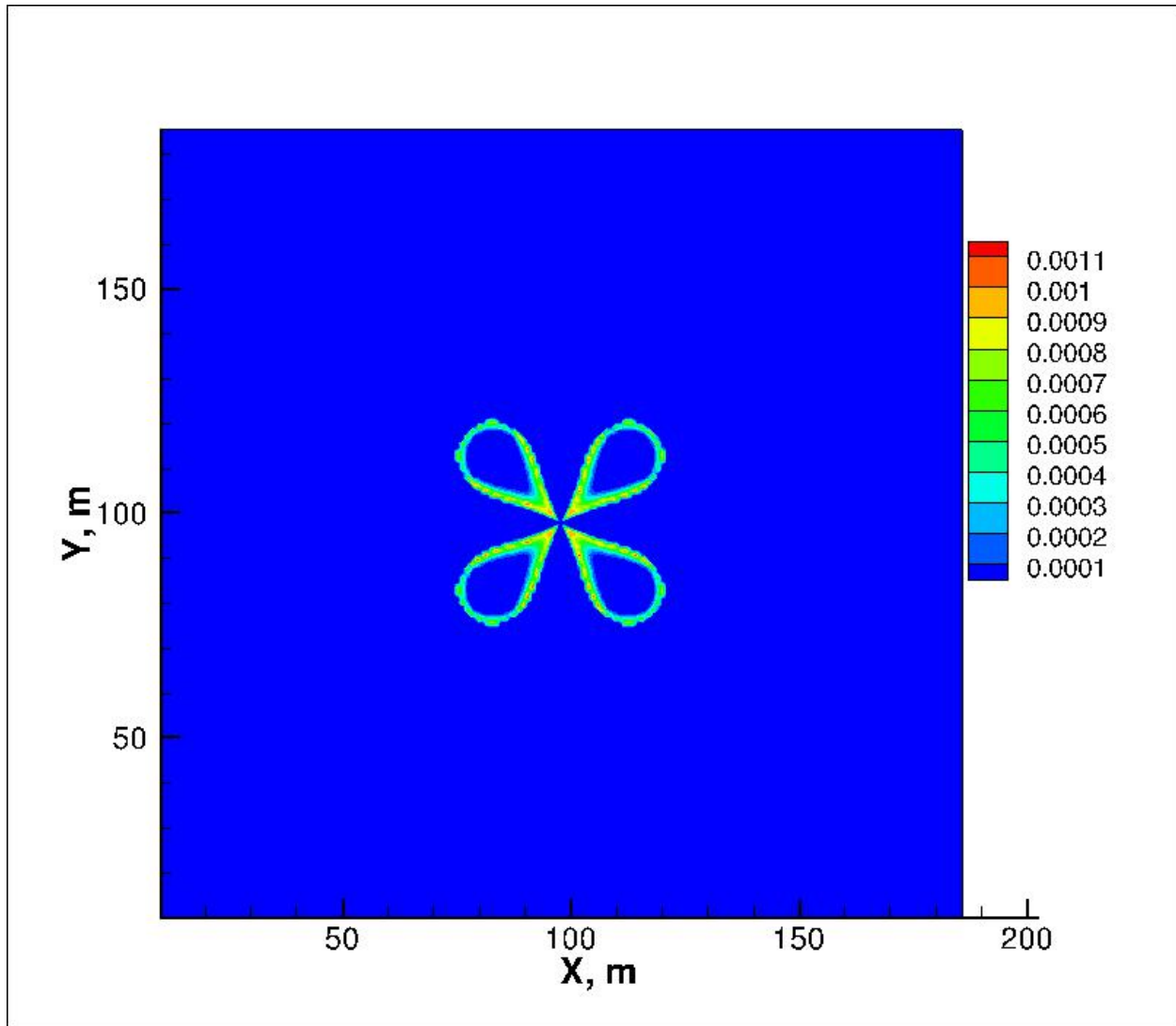


Figure 6.13 Aqueous sulfide concentration (M) distribution after 10 days of biostimulation from injection wells.

### 6.3.2 30 Days

As expected from the tracer studies, lactate from the injection wells reaches the production well in ~10 days. The lactate concentration contours in **Figure 6.14** at 30 days of biostimulation show that lactate arriving at the well has generally undergone minimal attenuation. Only the lactate transported along the flow paths with the longest travel times (i.e., outer edges of the four injectate plumes) exhibit attenuation. This is due to a combination of lactate oxidation and dispersion across the edges of the plume.

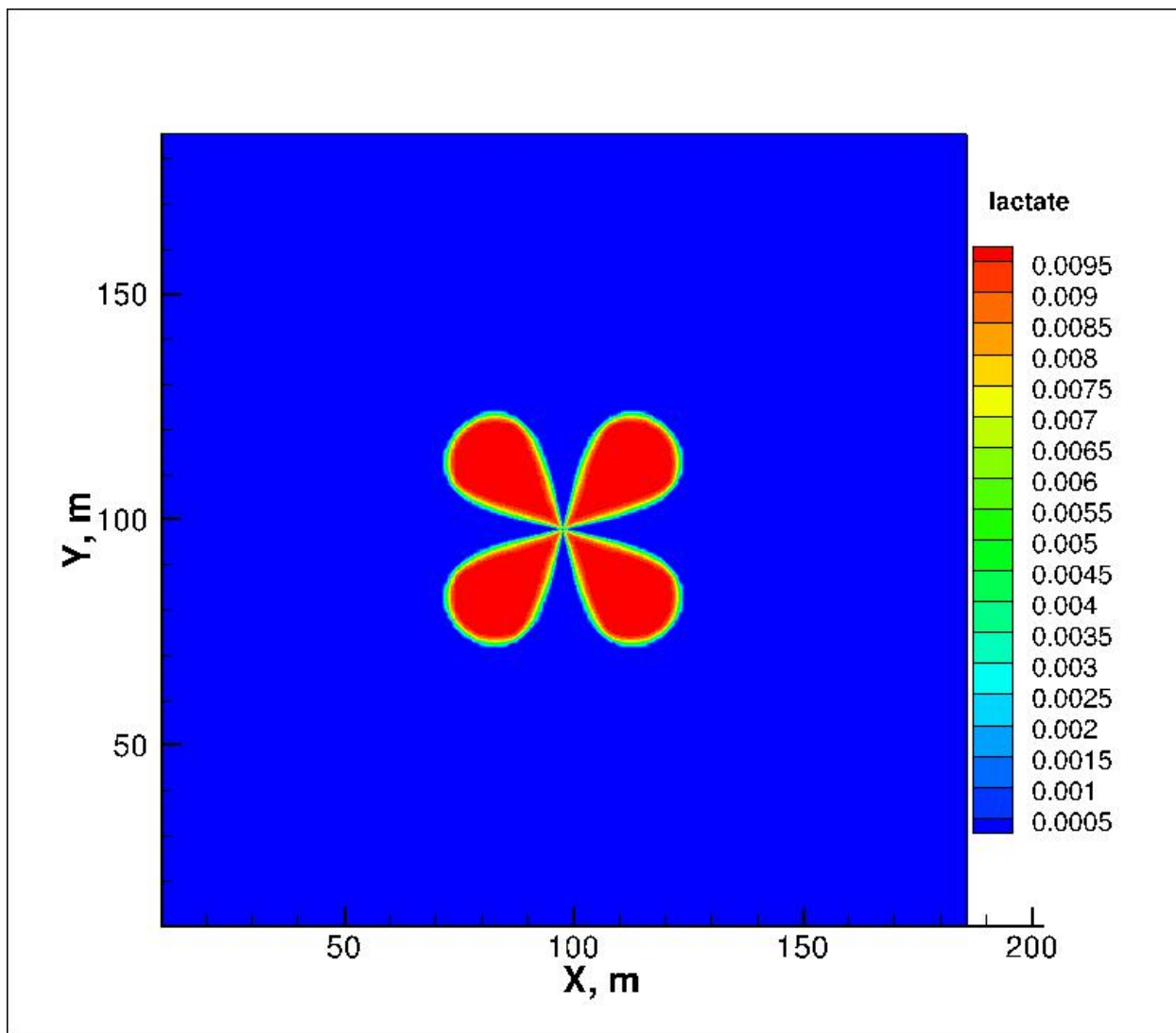


Figure 6.14 Lactate concentration (M) distribution after 30 days of injection from perimeter wells.

**Figure 6.15** shows that after 30 days acetate is found primarily along the perimeter of each injectate lobe. While acetate is being generated wherever lactate and electron acceptors are available, the kinetics of the lactate oxidation are sufficiently slow relative to the transport rates near the injection well that very little acetate is generated within a radius of ~10 m from the injection well. Outside of that radius, lactate oxidation produces sufficient acetate to drive Fe(III) TEAP reactions that begin to deplete crystalline (i.e., FeOOH) and phyllosilicate Fe(III) inside the injectate lobes. It is that process that consumes acetate in the lobes whereas along the perimeter of the lobes there are slower transport pathways, allowing more time for lactate oxidation which produces more acetate than the consumption in the Fe(III) TEAP. As in the earlier result at 2 days, the highest acetate concentrations occur in a central band through the outer fringe of the injectate lobe. This is where lactate has had sufficient time to react to produce acetate but insufficient time for acetate to significantly react with Fe(III) to deplete the acetate concentration. Basically, this location is a balance between transport and reaction

rates. On the outside of this acetate fringe, the lower acetate concentrations reflect the longer residence time, which allows more acetate to react. On the inside of this acetate fringe, the lower acetate concentration is the result of shorter residence time for lactate conversion to acetate and the consumption of acetate by the TEAP reactions.

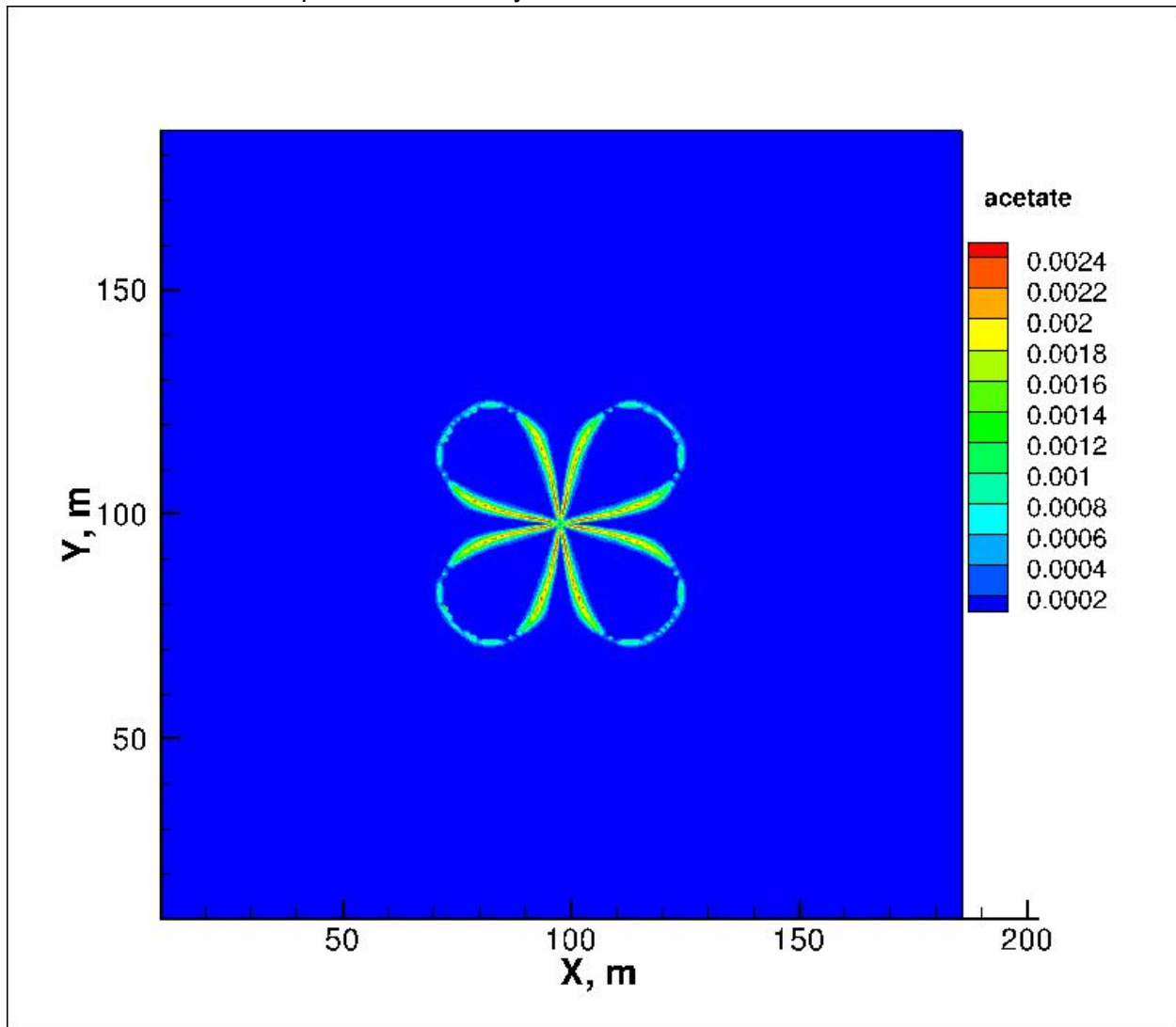


Figure 6.15 Acetate concentration (M) distribution after 30 days of injection from perimeter wells.

In **Figure 6.16**, the elevated Fe(II) concentrations are found on the perimeter of the four injectate lobes, distributed similarly to the acetate concentrations. In this case, however, the highest concentrations are in the central band furthest from the production well. This corresponds to the location where lactate has been in the system for the longest duration, which allows more time for acetate to be produced, and more time for that acetate to react with Fe(III) minerals. It should be noted that this Fe(II) distribution does not necessarily reflect where the Fe(II) originated from. The spatial distribution of goethite depletion, which occurs over much of the injectate lobe (described below), indicates where Fe(II) was initially produced. The

distribution of aqueous Fe(II) on the perimeter of the injectate lobes is the net result of the nonuniform flow field, lactate injection, and rates of Fe(III) and sulfate bioreduction and FeS mineral precipitation.

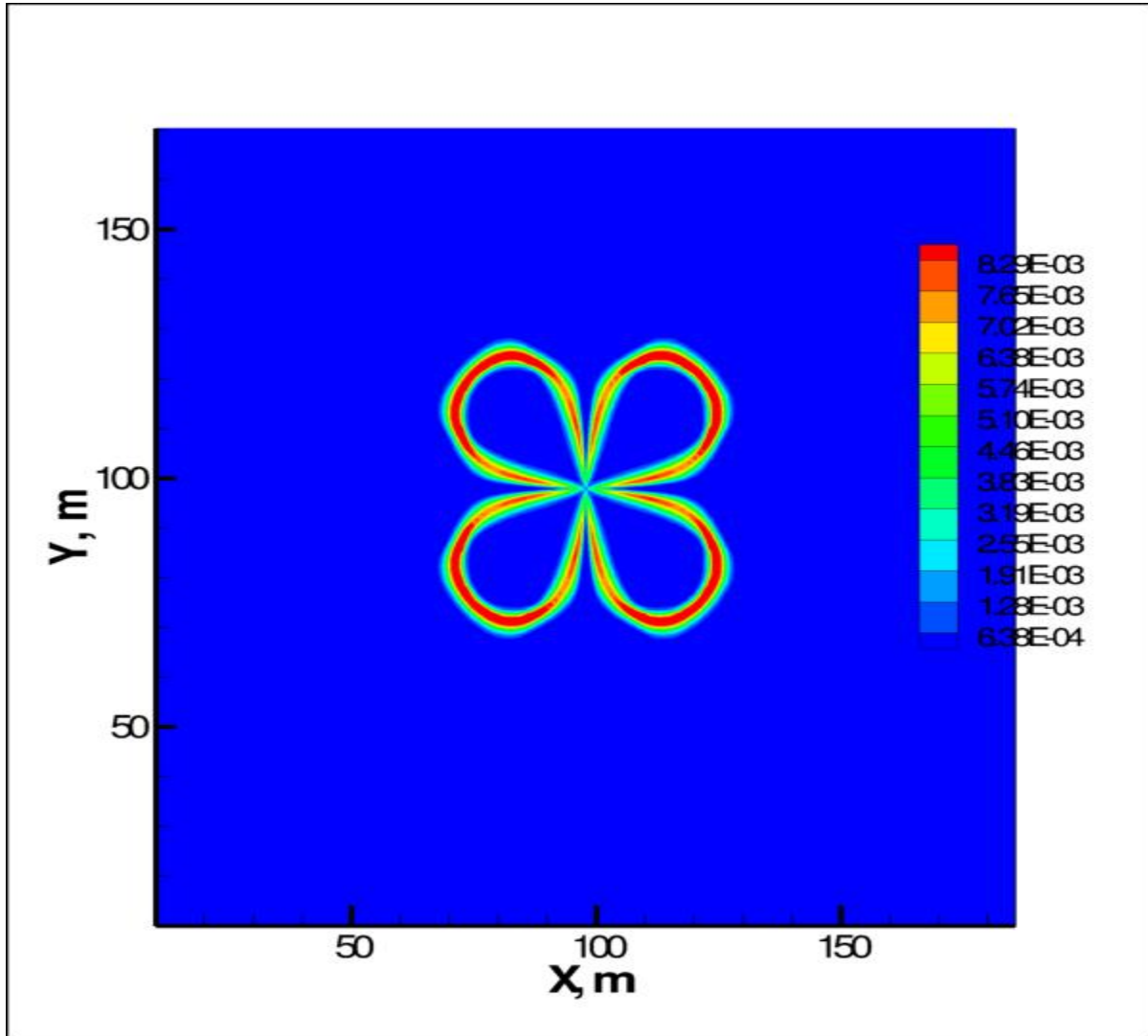


Figure 6.16 Aqueous Fe(II) concentration (M) distribution after 30 days of injection from perimeter wells.

Nearly all of the Fe(II) in solution is from the acetate-driven bioreduction of crystalline Fe(III) represented by goethite. In **Figure 6.17**, the zones of goethite depletion are clearly transport controlled. Near the well, very little acetate has been produced, limiting the Fe(II) that can be produced. Conversely, goethite is depleted within the injectate lobes away from the fastest flow paths to the production well.

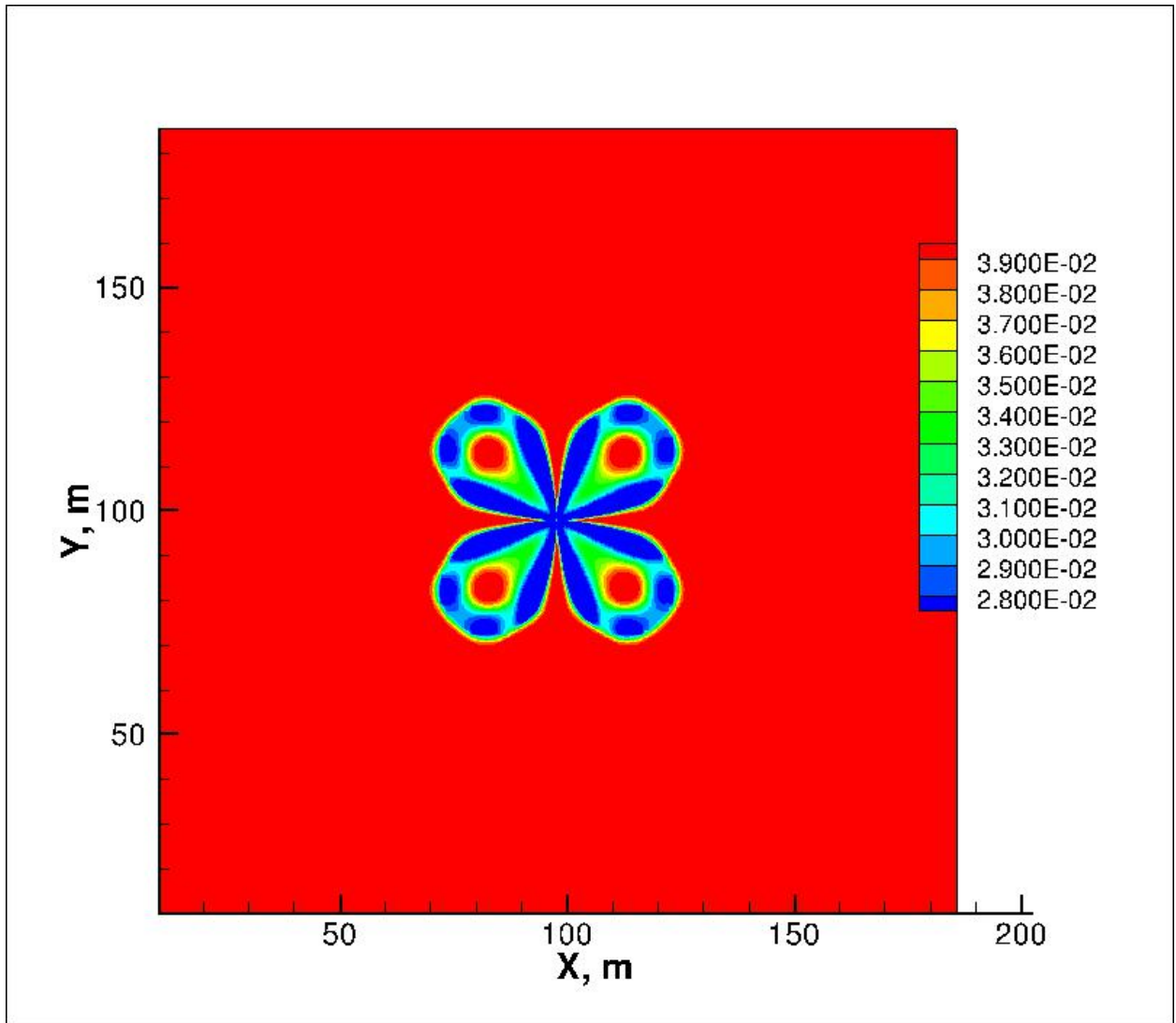


Figure 6.17 FeOOH (goethite) concentration (M) distribution after 30 days of injection from perimeter wells.

After the initial displacement of aqueous sulfate, there is essentially no sulfate in the injectate lobes (**Figure 6.18**).

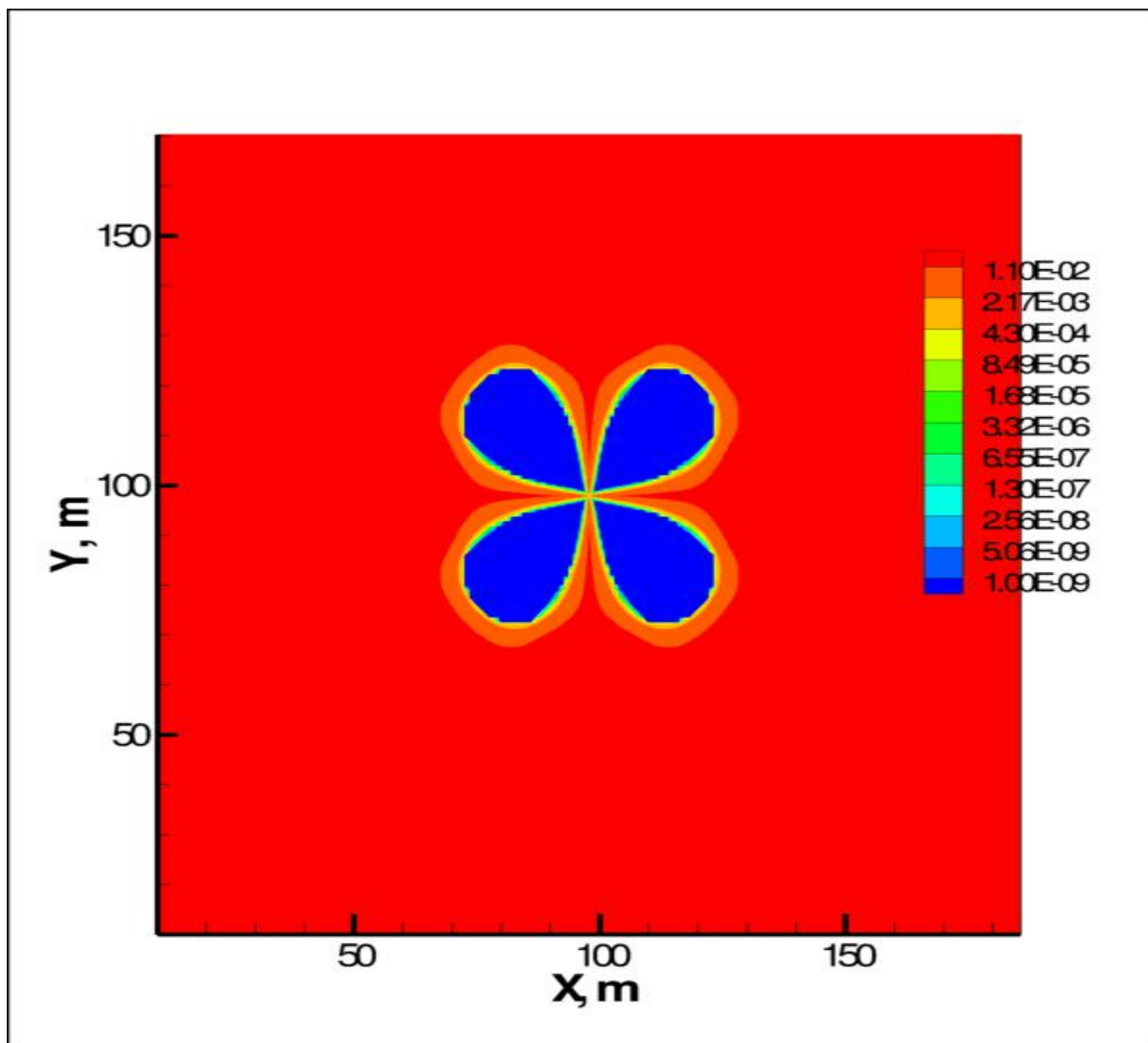


Figure 6.18 Sulfate concentration (M) distribution after 30 days of injection from perimeter wells.

The sulfide precipitated as FeS inside the injectate lobes after 30 days (**Figure 6.19**) is similar to the result after 10 days with a slightly larger spatial extent and larger zones of high concentrations. While sulfate from outside the injectate front can be entrained into the outer edges of the lobe by dispersion, the effect has minimal impact because of the small amount of sulfate that can contact and react with lactate to form sulfide.

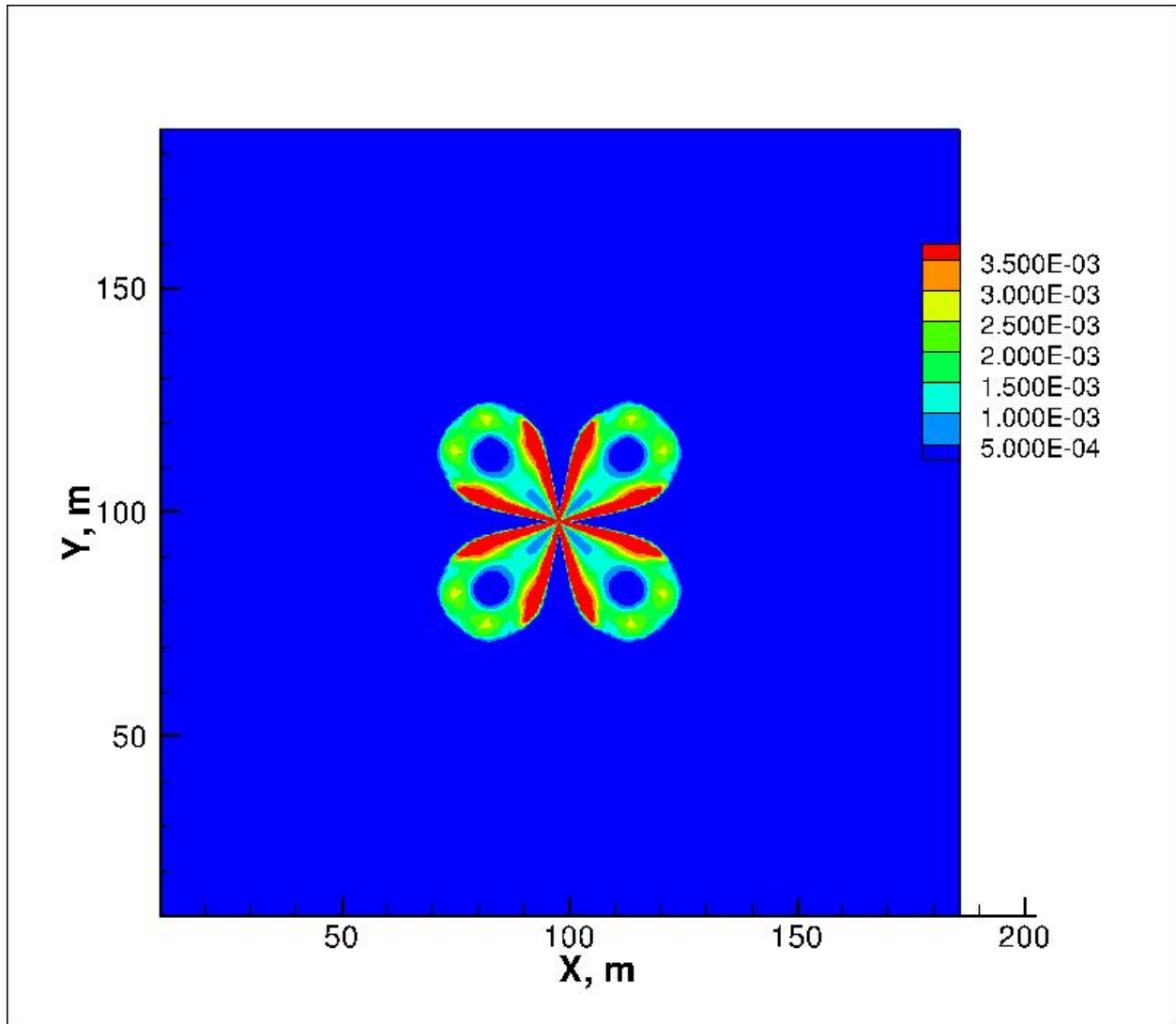


Figure 6.19 FeS concentration (M) distribution after 30 days of lactate biostimulation.

The sulfide concentration distribution (**Figure 6.20**) is largely unchanged from the 10 day result implying a pseudo-steady state of low-level sulfide production has set up.

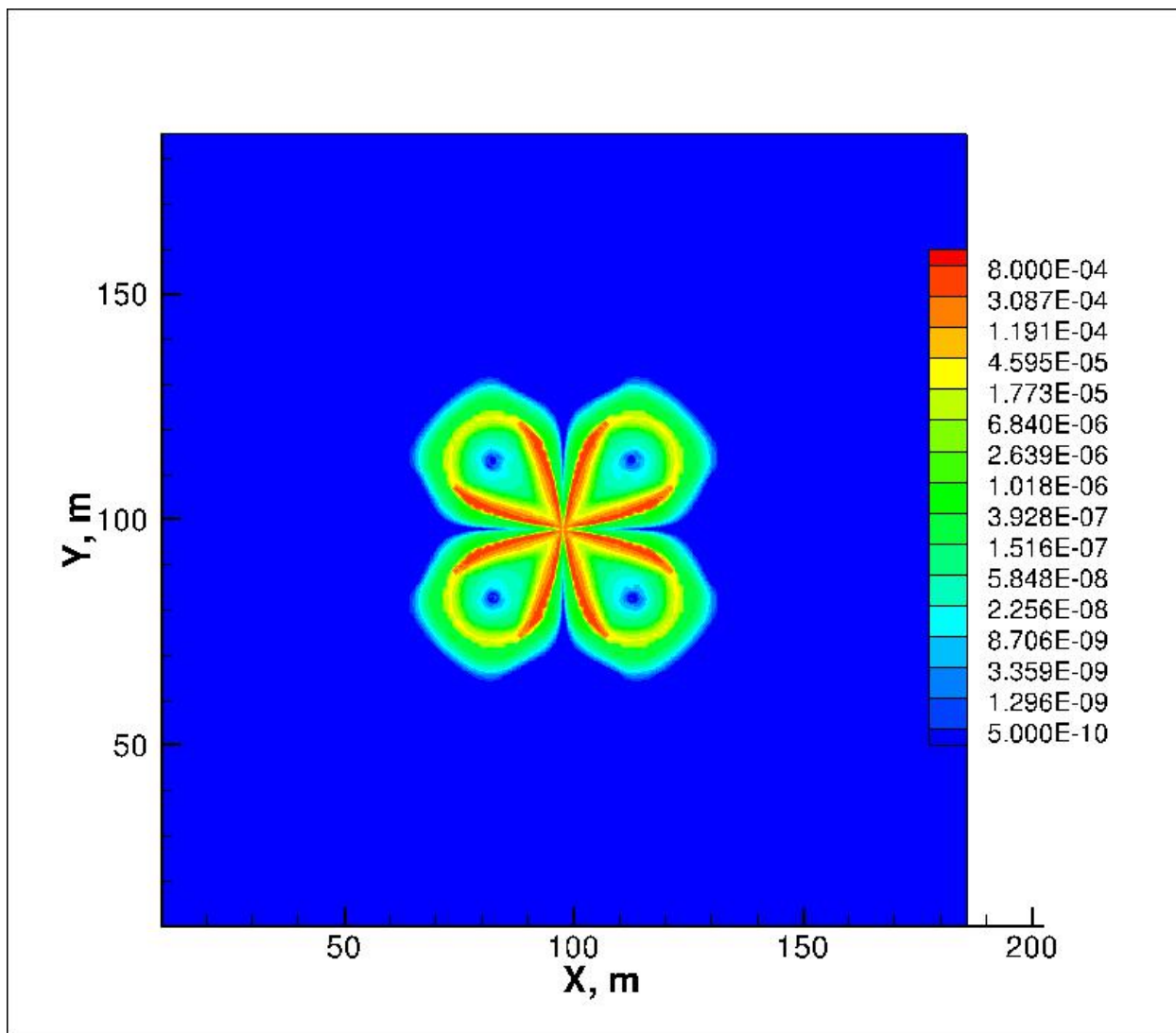


Figure 6.20 Aqueous sulfide concentration (M) distribution after 30 days of lactate biostimulation.

**Figure 6.21** shows the depletion of aqueous U(VI) throughout the injectate lobes after 30 days. The continuous cycle of lowering aqueous U(VI) concentrations via bioreduction to U(IV) and driving desorption of U(VI) from the sediments has led to a three orders of magnitude decrease in aqueous U(VI). The negligibly small aqueous U(VI) concentrations ( $\sim 1.0 \times 10^{-8}$  M) that are still present are due to the desorption of the adsorbed U(VI).

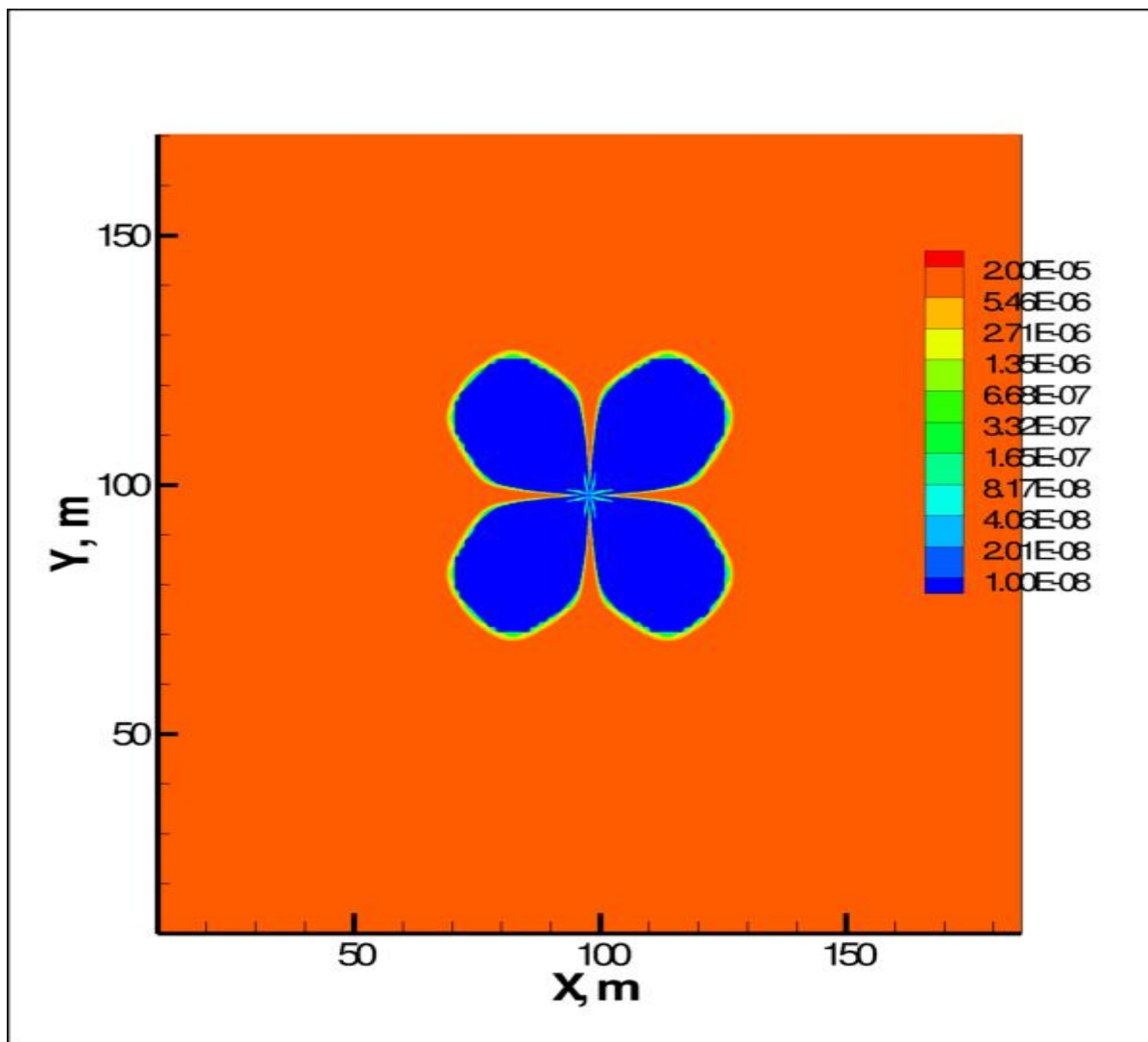


Figure 6.21 Aqueous U(VI) concentration (M) distribution after 30 days of lactate biostimulation.

**Figure 6.22** shows that the adsorbed U(VI) is largely depleted with the exception of the near well zone. As the adsorbed U(VI) controls the U(VI) in solution that is available for bioreduction, the U(VI) in the system after 30 days is negligible.

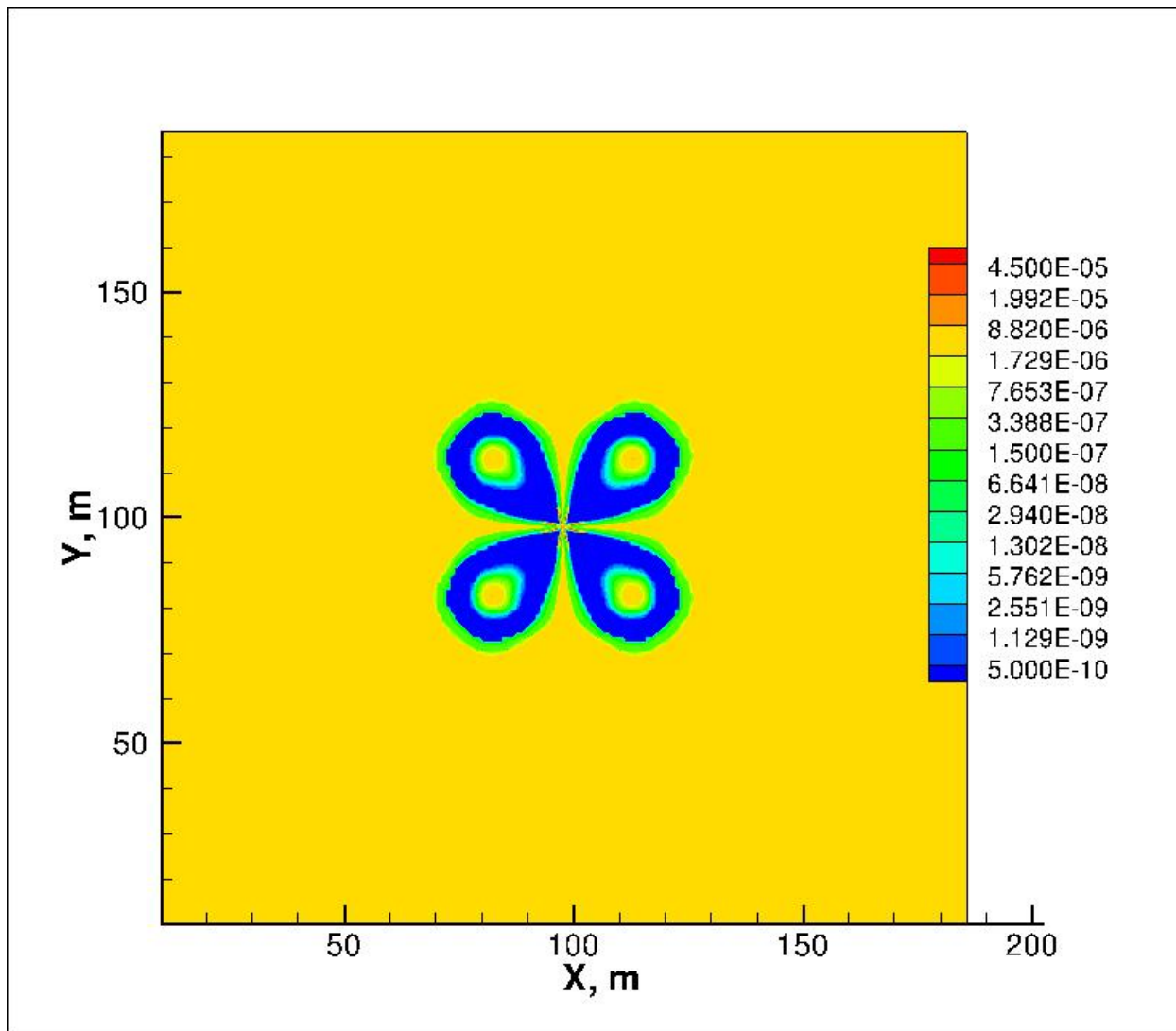


Figure 6.22 Adsorbed U(VI) concentration (M) distribution after 30 days of lactate biostimulation.

With much less U(VI) available in the system, there is negligible change in the amount of U(IV) produced in the system from acetate-stimulated bioreduction from the 10-day result (Figure 6.23).

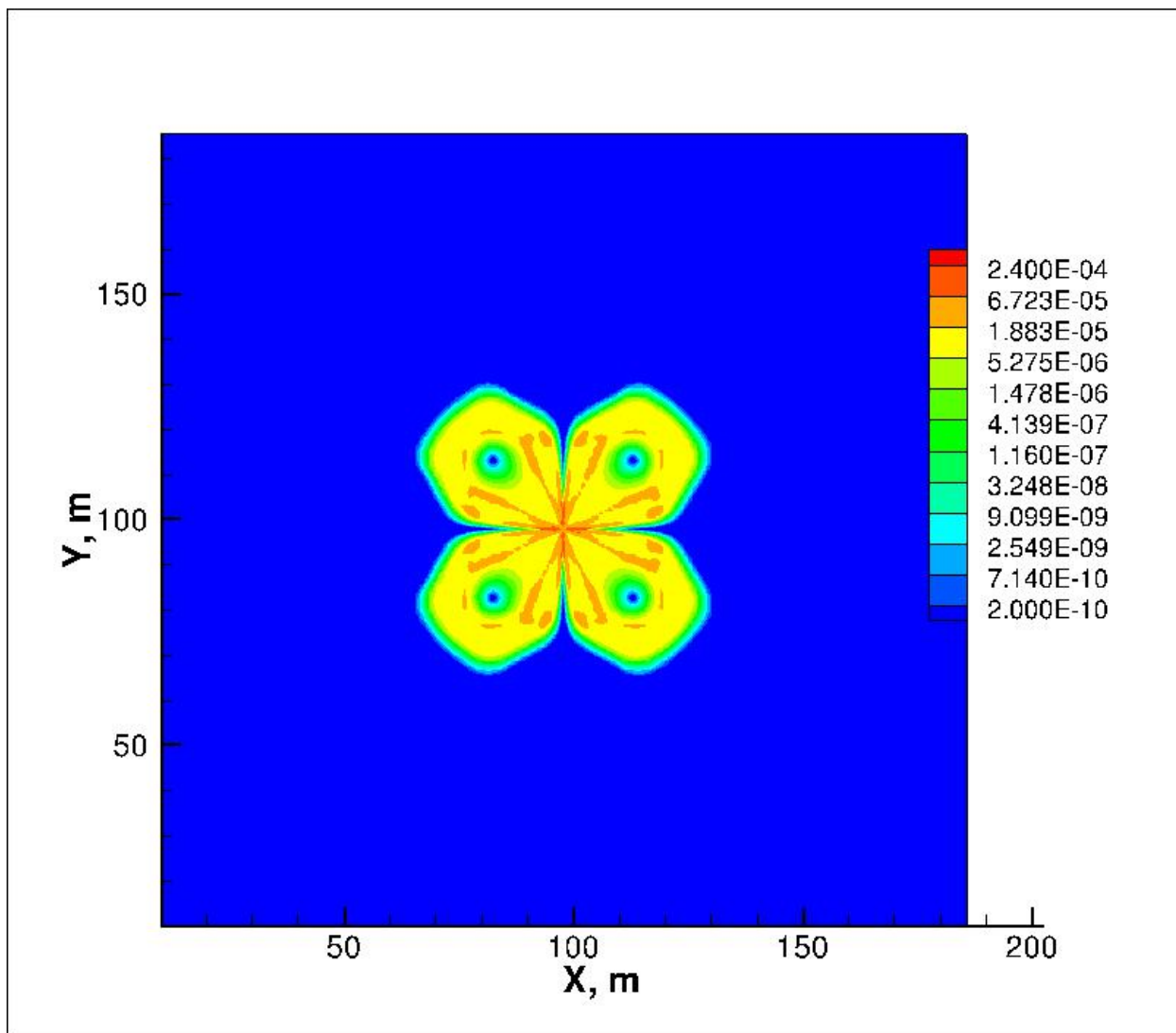


Figure 6.23 U(IV) concentration (M) distribution after 30 days of lactate biostimulation.

### 6.3.3 Modeling Results: Injectate without Terminal Electron Acceptors

The presented modeling results were based on an injectate without terminal electron acceptors (i.e., sulfate, U(VI)). The assumption was that the injectate would be recycled and the terminal electron acceptors would be removed in the bioreduction process. Under these simulated conditions, the general findings are

- A large fraction of the injected 10 mM lactate was not consumed by the time it reached the production well. This was due, in part, to the absence of sulfate in the injectate as well as the lack of a solid phase sulfate source. This limited the growth of sulfate reducing bacteria biomass, which is a direct control on the lactate reaction rate.

- Despite the relatively small fraction of lactate oxidized, the acetate produced from that oxidation was still sufficient to drive the reduction of the available U(VI). This implies that smaller lactate concentrations are likely to be equally effective at U(VI) bioreduction.
- Aqueous U(VI) will be displaced by the injectate and where bicarbonate from the microbially-mediated oxidation of lactate is sufficiently high, desorption of adsorbed U(VI) results. This process rapidly depletes the reservoir of labile U(VI) residing on the sediments.
- There is very little change in the mass of U(IV) precipitated after 30 days despite continuing, albeit rapidly declining, desorption from the sediments.

## 6.4 Background Injectate

In the previous section, the modeling assumed that the biologically-mediated TEAP reactions induced by the injection of 10 mM lactate would remove sulfate and U(VI) from the recycled groundwater used for the injectate. In this section, the modeling examines the other end member where the introduced injectate continuously retains the background water quality, including 10.6 mM sulfate and 0.3  $\mu\text{M}$  U(VI), (assumed baseline concentration) augmented by 3 mM lactate. The lowering of the injected lactate concentration from the 10 mM used previously to 3 mM reflects the assertion that smaller concentrations would still be effective in this modeled field scenario.

### 6.4.1 Lactate

In **Figure 6.24**, the continuous inclusion of the background terminal electron acceptors and lower 3 mM lactate concentration in the injectate leads to a rapid quasi-steady state of lactate concentrations limited to a small zone near the well. The distributions at days 2, 10, 20, and 30 are essentially identical. In this case, the addition of background levels of sulfate has resulted in the growth of SRB biomass which the lactate reaction rate is dependent upon. The quasi-steady state balances the lactate supply with the consumption through the lactate-based TEAP reactions.

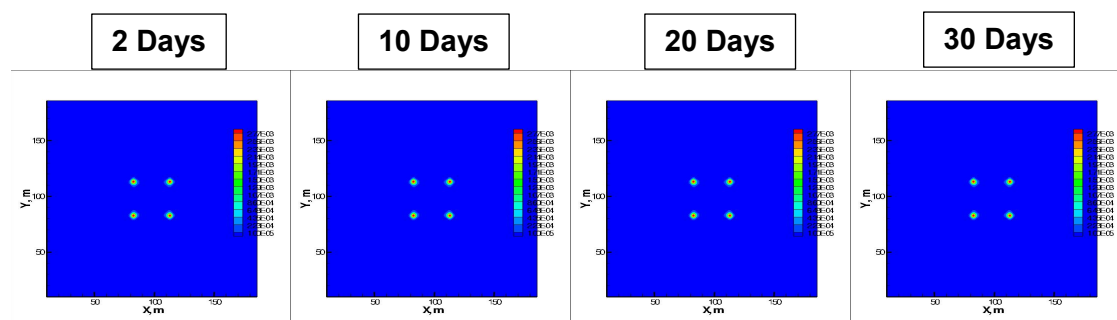


Figure 6.24 Lactate concentration distribution using continuous background concentrations of electron acceptors at 2, 10, 20, and 30 days.

### 6.4.2 Acetate

While the lactate concentration distribution is largely unchanged, the continuous production of acetate from the microbially-mediated lactate oxidation reactions results in a steadily increasing zone of elevated acetate concentrations (**Figure 6.25**). The growth of the elevated acetate zone is asymptotic over time as the highest acetate concentrations never reach the production well.

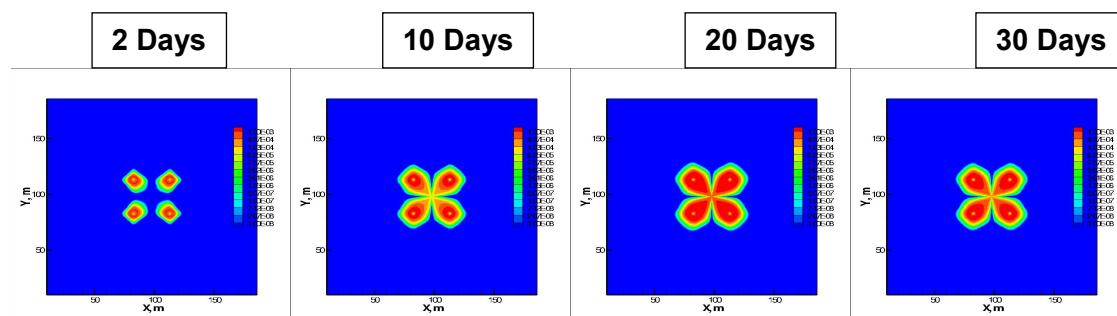


Figure 6.25 Acetate concentration distribution using continuous background concentrations of electron acceptors at 2, 10, 20, and 30 days.

### 6.4.3 U(VI)

While there is a low U(VI) background concentration in the injectate, 0.3 uM, the simulated aqueous U(VI) concentration distribution (**Figure 6.26**) is very similar to the previous injectate simulations. Aqueous U(VI) is largely displaced and is minimally supplied with U(VI) desorbing from the sediments.

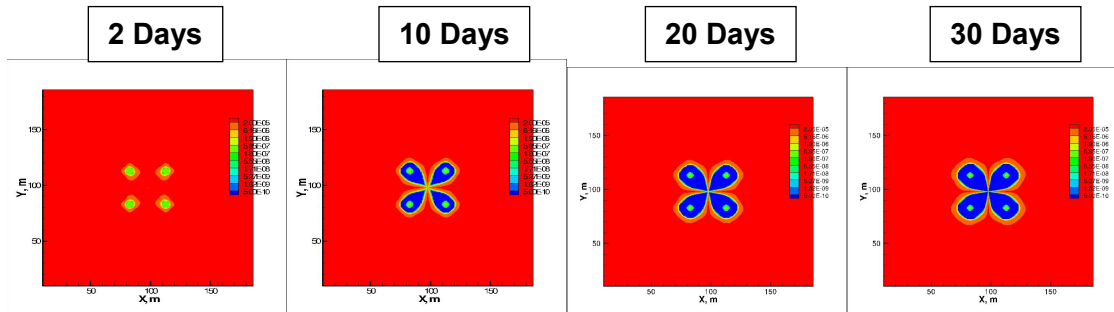


Figure 6.26 U(VI) concentration (M) distribution at 2, 10, 20, and 30 days using injectate with continuous background concentrations of electron acceptors.

#### 6.4.4 Adsorbed U(VI)

Similar to the previous injectate case, the adsorbed U(VI) is being largely depleted over the first 30 days (**Figure 6.27**). As the adsorbed U(VI) is the principal pool of labile U(VI) available for bioreduction, its depletion limits the amount of U(IV) produced.

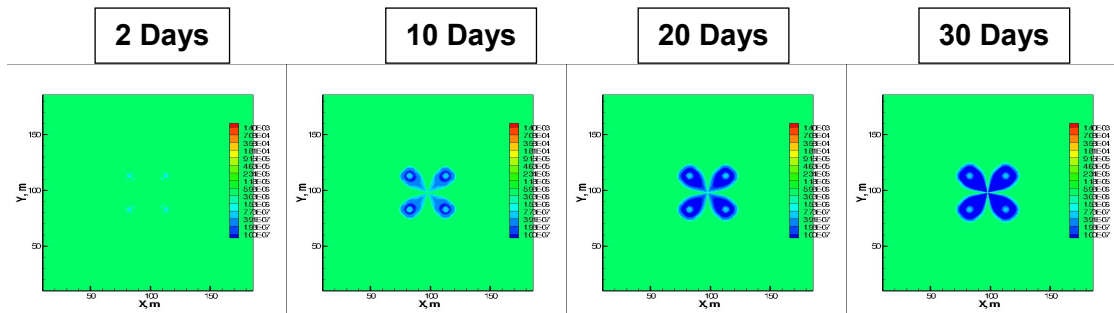


Figure 6.27 Adsorbed U(VI) concentration distribution at 2, 10, 20, and 30 days using injectate with continuous background concentrations of electron acceptors.

### 6.4.5 U(IV)

The production of U(IV) is thus asymptotic and the distribution of U(IV) concentrations is generally unchanged from 10 to 30 days (**Figure 6.28**).

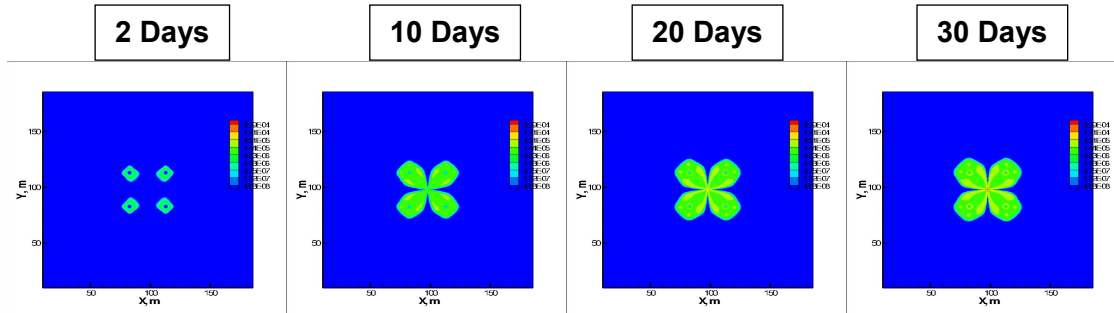


Figure 6.28 U(IV) mineral concentration (M) distribution at 2, 10, 20, and 30 days using injectate with continuous background concentrations of electron acceptors.

### 6.4.6 Fe(II)

Fe(III) is the principal terminal electron acceptor based on the amount consumed in microbially mediated TEAP reactions. **Figure 6.29** shows the asymptotic growth of Fe(II) in solution over the first 30 days. Highest concentrations are generally along the edges of the injectate lobes. The low aqueous Fe(II) concentrations in the vicinity of the well is the result of a combination of processes. The most reacted pool of Fe(III), FeOOH, is acetate-based. This means the availability of the acetate that is fueling the crystalline Fe(III) bioreduction is subject to lactate oxidation kinetics. Furthermore, the production of sulfide via lactate-based bioreduction of sulfate provides sulfide to react with the Fe(II) produced near the well.

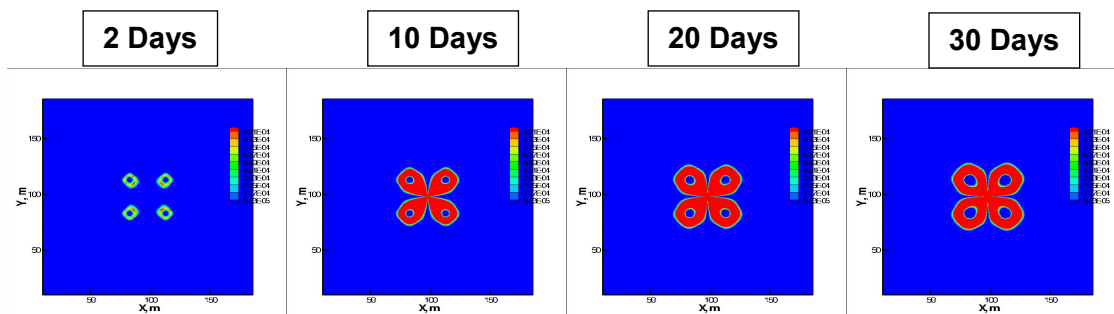


Figure 6.29 Aqueous Fe(II) concentration distribution at 2, 10, 20, and 30 days using injectate with continuous background concentrations of electron acceptors.

### 6.4.7 Phyllosilicate Fe(III)

Figures 6.30 and 6.31 show the minimal amount of phyllosilicate Fe(III) that is converted by either lactate- or acetate-based bioreduction.

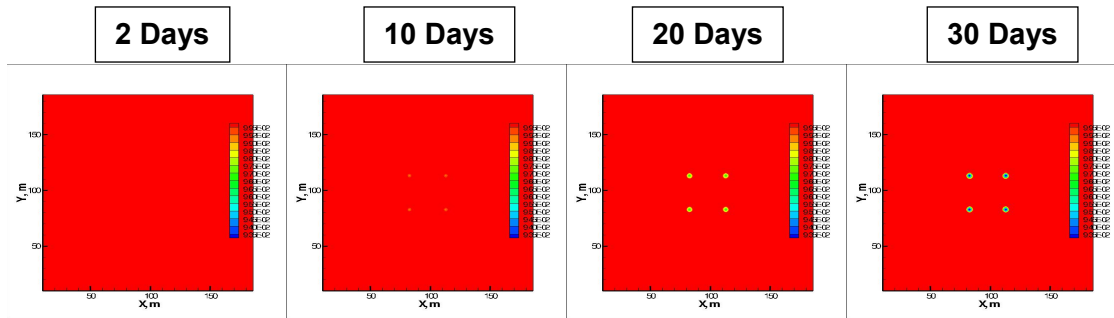


Figure 6.30 Lactate-based phyllosilicate Fe(III) concentration distribution at 2, 10, 20, and 30 days using injectate with continuous background concentrations of electron acceptors.

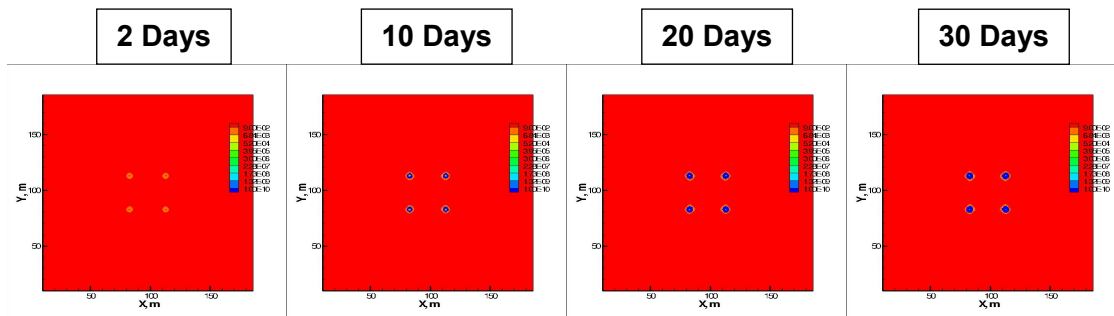


Figure 6.31 Acetate-based phyllosilicate Fe(III) concentration distribution at 2, 10, 20, and 30 days using injectate with continuous background concentrations of electron acceptors.

### 6.4.8 Goethite

Figure 6.32 shows the depletion of FeOOH mineral over the first 30 days of simulation. Only the small zone nearest the injection well is largely unreacted. The reductive FeOOH dissolution is controlled by acetate production which increases with the increasing residence time afforded by the slowing of pore velocity away from the wells.



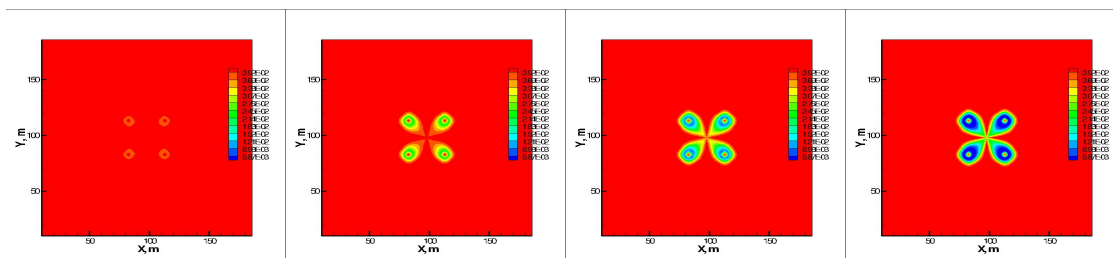


Figure 6.32 FeOOH (goethite) concentration distribution at 2, 10, 20, and 30 days using injectate with continuous background concentrations of electron acceptors.

### 6.4.9 FeS

The production of Fe(II) in the center of the lobe due to FeOOH dissolution is not reflected in the aqueous Fe(II) concentration distribution. This is because the formation of FeS (**Figure 6.33**) is consuming most of the aqueous Fe(II) in this region. In fact, the highest concentrations of FeS are in a zone centered around the injection well.

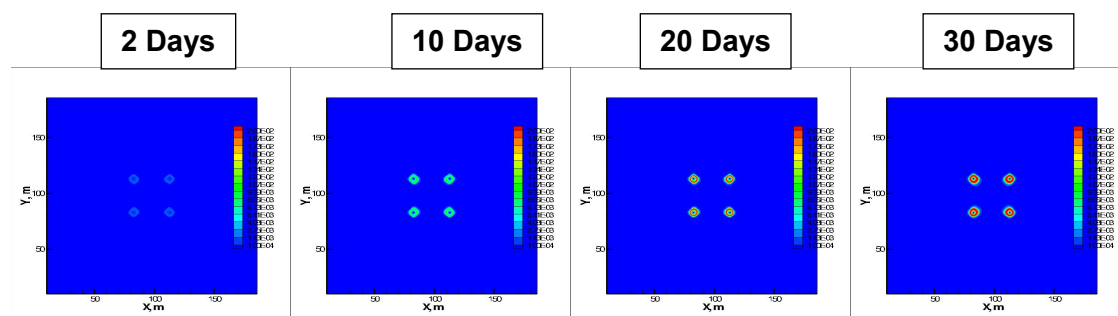


Figure 6.33 FeS mineral concentration distribution at 2, 10, 20, and 30 days using injectate with continuous background concentrations of electron acceptors.

### 6.4.10 Sulfate

While background sulfate is continuously being introduced through the injection well, sulfate concentrations are fairly uniform across the injectate lobe with the exception of a small zone around the injection well (**Figure 6.34**). This indicates that most of the 1 to 2 mM sulfate attenuation has occurred near the injection well and that these lower sulfate concentrations are then transported with negligible reaction after that. This is consistent with the rapid lactate consumption near the injection well which is primarily driven by the sulfate TEAP reaction, as evidenced by the negligible amount of lactate-based phyllosilicate Fe(III) reaction.

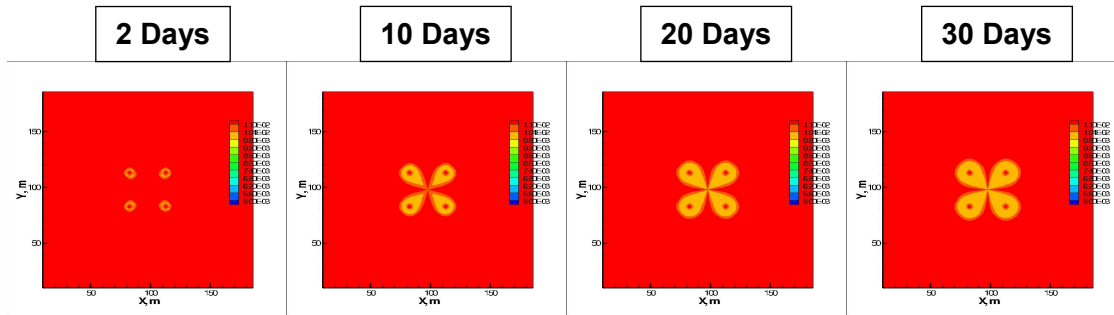


Figure 6.34 Aqueous sulfate concentration distribution at 2, 10, 20, and 30 days using injectate with continuous background concentrations of electron acceptors.

### 6.4.11 Sulfide

Unlike the residual sulfate that is transported with negligible reaction, the sulfide produced near the well reacts with the available Fe(II) to form FeS mineral. This occurs until the sulfide is largely depleted (**Figure 6.35**). This results in aqueous Fe(II) being found only in the parts of the injectate flow field that have been in the system the longest, the perimeter of the injectate lobes.

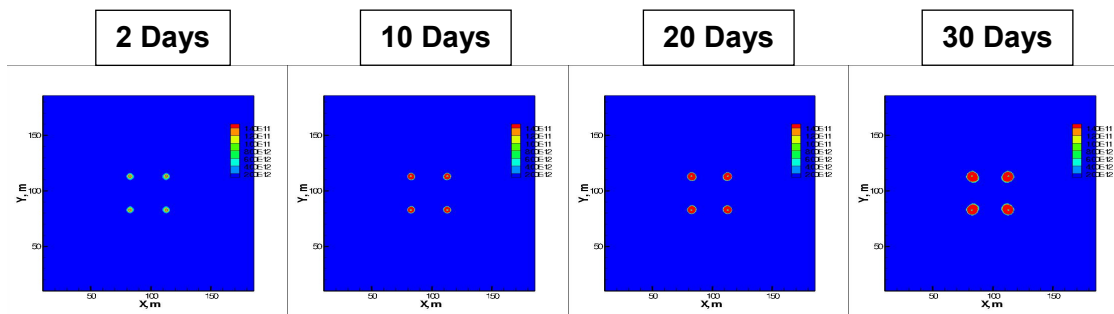


Figure 6.35 Aqueous sulfide concentration distribution at 2, 10, 20, and 30 days using injectate with continuous background concentrations of electron acceptors.

## 6.5 Summary of Field-Scale Model Findings

The findings that follow are based on a hypothetical scoping simulation of field-scale behaviors. The conceptualization of modeled processes, properties, and conditions is based on laboratory studies and general attributes of uranium ISR sites.

Two end member injectate water chemistry scenarios were modeled. In Section 6.3, the simulated injectate assumed that the recycling of biorestored groundwater with lactate amendment would effectively remove sulfate and U(VI) from solution, so these electron acceptors were not included in the injectate. In Section 6.4 the simulated injectate included background sulfate and U(VI) concentrations. Under both injectate scenarios, the aqueous uranium concentrations rapidly decreased to well below pre-baseline concentrations. This occurred after 30 days of lactate biostimulation using the reactions and rates determined from the laboratory studies. In the injectate-affected zones (“lobes”), aqueous and adsorbed U(VI) was generally depleted and U(IV) precipitated. The simulations were terminated after 30 simulated days because of the depletion of the solid phase U(VI) source, which led to essentially unchanging uranium concentrations in aqueous, sorbed, and mineral forms.

The behavior of Fe and S, however, was much more sensitive to injectate composition. In the absence of the electron acceptors, FeS (**Figure 6.19**) and aqueous sulfide (**Figure 6.20**) are distributed primarily away from the injection wells. This is consistent with displacement of aqueous sulfate by the injectate coupled with rate-limited sulfate bioreduction at the displacement front where lactate and sulfate coexist. Under the scenario with terminal electron acceptors in the injectate, the injection of sulfate and lactate allows continuous sulfate bioreduction in the vicinity of the well (**Figure 6.35**). Aqueous Fe(II), also being continuously produced principally by goethite bioreduction, reacts with the sulfide to form the secondary mineral FeS (**Figure 6.33**). This local accumulation of FeS near each injection well has about six times higher concentrations than the scenario without sulfate in the injectate. This could lead to potentially adverse effects on the hydraulics of the wellbore environment and thus, should be considered in the design controls for lactate, sulfate, and iron in the injectate.

While the time scale of uranium bioremediation in these simulations is similar to behaviors observed in bioremediation studies in less contaminated shallow aquifer systems, the idealizations in the modeling specification are thought to play a significant role in these results. In particular, the assumption of uniform material properties and the general accessibility of the solid-associated uranium for reaction will lead to the most rapid and complete uranium bioreduction. Higher initial concentrations of solid-associated U(VI), lower permeability zones that result in a slower release of U(VI), and more kinetic limitation of reaction rates would require longer periods of bioremediation to achieve similar results. While the modeling can accommodate more realistic attributes, it would still not be a substitute for a well-conceived field-driven experimental study. In part, this is due to the sensitivity of the engineered behaviors to site-specific geology, hydrology, biology, and geochemistry. In the absence of actual site geometries, conditions, and properties, the simulations are still capable of identifying issues for the bioremediation of uranium ISR sites as well as the design of a well-instrumented field study.

- The bioreduction of aqueous U(VI) to insoluble U(IV) removes U(VI) from the water column driving U(VI) desorption from the sediments. This cycle of liberating U(VI) into

solution followed by bioreduction progressively depletes the U(VI) from the treatment zone and establishes a lower redox potential for the system. Under the idealized modeling assumptions, the time scale of system stabilization is on the order of months.

- Even in the idealized hydrology and homogeneous property distribution, there are spatially variable distributions of uranium and other components of interest. This is because of the interplay between the spatially variable flow field (from the 5-spot well pattern) and the reaction kinetics which controls the availability of reactants for primary and subsidiary reactions. This results in behaviors that are different from the laboratory experiments even though the same reaction network and similar concentrations are employed: 1) rapid and complete consumption of lactate via the sulfate TEAP reaction, and 2) negligible impact of phyllosilicate Fe(III) TEAP reactions (lactate- and acetate-based).
- Injectate water quality can significantly affect the reaction rates of electron donors. This has implications for the recycling of groundwater from the production well as injectate. Assuming the maintenance of anaerobic conditions of the produced groundwater, terminal electron acceptors such as sulfate and U(VI) will be progressively removed. In particular, the progressive removal of sulfate as produced groundwater is recycled, amended with lactate, and re-injected, should reduce the amount of lactate needed. Thus, it's possible that the lactate supply can be reduced based on the monitoring of the produced groundwater. While this might reduce the potential for biofouling, it will also decrease the amount of FeS produced, which may slow the return to and/or weaken the maintenance of a stabilized low redox potential.
- In general, lactate concentrations considerably less than the 10 mM used in the laboratory column experiments are shown to be equally effective for U(VI) bioreduction. In an actual field implementation, this will be heavily dependent on the in situ rates.



## 7 Conclusions

A common restoration experience at uranium ISR sites is the persistence of elevated dissolved U(VI) (and other redox-sensitive metals) in spite of groundwater sweep, and above ground treatment (e.g., ion exchange, reverse osmosis). Restoring groundwater after uranium ISR extraction to the pre-operational baseline condition is not readily achievable. It typically takes many years to restore uranium ISR sites to regulatory standards. One motivation for this study was recent research, primarily in shallow aquifers, demonstrating that indigenous microorganisms could be stimulated to catalyze the conversion of U(VI) in contaminated groundwater to immobile U(IV), even when abiotic reductants were ineffective. In some of these uranium bioremediation field studies, vanadium and selenium present in the groundwater were also opportunistically reduced and removed from solution (Williams et al., 2012; Yelton et al., 2012).

The principal conclusion from this study is that engineered bioremediation of post-uranium ISR sites is a potentially viable alternative to standard restoration approaches. The experimental and modeling studies presented here suggest that biostimulation of the indigenous bacterial populations can be effective in lowering aqueous concentrations of uranium to acceptable levels. This takes place despite a very depauperate population of bacteria that may be the result of ISR operations or may be a natural characteristic of the site.

The naturally reducing and oxygen-depleted conditions that exist in uranium roll front aquifer systems are attributed, in part, to anaerobic bacteria in the presence of bioavailable organic carbon. These conditions are associated with very low concentrations of aqueous uranium, as well as redox sensitive metals (e.g., vanadium, selenium). Thus, the bioremediation principle proposed here is to return uranium ISR sites to their native hydrologic and geochemical conditions. The approach intends to (re-)establish an anaerobic microbial community that is operationally similar to the one that mediated the original formation of the uranium roll front ore zone. Working within the processes, properties, and conditions that a given aquifer will naturally support is thought to be more likely to succeed than engineering a new regime that must be artificially maintained. Conversely, the farther the targeted conditions are manipulated away from the natural unmitigated state of the subsurface system, the more difficult it will be to achieve long-term success.

The potential for engineered bioremediation was supported by batch, column, and solid phase studies presented in Section 3.0 using microbiologically preserved sediments from a post-ISR site at the Kingsville Dome operation of Uranium Resources, Inc. One advantage of using the Kingsville Dome sediments was that the maximum particle size of the field sample was less than 1 mm, which allowed the sediments to be used directly in the column experiments without the removal of the larger size fractions. This minimized one scale-up issue regarding the appropriateness of using the set of processes, reactions, and rates characterized from the column experiments to model the hypothetical field situation. The continuous introduction of 10 mM lactate into sediment columns resulted in the stimulation of indigenous microorganisms that continuously and effectively removed 20  $\mu\text{M}$  (5 mg/L) U(VI) in the influent over the  $\sim 1$  day column residence time, with resulting effluent uranium concentrations of less than 0.05  $\mu\text{M}$ .

Analyses of sediments recovered from columns at the end of the biostimulation stage showed that the sequestered uranium was primarily U(IV).

The conceptualization of the processes simulated during biostimulation begins with the bioreduction of aqueous U(VI) to sparingly soluble U(IV). This leads to the removal of U(VI) from solution and the elevation of bicarbonate concentrations, conditions that thermodynamically favor the desorption of U(VI) from the sediments. This cycle of U(VI) bioreduction and desorption progressively depletes aqueous U(VI) from the treatment zone and establishes a lower redox potential for the system. Under the idealized modeling assumptions, the time scale of system stabilization is on the order of months.

While the efficiency of uranium removal had some similarity to previous experimental investigations of biostimulation in shallow aquifer sediments, an important finding was that the biogeochemical processes also had some distinct differences: 1) lactate appeared to inhibit the bioreduction of U(VI) meaning that acetate, the product of lactate oxidation, was the primary electron donor for the U(VI) TEAP, 2) sulfate bioreduction was relatively small and independent of excess acetate, and 3) lactate- and acetate-specific Fe(III) pools were the most straightforward modeling assumptions to account for the subsequent rise in acetate concentrations to the near-maximum stoichiometric conversion from lactate. The interpretation of biogeochemical processes that are different than those observed in shallow sites, is strengthened by electron balances from the column studies that suggest, given the available Fe pools in the sediment, other processes are needed to account for the observed lactate/acetate consumption.

An important observation is that despite the very low biomass in the post-ISR sediment, biostimulation of metal-reducing bacteria led to essentially complete conversion of U(VI) to immobile U(IV), as well as a lowered redox potential that maintains the stability of the reduced uranium. The sediment sample from the field contained sulfate reducing bacteria, but no detectable *Geobacter*, which is commonly identified in shallow aquifer field biostimulation experiments. Lactate biostimulation of post-ISR sediments resulted in a different consortium of dominant microorganisms than observed in shallow aquifer sediments. This was characterized, in part, by the dominance of *Rhizobium* species that have been found in uranium-contaminated groundwater and sulfate reducing bacteria observed on filters collected during the late bioreduction phase of the column experiments. Five species of *Geobacter* were identified but at very low abundances. An open question is: "To what extent did exposure to the oxygenated lixiviant disrupt the pre-ISR microbial community?"

The effectiveness of bioremediation as a viable long-term remediation strategy requires conditions that maintain the stability of bioreduced uranium and other solid-associated redox-sensitive contaminants. As discussed in Chapter 3, introducing suboxic levels of dissolved oxygen (6  $\mu\text{M}$ ) into the column of bioreduced sediments resulted in the oxidative remobilization and elution of uranium. Clearly, dissolved oxygen can disrupt bioremediation and is an important parameter to monitor. A more thorough understanding of mechanisms resulting in oxidation and remobilization of bioreduced uranium is needed.

In the field, dissolved oxygen can enter the bioreduction zone through a variety of scenarios. It is conceivable that the pre-operational hydrology and oxidant load in the ore zone, (i.e., the

natural conditions that will be relied upon to maintain the restored ISR site) may limit the bioremediation efficiency or effectiveness. Over time, uranium ISR operations will load oxygen into less mobile regions of the porous media. After uranium ISR operations cease, the residual oxygen in these less mobile regions may become long-term diffusion-limited sources. Even during restoration, handling at the ground surface of the recycled and reinjected groundwater may inadvertently allow oxygen to be continuously introduced into the aquifer. Another scenario is for oxygenated water upgradient of the uranium roll front to be drawn through the ore zone by the flow field induced by pumping and injection wells during ISR or restoration. In general, there is a need to know what oxygen levels (and their duration) in the field can be tolerated by the bioremediation. This includes determining baseline levels of oxygen and/or nitrate that may limit the effectiveness of in situ bioremediation.

Even under the idealized hydrology and homogeneous solid phase property distribution, there are spatially variable distributions of uranium and other components of interest. This is because of the interplay between the spatially variable flow field induced by the operation of the 5-spot well pattern and the reaction kinetics which controls the availability of reactants for primary and subsidiary reactions. This results in behaviors that are different from the laboratory column experiments even though the same reaction network and similar concentrations are employed. These differences include 1) rapid and complete consumption of lactate via the sulfate TEAP reaction, and 2) negligible impact of phyllosilicate Fe(III) TEAP reactions (lactate- and acetate-based).

Based on the field-scale bioremediation modeling, injectate water quality can significantly affect the TEAP reaction rates. This has implications for the recycling of groundwater from the production well as injectate. Assuming the maintenance of anaerobic conditions of the produced groundwater, terminal electron acceptors such as sulfate and U(VI) will be progressively removed. In particular, the removal of sulfate should reduce the amount of lactate needed. Thus, it is possible that the lactate supply can be reduced based on the monitoring of the produced groundwater. While this might reduce the potential for biofouling, it will also decrease the amount of FeS produced. FeS and other Fe(II) minerals can suppress U(IV) reoxidation and remobilization of U(VI) by providing a reservoir of low redox potential (Abdelouas et al., 1999). This tradeoff between injectate concentration, biofouling, redox potential, and U(VI) bioreduction is a critical design issue for field-scale bioremediation.

Some of the findings from this study also relate to current ISR practices.

- It is very important to maintain anoxic conditions in the recirculated water used for reinjection during restoration. This will facilitate the removal of oxygen from the ore zone and the return to low redox potential conditions.
- The use of pumping and injection wells in an ISR wellfield results in a nonuniform flow field. While the zone of influence in the formation for the wellfield certainly has a pore volume associated with it, flow rates are location-dependent. Thus, the injection of one pore volume of solution into the formation does not mean that the entire matrix pore volume is exposed to the injectate. Some parts of the pore volume (e.g., along the most direct flow paths between the injection wells and the production well) are exposed to

considerably more injectate than paths with longer travel times. At some locations, several pore volumes will have been injected before injectate arrival.

The uranium bioremediation studies in shallow aquifers, laboratory studies with ISR sediments, and hypothetical field bioremediation simulations generally support the potential use of engineered biostimulation to catalyze the reduction of uranium and other redox-sensitive metals common to post-ISR groundwater. Absent from the weight of evidence for bioremediation of uranium ISR sites is a well-conceived field study. The few attempts to stimulate bioremediation of post-ISR aquifers via injection of electron donors (e.g., Smith Ranch) have yielded mixed results. The anecdotal descriptions of these attempts are insufficient to determine how bioremediation was engineered and monitored. We are, however, aware of a recent field bioremediation experiment performed at the Kingsville Dome ISR site using dissolved hydrogen as the electron donor to stimulate indigenous microorganisms that lowered U(VI) concentrations to pre-operational conditions and maintained those concentrations for 2 years (Cabezas et al., 2011).

## 7.1 Considerations

While the results of this study are generally supportive of a bioremediation alternative for uranium ISR sites, a significant weakness of the study is the lack of accounting for the natural physical and biogeochemical complexities in the subsurface environment. Spatially variable property distributions at multiple scales (e.g., intra- and inter-particle, pore- and continuum) lead to transport limitations in the delivery of reagents (e.g., lixiviants, reductants, electron donor) as well as the leaching of uranium (and other pollutants of interest) from the sediments. Superimposed on these physical heterogeneities are complex mineral assemblages and organic matter distributions that can have a profound effect on the biogeochemical reactions that underlie the bioremediation principle. This is the motivation for the principal recommendation from this study: the need for well-conceived field-studies. The recognition here is that the unique attributes of each ISR site are likely to prevent a “one size fits all” approach to bioremediation. So it is important to develop a sufficiently mechanistic understanding of the site-specific processes, properties, and conditions controlling bioremediation. This will facilitate determinations whether biostimulation can succeed and, if it can, what approach will be the most effective for a given site.

## 7.2 Potential Approach

The first specific consideration is to routinely measure dissolved oxygen and oxidation-reduction potential (ORP) or Eh. This is absolutely critical for the monitoring of redox-sensitive processes, yet is not generally performed or included in ISR guidelines for water quality indicators (cf., (NRC, 2009a) . These measurements would facilitate the assessment of the state of the post-ISR aquifer and potentially restoration effectiveness. Multiparameter sondes less than 2 inches in diameter are capable of being deployed at depths up to 250 meters. They can include pH, temperature, and specific conductivity measurements, which would provide additional information on the biogeochemical response to biostimulation.

Another consideration is to conduct laboratory studies using recovered post-ISR sediments and groundwater that have preserved the microbial consortia through maintenance of anaerobic conditions and refrigeration. The inclusion of laboratory studies was motivated by the differences in microbial consortia and behavior observed in the two biostimulated subsurface settings: uranium-contaminated groundwater plume in shallow unconfined aquifers and deep post-ISR confined aquifer. It is possible that the groundwater dissolved oxygen and metals concentrations immediately following the cessation of lixiviant injection may be sufficiently elevated to have toxicity effects on the microbial community. Thus, it may be necessary to employ a groundwater sweep to lower the initial post-ISR transient of elevated concentrations in chemical components of concern. In either case, laboratory biostimulation studies will be used to identify which electron donor-electron acceptor- microorganism combination is best suited to the site-specific situation, as well as potential optimizations in the electron donor delivery (e.g., pulsed), concentration, and duration. Possible electron donors include lactate, ethanol, acetate, and possibly hydrogen if a carbon source is included. It is very important for the laboratory experiments to replicate the biogeochemical conditions (e.g., pH, alkalinity, major ions, nutrients, terminal electron acceptors, etc.) as closely as possible. In this study, bicarbonate and sulfate concentrations directly impacted uranium behavior and the rate of lactate consumption.

With the current limited understanding of the processes controlling restoration, reactive transport modeling can be a useful tool to systematically couple transport and reaction processes for the assessment of conceptual process models. Similar to the approach in this study, the modeling framework can initially be built based on laboratory column experiments targeting the most effective electron donors and associated concentrations.

The leap to the field scale will require considerable monitoring data to guide the refinement of the process and constrain the modeling approach. Monitoring groundwater during bioremediation should include: temperature, dissolved oxygen, ORP/Eh, pH, alkalinity, major ions, nutrients, and terminal electron acceptors. This is consistent with the need for comprehensive field studies that focus on in situ bioremediation at ISR sites. Given the complexity of the bioremediation behaviors observed in the column study presented in this report (e.g., metabolic lag, inhibition, terminal electron acceptor pools, depletion, etc.), it is difficult to conceive an alternative to modeling. Thus, there is a need to increase the availability of reactive transport simulators and familiarize more practitioners with their use. One important aspect of modeling is that it provides an organizing principle for systematically addressing knowledge and data gaps. In this respect, modeling supports a technical basis for data collection activities.

### **7.2.1 Field Characterization and Monitoring**

In the first NUREG/CR of this series, “Technical Basis for Assessing Uranium Bioremediation Performance (Long et al., 2008),” background on uranium bioremediation, principles for collecting data, performing experiments and modeling, and a set of prioritized list of site information and performance monitoring parameters were identified (**Table 7.1**). The recommendations were based on DOE-sponsored research programs targeting uranium-contaminated plumes in shallow alluvial aquifers. Most of those recommendations are also

applicable to ISR sites where bioremediation is being considered. In **Figure 7.1**, we reproduce the summary of activities leading to full-scale field deployment. More recently, the U.S. EPA released a draft technical report on post-closure monitoring of uranium ISR sites (EPA, 2011), which has since been reviewed by their Science Advisory Board. The motivation for the report was to update the environmental protection standards to better address groundwater impacts of ISR uranium extraction. A principal focus was the sustainability of aquifer conditions at the end of restoration. The monitoring objectives (e.g., detection and compliance monitoring, long-term stewardship) also overlap with potential bioremediation implementations. We have adapted **Table 7.1** to include some of the specific recommendations of the EPA report.

Table 7.1 Prioritized Information and Monitoring Parameters for Assessment of Bioremediation of U(VI). Adapted from Long et al. (2008).

<b>Necessary Site Information: Uranium Distribution, Magnitude, Form, and Mobility</b>		
<b>Information area/parameter</b>	<b>Desired Range*</b>	<b>Comments</b>
Form of uranium and associated mobility/labability	± 30% of estimate	Experiments and sediment extractions to identify uranium form and potential for future mobility based on labile fraction. Evidence for insoluble uranium phase or vadose zone sources of uranium are particularly important.
Groundwater flow velocity (Darcy flux) and direction	±30% of estimate	Seasonal and episodic impact critical
Site hydrogeology: hydraulic conductivity, porosity, dispersivity, hydrofacies	NA	Fundamental to both site and process conceptual model
Remediation process conceptual model	NA	Fundamental to prioritization of monitoring parameters
Particle size characteristics including pore size distribution and surface area	NA	Reactive surface area, clays, upscaling lab to field
pH,DO, ORP, specific conductivity, and temperature measured at time of groundwater sampling in background and treatment zone using flow-cell with multiparameter probe	DO<0.5, ORP<0, conductivity initial increase, pH ~ steady	Values used as overall dynamic indicator of impact of bioremediation on subsurface geochemistry. Linkage of U(VI) concentrations with parameter change evidence for bioremediation process conceptual model
Aqueous electron acceptors and reduction byproducts in background and treatment zone: nitrate, nitrite, ammonium, Mn(IV/II), sulfate, sulfide	NA	Significant concentrations of oxygen and/or other electron acceptors above the U TEAP on the redox ladder must be addressed by the bioremediation strategy and their reduction products monitored. Sulfur isotopic analyses may provide supplemental information.
Fe(III) mineral abundance	NA	Fe(III) minerals provide sorption sites for Fe(II) & U(VI), terminal electron acceptor for iron-reducing bacteria, dissolved Fe(II) source
Fe(II), sulfide measured in field at time of sampling for U(VI) (up- gradient, treatment zone, and down-gradient)	Increasing Fe(II); sulfide indicator of sulfate reduction	Maintaining metal reduction may optimize U(VI) removal from groundwater; sulfate reduction may enhance long-term immobilization in sulfate-rich systems
Electron donor concentration in treatment zone	>0	Evidence of delivery and treatment zone distribution; consumption calculation based on tracer data
Tracer for electron donor	>0 in treatment zone	Typically Br is used for conservative tracer, accurate indication of donor distribution

Alkalinity, pCO <sub>2</sub> (measured in the field)	NA	Indicator of carbonate geochemistry, dissolved carbonate/bicarbonate forms strong anionic complexes with U(VI) to decrease its adsorption and increase its solubility and mobility
Concentration and oxidation states of metals (primary: U, V, Se, Mo, Mn, Fe, As, Ra, secondary: Ba, Cd, Cr, Pb, Ni, Ag, Th, Hg)	NA	Metal contaminants of interest including their redox status, TEAP reaction kinetics, solubility and sorption
Depth discrete U(VI) data (upper/mid/lower part of contaminated zone)	Regulatory Compliance Criteria	Decreased effectiveness of treatment in the uppermost part of the saturated zone may be problematic
Major cations and anions	NA	Provides additional evidence for dominant geochemical aqueous complexation and mineral solubility reactions
Impact of treatment process on groundwater flow directions	Dependent on background flow	Provides assurance that groundwater is not rerouted around treatment zone
<b>Desirable Performance Monitoring Parameters</b>		
<b><i>Parameter/Method</i></b>	<b><i>Desired Range or Response*</i></b>	<b><i>Comments</i></b>
In situ redox status of U using in situ sediment incubators (ISIs)	Significant U(IV) present	Evidence that precipitation of U(IV) is occurring in situ obtained via differential U extraction.
Microbiological assessment using coupons or in situ incubators	Shift to metal and/or sulfate reduction	Evidence for desired in situ microbial respiration obtained from deploying coupons or in situ incubators in well bores and periodically measuring microbial parameters (see text for additional discussion)
Depth-discrete sediment sampling/extraction for U, Fe, AVS; V, Se, Mo, Mn, As, Ra	NA	Evidence for conversion of terminal electron acceptors
Major dissolved gas components in groundwater: O <sub>2</sub> , N <sub>2</sub> , CO <sub>2</sub> , H <sub>2</sub> S, methane; CO, N <sub>2</sub> O	NA	Evidence for key TEAPs and microbial metabolism
Time-lapse GPR cross-well or electrical measurements	Shift in geophysical attributes in zone of electron donor	Indicates two-dimensional distribution of electron donor, although impact of other transformations on geophysical signatures must be assessed and errors associated with tomographic inversion procedures can 'smear' amendment boundary.

Table 7.1 (Continued)

<b>Optional Performance Monitoring Parameters</b>		
<b><i>Parameter/Method</i></b>	<b><i>Desired Range or Response*</i></b>	<b><i>Comments</i></b>
Depth-discrete data for mandatory geochemical parameters	NA	Characterizes spatial distribution of fundamental biogeochemistry in aquifer
Depth-discrete data for desirable monitoring parameters	NA	Characterizes spatial distribution of desired biogeochemical reactions in aquifer
Impact of treatment process on hydraulic properties	<15% change	Documents possible system clogging of pores
Organic and inorganic carbon analyses	NA	More accurate documentation of natural organic carbon sources carbonate geochemistry
Microbiological assessment performed directly on sampling of treatment zone materials	Shift to metal and/or sulfate reduction	Measurements directly on groundwater filtrates or sediment cores provide "gold standard" assessment of microbial community structure (e.g., PLFA, 16S, DNA/RNA chip arrays, or functional chip arrays)
In situ redox status of U by direct sampling of in situ materials		U(IV)/U(VI) measurements on in situ sediments provide "ground truth" for U bioreduction; similarly for V, Se, Mn
Time-lapse electrical resistivity and self potential tomography	NA	Can indicate the 3-D distribution of dominant TEAPs
Time-lapse seismic tomography	NA	Sensitive to gas evolution and secondary mineral precipitation
NA = not applicable		
*Based on expected values judge to have an impact on MCL.		

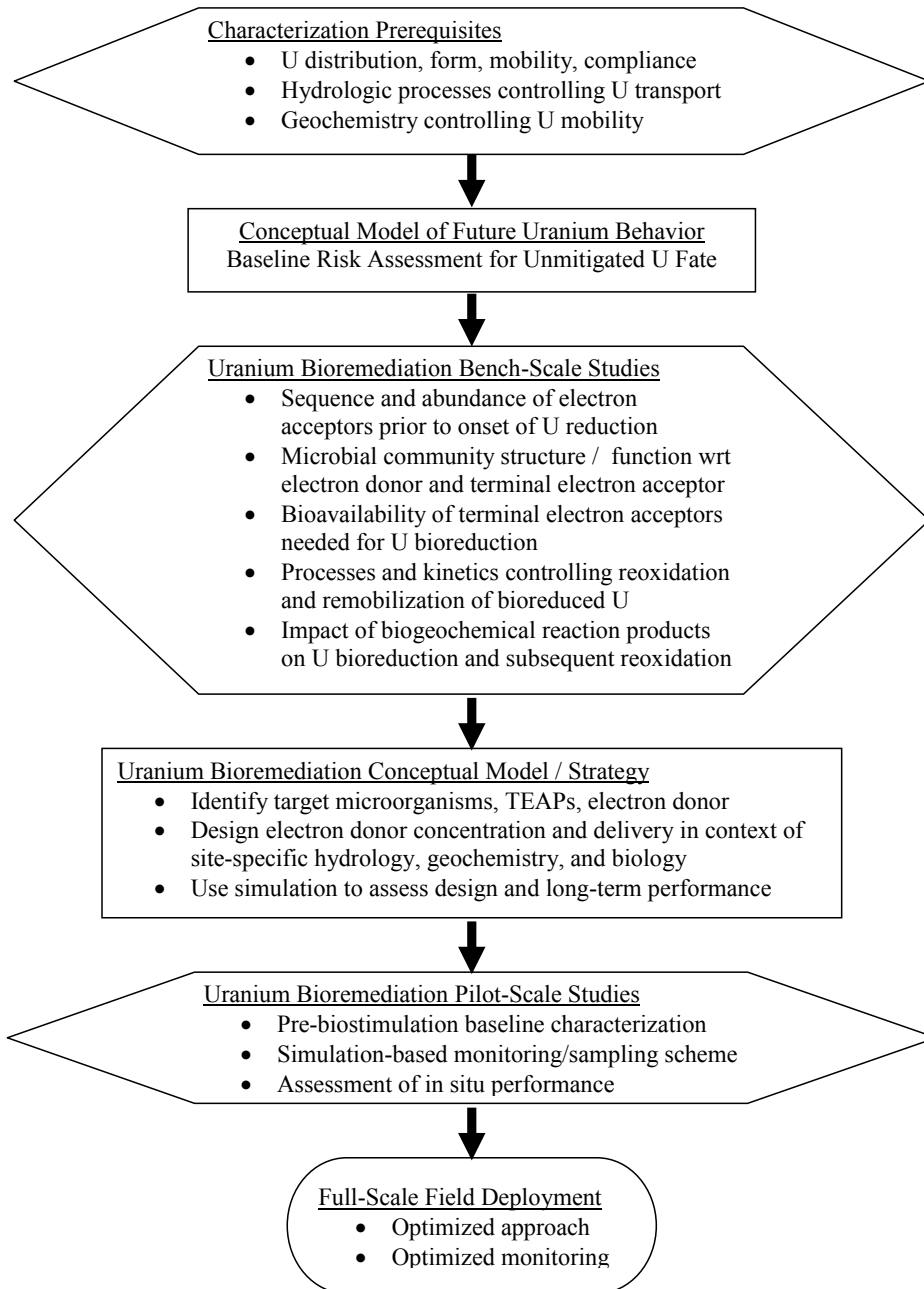


Figure 7.1 Summary of activities leading to full-scale bioremediation deployment in the field. Hexagons represent characterization steps. Rectangles represent analysis and design steps (Long et al., 2008).

### **7.2.3 Long-Term Monitoring**

Post-restoration stability monitoring begins when regulators determine that restoration is complete and a steady-state has been established. The duration of stability phase monitoring is specified in the license application but has historically been as short as 6 months. This period has been shown to be insufficient at some well fields monitored for longer periods of time, where increasing contaminant concentrations were discovered. More recently, the trend has been to increase the monitoring period to a year; however, the actual period of stabilization can be several years if low permeability zones that are sequestering contaminants or leachants become significant sources. With this potential behavior, a longer-term performance-based approach that matches the site-specific time scales would seem to be appropriate.



## 8 Reference List

- Abdelouas, A., Lutze, W., Gong, W., Nuttall, E.H., Strietelmeier, B.A. and Travis, B.J., 2000. Biological reduction of uranium in groundwater and subsurface soil. *Science of the Total Environment*, 250(1–3): 21-35.
- Abdelouas, A., Lutze, W. and Nuttall, H.E., 1999. Oxidative dissolution of uraninite precipitated on Navajo sandstone. *Journal of Contaminant Hydrology*, 36(3-4): 353-375.
- Alessi, D.S., Uster, B., Veeramani, H., Suvorova, E.I., Lezama-Pacheco, J.S., Stubbs, J.E., Bargar, J.R. and Bernier-Latmani, R., 2012. Quantitative Separation of Monomeric U(IV) from UO<sub>2</sub> in Products of U(VI) Reduction. *Environmental Science & Technology*, 46(11): 6150-6157.
- Anderson, R.T., Rooney-Varga J.N., Gaw, C.V., Lovley, D.R. 1998, Anaerobic benzene oxidation in the Fe(III) reduction zone of petroleum contaminated aquifers: *Environmental Science and Technology*, v. 32, p.1222–1229.
- Anderson, R.T., Vrionis, H.A., Ortiz-Bernad, I., Resch, C.T., Long, P.E., Dayvault, R., Karp, K., Marutzky, S., Metzler, D.R., Peacock, A., White, D.C., Lowe, M. and Lovley, D.R., 2003. Stimulating the in situ activity of *Geobacter* species to remove uranium from the groundwater of a uranium-contaminated aquifer. *Applied and Environmental Microbiology*, 69(10): 5884-5891.
- Arrendondo, A. G., 1991, The Geology and Hydrology of the Kingsville Dome In-situ Leach Uranium Mine: M.S. Thesis, Texas A & M University, Kingsville Texas.
- Barlett, M., Moon, H.S., Peacock, A.A., Hedrick, D.B., Williams, K.H., Long, P.E., Lovley, D. and Jaffe, P.R., 2012. Uranium reduction and microbial community development in response to stimulation with different electron donors. *Biodegradation*, 23(4): 535-546.
- Baveye, P., Vandevivere, P., Hoyle, B.L., DeLeo, P.C., and Sanchez De Lozada, D., 1998, Environmental impact and mechanisms of the biological clogging of saturated soils and aquifer materials: *Critical Reviews in Environmental Science and Technology*, v. 28, no. 2, p. 123-191.
- Bernhard, G., Geipel, G., Reich, T., Brendler, V., Amayri, S. and Nitsche, H., 2001. Uranyl(VI) carbonate complex formation: Validation of the Ca<sub>2</sub>UO<sub>2</sub>(CO<sub>3</sub>)<sub>3</sub>(aq.) species. *Radiochimica Acta*, 89(8): 511-518.
- Bernier-Latmani, R., Veeramani, H., Vecchia, E.D., Junier, P., Lezama-Pacheco, J.S., Suvorova, E.I., Sharp, J.O., Wigginton, N.S. and Bargar, J.R., 2010. Non-uraninite Products of Microbial U(VI) Reduction. *Environmental Science & Technology*, 44(24): 9456-9462.
- Beyenal, H., Sani, R.K., Peyton, B.M., Dohnalkova, A.C., Amonette, J.E., and Lewandowski, Z., 2004, Uranium Immobilization by Sulfate-Reducing Biofilms: *Environmental Science and Technology*, v. 38, no. 7, p. 2067-2074.

- Bi, Y., Hyun, S.P., Kukkadapu, R., and Hayes, K.F., 2013, Oxidative dissolution of UO<sub>2</sub> in a simulated groundwater containing synthetic nanocrystalline mackinawite: *Geochimica et Cosmochimica Acta*, v. 102, p. 175-190.
- Borch, T., Roche, N. and Johnson, T.E., 2012. Determination of contaminant levels and remediation efficacy in groundwater at a former in situ recovery uranium mine. *Journal of Environmental Monitoring*, 14(7): 1814-1823.
- Boyanov, M.I., Fletcher, K.E., Kwon, M.J., Rui, X., O'Loughlin, E.J., Löffler, F.E. and Kemner, K.M., 2011. Solution and Microbial Controls on the Formation of Reduced U(IV) Species. *Environmental Science & Technology*, 45(19): 8336-8344.
- Brooks, S.C., Fredrickson, J.K., Carroll, S.L., Kennedy, D.W., Zachara, J.M., Plymale, A.E., Kelly, S.D., Kemner, K.M. and Fendorf, S., 2003. Inhibition of bacterial U(VI) reduction by calcium. *Environmental Science & Technology*, 37(9): 1850-1858.
- Brunk, C.F., Avaniss-Aghajani, E., Brunk, C.A. 1996, A computer analysis of primer and probe hybridization potential with bacterial small-subunit rRNA sequences: *Applied and Environmental Microbiology*, v. 62, p. 872–879.
- Cabezas, J., Clapp, L.W. and Gamboa, Y., 2011. Pilot study to evaluate hydrogen injection for stimulating reduction and immobilization of uranium in groundwater at an ISR mining site, Geological Society of America Annual Meeting. Geological Society of America, Minneapolis, MN.
- Callister, S.J., Wilkins, M.J., Nicoral, C.D., Williams, K.H., Banfield, J.F., VerBerkmoes, N.C., Hettich, R.L., N'Guessan, A.L., Mouser, P.J., Elifantz, H., Smith, R.D., Lovley, D.R., Lipton, M.S. and Long, P.E., 2010. Analysis of Biostimulated Microbial Communities from Two Field Experiments Reveals Temporal and Spatial Differences in Proteome Profiles. *Environmental Science and Technology*, In Press.
- Cameco-Resources, 2009. Mine Unit B Ground Water Restoration, Smith Ranch-Highland Operation, Glenrock, Wyoming.
- Cameco-Resources, 2012. Smith Ranch Project Source Material License No. SUA-1548 Renewal, U.S. Nuclear Regulatory Commission, Washington, D.C. .
- Campbell, K.M., Kukkadapu, R., Qafoku, N.P., Peacock, A.D., Leshner, E., Williams, K.H., Bargar, J.R., Wilkins, M.J., Figueroa, L., Ranville, J., Davis, J.A. and Long, P.E., 2012. Geochemical, mineralogical and microbiological characteristics of sediment from a naturally reduced zone in a uranium-contaminated aquifer. *Applied Geochemistry*, 27: 1499-1511.
- Campbell, K.M., Veeramani, H., Urich, K.U., Blue, L.Y., Giammar, D.E., Bernier-Latmani, R., Stubbs, J.E., Suvorova, E., Yabusaki, S., Lezama-Pacheco, J.S., Mehta, A., Long, P.E. and Bargar, J.R., 2011. Oxidative Dissolution of Biogenic Uraninite in Groundwater at Old Rifle, CO. *Environmental Science & Technology*, 45(20): 8748-8754.
- Cardenas, E., Wu, W.M., Leigh, M.B., Carley, J., Carroll, S., Gentry, T., Luo, J., Watson, D., Gu, B.H., Ginder-Vogel, M., Kitanidis, P.K., Jardine, P.M., Zhou, J.Z., Criddle, C.S., Marsh, T.L. and Tiedje, J.M., 2010. Significant Association between Sulfate-Reducing Bacteria and Uranium-Reducing Microbial Communities as Revealed by a Combined Massively Parallel Sequencing-Indicator Species Approach. *Applied and Environmental Microbiology*, 76(20): 6778-6786.

- Cline, J.D., 1969, Spectrophotometric determination of hydrogen sulfide in natural waters: *Limnology and Oceanography*, v. 14, p. 454-458.
- Crow Butte Resources, I., 2000. Mine Unit 1 Restoration Report, Crow Butte Uranium Project, Crow Butte Resources, Inc., Crawford, Nebraska.
- Davis, J.A. and Curtis, G.P., 2007. Consideration of Geochemical Issues in Groundwater Restoration at Uranium In-Situ Leach Mining Facilities. Report NUREG CR--6870, Nuclear Regulatory Commission, Rockville, MD.
- Davis, J.A., Curtis, G.P., Wilkins, M.J., Kohler, M., Fox, P., Naftz, D.L. and Lloyd, J.R., 2006. Processes affecting transport of uranium in a suboxic aquifer. *Physics and Chemistry of the Earth*, 31(10-14): 548-555.
- Dong, W.M. and Brooks, S.C., 2006. Determination of the formation constants of ternary complexes of uranyl and carbonate with alkaline earth metals ( $Mg^{2+}$ ,  $Ca^{2+}$ ,  $Sr^{2+}$ , and  $Ba^{2+}$ ) using anion exchange method. *Environmental Science & Technology*, 40(15): 4689-4695.
- Dong, W.M., Ball, W.P., Liu, C.X., Wang, Z.M., Stone, A.T., Bai, J. and Zachara, J.M., 2005. Influence of calcite and dissolved calcium on uranium(VI) sorption to a Hanford subsurface sediment. *Environmental Science & Technology*, 39(20): 7949-7955.
- Englert, A., Hubbard, S.S., Williams, K.H., Li, L. and Steefel, C.I., 2009. Feedbacks Between Hydrological Heterogeneity and Bioremediation Induced Biogeochemical Transformations. *Environmental Science & Technology*, 43(14): 5197-5204.
- EPA, 2011. Considerations Related to Post-Closure Monitoring of Uranium In-Situ Leach/In-Situ Recovery (ISL/ISR) Sites, U.S. Environmental Protection Agency, Washington, D.C.
- Fang, Y., Wilkins, M.J., Yabusaki, S.B., Lipton, M.S. and Long, P.E., 2012. Evaluation of a Genome-Scale In Silico Metabolic Model of *Geobacter Metallireducens* Using Proteomic Data from a Field Biostimulation Experiment. *Applied and Environmental Microbiology* 78(24): 8735-8742.
- Fang, Y., Yabusaki, S.B., Morrison, S.J., Amonette, J.P. and Long, P.E., 2009. Multicomponent reactive transport modeling of uranium bioremediation field experiments. *Geochimica Et Cosmochimica Acta*, 73(20): 6029-6051.
- Fang, Y.L., Yabusaki, S.B. and Yeh, G.T., 2006. A general simulator for reaction-based biogeochemical processes. *Computers & Geosciences*, 32(1): 64-72.
- Fang, Y.L., Yeh, G.T. and Burgos, W.D., 2003. A general paradigm to model reaction-based biogeochemical processes in batch systems. *Water Resources Research*, 39(4)(4): -.
- Fuller, C.C., Van Geen, A., Baskaran, M., and Anima, R., 1999, Sediment chronology in San Francisco Bay, California, defined by  $^{210}Pb$ ,  $^{234}Th$ ,  $^{137}Cs$ , and  $^{239,240}Pu$ : *Marine Chemistry*, v. 64, no. 1-2, p. 7-27.
- Galloway, W.E. 1977, Catahoula Formation of the Texas coastal plain: depositional systems, composition, structural development, ground-water flow history, and uranium deposition: The University of Texas at Austin, Bureau of Economic Geology Report of Investigations No. 87
- Geets, J., Borrernans, B., Diels, L., Springael, D., Vangronsveld, J., van der Lelie, D., Vanbroekhoven, K., 2006, DsrB genebased DGGE for community and diversity surveys of sulfate-reducing bacteria: *J Microbiol Methods*, v. 66, p. 194-205.

- Gu, B.H., Wu, W.M., Ginder-Vogel, M.A., Yan, H., Fields, M.W., Zhou, J., Fendorf, S., Criddle, C.S. and Jardine, P.M., 2005. Bioreduction of uranium in a contaminated soil column. *Environmental Science & Technology*, 39(13): 4841-4847.
- Guillaumont, R., Fanghanel, T., Fugen, J., Grenthe, I., Neck, V., Palmer, D.A. and Rand, M.H., 2003. *Chemical Thermodynamics 5. Update on the Chemical Thermodynamics of Uranium, Neptunium, Plutonium, Americium, and Technetium*. Nuclear Energy Agency. Elsevier, Amsterdam.
- Habicht, K.S., and Canfield, D.E., 1997, Sulfur isotope fractionation during bacterial sulfate reduction in organic-rich sediments: *Geochimica et Cosmochimica Acta*, v. 61, no. 24, p. 5351-5361.
- Hall, S., 2009. Groundwater restoration at uranium in-situ recovery mines, south Texas coastal plain, U.S. Geological Survey Open-File Report 2009-1143.
- Holmes, D.E., Finneran, K.T., O'Neil, R.A., Lovley, D.R., 2002, Enrichment of members of the family Geobacteraceae associated with stimulation of dissimilatory metal reduction in Uranium-contaminated aquifer sediments: *Applied and Environmental Microbiology*, v. 68, p.2300-2306.
- Holmes, D.E., O'Neil, R.A., Vrionis, H.A., N'Guessan, L.A., Irene, O.R., Larrahondo, M.J., Adams, L.A., Ward, J.A., Nicoll, J.S., Nevin, K.P., Chavan, M.A., Johnson, J.P., Long, P.E., Lovley, D.R. 2007, Subsurface clade of Geobacteraceae that predominates in a diversity of Fe(III)-reducing subsurface environments: *ISME Journal*, v. 1, p. 663-677.
- Hsieh, Y-P., and Yang, C-H., 1989, Diffusion methods for the determination of reduced inorganic sulfur species in sediments: *Limnology & Oceanography*, v. 34, no. 6, p. 1126-1130.
- Hsieh, Y-P., Chung, S-W., Tsau, Y-J., and Sue, C-T., 2002, Analysis of sulfides in the presence of ferric minerals by diffusion methods: *Chemical Geology*, v. 182, no. 2-4, p. 195-201.
- Hua, B., and Deng, B., 2008, Reductive immobilization of uranium(VI) by amorphous iron sulfide: *Environmental Science & Technology*, v. 42, no. 23, p. 8703-8708.
- Hunter, K.S., Wang, Y.F. and Van Cappellen, P., 1998. Kinetic modeling of microbially-driven redox chemistry of subsurface environments: coupling transport, microbial metabolism and geochemistry. *Journal of Hydrology*, 209(1-4): 53-80.
- Hyun, S.P., Davis, J.A., Sun, K., and Hayes, K.F., 2012, Uranium(VI) reduction by iron(II) monosulfide mackinawite: *Environmental Science & Technology*, v. 46, no. 6, p. 3369-3376.
- Jeon, B.H., Dempsey, B.A., Burgos, W.D., Barnett, M.O. and Roden, E.E., 2005. Chemical reduction of U(VI) by Fe(II) at the solid-water interface using natural and synthetic Fe(III) oxides. *Environmental Science & Technology*, 39(15): 5642-5649.
- Jones, E.J.P. ,Voytek, M.A. ,Lorah, M.M., Kirshtein, J.D., 2006, Characterization of a Microbial Consortium Capable of Rapid and Simultaneous Dechlorination of 1,1,2,2-Tetrachloroethane and Chlorinated Ethane and Ethene Intermediates: *Bioremed Journal*, v. 10, p.153-168.

- Junier, P., Fruttschi, M., Wigginton, N.S., Schofield, E.J., Bargar, J.R., and Bernier-Latmani, R., 2009, Metal reduction by spores of *Desulfotomaculum reducens*: *Environmental Microbiology*, v. 11, no. 12, p. 3007-3017.
- Komlos, J., Kukkadapu, R.K., Zachara, J.M., and Jaffé, P.R., 2007, Biostimulation of iron reduction and subsequent oxidation of sediment containing Fe-silicates and Fe-oxides: Effect of redox cycling on Fe(III) bioreduction: *Water Research*, v. 41, no. 13, p. 2996-3004.
- Komlos, J., Mishra, B., Lanzirrotti, A., Myneni, S.C.B. and Jaffe, P.R., 2008a. Real-time speciation of uranium during active bioremediation and U(IV) reoxidation. *Journal of Environmental Engineering-Asce*, 134(2): 78-86.
- Komlos, J., Moon, H.S., and Jaffé, P.R., 2008a, Effect of sulfate on the simultaneous bioreduction of iron and uranium: *Journal of Environmental Quality*, v. 37, no. 6, p. 2058-2062.
- Komlos, J., Peacock, A., Kukkadapu, R.K. and Jaffe, P.R., 2008b. Long-term dynamics of uranium reduction/reoxidation under low sulfate conditions. *Geochimica Et Cosmochimica Acta*, 72(15): 3603-3615.
- Kuivila, K.M., Murray, J.W., Devol, A.H., and Novelli, P.C., 1989, Methane production, sulfate reduction and competition for substrates in the sediments of Lake Washington: *Geochimica et Cosmochimica Acta*, v. 53, no. 2, p. 409-416.
- Lands, C.o.H.M.o.F. and Council, N.R., 1999. *Hardrock Mining on Federal Lands*. The National Academies Press.
- Lane, D. J. 1991. 16S/23S rRNA sequencing. In: *Nucleic acid techniques in Bacterial Systematics*, E. Stackebrandt and M. Goodfellow, eds., John Wiley and Sons, New York, NY. pp. 115–148.
- Lee, J-H., Fredrickson, J.K., Kukkadapu, R.K., Boyanov, M.I., Kemner, K.M., Lin, X., Kennedy, D.W., Bjornstad, B.N., Konopka, A.E., Moore, D.A., Resch, C.T., and Phillips, J.L., 2012, Microbial reductive transformation of phyllosilicate Fe(III) and U(VI) in fluvial subsurface sediments: *Environmental Science and Technology*, v. 46, no. 7, p. 3721-3730.
- Li, L., Steefel, C.I., Kowalsky, M.B., Englert, A. and Hubbard, S.S., 2010. Effects of physical and geochemical heterogeneities on mineral transformation and biomass accumulation during biostimulation experiments at Rifle, Colorado. *Journal of Contaminant Hydrology*, 112(1-4): 45-63.
- Li, L., Steefel, C.I., Williams, K.H., Wilkins, M.J. and Hubbard, S.S., 2009. Mineral Transformation and Biomass Accumulation Associated With Uranium Bioremediation at Rifle, Colorado. *Environmental Science & Technology*, 43(14): 5429-5435.
- Liu, C.X., Zachara, J.M., Zhong, L.R., Kukkadupa, R., Szecsody, J.E. and Kennedy, D.W., 2005. Influence of sediment bioreduction and reoxidation on uranium sorption. *Environmental Science & Technology*, 39(11): 4125-4133.
- Long, P.E., Yabusaki, S.B., Meyer, P.D., Murray, C.J. and N'Guessan, A.L., 2008. *Technical Basis for Assessing Uranium Bioremediation Performance*. NUREG/CR-6973, U.S. Nuclear Regulatory Commission.

- Lovley, D.R., and Klug, M.J., 1986, Model for the distribution of sulfate reduction and methanogenesis in freshwater sediments: *Geochimica et Cosmochimica Acta*, v. 50, no. 1, p. 11-18.
- Lovley, D.R., and Phillips, E.J.P., 1987. Rapid assay for microbially reducible ferric iron in aquatic sediments: *Applied and Environmental Microbiology*, v. 53, no. 7, p. 1536-1540.
- Lovley, D.R., and Phillips, E.J.P., 1992, Bioremediation of uranium contamination with enzymatic uranium reduction: *Environmental Science & Technology*, v. 26, no. 11, p. 2228-2234.
- Lovley, D.R., Phillips, E.J.P., Gorby, Y.A. and Landa, E.R., 1991. Microbial Reduction of Uranium: *Nature*, 350(6317): 413-416.
- Lovley, D.R., Roden, E.E., Phillips, E.J.P., and Woodward, J.C., 1993, Enzymatic iron and uranium reduction by sulfate-reducing bacteria: *Marine Geology*, v. 113, no. 1-2, p. 41-53.
- Luo, J., Wu, W.M., Carley, J., Ruan, C.M., Gu, B.H., Jardine, P.M., Criddle, C.S. and Kitanidis, P.K., 2007. Hydraulic performance analysis of a multiple injection-extraction well system. *Journal of Hydrology*, 336(3-4): 294-302.
- Lusher, J., 2003. Standard Review Plan for In Situ Leach Uranium Extraction License Applications, U.S. Nuclear Regulatory Commission, Washington, D.C. 20555.
- Martens, C.S., and Val Klump, J., 1980, Biogeochemical cycling in an organic-rich coastal marine basin-I. Methane sediment-water exchange processes: *Geochimica et Cosmochimica Acta*, v. 44, no. 3, p. 471-490.
- Maurer, M., and Rittmann, B.E., 2004, Modeling intrinsic bioremediation for interpret observable biogeochemical footprints of BTEX biodegradation: The need for fermentation and abiotic chemical processes: *Biodegradation*, v. 15, no. 6, p. 405-417.
- Mayhew, L.E., Webb, S.M., and Templeton, A.S., 2011, Microscale imaging and identification of Fe speciation and distribution during fluid-mineral reactions under highly reducing conditions: *Environmental Science & Technology*, v. 45, no. 10, p. 4468-4474.
- Moon, H.S., Komlos, J. and Jaffe, P.R., 2007. Uranium reoxidation in previously bioreduced sediment by dissolved oxygen and nitrate. *Environmental Science & Technology*, 41(13): 4587-4592.
- Moon, H.S., Komlos, J. and Jaffé, P.R., 2009. Biogenic U(IV) oxidation by dissolved oxygen and nitrate in sediment after prolonged U(VI)/Fe(III)/SO<sub>4</sub><sup>2-</sup> reduction. *Journal of Contaminant Hydrology*, 105(1-2): 18-27.
- Moon, H.S., McGuinness, L., Kukkadapu, R.K., Peacock, A.D., Komlos, J., Kerkhof, L.J., Long, P.E., and Jaffé, P.R., 2010, Microbial reduction of uranium under iron- and sulfate-reducing conditions: Effect of amended goethite on microbial community composition and dynamics: *Water Research*, v. 44, no. 14, p. 4015-4028.
- Muyzer, G., and Stams, A.J.M., 2008, The ecology and biotechnology of sulphate-reducing bacteria: *Nature Reviews Microbiology*, v. 6, no. 6, p. 441-454.

- Nicot, J-P, B. Scanlon, C. Yang, J. Gates, 2010, Geological and Geographical Attributes of the South Texas Uranium Province: Bureau of Economic geology, The University of Texas at Austin, Austin Texas, 78713-8924
- NRC, 1997. Final Environmental Impact Statement to Construct and Operate the Crownpoint Uranium Solution Mining Project, Crownpoint, New Mexico NUREG-1508, U.S. Nuclear Regulatory Commission, Washington, D.C.
- NRC, 2009a. Generic Environmental Impact Statement for In-Situ Leach Uranium Milling Facilities NUREG-1910, U.S. Nuclear Regulatory Commission, Washington, D.C.
- NRC, 2009b. "Staff Assessment of Groundwater Impacts from Previously Licensed In-Situ Uranium Recovery Facilities." Memorandum from C. Miller to Chairman Jaczko, et al., July 10, 2009. Nuclear Regulatory Commission, Washington, D.C.
- NRC, 2009c. Data on Groundwater Impacts at the Existing ISR Facilities, ML091770385, U.S. Nuclear Regulatory Commission, Washington, D.C.
- NRC, 2009d. NRC Regulatory Issue Summary 2009-05, Uranium Recovery Policy Regarding (1) The Process for Scheduling Licensing Reviews of Applications for New Uranium Recovery Facilities and (2) The Restoration of Groundwater at Licensed uranium in situ Recovery Facilities, April 2009, ML083510622, U.S. Nuclear Regulatory Commission, Washington, DC.
- Oremland, R.S., Marsh, L.M., and Polcin, S., 1982, Methane production and simultaneous sulphate reduction in anoxic, salt marsh sediments: *Nature*, v. 296, no. 5853, p. 143-145.
- Parkhurst, D.L. and Appelo, C.A.J., 1999. User's Guide to PHREEQC (Version 2) ---- A Computer Program for Speciation, Batch-Reaction, One-Dimensional Transport, and Inverse Geochemical Calculations, U.S. Geological Survey, Denver, CO.
- Poulton, S.W., Krom, M.D. and Raiswell, R., 2004. A revised scheme for the reactivity of iron (oxyhydr)oxide minerals towards dissolved sulfide: *Geochimica et Cosmochimica Acta*, 68(18): 3703-3715.
- Sanchez de Lozada, D., Vandevivere, P., Baveye, P., and Zinder, S., 1994, Decrease of the hydraulic conductivity of sand columns by *Methanosarcina barkeri*: *World Journal of Microbiology and Biotechnology*, v. 10, no. 3, p. 325-333.
- Sani, R.K., Peyton, B.M., Dohnalkova, A. and Amonette, J.E., 2005. Reoxidation of reduced uranium with iron(III) (hydr)oxides under sulfate-reducing conditions: *Environmental Science & Technology*, 39(7): 2059-2066.
- Schmidt, C., 1987. Groundwater restoration and stabilization at the Ruth ISL Test Site in Wyoming, USA, In *Situ Leaching of Uranium: Technical, Environmental and Economic Aspects*. International Atomic Energy Agency, Vienna, Austria.
- Schofield, E.J., Veeramani, H., Sharp, J.O., Suvorova, E., Bernier-Latmani, R., Mehta, A., Stahlman, J., Webb, S.M., Clark, D.L., Conradson, S.D., Ilton, E.S., and Bargar, J.R., 2008, Structure of biogenic uraninite produced by *Shewanella oneidensis* strain MR-1: *Environmental Science & Technology*, v. 42, no. 21, p. 7898-7904.
- Sharp, J.O., Lezama-Pacheco, J.S., Schofield, E.J., Junier, P., Ulrich, K.U., Chinni, S., Veeramani, H., Margot-Roquier, C., Webb, S.M., Tebo, B.M., Giammar, D.E., Bargar, J.R. and Bernier-Latmani, R., 2011. Uranium speciation and stability after reductive

- immobilization in aquifer sediments. *Geochimica et Cosmochimica Acta*, 75(21): 6497-6510.
- Singer, D.M., Farges, F., and Brown Jr., G.E., 2009, Biogenic nanoparticulate  $UO_2$ : Synthesis, characterization, and factors affecting surface reactivity: *Geochimica et Cosmochimica Acta*, v. 73, no. 12, p. 3593-3611.
- Stookey, L.L. 1970. Ferrozine – A new spectrophotometric reagent for iron. *Anal. Chem.*, v. 42, p.779-781.
- Stucker, V.K., Williams, K.H., Robbins, M.J. and Ranville, J.F., 2012. Arsenic geochemistry in a biostimulated aquifer: An aqueous speciation study (in review): *Environmental Toxicology and Chemistry*.
- Suzuki, Y., Kelly, S.D, Kemner, K.M, and Banfield, J.F. 2004, Enzymatic U(VI) reduction by *Desulfosporosinus* species: *Radiochimica Acta*, v. 92, p. 11–16.
- Tuominen, L., Kairesalo, T., and Hartikainen, H., 1994, Comparison of methods for inhibiting bacterial activity in sediment: *Applied and Environmental Microbiology*, v. 60, no. 9, p. 3454-3457.
- Ulrich, K.-., Ilton, E.S., Veeramani, H., Sharp, J.O., Bernier-Latmani, R., Schofield, E.J., Bargar, J.R., and Giammar, D.E., 2009, Comparative dissolution kinetics of biogenic and chemogenic uraninite under oxidizing conditions in the presence of carbonate: *Geochimica et Cosmochimica Acta*, v. 73, no. 20, p. 6065-6083.
- Uranium Resources, Inc, 2012, 2011 Annual Report, Annual meeting of Stockholders, June 2012.
- Veeramani, H., Alessi, D.S., Suvorova, E.I., Lezama-Pacheco, J.S., Stubbs, J.E., Sharp, J.O., Dippon, U., Kappler, A., Bargar, J.R. and Bernier-Latmani, R., 2011. Products of abiotic U(VI) reduction by biogenic magnetite and vivianite: *Geochimica et Cosmochimica Acta*, 75(9): 2512-2528.
- Veeramani, H., Scheinost, A. C., Monsegue, N., Qafoku, N. P., Kukkadapu, R., Newville, M., Lanzirrotti, A., Pruden, A., Murayama, M., and Hochella, M.F., 2013. Abiotic Reductive Immobilization of U(VI) by Biogenic Mackinawite: *Environmental Science & Technology*, v. 47, no. 5, p. 2361-2369.
- Vrionis, H.A., Anderson, R.T., Ortiz-Bernad, I., O'Neill, K.R., Resch, C.T., Peacock, A.D., Dayvault, R., White, D.C., Long, P.E. and Lovley, D.R., 2005. Microbiological and geochemical heterogeneity in an in situ uranium bioremediation field site. *Applied and Environmental Microbiology*, 71(10): 6308-6318.
- Wagner, M., Roger, A.J., Flax, J.L., Brusseau, G.A., Stahl, D.A., 1998, Phylogeny of dissimilatory sulfite reductases supports an early origin of sulfate respiration: *J Bacteriol*, v. 180, p.2975–2982.
- Wan, J., Tokunaga, T.K., Brodie, E., Wang, Z., Zheng, Z., Herman, D., Hazen, T.C., Firestone, M.K., and Sutton, S.R., 2005, Reoxidation of bioreduced uranium under reducing conditions: *Environmental Science & Technology*, v. 39, no. 16, p. 6162-6169.

- Webb, S.M., 2005. SIX PACK: a graphical user interface for XAS analysis using IFEFFIT. *Phys. Scripta*, v. T115, p. 1011-1034.
- Williams, K.H., Long, P.E., Davis, J.A., Wilkins, M.J., N'Guessan, A.L., Steefel, C.I., Yang, L., Newcomer, D., Spane, F.A., Kerkhof, L.J., McGuinness, L., Dayvault, R. and Lovley, D.R., 2011. Acetate Availability and its Influence on Sustainable Bioremediation of Uranium-Contaminated Groundwater. *Geomicrobiology Journal*, 28(5-6): 519-539.
- Williams, K.H., Wilkins, M.J., N'Guessan, A.L., Arey, B., Dodova, E., Dohnalkova, A., Holmes, D.E., Yang, L., Lovley, D.R., Banfield, J.F. and Long, P.E., 2012. Field evidence of selenium bioreduction in a uranium contaminated aquifer (in review). *Environ. Microbiol. Rep.*
- Wilson, T.A., Amirbahman, A., Norton, S.A., Voytek, M.A., 2010, A record of phosphorus dynamics in oligotrophic lake sediment: *J. Paleolimnol*, v. 44, p.279-294.
- Wrighton, K.C., Thomas, B.C., Sharon, I., Miller, C.S., Castelle, C.J., VerBerkmoes, N.C., Wilkins, M.J., Hettich, R.L., Lipton, M.S., Williams, K.H., Long, P.E. and Banfield, J.F., 2012. Fermentation, Hydrogen and Sulfur Metabolism in Multiple Uncultivated Bacterial: Phyla. *Science*, 337.
- Wu, W.M., Carley, J., Fienen, M., Mehlhorn, T., Lowe, K., Nyman, J., Luo, J., Gentile, M.E., Rajan, R., Wagner, D., Hickey, R.F., Gu, B.H., Watson, D., Cirpka, O.A., Kitanidis, P.K., Jardine, P.M. and Criddle, C.S., 2006a. Pilot-scale in situ bioremediation of uranium in a highly contaminated aquifer. 1. Conditioning of a treatment zone. *Environmental Science & Technology*, 40(12): 3978-3985.
- Wu, W.M., Carley, J., Gentry, T., Ginder-Vogel, M.A., Fienen, M., Mehlhorn, T., Yan, H., Caroll, S., Pace, M.N., Nyman, J., Luo, J., Gentile, M.E., Fields, M.W., Hickey, R.F., Gu, B.H., Watson, D., Cirpka, O.A., Zhou, J.Z., Fendorf, S., Kitanidis, P.K., Jardine, P.M. and Criddle, C.S., 2006b. Pilot-scale in situ bioremediation of uranium in a highly contaminated aquifer. 2. Reduction of U(VI) and geochemical control of U(VI) bioavailability. *Environmental Science & Technology*, 40(12): 3986-3995.
- Yabusaki, S.B., Fang, Y., Long, P.E., Resch, C.T., Peacock, A.D., Komlos, J., Jaffe, P.R., Morrison, S.J., Dayvault, R.D., White, D.C. and Anderson, R.T., 2007. Uranium removal from groundwater via in situ biostimulation: Field-scale modeling of transport and biological processes. *Journal of Contaminant Hydrology*, 93(1-4): 216-235.
- Yabusaki, S.B., Fang, Y., Waichler, S.R. and Long, P.E., 2010. Processes, Properties, and Conditions Controlling In Situ Bioremediation of Uranium in Shallow, Alluvial Aquifers, NUREG/CR-7014, Nuclear Regulatory Commission, Washington, D.C.
- Yabusaki, S.B., Fang, Y., Williams, K.H., Murray, C.J., Ward, A.L., Dayvault, R.D., Waichler, S.R., Newcomer, D.R., Spane, F.A. and Long, P.E., 2011. Variably saturated flow and multicomponent biogeochemical reactive transport modeling of a uranium bioremediation field experiment. *Journal of Contaminant Hydrology*, 126(3-4): 271-290.
- Yabusaki, S.B., Fang, Y.L. and Waichler, S.R., 2008. Building conceptual models of field-scale uranium reactive transport in a dynamic vadose zone-aquifer-river system. *Water Resources Research*, 44(12): 24.
- Ye, S., Sleep, B.E., and Chien, C., 2009, The impact of methanogenesis on flow and transport in coarse sand: *Journal of Contaminant Hydrology*, v. 103, no. 1-2, p. 48-57.

Yelton, A.P., Williams, K.H., Wrighton, K.C., Handley, K.M. and Banfield, J.F., 2012. Vanadate and acetate biostimulation of contaminated sediments decreases diversity, selects for specific taxa and decreases aqueous V<sup>5+</sup> concentration (in review). *Applied and Environmental Microbiology*.

Zheng, Z.P., Tokunaga, T.K. and Wan, J.M., 2003. Influence of calcium carbonate on U(VI) sorption to soils. *Environmental Science and Technology*, 37: 5603-5608.

**BIBLIOGRAPHIC DATA SHEET**

(See instructions on the reverse)

NUREG/CR-7167

2. TITLE AND SUBTITLE

Assessing the Potential for Bioremediation of Uranium In Situ Recovery Sites

3. DATE REPORT PUBLISHED

MONTH

YEAR

June

2014

4. FIN OR GRANT NUMBER

N6651 and N6648

5. AUTHOR(S)

S. B. Yabusaki, Y. Fang, S.R. Waichler, C. C. Fuller,  
K. Akstin, P.E. Long, and M. Fuhrmann

6. TYPE OF REPORT

Technical

7. PERIOD COVERED (Inclusive Dates)

8. PERFORMING ORGANIZATION - NAME AND ADDRESS (If NRC, provide Division, Office or Region, U. S. Nuclear Regulatory Commission, and mailing address; if contractor, provide name and mailing address.)

Pacific Northwest National Laboratory, Richland, WA 99352  
and U.S. Geological Survey, Menlo Park, CA 94025

9. SPONSORING ORGANIZATION - NAME AND ADDRESS (If NRC, type "Same as above", if contractor, provide NRC Division, Office or Region, U. S. Nuclear Regulatory Commission, and mailing address.)

Division of Risk Assessment, Office of Nuclear Regulatory Research, U.S. Nuclear Regulatory Commission, Rockville, MD 20852

10. SUPPLEMENTARY NOTES

11. ABSTRACT (200 words or less)

In-situ recovery (ISR) of uranium, in which oxidizing solutions are injected into the subsurface to liberate uranium from its solid matrix, results in groundwater contamination that needs to be remediated. As a result, many of the post-operational contaminants found at ISR sites are in oxidized, soluble forms. In situ bioremediation (ISB) is the stimulation of indigenous microorganisms by adding electron donors (e. g. acetate) to groundwater, catalyzing the immobilization of targeted contaminants. This report assesses the potential effectiveness of ISB to chemically reduce these contaminants to their immobile forms through a series of batch and column experiments, reaction product characterization, microbial analysis, and coupled process modeling of hypothetical field-scale ISR restoration including: coupled flow, transport, and biogeochemical processes. The models are intended to help integrate and scale up the predicted effects from the laboratory to the field. The experimental and modeling studies presented here suggest that biostimulation of indigenous bacterial populations can be effective in lowering aqueous concentrations of uranium at ISR sites to acceptable levels. While bioremediation has the potential for more effective restoration, shorter remediation times, and lower cost, it is an unproven technology that relies on the stability of uranium and other metals that are left in place.

12. KEY WORDS/DESCRIPTORS (List words or phrases that will assist researchers in locating the report.)

bioremediation, bioremediation, in situ recovery, in situ leach, uranium, in situ bioremediation, groundwater

13. AVAILABILITY STATEMENT

unlimited

14. SECURITY CLASSIFICATION

(This Page)

unclassified

(This Report)

unclassified

15. NUMBER OF PAGES

16. PRICE



Federal Recycling Program





**UNITED STATES  
NUCLEAR REGULATORY COMMISSION**  
WASHINGTON, DC 20555-0001  
-----  
OFFICIAL BUSINESS



**NUREG/CR-7167**

**Assessing the Potential for Bioremediation of Uranium In Situ Recovery Sites**

**June 2014**